

Novel Systems for Bioimaging and Photodynamic Therapy: BODIPY dyes and silica-based nanocarriers

PhD Thesis by

Ruth Prieto Montero

Under Supervision of
Dr. Virginia Martinez Martinez and Prof. Iñigo Lopez Arbeloa

Leioa, 13th of March 2020

A mi familia

Agradecimientos

Para empezar me gustaría dar las gracias a todos aquellos que de alguna manera han contribuido al desarrollo de esta tesis doctoral.

En primer lugar agradecer a la Universidad del País Vasco (UPV/EHU) por la concesión de una beca predoctoral que me ha permitido llevar a cabo este trabajo en el grupo de Espectroscopia Molecular bajo la supervisión de Dr. Virginia Martínez Martínez y el Prof. Iñigo López Arbeloa. Agradecerles a ellos, mis directores, la confianza depositada, esfuerzo y apoyo durante estos cuatro años. Dar las gracias también a mis compañeros de laboratorio, a Nerea con quien di los primeros pasos de lo que sería esta tesis, a Rebeca, Ainhoa y Eurne con quienes he compartido despacho, hacéis que la rutina sea menos rutina, y como no al resto del grupo Edu, Jorge, Leire, Hegoi, Teresa, Xabi, Carolina, por los buenos ratos que hemos pasado juntos, habéis hecho que estos años pasen volando.

Por otro lado, agradecer el apoyo científico recibido por los Servicios Generales de la Facultad de Ciencia y Tecnología de la UPV/EHU (SGIKER), por las medidas de Espectroscopia de Fotones emitidos por Rayos X, Microscopia Electrónica de Barrido y Microscopia Electrónica de Trasmisión y a la Dr. Maite Insausti de Química Inorgánica (UPV/EHU) por dejarnos hacer uso del Dynamic Light Scattering.

Además, he de mencionar los grupos de investigación con los que hemos colaborado y que han hecho posible que esta tesis sea multidisciplinar. Los grupos de síntesis orgánica dirigidos por la Dr. M.J. Ortiz y el Prof. S. Moya (Universidad Complutense de Madrid) y por el Dr. J.L. Chiara (Instituto de Química Orgánica General en Madrid) junto con los grupos que han llevado a cabo los ensayos *in vitro*, la Prof. Á. Villanueva (Universidad Autónoma de Madrid), la Dr. M. D. Chiara (Universidad de Oviedo y Hospital Central de Asturias) y especialmente al Dr. Alberto Katsumiti (UPV/EHU). Gracias por vuestra profesionalidad, y compromiso.

Añadir, mi sincero agradecimiento al Dr. Carlos Baleizão por acogerme junto con Dr. Jose Paulo Farinha y Prof. José Manuel Gaspar Martinho en su grupo en el centro de Química Física Molecular del Instituto Técnico durante mi estancia en Lisboa. Igualmente, gracias a todo el grupo y especialmente a Tiago e Ines por la ayuda recibida tanto a nivel científico como a nivel personal. Moito Obrigada.

II

Por último, pero no menos importante quería agradecer a todas las personas que desde fuera del mundo científico han formado parte de esta etapa, porque me habéis ayudado a sacar esta tesis adelante. A mis amigas, por los momentos de desconexión, a Ene por obligarme a romper con la rutina y estar siempre dispuesto a ayudarme y finalmente a mi familia; primos, tíos, abuelos y primordialmente a mi hermano y a mis padres que habéis tenido la paciencia de estar ahí día a día apoyándome, animándome y cuidándome. Hacéis que todo sea más fácil. Asko maite zaituztet.

Thank you very much to everybody, Muchas gracias a todos, Moito obrigada.

Summary

Novel dyes, mainly based on the BODIPY chromophore, together with new synthesized photoactive hybrid nanosystems are proposed for their potential implement in medical applications, particularly, bioimaging and photodynamic therapy (PDT), for cancer diseases.

Different substitution patterns on the BODIPY allows the modulation of its chemophysical properties on demand. Firstly, the control modification of the dye skeleton has promoted advanced fluorescence biomarkers, with enhanced solubility in aqueous media and selectivity for a specific organelle of the cell, *i.e.* mitochondrial, by the addition of hydrophilic tags and specific biomolecules, respectively. Secondly, the functionalization of BODIPY is aimed to attain improved photosensitizers with high singlet oxygen production, by the introduction of halogen atoms together with π -conjugated systems to shift the absorption into the clinic window or by attaching electron-donor groups to activate intramolecular charge transfer states able to balance fluorescence capability and oxygen generation for theragnostic applications (imaging + PDT).

Moreover, new synthesized spherical silica nanoparticles (nonporous, mesoporous and ormosil) of around 50 nm and synthetic laponite nanoclays of around 100 nm were used as carriers for dyes, fluorophores (mainly loaded in the core) or photosensitizers (covalently linked at the external surface), for bioimaging and photodynamic therapy, respectively. The nanosystems are further functionalized with polyethylene glycol and folic acid to enhance their stability in water and selectivity for tumor cells, respectively.

The photophysical properties of both types of systems, chromophores and photoactive hybrid nanomaterials have been characterized by absorption and fluorescence (steady-state and time-correlated) spectroscopies and the singlet oxygen is monitored by direct method recording its luminescence at 1270 nm. Information about triplet states are gained by *ns*-transient absorption spectroscopy photolysis laser and by recording the phosphorescence emission at 77 K. Besides, the morphology, size distribution, and chemical composition of synthesized hybrid nanosystems have widely been studied by different techniques: SEM, TEM, XPS, FTIR, DLS and ¹H-NMR. Moreover, the viability of these systems to internalize, stain specific organelle of the cells and the phototoxic action under suitable irradiation and cytotoxic effects in dark conditions are also analyzed in vitro assays with HeLa and SCC38 cells.



Resumen

En este trabajo se han propuesto nuevos colorantes basados principalmente en la estructura del cromóforo BODIPY, así como nuevos nanosistemas híbridos fotoactivos para su potencial implementación en el campo de la biomedicina, en particular para bioimagen y terapia fotodinámica del cáncer.

En primer lugar, el desarrollo de nuevos biomarcadores fluorescentes se ha basado en la modificación del cromóforo BODIPY para mejorar su solubilidad en medios acuosos y su selectividad hacia orgánulos específicos de la célula, *i.e.* mitocondria. Para ello, se añadieron a la estructura molecular del colorante grupos hidrofílicos y biomoléculas específicas, respectivamente. Posteriormente, el BODIPY se funcionalizó con el objetivo de lograr fotosensibilizadores con alta producción de oxígeno singlete: por un lado, mediante la introducción de átomos halogenados además de sistemas π -conjugados que desplazan la absorción hacia la región roja dentro de la ventana clínica, y por otro lado, anclando grupos dadores de electrones que activan un estado de transferencia de carga intramolecular capaz de modular la capacidad fluorescente y la generación de oxígeno singlete, apropiados para aplicaciones teranósticas.

Además, se sintetizaron tres tipos de nanopartículas esféricas de sílice (no porosas, mesoporosas y ormosil) de entorno a 50 nm de diámetro, que junto con una nanoarcilla sintética (laponita) de unos 100 nm, se utilizaron como transportadores de colorantes: fluoróforos (principalmente ocluidos en el interior) o fotosensibilizadores (unidos covalentemente en la superficie externa). Estos nanosistemas se funcionalizaron además con polietilén glicol y ácido fólico para mejorar su estabilidad en agua y su selectividad hacia células tumorales.

Las propiedades fotofísicas de todos los sistemas, cromóforos y nanomateriales, se han caracterizado por espectroscopia de absorción y fluorescencia (estado estacionario y correlacionado en el tiempo) y la generación de oxígeno singlete se ha determinado por un método directo registrando la luminiscencia a 1270 nm. Además, se ha obtenido información de los estados tripletes mediante su absorción transitoria por fotólisis láser y su espectro de fosforescencia a 77 K. La morfología, tamaño y composición química de los nanosistemas ha sido ampliamente caracterizada por técnicas como SEM, TEM, XPS, FTIR, DLS y $^1\text{H-NMR}$. Finalmente, la internalización, citotoxicidad en oscuridad y la acción fototóxica bajo una radiación específica de los sistemas más prometedores ha sido testada en experimentos *in vitro* con células HeLa y SCC38.

Index

Chapter 1: Introduction	1
Bibliography	7
Chapter 2: Theoretical Bases: Dyes spectroscopy	11
2.1. Unimolecular Photophysical processes	13
2.1.1 Fluorescence	17
2.2. Bimolecular processes	21
2.2.1 Molecular aggregation	22
2.2.2 Photoinduced charge transfer and electron transfer	25
2.2.3 Förster Resonance Energy Transfer	27
2.2.4 Collisional quenching	29
2.2.5 Oxygen as a quencher: singlet oxygen	30
2.2.5.1 Photosensitization mechanism	31
2.2.5.2 Singlet Oxygen Characterization	32
2.3. Bibliography	37
Chapter 3: Experimental Section	39
3. 1 Synthesis of Multifunctional Silica Nanoparticles	42
3.1.1. Synthesis of Silica Nanoparticles	42
3.1.1.1. Synthesis of nonporous silica nanoparticles	42
3.1.1.2. Synthesis of mesoporous silica nanoparticles	44
3.1.1.3. Synthesis of organically modified silica nanoparticles	46
3.1.2. Synthesis of Photoactive Silica Nanoparticles	47
3.1.2.1. “Core” functionalization	48
3.1.2.2. “Shell” functionalization	50
3.2. Experimental Techniques	58
3.2.1. Structural and Chemical Characterization	58
3.2.1.1. Scanning Electron Microscopy and Transmission	

Electron Microscopy	58
3.2.1.2. Dynamic Light Scattering	58
3.2.1.3. X-ray Photoelectron Spectroscopy	60
3.2.1.4. Proton Nuclear Magnetic Resonance	60
3.2.1.5. Infrared-Attenuated Total Reflectance	61
3.2.1.6. Dye quantification	61
3.2.2. Photophysical Characterization	62
3.2.2.1. UV-Vis NIR-spectroscopy	62
3.2.2.2. Fluorescence emission, quantum yield, lifetimes and phosphorescence	64
3.2.2.3. Singlet oxygen emission by direct measurements	65
3.2.2.4. Laser flash-photolysis	66
3.2.2.5. Photostability measurements	67
3.2.2.6. Quantum mechanics calculations	67
3.3. In vitro HeLa cells studies	68
3.3.1. Cells culture	68
3.3.2. Sample preparation	69
3.3.3. Internalization and subcellular localization	69
3.3.4. Photodynamic treatment	69
3.3.5. Cell viability (MTT) assay	71
3. 4 Bibliography	72
Chapter 4: New BODIPY-based dyes for bioimaging and Photodynamic Therapy	75
4.1 BODIPYs for fluorescence bioimaging	83
4.1.1 Soluble BODIPYs in aqueous media	84
4.1.1.1 Photophysical properties and discussion	87
4.1.1.2 Live cells imaging studies	94
4.1.1.3 Conclusions	95
4.1.2 Carnitine-BODIPY probes as mitotrackers	96

4.1.2.1 Photophysical properties and discussion	97
4.1.2.2 Live cells imaging	99
4.1.2.3 Conclusions	101
4.2 BODIPYs for Photodynamic Therapy	102
4.2.1. Halogen BODIPYs	104
4.2.1.1 MethylThio-BODIPY as standard reference	104
4.2.1.2 Iodinated-BODIPYs in the red region	119
4.2.2. Halogen-free BODIPY	130
4.2.2.1 Binol BODIPYs	130
4.2.2.2 Enamine-based BODIPYs	142
4.3 Bibliography	156
Chapter 5: Nanoparticles for bioimaging and Photodynamic Therapy	167
5.1. Photoactive Spherical Silica nanoparticles	173
5.1.1 Structural characterization	177
5.1.1.1 Nonporous nanoparticles	177
5.1.1.2 Mesoporous nanoparticles	179
5.1.1.3 Ormosil nanoparticles	183
5.1.1.4 Conclusions	185
5.1.2 Fluorescent silica nanoparticles for bioimaging	185
5.1.2.1 Dye embedded into nanoparticles core	186
5.1.2.2 Dye grafted at nanoparticles shell	193
5.1.2.3 In vitro experiments	194
5.1.2.4 Conclusions	197
5.1.3 Photosensitizer-silica nanoparticles for photodynamic therapy	197
5.1.3.1 PS-silica nanoparticles with rose bengal	198
5.1.3.2 Other-PS-silica nanoparticles	205
5.1.3.3 Conclusions	214
5.2. Laponite-Clay as nanocarrier for Photodynamic Therapy	215

5.2.1 Structural characterization	217
5.2.2 Rose Bengal and Laponite nanoparticle for Photodynamic Therapy	217
5.2.3 In vitro experiments	219
5.2.4 Conclusions	220
5.3. Bibliography	222
General Conclusions	227
List of publications	233

1

INTRODUCTION

INTRODUCTION

In the XXI century, treat and cure cancer disease has become one of the utmost challenges. This disease causes 7.6 million of death every year, being after heart disease, the illness with the highest mortality rate. Furthermore, it is expected that this number increases up 13.1 million for 2030.¹ Until now, several treatments are applied against cancer, although depending on the type of cancer an effective cure has not been found yet. The most conventional cancer treatments, besides surgery, are based on chemo- or radio-therapy. They are applied with the intention of controlling, reducing or eliminating tumor cells, but they have several limitations. Indeed, these treatments usually cause side effects owing to their lack of selectivity for cancer cells and inducing high toxicity to the normal cells. On the other hand, the difficulties of quick detection decrease the patient probability to survive.^{2,3}

Thus, scientists and medical doctors are dedicating great efforts in widening the knowledge about this disease in order to be able to enhance detection methods and treatments against it. Indeed, in the last years, the number of publications about cancer has increased exponentially, Figure 1.1. Despite their efforts, the ideal system or strategy to cure this disease has not been developed yet.

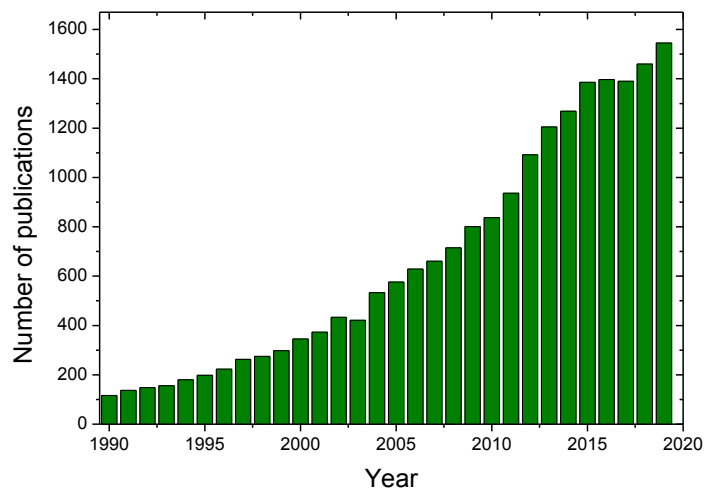


Figure 1.1. Publications about cancer per year from 1990 to December 2019 by SciFinder database.

Particularly, this thesis is focused on the study of new systems with potential applications in the detection and treatment of cancer diseases.

On the one hand, advanced fluorescent biomarkers susceptible to be used in optical microscopy as detection method are proposed. In this context, fluorescence microscopy is less aggressive respect to other imaging techniques (Computed Tomography, CT, Magnetic Resonance Image, MRI, or Positron Emission Tomography, PET), avoiding harmful irradiation or magnetic fields and offering high sensitivity and resolution and real time tracking a certain biological activities by *in vitro* or *in vivo* experiments.⁴⁻⁶ Indeed, there are currently several surgical camera systems approved by FDA (U.S. Food and Drug Administration), for instance, Fluorescence-Assisted Resection and Exploration (FLARE), Photo Dynamic Eye (PDE) or Hyper Eye Medical System (HEMS).⁷⁻⁹ Nevertheless, the main limitations of this technique are, its low depth penetration into the tissues inherent of visible or infrared light respect to other irradiation sources (*i.e.* X-ray), and that most all of the fluorophores approved by FDA for clinical work are non-targeted dyes, showing a low selectivity for tumor cells.^{10,11} For that reason, new fluorescent cancer biomarkers are required to fulfill key conditions to improved early-diagnosis.

On the other hand, new photo drug agents (photosensitizer) are proposed to be implemented in photodynamic therapy (PDT), chosen as a minimally invasive and complementary cancer treatment with respect to other common procedures, radiotherapy, chemotherapy or surgery. PDT is based on the action of a photosensitizer (PS), able to produce cytotoxic species, mainly singlet oxygen, by the activation of confined visible light irradiation in the tissue, reducing size effect of traditional methods. Nowadays, this treatment is being applied in dermatology against actinic keratosis and although the clinical use of PDT is often compromised by the limited penetration depth of visible light, preclinical and clinical trials have proven to be effective in early-stage tumors or in the palliation of advanced cancers, such as skin, head, neck, esophageal or lung cancer, improving patient survival.¹²⁻¹⁵ In this context, there are diverse PSs approved by FDA, but they suffer from some limitations such as solubility problems and poor selectivity to malignant tissues.¹⁶⁻¹⁹ Then, a huge effort is devoted to making this treatment more effective by the design of improved PSs.

Thus, one of the main goals of this thesis is the study of new molecules (chromophores) with improved features in terms of solubility and selectivity as well as

with high fluorescence or high singlet oxygen production or even a balance between both properties for theragnosis applications (bioimaging + PDT). For the dual purpose, detect and treat cancer, visible light is used as source of activation of the photoactive agents (fluorescent dyes and photosensitizers).

A second main objective in this work is the use of different nanosystems as carriers for these chromophores in order to enhance their delivery into tumor cells. Nanoparticles will increase their selectivity, protect them from degradation by plasma components and increase their solubility in physiological media.²⁰⁻²⁵ All these aspects will lower the required photoactive drug doses, minimizing side effects and consequently increasing the therapeutic efficacy. Although there are many kinds of nanoparticles based on different materials, metallic (gold, iron or quantum dots) and non-metallic (micelles, liposomes, polymeric nanoparticles, carbon nanotubes),^{1,3} silica-based nanoystems are selected due to their high surface area, easy functionalization, good biocompatibility, and optically transparency.^{21,26-29}

In this regard, the results of this thesis are divided into two main sections, to obtain promising systems for bioimaging and photodynamic therapy, following different approaches: *i*) the modification of the molecular structure of chromophores to tune key properties and, *ii*) the use of nanocarriers (silica nanoparticles and nanoclays) as dye delivery vehicles.

- i) The family of BODIPY is chosen to be chemically manipulated due to their excellent photophysical properties and its great versatile chemistry (Chapter 4).^{30,31} The first section (section 4.1) is dedicated to the BODIPY core functionalization to increase the solubility in aqueous media by tethering hydrophilic groups (section 4.1.1) and to enhance the selectivity to a particular organelle cell, *i.e.* mitochondria attaching a biomolecule of interest (section 4.1.2). The second part of chapter 4 (section 4.2) is focused on the modification of the BODIPY chromophore to attain improved photosensitizers with high singlet oxygen production by attaching heavy atoms (section 4.2.1) to increment the population of the triplet state and adding of electron-donating groups to induce an intracharge transfer (ICT) states that facilitates the transition to the triplet states³²⁻³⁶
- ii) Silica-based nanoparticles are used as carriers for different dyes (Chapter 5). In section 5.1, spherical silica nanoparticles (nonporous, mesoporous and ormosil) are synthesized with commercial fluorophore trapped in the core and photosensitizers (commercial and new BODIPY-based) anchored at the external surface. Besides,

the shell is coated with polyethylene glycol (PEG) to increase their stability in water and blood circulation time and finally functionalized with folic acid (FA) to specifically target cancer cells.^{25,37-42} A similar functionalization approach is followed in section 5.2, for a nanosilicate, laponite-clay, as carrier.^{29,43}

The morphology, size distribution and external composition of dye loaded silica-based nanoparticles are fully detailed. Moreover, the photophysical properties of all the systems are widely characterized and the photoactivity action of the most promising agents is tested by in vitro assays mainly in HeLa but also in SCC38 cells.

Bibliography

1. Lucky, S. S., Soo, K. C. & Zhang, Y. Nanoparticles in Photodynamic Therapy. *Chem. Rev.* **115**, 1990–2042 (2015).
2. Chaturvedi, V. K., Singh, A., Singh, V. K. & Singh, M. P. Cancer Nanotechnology: A New Revolution for Cancer Diagnosis and Therapy. *Curr. Drug Metab.* **20**, 416–429 (2018).
3. Mirabello, V., Calatayud, D. G., Arrowsmith, R. L., Ge, H. & Pascu, S. I. Metallic nanoparticles as synthetic building blocks for cancer diagnostics: from materials design to molecular imaging applications. *J. Mater. Chem. B* **3**, 5657–5672 (2015).
4. Robertson, T., Bunel, F. & Roberts, M. Fluorescein Derivatives in Intravital Fluorescence Imaging. *Cells* **2**, 591–606 (2013).
5. Singh, K., Rotaru, A. M. & Beharry, A. A. Fluorescent Chemosensors as Future Tools for Cancer Biology. *ACS Chem. Biol.* **13**, 1785–1798 (2018).
6. Zhu, S., Tian, R., Antaris, A. L., Chen, X. & Dai, H. Near-Infrared-II Molecular Dyes for Cancer Imaging and Surgery. *Adv. Mater.* **31**, 1–25 (2019).
7. Aoki, T., Murakami, M., Yasuda, D., Shimizu, Y., Kusano, T., Matsuda, K., Niiya, T., Kato, H., Murai, N., Otsuka, K., Kusano, M. & Kato, T. Intraoperative fluorescent imaging using indocyanine green for liver mapping and cholangiography. *J. Hepatobiliary. Pancreat. Sci.* **17**, 590–594 (2010).
8. Tummers, Q. R. J. G., Boonstra, M. C., Frangioni, J. V., Van De Velde, C. J. H., Vahrmeijer, A. L. & Bonsel, B. A. Intraoperative near-infrared fluorescence imaging of a paraganglioma using methylene blue: A case report. *Int. J. Surg. Case Rep.* **6**, 150–153 (2015).
9. Yoshida, M., Kubota, K., Kuroda, J., Ohta, K., Nakamura, T., Saito, J., Kobayashi, M., Sato, T., Beck, Y., Kitagawa, Y. & Kitajima, M. Indocyanine green injection for detecting sentinel nodes using color fluorescence camera in the laparoscopy-assisted gastrectomy. *J. Gastroenterol. Hepatol.* **27**, 29–33 (2012).
10. Garland, M., Yim, J. J. & Bogyo, M. A Bright Future for Precision Medicine: Advances in Fluorescent Chemical Probe Design and Their Clinical Application. *Cell Chem. Biol.* **23**, 122–136 (2016).
11. Velde, E. A. te, Veerman, T., Subramaniam, V. & Ruers, T. The use of fluorescent dyes and probes in surgical oncology. *Eur. J. Surg. Oncol.* **36**, 6–15 (2010).
12. Dąbrowski, J. M. & Arnaut, L. G. Photodynamic therapy (PDT) of cancer: From local to systemic treatment. *Photochem. Photobiol. Sci.* **14**, 1765–1780 (2015).

13. Hopper, C. Photodynamic therapy: A clinical reality in the treatment of cancer. *Lancet Oncol.* **1**, 212–219 (2000).
14. Moghissi, K., Dixon, K. & Gibbins, S. A Surgical View of Photodynamic Therapy in Oncology: A Review. *Surg. J.* **01**, e1–e15 (2015).
15. Lin, J. & Wan, M. T. Current evidence and applications of photodynamic therapy in dermatology. *Clin. Cosmet. Investig. Dermatol.* **7**, 145 (2014).
16. DeRosa, M. Photosensitized singlet oxygen and its applications. *Coord. Chem. Rev.* **233–234**, 351–371 (2002).
17. Nonell, S. & Flors, C. *Singlet Oxygen, Applications in Biosciences and Nanosciences*. (Royal Society of Chemistry, 2016).
18. Huang, Z. A review of progress in clinical photodynamic therapy. *Technol. Cancer Res. Treat.* **4**, 283–293 (2005).
19. Stallivieri, A., Colombeau, L., Jetpisbayeva, G., Moussaron, A., Myrzakhmetov, B., Arnoux, P., Acherar, S., Vanderesse, R. & Frochot, C. Folic acid conjugates with photosensitizers for cancer targeting in photodynamic therapy: Synthesis and photophysical properties. *Bioorganic Med. Chem.* **25**, 1–10 (2017).
20. Alexis, F., Pridgen, E., Molnar, L. K. & Farokhzad, O. C. Factors affecting the clearance and biodistribution of polymeric nanoparticles. *Mol. Pharm.* **5**, 505–515 (2008).
21. Mai, W. X. & Meng, H. Mesoporous silica nanoparticles: A multifunctional nano therapeutic system. *Integr. Biol.* **5**, 19–28 (2013).
22. Pérez-Herrero, E. & Fernández-Medarde, A. Advanced targeted therapies in cancer: Drug nanocarriers, the future of chemotherapy. *Eur. J. Pharm. Biopharm.* **93**, 52–79 (2015).
23. Bobo, D., Robinson, K. J., Islam, J., Thurecht, K. J. & Corrie, S. R. Nanoparticle-Based Medicines: A Review of FDA-Approved Materials and Clinical Trials to Date. *Pharm. Res.* **33**, 2373–2387 (2016).
24. Martins Estevão, B., Miletto, I., Marchese, L. & Gianotti, E. Optimized Rhodamine B labeled mesoporous silica nanoparticles as fluorescent scaffolds for the immobilization of photosensitizers: a theranostic platform for optical imaging and photodynamic therapy. *Phys. Chem. Chem. Phys.* **18**, 9042–9052 (2016).
25. Bharathiraja, S., Moorthy, M. S., Manivasagan, P., Seo, H., Lee, K. D. & Oh, J. Chlorin e6 conjugated silica nanoparticles for targeted and effective photodynamic therapy. *Photodiagnosis Photodyn. Ther.* **19**, 212–220 (2017).
26. Martínez-Carmona, M., Lozano, D., Baeza, A., Colilla, M. & Vallet-Regí, M. A novel visible light responsive nanosystem for cancer treatment. *Nanoscale* **9**,

- 15967–15973 (2017).
27. Wu, S.-H., Mou, C.-Y. & Lin, H.-P. Synthesis of mesoporous silica nanoparticles. *Chem. Soc. Rev.* **42**, 3862 (2013).
 28. Mousa, M., Evans, N. D., Oreffo, R. O. C. & Dawson, J. I. Clay nanoparticles for regenerative medicine and biomaterial design: A review of clay bioactivity. *Biomaterials* **159**, 204–214 (2018).
 29. Xu, F., Liu, M., Li, X., Xiong, Z., Cao, X., Shi, X. & Guo, R. Loading of indocyanine green within polydopamine-coated laponite nanodisks for targeted cancer photothermal and photodynamic therapy. *Nanomaterials* **8**, 1–16 (2018).
 30. Bañuelos, J. BODIPY Dye, the Most Versatile Fluorophore Ever? *Chem. Rec.* **16**, 335–348 (2016).
 31. Loudet, A. & Burgess, K. BODIPY dyes and their derivatives: Syntheses and spectroscopic properties. *Chem. Rev.* **107**, 4891–4932 (2007).
 32. Blázquez-Moraleja, A., Álvarez-Fernández, D., Prieto Montero, R., García-Moreno, I., Martínez-Martínez, V., Bañuelos, J., Sáenz-de-Santa-María, I., Chiara, M. D. & Chiara, J. L. A general modular approach for the solubility tagging of BODIPY dyes. *Dye. Pigment.* **170**, 107545 (2019).
 33. Blázquez-Moraleja, A., Sáenz-de-Santa María, I., Chiara, M. D., Álvarez-Fernández, D., García-Moreno, I., Prieto-Montero, R., Martínez-Martínez, V., López Arbeloa, I. & Chiara, J. L. Shedding light on the mitochondrial matrix through a functional membrane transporter. *Chem. Sci.* **11**, 1052–1065 (2020).
 34. Jiménez, J., Prieto-Montero, R., Maroto, B. L., Moreno, F., Ortiz, M. J., Oliden-Sánchez, A., López-Arbeloa, I., Martínez-Martínez, V. & Moya, S. Manipulating Charge Transfer States in BODIPYs: A Model Strategy to Rapidly Develop Photodynamic Theragnostic Agents. *Chem. – A Eur. J.* **26**, 601–605 (2020).
 35. Kim, B., Sui, B., Yue, X., Tang, S., Tichy, M. G. & Belfield, K. D. In Vitro Photodynamic Studies of a BODIPY-Based Photosensitizer. *European J. Org. Chem.* **2017**, 25–28 (2017).
 36. Bui, H. T., Mai, D. K., Kim, B., Choi, K.-H., Park, B. J., Kim, H.-J. & Cho, S. Effect of Substituents on the Photophysical Properties and Bioimaging Application of BODIPY Derivatives with Triphenylamine Substituents. *J. Phys. Chem. B* **123**, 5601–5607 (2019).
 37. Baleiz, C. Hybrid smart mesoporous silica nanoparticles for theranostics. *Nanomedicine* **10**, 2311–2314 (2015).
 38. Manzano, M. & Vallet-Regí, M. Mesoporous Silica Nanoparticles for Drug Delivery. *Adv. Funct. Mater.* **30**, 1902634 (2020).

39. Sanchez, C., Julián, B., Belleville, P. & Popall, M. Applications of hybrid organic–inorganic nanocomposites. *J. Mater. Chem.* **15**, 3559–3592 (2005).
40. Kabanov, V., Press, D. J., Huynh, R. P. S., Shimizu, G. K. H. & Heyne, B. Assessment of encapsulated dyes' distribution in silica nanoparticles and their ability to release useful singlet oxygen. *Chem. Commun.* **54**, 6320–6323 (2018).
41. Martins Estevão, B., Cucinotta, F., Hioka, N., Cossi, M., Argeri, M., Paul, G., Marchese, L. & Gianotti, E. Rose Bengal incorporated in mesostructured silica nanoparticles: structural characterization, theoretical modeling and singlet oxygen delivery. *Phys. Chem. Chem. Phys.* **17**, 26804–26812 (2015).
42. Ribeiro, T., Raja, S., Rodrigues, A. S., Fernandes, F., Baleizão, C. & Farinha, J. P. S. NIR and visible perylenediimide-silica nanoparticles for laser scanning bioimaging. *Dye. Pigment.* **110**, 227–234 (2014).
43. Tomás, H., Alves, C. S. & Rodrigues, J. Laponite®: A key nanoplatform for biomedical applications? *Nanomedicine Nanotechnology, Biol. Med.* **14**, 2407–2420 (2018).

2

THEORETICAL BASES: Dye spectroscopy

2.1. <u>Unimolecular Photophysical processes</u>	13
2.1.1 Fluorescence	17
2.2. <u>Bimolecular processes</u>	21
2.2.1 Molecular aggregation	22
2.2.2 Photoinduced charge transfer and electron transfer	25
2.2.3 Förster Resonance Energy Transfer	27
2.2.4 Collisional quenching	29
2.2.5 Oxygen as a quencher; singlet oxygen	30
2.2.5.1 Photosensitization mechanism	31
2.2.5.2 Singlet Oxygen Characterization	32
2.3. <u>Bibliography</u>	37

Theoretical bases

Since this work is largely based on dyes (fluorophores and photosensitizers) in this chapter, the main theoretical background of dye spectroscopy is explained.

In the first section, the most important photophysical aspects related to the dye properties are described. It is detailed the fundamental bases of the main unimolecular photophysical processes (section 2.1.) including absorption and emission, emphasizing fluorescence (section 2.1.1). The second part (section 2.2) is dedicated to the bimolecular processes involved during this work, such as molecular aggregation (section 2.2.1), photoinduced charge transfer and electron transfer (section 2.2.2) and Förster resonance energy transfer (section 2.2.3). At the end of this section collisional quenching is also described (section 2.2.4), and a special section is focused on the singlet oxygen generation (section 2.2.5).

2.1 Unimolecular Photophysical Processes

Generally, photophysical processes are those that involve transits between electronic states by the excitation of the sample through non-ionizing electromagnetic radiation. They include the excitation process from the ground state to excited electronic states and the deactivation of those excited states via radiative or non-radiative paths. These following phenomena are considered as the main unimolecular processes.

In the Jablonski diagram, Figure 2.1, the most important photophysical processes are depicted.¹ This diagram is a simple and visual scheme to explain properly all of these unimolecular processes, in gas phases or in diluted solutions.

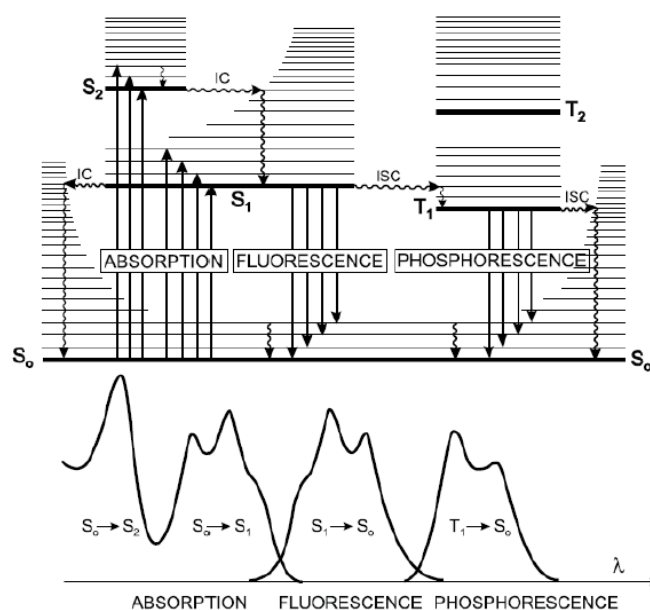


Figure 2.1. Jablonski diagram (top) and illustration of the relative position of absorption, fluorescence and phosphorescence spectra (bottom) ¹

Ground state is generally considered a singlet state (S_0) because most organic molecular systems are at this level at room temperature. Then, when a molecule is excited by the absorption of a photon, depending on the energy of this photon, an electron jumps from the ground state (S_0) to one of its excited states (S_1, S_2, \dots) involving different vibrational levels (ν) (Figure 2.1 solid arrows). This excitation process is very fast ($\approx 10^{-15}$ s), the electron has no time to reverse its spin, and consequently, the excitation usually maintains its multiplicity (from S_0 to S_1 or S_2). As a result, transitions to states with different multiplicity, *i.e.*, S_0 to T_1 are not usual.

The absorption can be experimentally measured following equation 2.1, where I_a is the intensity of absorbed light, I_0 the intensity of the incident light through the sample and I_T the fraction of transmitted light.

$$I_a = I_0 - I_T \quad \text{eq.2.1}$$

The absorption intensity is related to the absorbance of the chromophore (A), which is proportional to sample concentration in M (c), the optical path in cm (l) and the molar absorption coefficient in $M^{-1} \text{ cm}^{-1}$ (ϵ), following the Lambert-Beer law,¹

equation 2.2. The last parameter, ϵ is the capability of the sample to absorb light in a specific wavelength and it is characteristic of each molecule.

$$A = \lg(I_0/I_T) = \epsilon c l \quad \text{eq.2.2}$$

Another way to evaluate the absorption probability is considering the oscillator strength (f) which indicates the probability of the transition. It is a dimensionless parameter with values oscillates between 0 and 1, being value 0 a forbidden transition and near 1 an allowed transition. The oscillator strength is determined by the integration of the area under the curve of absorption, equation 2.3, where n is the refraction index and $\bar{\nu}$ the wavenumber (cm^{-1}).^{1,2}

$$f = \frac{4.39 \cdot 10^{-9}}{n} \int \epsilon(\bar{\nu}) d\bar{\nu} \quad \text{eq.2.3}$$

Independently of which state is populated after excitation, usually the deactivation to the ground state occurs from the lowest vibrational state ($v = 0$) of the first electronic excited state (S_1). Generally, the molecular systems lose the excess of energy passing from high vibrational levels ($v = n$) and higher electronic states (S_n), to lowest vibrational level ($v = 0$) and to the first excited state (S_1) through vibrational relaxations and non-radiative processes called internal conversion (IC), Figure 2.1 zigzagging arrows. These processes occur in hundreds of femtoseconds; vibrational relaxation in range of 10^{-14} to 10^{-11} s ($v = n \rightsquigarrow v = 0$) and internal conversion ($S_n \rightsquigarrow S_1$) in around 10^{-11} to 10^{-8} s. Indeed, they are generally much faster than the lifetime of the first excited state (of around several nanoseconds).¹

Once, an electron is in lower excited state, S_1 ($v = 0$), different and competitive deactivation processes can occur during the lifetime of S_1 ($v = 0$):

- i) A radiative deactivation, emitting a photon, process denoted as fluorescence ($S_1 \rightarrow S_0$), which corresponds to an electronic transition between states of the same multiplicity and it is characterized by a k_{r} rate constant in the range of 10^9 - 10^7 s^{-1} . Note here that since absorption and emission are very fast processes, the nuclei do not change their excited state configuration and according to the Born-Oppenheimer approximation, there are no changes in the configuration of the nuclei during the electronic transitions (Franck-Condon principle).¹ For this reason, electronic transitions are represented by vertical lines in the Jablonski diagram

(Figure 2.1.). The fluorescence process will be further detailed below (section 2.1.1).

- ii) A non-radiative process from the first excited state to the ground state ($S_1 \rightsquigarrow S_0$), called internal conversion (IC). It is a really fast vibrational deactivation process and is defined by the constant rate k_{ic} (10^{11} - 10^9 s⁻¹).¹ This process is represented as a horizontal arrow in the Jablonski diagram (Figure 2.1.).
- iii) A different non-radiative process from the first excited state to a triplet state ($S_1 \rightsquigarrow T_1$), involving a change in the multiplicity. This process is called intersystem crossing (ISC) and its constant rate is denoted as k_{isc} (10^8 - 10^3 s⁻¹). This transition is relatively inefficient in most organic dyes. Nevertheless, there are some strategies in order to improve the ISC probability based on the spin-orbit coupling mechanism, such as π -systems loops, carbonyl substituent groups or heavy atoms.³⁻⁷ In the case of heavy atoms the increase in the atomic number (Z) extending the spin-orbit coupling, though the rise in the interaction between the electron spin and its movement around the nucleus. This improvement in intersystem crossing probability has a great interest in applications such as singlet oxygen (explained later in section 2.2.5). Here, T_1 ($v = 0$) is populated and it can deactivate to the ground state through the non-radiative intersystem crossing process, $k_{isc} (T_1 \rightsquigarrow S_0)$, or through a radiative deactivation, named phosphorescence, $k_{ph} (T_1 \rightarrow S_0)$, (Figure 2.1). However, owing to the long lifetime of the triplet state (10^{-6} - 1 s) in comparison with the average lifetime of an excited singlet state (10^{-9} - 10^{-7} s), the systems usually relax by non-radiative deactivation, losing the excitation energy for example by collisions, generally denoted as collisional quenching, being molecular oxygen one of the best-known collisional quencher (more details later in section 2.2). For this reason, phosphorescence emission is mainly detected at low temperatures or in rigid systems where collisional processes are minimized.

The combination of these processes generates different spectra in terms of their shape, position (wavelength) and intensity (Figure 2.1 bottom). Therefore, the fluorescence band will appear at lower energy than absorption and at higher energy than phosphorescence. The intensity of the emission band will depend on the contribution of the internal conversion and intersystem crossing which are competitive processes of fluorescence.

Fluorescence is a great important property, which can be applied to a wide range of studies related to chemical and biological research areas. The fluorescence measurements can provide information about many molecular processes. In this work, the fluorescence of the compounds is extensively applied, and therefore a special section is dedicated below to this phenomenon.

2.2.1 Fluorescence

Regarding the shape of the fluorescence emission, it is commonly the mirror image of the first absorption band since vibrational levels of the S_0 and S_1 states are very similar. This statement is true when there are no important changes in the molecular geometry after excitation, Figure 2.2. However, the 0-0 transition should appear at higher wavelengths (lower energies) than the absorption band, attributed to the solvent relaxation, which is usually larger in S_1 owing to the increase of the dipolar moment upon excitation. The energy gap between the maximum of the bands of absorption and fluorescence is denoted as Stokes shift ($\Delta\nu_{st}$).

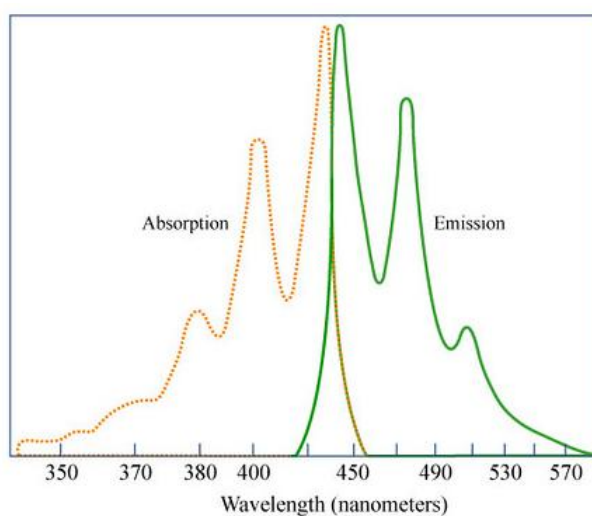


Figure 2.2. Absorption and emission spectra of perylene as an illustrative example of the “mirror image” rule.

The fluorescence intensity (I_{fl}) depends on the amount of population in the emissive state ($[S_1]$) and its deactivation constant (k_{fl}), according to equation 2.4.

$$I_{fl} = k_{fl} [S_1] \quad \text{eq.2.4}$$

The population of the emissive state is ruled by the number of photons absorbed in the excitation process, *i.e.* the absorption intensity (I_a). Thus, the fluorescence emission is quantified by fluorescence quantum yield (Φ_{fl}) defined as the relation between emission intensity radiation (I_{fl}) and the total absorption radiation (I_a), (equation 2.5).

$$\Phi_{fl} = \frac{I_{fl}}{I_a} \quad \text{eq.2.5}$$

Nonetheless, the deactivation of S_1 depends not only on the fluorescence deactivation, characterized by k_{fl} but also on non-radiative processes, k_{nr} : internal conversion (IC) and intersystem crossing (ISC), $k_{nr}=k_{ic}+k_{isc}$, described above, which are competitive processes, equation 2.6. This means that in stationary excitation conditions and for unimolecular systems (in gas phase or diluted solution) the fluorescence quantum yield could be expressed as the ratio between fluorescence rate over the all possible deactivation rate, equation 2.7

$$I_a = k_{fl} [S_1] + k_{ic} [S_1] + k_{isc} [S_1] \quad \text{eq.2.6}$$

$$\Phi_{fl} = \frac{k_{fl}}{k_{fl}+k_{ic}+k_{isc}} = \frac{k_{fl}}{k_{fl}+k_{nr}} \quad \text{eq.2.7}$$

Experimentally, fluorescence quantum yield could be determined in solution by the relative method, by comparing the fluorescence intensity of the sample with a reference whose quantum yield is known (Φ_{fl}^r) measured in identical conditions (*i.e.* with similar absorbance under the same excitation wavelength). Then, equation 2.8 is applied.

$$\Phi_{fl} = \Phi_{fl}^r \frac{n^2}{(n^r)^2} \frac{F}{F^r} \frac{A}{A^r} \quad \text{eq.2.8}$$

where F is the area behind the curve of the emission band, A is the absorbance at the excitation wavelength and n is the refractive index of the solvent. Note that the subscript r refers to the known reference sample.

Unfortunately, not always there is a suitable reference and this method cannot be followed for every sample. In those cases, the absolute method to deduce the emission

quantum yield is applied. For that, an integrating sphere is required and the quantum yield is measured using a white scatter (solvent or matrix) with a diffuse reflectance of 100% and compared with the sample. Both measures are carried out in the same conditions, including the registration of the range of lamp emission, Figure 2.3. The first scan (blue) is obtained from a reference scatter, which must exhibit a diffuse reflectance of 100%, while the second scan (red) is obtained by scanning the sample under study.

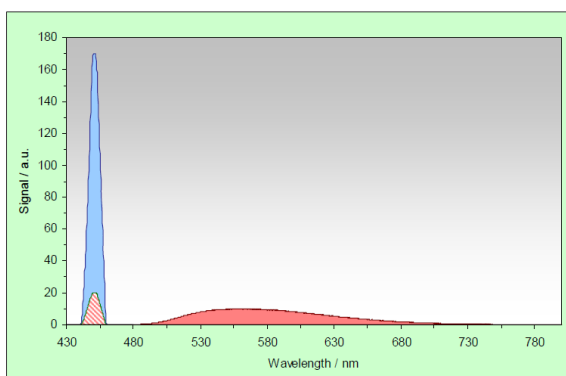


Figure 2.3. An example of quantum yield measurement in an integrating sphere

After the experimental measurement, the absolute quantum yield is obtained from the difference between S_R , the scatter of the lamp (blue area in Figure 2.3) and S_S the reflection of the sample (red hatched area in Figure 2.3), which gives the number of photons absorbed, and F_S the emission of the sample (red area in Figure 2.3), by equation 2.9:

$$\Phi_{fl} = \frac{F_S}{S_R - S_S} \quad \text{eq.2.9}$$

Besides the fluorescence quantum yield, another important parameter related to the fluorescence is the lifetime (τ_{fl}) of the first singlet excited state. The lifetime is defined as the average time that the first excited state is populated before its return to the ground state. As it is mentioned before, the depopulation from the S_1 involves the three deactivation constants: fluorescence as radiative and internal conversion and intersystem crossing as non-radiative, for this reason, the lifetime could be defined following equation 2.10.

$$\tau_{fl} = \frac{1}{k_{fl} + k_{ic} + k_{isc}} = \frac{1}{k_{fl} + k_{nr}} \quad \text{eq.2.10}$$

Therefore, by the combination of eq.2.7 and 2.10, the close relation between fluorescence lifetime and fluorescence quantum yield is demonstrated, equation 2.11.

$$\Phi_{fl} = k_{fl} \tau_{fl} \quad \text{eq.2.11}$$

The fluorescence lifetime can be experimentally obtained by recording the evolution of the fluorescence intensity with the time after excitation. The fluorescence intensity for a fluorescent molecule that shows a decay curve with monoexponential kinetics can be described as eq. 2.12:

$$I_{fl}(t) = I_{fl,0} e^{-t/\tau_{fl}} \quad \text{eq.2.12}$$

being $I_{fl,0}$ the intensity immediately after the excitation pulse.

The lifetime is determined from the slope of the logarithmic representation of this, equation 2.13 and Figure 2.4.⁸

$$\ln(I_{fl}(t)) = \ln(I_{fl,0}) - t/\tau_{fl} \quad \text{eq.2.13}$$

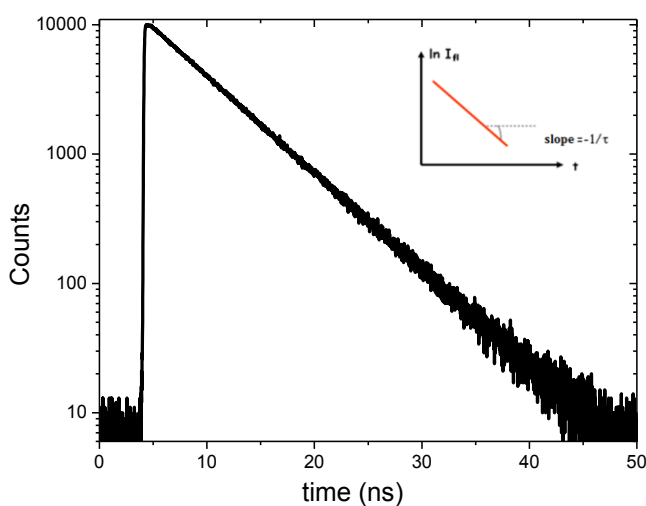


Figure 2.4. Example of fluorescence decay curve (outside),⁸ an example of logarithmic representation (eq.2.13) to obtain the lifetime (inside)

In this context, the fluorescence decay curve (Figure 2.4) is experimentally recorded by time resolved fluorescence measurement (more details of the set up in the experimental section, chapter 3).

Note here that, in fluorescence, it is important to take into account the so-called inner filter effects. It is a common problem and it drastically affects both emission spectra (shape and intensity) and the fluorescence lifetime. In high optical dense solutions occur an attenuation of the excitation light, a distortion of the emission band and an increase in the lifetime as a result of the reabsorption of the emitted light by the sample itself, when the excitation and emission spectra overlap. To avoid inner filters the most convenient is the use of a diluted solution (with an optical density ≤ 0.1). When the study must be done at high concentrations, then, the optical path should be reduced by using thinner cuvettes or by placing the cuvette in a front-face configuration (more details in the experimental section, chapter 3).

This effect is indeed an artifact to take into consideration to properly measure the fluorescence properties of a sample. However, there are many other processes able to quench the fluorescence as a result of different interactions. These processes are now described in section 2.2.

2.2 Bimolecular processes

A great variety of *intra* or *inter* molecular interactions can result in a decrease in the fluorescence intensity. These include complex formation, collisional quenching or energy transfer processes. These interactions are usually considered bimolecular processes since the quencher and the fluorophore are not covalently linked (intermolecular process). However, most of them can also occur through intramolecular interaction, *i.e.* in a linked pair dyads.

The bimolecular processes are divided into two main types: *i*) Static quenching is considered when a non-fluorescence complex is formed in the ground state and, *ii*) dynamic quenching is a time-dependent process that takes place in the excited state of the fluorophore within its fluorescence lifetime. Note that none of these quenching mechanisms involves a chemical modification of the molecules.

Nevertheless, these molecular interactions are completely different from each other, not only for their mechanism (static or dynamic quenching) but also for the nature of quencher. For instance, molecular aggregation is a fluorescence quenching induced by the formation of a complex in the ground state of the same species, usually called monomers. However, charge-transfer complex (CT complex) is formed by the association of two molecules with different electron-donating and electron-withdrawing capacity. Another typical fluorescence quenching is the collisional quenching of a fluorophore with other species such as molecular oxygen. All these mechanisms can be considered as short-range quenching processes that can take place at a short distance (several Å). However, a molecule can be also quenched at much longer distances (up to 100 Å) by a Förster Resonance Energy Transfer process.

All these bimolecular mechanisms will be described below. As this thesis is mainly focused on singlet oxygen generation and its potential application in biomedicine, this latter phenomenon will be widely described at the end of this section (section 2.2.5).

2.2.1 Molecular aggregation

In some applications, a high optical density is required, and as said before, high optical dense samples can cause a decrease in the fluorescence intensity by the inner filter effect. Besides, at high dye concentrations can also form aggregates and consequently change their photophysical properties. In this sense, molecular aggregation can drastically modify the absorption and emission spectra, decreasing significantly the fluorescence quantum yield.

On the one hand, molecular aggregation in the ground state could modify the absorption spectrum, the shape, and position of the band.⁹ Generally, the main absorption band decreases in the detriment of the formation of new bands, which can appear at higher or lower energies depending on the geometry of aggregates. This phenomenon is called the metachromatic effect. At moderate dye concentration, dimers are usually formed in the first stage and based on their absorption spectrum characteristic, geometrical parameters could be predicted by Exciton Theory.¹⁰ This is a quantum mechanics method that takes into account the electrostatic interactions between the dipole moments of the monomers and envisages different electronic energy diagrams.

In other words, if two species are in close distance 2-10 Å, Exciton Theory predicts a splitting of the excited state of monomer into two different excited states for the dimer. The energy gap, between these excited states and the transition probabilities from the ground state to those excited states, depends on the distance between monomers and on the relative orientation of the transition dipole vectors in the aggregate. The two following angles define the geometry of the monomers in the dimer: θ is the angle between the direction of the dipolar moments and the linking line of the molecular centers and α , is the angle between the orientations of the transition dipole moments of the monomers in the dimer (Figure 2.5).

The different geometries of the dimers and their characteristic spectroscopic properties according to the angles and positions between monomeric molecules are schematically depicted in Figure 2.5. In general, dimers are classified in two main geometries; aggregate H-type (case A) and aggregate J-type (case B), even though aggregates use to adopt geometries with intermediate angles, case C or D. Every possibility is explained below:

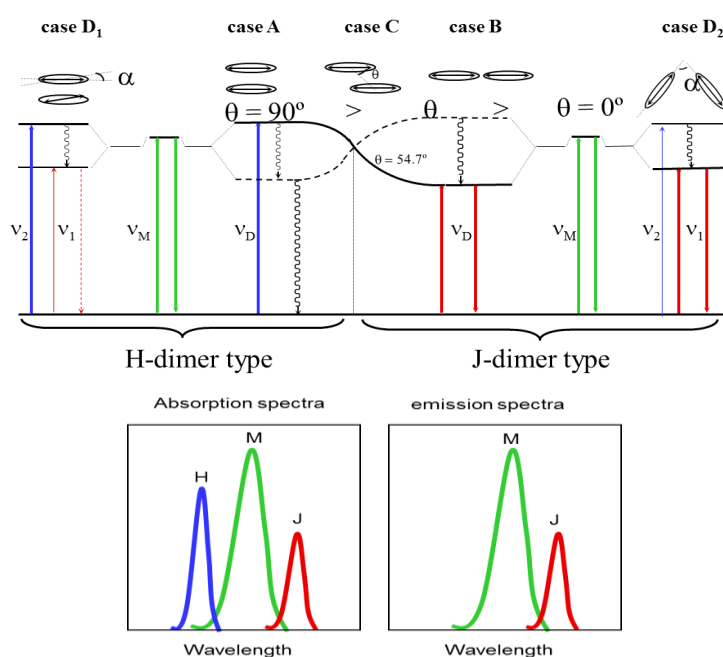


Figure 2.5. Exciton splitting of the electronic states for different geometric dispositions of the monomer units in a dimer (top), scheme of absorption and fluorescence band positions of H- and J-dimer respect to the monomer band (bottom).

Case A, called H-dimer, is a perfect sandwich dimer. The dipole moments are perfectly aligned and in parallel planes. In this situation the angles of the dimer are $\theta = 90^\circ$ and $\alpha = 0^\circ$, and their characteristic absorption band is placed at higher energies than the monomer, (Figure 2.5 blue band and green band, respectively). This type of aggregates are not fluorescence due to their depopulation is through non-radiative processes and causes an effective quenching of the monomer fluorescence.¹⁰

Case B, denoted as J-dimer, is when the monomers are disposed in a head-to-tail disposition. In this case, the monomers are in line with characteristic angles $\theta = 0^\circ$ and $\alpha = 0^\circ$, being the dipole moments coplanar. J-dimer could be fluorescent and its absorption and fluorescence band present a bathochromic shift with respect to the monomer (Figure 2.5 red and green band respectively).

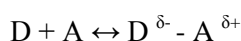
Case C, is named co-planar dimer, $\alpha = 0^\circ$, but $0^\circ < \theta < 90^\circ$. The location of the band depends on the θ value if it is higher than 54.7° the aggregate acts as an H-dimer and the band suffers a hypochromic shift. In contrast, if θ is lower than 54.7° , it behaves as J-dimer with a bathochromic shift and could be potentially fluorescent. Adding that in the case of $\theta = 54.7^\circ$ splitting effect should not be expected.

Case D, in this case, two situations could be differentiated; D_1 and D_2 . In both the H and J absorption bands appear in the spectrum. D_1 is a twisted sandwich dimer with angles $\theta = 90^\circ$ and α can be any value. On the other hand, D_2 oblique head-to-tail dimer with $\theta = 0^\circ$ and an α can be any value. Adding, although both bands appear in every case, the H-band is more intense for D_1 while the J-band is for D_2 .

The type and the proportion of aggregate will depend not only on the concentration of the dye but also on the aggregation constants. These constants are at the same time dependent on other factors as the molecular structure of the dye, temperature and the medium. The molecular aggregation is considered an important quenching process because although some geometries can theoretically be fluorescent, their relative quantum yield is generally much smaller than that of the monomer.

2.2.2 Photoinduced charge transfer and electron transfer

Another process of quenching in the ground state is a charge-transfer complex (CT complex) or electron-donor-acceptor complex. It is formed by the interaction of two molecules in the ground state in which a fraction of electronic charge is transferred from the electron donor to the electron acceptor entities. This complex can usually undergo an electronic transition, different from their isolated species, usually in the visible region of the electromagnetic spectrum. These optical absorption bands are often referred to as charge-transfer bands (CT bands).



Besides, this charge transfer process can also happen as an intramolecular mechanism, where the acceptor and donor are different moieties of the same molecule, *i.e.* linked Donor-Acceptor Pairs and the phenomenon is called ***intramolecular charge-transfer (ICT) process***. However, the ICT process is generally promoted in the photoexcited state. The photoexcitation facilitates the transfer of an electron from one part of a molecule/ion to its other part in the excited state, which makes the charge distribution in the excited state markedly different from that in the ground state. The ICT in organic molecules can be emissive, which is in detriment of the fluorescence of the S_1 locally excited (LE) state of the molecule, Figure 2.6. ICT emission is characterized by a broad and red-shifted band respect to the LE state and is generally favored in polar solvents (Figure 2.6).¹¹ In some molecules, and depending on the polarity of the solvent, fluorescence from the LE and ICT states can reach the corresponding Franck–Condon states giving rise to dual fluorescence (Figure 2.6). Generally, as the solvent polarity increased, larger is Stokes-shift of the ICT fluorescence (due to a greater stabilization by the solvent in the excited state) and the higher is the quenching of LE emission.^{1,2}

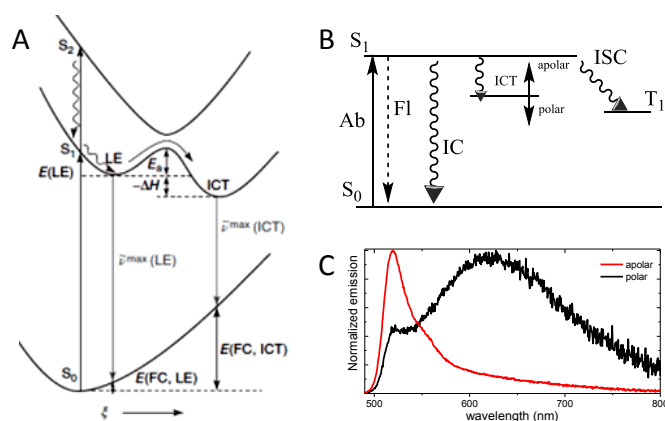


Figure 2.6. (A) Schematic representation of intramolecular charge transfer (ICT). The vertical coordinate represents energy, while the horizontal coordinate (ξ) comprises all molecular changes accompanying the LE \rightarrow ICT reaction, such as changes in bond lengths and bond angles. (B) Scheme of deactivation processes from S_1 showing intramolecular charge transfer and (C) an example of fluorescence spectrum in an apolar solvent (red) and the ICT emission band (black) in a polar solvent (right).⁸

Similarly, as the *intra charge transfer* process, **photoinduced electron transfer (PET) process** is known as an *inter* or *intra* molecular photophysical process by which an electron is transferred from donor to acceptor, after excitation. Due to PET process, charge separation is generated and redox reaction can take place in excited state.²

Excited fluorophores can be either the electron acceptor or the electron donor and the direction of the electron transferring in the excited state is defined by the oxidation and reduction potential of the ground and excited states, Figure 2.7. If the excited species acts as acceptor is called reductive-PET. In this case, the ground state (HOMO = “Highest Occupied Molecular Orbital”) of the donor lies higher in energy than that of the acceptor and can transfer an electron to the acceptor’s HOMO.

In contrast, if the excited species acts as donor, the excited state (LUMO= “Lowest Unoccupied Molecular Orbital”) of the acceptor lies below and the electron can jump from the LUMO of the excited state of the donor to the LUMO of the acceptor (Figure 2.7).

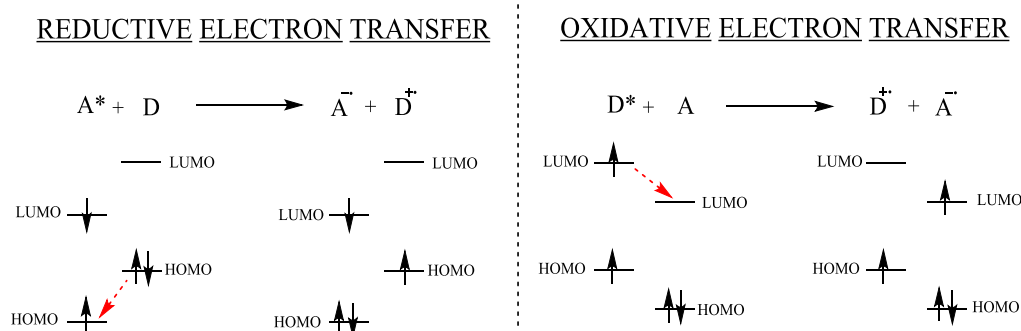


Figure 2.7. Scheme of reductive (left) and oxidative (right) electron transfer¹

The electron transfer process competes with radiative decay to the ground state, substantially diminishing the fluorescence quantum yield. Indeed, PET is the widely accepted mechanism for the behavior of a class of “turn-on” fluorescent chemosensors that fluoresce is shown only in the presence of targeted analytes.

2.2.3 Föster Resonance Energy Transfer

In the Föster resonance energy transfer (FRET) are also involved two molecules of different nature. FRET is a physical process that consists of an energy transfer between a donor molecule (D) in the excited state and an acceptor molecule (A) in the ground state, as the result of long-range dipole-dipole interactions (Coulombic interaction). Differently as the two former processes, the radiationless energy transfer can take place over relatively long distances (10-100 Å), Figure 2.8.² FRET results in a decrease in the fluorescence intensity and lifetime of the donor and an enhancement the fluorescence of the acceptor in the case that acceptor is fluorescent; if the acceptor is not fluorescence the energy is dissipated as heat.

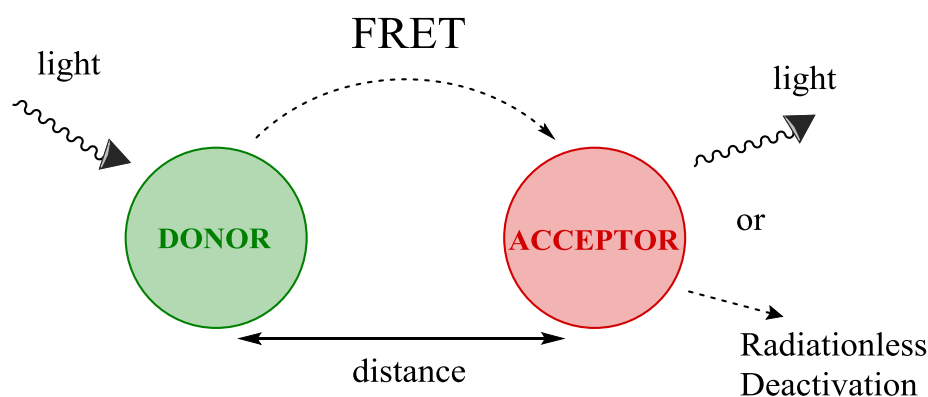


Figure 2.8. Scheme of FRET phenomenon between donor (green) and acceptor (red)

The FRET efficiency depends on several parameters such as the concentration of the molecules, their distribution, their photophysical properties, and especially on the distance between each other. The theory of the FRET is moderately complex, so only the final equation to calculate the rate of energy transfer from a donor to an acceptor ($k_T(r)$) is shown, equation 2.14.²

$$k_T(r) = \frac{Q_D \kappa^2}{\tau_D r^6} \left(\frac{9000(\text{Ln}10)}{128\pi^5 N n^4} \right) \int_0^\infty F_D(\lambda) \epsilon_A(\lambda) \lambda^4 d\lambda \quad \text{eq.2.14}$$

where Q_D is the fluorescence quantum yield of the donor in absence of the acceptor, τ_D is the donor lifetime in absence of acceptor, N is the Avogadro's number, n is the refractive index of the medium, r is the distance between donor and acceptor, $F_D(\lambda)$ is the corrected fluorescence intensity of the donor in the wavelength range λ to $\lambda + \Delta\lambda$ respect to the total intensity (area under the curve) normalized to unity, $\epsilon_A(\lambda)$ is the absorption coefficient of the acceptor at λ , and κ^2 is a factor to describe the relative orientation of the transition dipoles of the donor and the acceptor species ($\kappa^2 =$ is approximately 2/3 in isotropic medium).² FRET process requires an overlap between the fluorescence spectrum of the donor and absorption spectrum of the acceptor.

As it is mentioned previously, the distance between two chromophores is the most significant parameter (r^{-6}) in FRET phenomenon, with typical distances between 20 and 60 Å. Indeed, Förster distance (R_0) is determined as the distance between donor and acceptor in which the FRET efficiency is 50 %, equation 2.15, where $J(\lambda)$ is the spectral overlap.²

$$R_0^6 = 8.79 \cdot 10^{-5} (\kappa^2 n^{-4} Q_D J(\lambda)) \quad \text{eq.2.15}$$

Thus, the concentration of both molecules is a crucial factor since it can determine the distance between molecules. If the concentration is low, the distance will be high ($r > 2R_0$) and then the FRET hardly will occur. In contrast, if the concentration is high ($r < 2R_0$) the FRET could happen.¹² Finally, it is possible to calculate the FRET efficiency (Φ_{FRET}) though the donor lifetime in the presence (τ) and the absence of acceptor (τ_0), equation 2.16.

$$\Phi_{\text{FRET}} = 1 - \frac{\tau}{\tau_0} \quad \text{eq.2.16}$$

Note here that as a result of the huge dependence on the efficiency of the FRET with the distance is often referred to a “spectroscopic ruler” and this process is widely used to measure distance in important biological processes such as protein conformations labeled with a suitable donor-acceptor chromophore pair.

2.2.4 Collisional quenching

Conversely, as the above mechanism, collisional quenching occurs when the excited state of a fluorophore is deactivated upon molecular contact with a quencher, Q, in solution. It is a diffusion-limited process as they interact upon collision and is consequently considered a short-range ($< 2 \text{ \AA}$) process. There are many molecules that act as collisional quenchers such as oxygen, halogens, amines, etc. The deactivation of fluorescence by a quencher is determined k_q , and the Φ_{fl} in presence of the quencher is re-defined by equation 2.17. Combining this equation with equation 2.7 in absence of the quencher the denoted as Stern-Volmer equation is obtained, equation 2.18:

$$\Phi_{\text{fl}} = \frac{k_{fl}}{k_{fl} + k_{ic} + k_{isc} + k_q} \quad \text{eq. 2.17}$$

$$\Phi_{\text{fl}}^0 / \Phi_{\text{fl}} = I_0 / I = 1 + k_q \tau_0 [Q] = 1 + K_{\text{SV}} [Q] \quad \text{eq. 2.18}$$

being I_0 and I the fluorescence intensities in the absence and the presence of the quencher respectively, k_q is the bimolecular quenching constant and τ_0 the lifetime of the fluorophore in the absence of the quencher. The K_{SV} is denoted as the Stern-Volmer quenching constant. From the linear representation of I_0/I against $[Q]$ the bimolecular quenching k_q is determined.

On the other hand, an interesting parameter related to this diffusion control mechanism is the diffusion constant, k_{diff} , calculated by Stokes-Einstein, for two (equal) solid spheres in a given solvent, equation. 2.19.^{13,14}

$$k_{diff} = \frac{8K_B T}{3\eta} \quad \text{eq.2.19}$$

where K_B is de Boltzmann constant, T is the temperature, and η is the viscosity of the solvent.

If quenching is diffusion-limited, $k_q \sim k_{diff}$ and should be inversely proportional to the viscosity of the solution.

2.2.5 Oxygen as a quencher: singlet oxygen

One of the most significant collisional quenchers is molecular oxygen. The mechanism, by which oxygen quenches, is related to its particular electronic configuration in the ground and excited states. Two unpaired electrons occupied π^* orbital with parallel spin. This electronic configuration is designated as O_2 (${}^3\Sigma_g^-$) or 3O_2 . Superscript 3 means that it corresponds to a triplet state, Σ indicates the orbital angular momentum (M_L) is equal to 0 and g is the symmetry of the molecule. So, the oxygen is a triplet spin in its ground state but its two lower electronically excited states are spin-singlet states designated as 1O_2 , ${}^1\Delta_g$ (94.3 kJ/mol) and O_2 , ${}^1\Sigma_g^+$ (158 kJ/mol), being these transitions forbidden according to electric-dipole selection rules, Figure 2.9.¹⁵

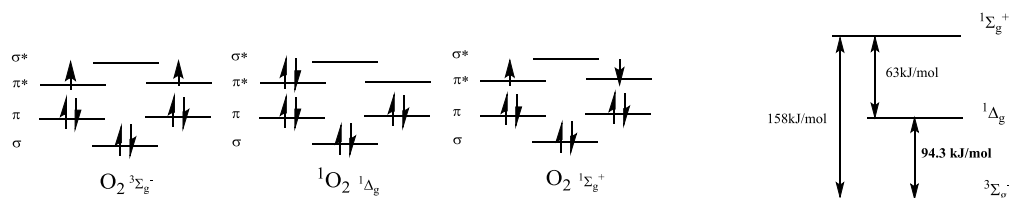


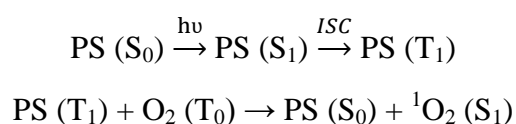
Figure 2.9. Molecular orbital diagrams for ground-state molecular oxygen and oxygen excited states (left), energy levels of oxygen (right)¹⁵

Oxygen is an excellent electron acceptor and could generate *reactive oxygen species* (ROS) which are strong oxidants, such as superoxide radical anion (O_2^-), hydroxyl radical (OH^\cdot) or hydrogen peroxide (H_2O_2). Nevertheless, the first excited state of

oxygen; Singlet Oxygen ($^1\text{O}_2$) is the best oxidant species; $E_{\text{red}} = -0.15\text{V}$ for $^3\text{O}_2$ and $E_{\text{red}} = 0.79\text{V}$ for $^1\text{O}_2$ in water. Indeed, $^1\text{O}_2$ is really an interesting species because it could be used in several applications such as photoactivated herbicides and insecticides, photodynamic therapy of cancer, photosterilization of blood products or in wastewater treatments.^{15,16} For these reasons, in the last years, many studies were carried out to characterize its properties and control its production.

2.2.5.1 Photosensitization mechanism

The main mechanism to generate $^1\text{O}_2$ is via photosensibilization, particularly by triplet-triplet sensitization.^{4,5,17} Photosensitizer (PS) is excited under appropriate wavelength, absorbing the radiation ($S_0 \rightarrow S_1$) and going through intersystem crossing to its triplet excited state (T_1). Before the deactivation process to the ground state (S_0), it transfers its energy to the environmental oxygen ($^3\Sigma_g^-$) generating $^1\text{O}_2$ ($^1\Delta_g$) without any chemical alteration, Scheme 2.1 and Figure 2.10.



Scheme 2.1. Oxygen singlet generation through photosensitizer

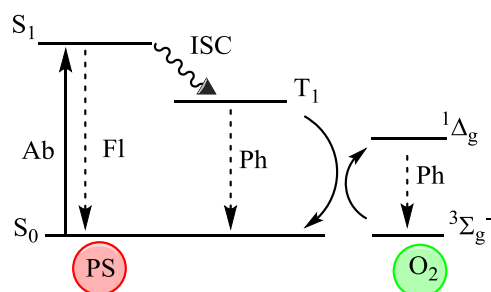


Figure 2.10. Schematic description of singlet oxygen activation by photosensitizer

These photosensitizers are usually organic molecules or metal complexes. Currently, there are a wide variety of families of PSs; xanthenes-type dyes, anthracenes, porphyrins, anthraquinone derivatives, benzophenone derivatives, metal-bases complexes and fullerenes.¹⁶ These photosensitizers have to fulfill some

requirements to be an efficient singlet oxygen generator; *i*) a high absorption coefficient in the spectral region of the excitation light; *ii*) a high intersystem crossing (ISC) quantum yield, *iii*) a long triplet lifetime, *iv*) a triplet energy higher than the energy gap between the ground O₂ (³Σ_g) and the first excited O₂ (¹Δ_g) states (94.2 kJ/mol), *v*) a high quantum yield of singlet oxygen production Φ_Δ, preferably independent of media such as solvent polarity, *vi*) a high thermal and photochemical stability, *vii*) a low reaction rate of self-quenching itself minimizing the quantum yield (Φ_Δ) dependence on the sensitizer concentration.

2.2.5.2 Singlet Oxygen Characterization

Singlet Oxygen is characterized through its luminescence at 1276 nm. To know the efficiency of a new PS to generate singlet oxygen, its quantum yield (Φ_Δ) is quantified. This parameter could be defined as the ratio of singlet oxygen molecules produced divided by the number of photons absorbed by the PS, equation 2.20.

$$\Phi_{\Delta} = \frac{\text{number of produced } ^1\text{O}_2 \text{ molecules}}{\text{number of absorbed photons}} \quad \text{eq. 2.20}$$

Singlet oxygen quantum yield depends on the amount of PS which populates the triplet state and the efficiency of the ³PS to transfer its energy to environment oxygen to produce ¹O₂. Therefore, Φ_Δ could be defined using the quantum yield of triplet formation (Φ_T) or the quantum yield of intersystem crossing (Φ_{ISC}) and the efficiency of energy transfer (Φ_{en}), equation 2.21.

$$\Phi_{\Delta} = \Phi_{T} \Phi_{\text{en}} \quad \text{eq.2.21}$$

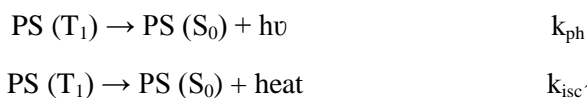
where Φ_T is defined as the rate between intersystem crossing and all deactivation processes, equation 2.22, and Φ_{en} as the proportion of triplet excited state quenched by O₂ (P_{O₂}^T) multiply by the fraction of PS triplet excited state quenched by O₂ yielding ¹O₂ (f_Δ^T), equation 2.23.

$$\Phi_{T} = \frac{k_{isc}}{k_{fl} + k_{ic} + k_{isc}} \quad \text{eq.2.22}$$

$$\Phi_{\text{en}} = P_{O_2}^T f_{\Delta}^T \quad \text{eq. 2.23}$$

Regarding the photosensitizers, in absence of molecular oxygen in the media (unimolecular process), it could be deactivated from T_1 to S_0 by a radiative process; phosphorescence (k_{ph}) or by a non-radiative process (k_{isc}), scheme 2.2.

Deactivation of the triplet state

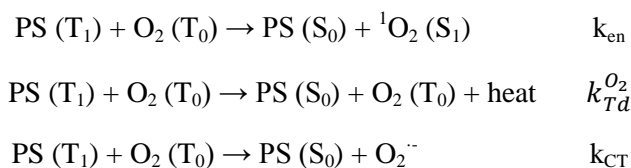


Scheme 2.2. Photosensitizer monomolecular deactivation routes

Therefore, the rate of the deactivation of the triplet state by unimolecular process is:

$$k^T = k_{ph}^T + k_{isc}^T \quad \text{eq.2.24}$$

Nevertheless, in presence of oxygen O_2 (T_0) (bimolecular processes), there are three more potential deactivation routes of PS from its triplet state (T_1) to the ground state (S_0), scheme 2.3; *i*) an energy transfer (k_{en}) from the PS (T_1) generating singlet oxygen, 1O_2 (S_1), *ii*) a physical deactivation mainly by the solvent ($k_{Td}^{O_2}$) and *iii*) electron transfer (k_{CT}) generating superoxide ($^{\cdot}O_2^-$), which is a precursor of most of the other reactive oxygen species (H_2O_2 , $^{\cdot}OH$), scheme 2.3.



Scheme 2.3. Photosensitizer bimolecular deactivation routes

These three deactivate constants depends on the oxygen concentration (bimolecular processes) and are involved in the total rate constant of the quenching of the triplet state 3PS by O_2 (k_q^{PS}):

$$k_q^{PS} = k_{en} + k_{Td}^{O_2} + k_{CT} \quad \text{eq.2.25}$$

These five routes (unimolecular and bimolecular processes) are involved in the photosensitizer deactivation and they are competitive processes to each other.

For instance, if $k_q^{PS}[O_2]$ is much larger than k^T , the triplet lifetime is long enough and all the molecules of the photosensitizer in the triple state (3PS) are quenched by oxygen. Therefore, the fraction of triplet excited states quenched by O_2 ($P_{O_2}^T$) would be 1, equation 2.26, and consequently $\Phi_T/\Phi_\Delta \approx 1$, eq 2.21, being $\Phi_{en} \approx 1$ and the fraction of this 3PS quenched by O_2 which produce 1O_2 ($f_\Delta^T=1$), which could be also defined as equation 2.27.

$$P_{O_2}^T = \frac{k_q^{PS}[O_2]}{k_{ph} + k_{isc} + k_q^{PS}[O_2]} \quad \text{eq.2.26}$$

$$f_\Delta^T = \frac{k_{en}}{k_q^{PS}} \quad \text{eq.2.27}$$

The fraction of triplet excited states quenched by O_2 ($P_{O_2}^T$) can be also described in function of triplet lifetime in the presence (τ_T) and in the absence of oxygen (τ_T^0), equation 2.28, according to the definition of τ_T and (τ_T^0) in equation 2.29-2.30.

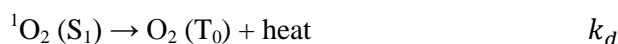
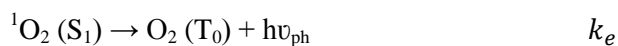
$$P_{O_2}^T = \tau_T k_q^{PS}[O_2] = 1 - \frac{\tau_T}{\tau_0} \quad \text{eq.2.28}$$

$$\tau_T = \frac{1}{k_{ph} + k_{isc} + k_q^{PS}[O_2]} \quad \text{eq.2.29}$$

$$\tau_T^0 = \frac{1}{k_{ph} + k_{isc}} \quad \text{eq.2.30}$$

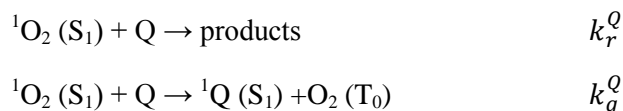
The product $\tau_T k_q^{PS}$ in eq. 2.27 is called Stern-Volmer constant K_{SV} (see former section 2.2.4).

Regarding the singlet oxygen species 1O_2 (S_1), it could follow different deactivation routes to go back to its ground state O_2 (T_0), scheme 2.4. First, singlet oxygen could be deactivated by a radiative process characterized by phosphorescence at 1276 nm (k_e) or by a non-radiative process, denoted as physical deactivation (k_d) by the solvent.



Scheme 2.4. Singlet oxygen unimolecular deactivation routes

If in the media, there is a quencher molecule, that may be the photosensitizer itself (Q=PS), other two deactivation routes should be taken into account; a collisional quenching by Q (k_r^Q) and deactivation by energy transfer to Q from $^1\text{O}_2$ (k_q^Q).



Scheme 2.5. Singlet oxygen bimolecular deactivation routes in the presence of a quencher

On the one hand, the unimolecular deactivation paths are included in the decay rate (k_Δ) (generally $k_e \ll k_d$ in most solvents, equation 2.31). Note here that singlet oxygen deactivation constant (k_Δ) is directly related to the solvent, ($k_\Delta \approx k_d$).¹⁸ This is because of the properties of the solvents and its possible interactions with the singlet oxygen have an effect on the radiative and non-radiative deactivation processes.

$$k_\Delta = k_e + k_d \approx k_d \quad \text{eq.2.31}$$

On the other hand, the bimolecular processes are included in the rate constant of $^1\text{O}_2$ total quenching (k_t^Q), according to equation 2.32

$$k_t^Q = k_r^Q + k_q^Q \quad \text{eq.2.32}$$

Thus, the $^1\text{O}_2$ lifetime in absence and presence of quencher are described in equation 2.32 and 2.33, respectively.

$$\tau_\Delta = \frac{1}{k_d} \quad \text{eq.2.33}$$

$$\tau_\Delta^Q = \frac{1}{k_d + k_t^Q[Q]} \quad \text{eq.2.32}$$

Note here that the singlet oxygen quantum yield, Φ_Δ could be also described as the quantum yield of $^1\text{O}_2$ emission (Φ_e), the radiative deactivation rate constant of $^1\text{O}_2$ (k_e) and the singlet oxygen lifetime (τ_Δ^Q), equation 2.35.

$$\Phi_\Delta = \frac{\Phi_e}{k_e \tau_\Delta^Q} \quad \text{eq.2.35}$$

The radiative deactivation (k_e) is drastically decrease in protic solvents with O-H bonds such as H_2O or MeOH , while in solvents with C-H bonds and even more with C-Cl/F bonds is favored, attributed to electronic to vibrational energy transfer

interactions. This interaction modifies also the singlet oxygen lifetime (τ_{Δ}) *i.e.* such as $\tau_{\Delta(\text{MeOH})} = 10 \mu\text{s}$ and $\tau_{\Delta(\text{MeOD})} = 37 \mu\text{s}$.^{19,20}

Experimentally, this determination is obtained comparing the signal of the new photosensitizer with a reference photosensitizer with known singlet oxygen quantum yield (Φ_{Δ}^R), both at the same conditions (solvent, irradiation wavelength and similar absorbance at excitation wavelength) following equation 2.36.

$$\frac{\Phi_{\Delta}^{\text{PS}}}{\Phi_{\Delta}^{\text{R}}} = \frac{S_{\text{e}}^{\text{PS}}}{S_{\text{e}}^{\text{R}}} \frac{\alpha^{\text{R}}}{\alpha^{\text{PS}}} = \frac{\Phi_{\Delta}^{\text{PS}}}{\Phi_{\Delta}^{\text{R}}} \frac{k_{\text{d}}^{\text{R}} + k_{\text{t}}^{\text{R}}[\text{PS}^{\text{R}}]}{k_{\text{d}}^{\text{PS}} + k_{\text{t}}^{\text{PS}}[\text{PS}]} \quad \text{eq.2.36}$$

where Φ_{Δ}^{R} is the singlet oxygen quantum yield of the known reference, S_{e} is the singlet oxygen signal intensity at 1276 nm for reference (R) and photosensitizer (PS) and α is an absorption factor given by equation 2.37

$$\alpha = 1 - 10^{-A} \quad \text{eq. 2.37}$$

where A is the absorbance of the photosensitizer and reference in the excitation wavelength, the difference between both absorbances should not be significant.

This expression 2.36 simplifies in equation 2.38 when $k_{\text{t}}[\text{PS}^{\text{R}}] \ll k_{\text{d}}$. This condition is fulfilled in the range of concentration considered in this work.²¹

$$\frac{S_{\text{e}}^{\text{PS}}}{S_{\text{e}}^{\text{R}}} \frac{\alpha^{\text{R}}}{\alpha^{\text{PS}}} = \frac{\Phi_{\Delta}^{\text{PS}}}{\Phi_{\Delta}^{\text{R}}} \frac{1}{1 + \tau_{\Delta} k_{\text{t}}[\text{PS}]} \quad \text{eq.2.38}$$

Under this condition, the representation of $(S_{\text{e}}^{\text{R}}/S_{\text{e}}^{\text{PS}}) (\alpha^{\text{PS}}/\alpha^{\text{R}}) = f([\text{PS}])$ should be linear and give the value of k_{t}^{PS} which theoretically is $k_{\text{t}}[\text{PS}] < 0.1 k_{\text{d}}$. Moreover, when $\tau_{\Delta} k_{\text{t}}[\text{PS}] \ll 1$ (or $k_{\text{t}}^{\text{PS}}[\text{PS}] \ll k_{\text{d}}$), indicates that there is a negligible $^1\text{O}_2$ quenching by the PS in the range of concentrations used and the ratio $S_{\text{e}}^{\text{R}}/S_{\text{e}}^{\text{PS}}$ does not depend on the PS concentration and the quantum yield of $^1\text{O}_2$ production by the PS is determined by equation 2.39

$$\Phi_{\Delta}^{\text{PS}} = \Phi_{\Delta}^{\text{R}} \frac{S_{\text{e}}^{\text{PS}}}{S_{\text{e}}^{\text{R}}} \frac{\alpha^{\text{R}}}{\alpha^{\text{PS}}} \quad \text{eq. 2.39}$$

This is the final equation used in this work to determine the singlet oxygen quantum yield of the new photosensitizer in solution and hybrid nanosystems in suspension.

2.3 Bibliography

1. Valeur, B. *Molecular Fluorescence - Principles and Applications. Methods* (2001). doi:10.1002/3527600248.
2. Lakowicz, J. R. & Masters, B. R. *Principles of Fluorescence Spectroscopy, Third Edition. Journal of Biomedical Optics* (2008). doi:10.1117/1.2904580.
3. Gartzia-Rivero, L., Sánchez-Carnerero, E. M., Jiménez, J., Bañuelos, J., Moreno, F., Maroto, B. L., López-Arbeloa, I. & De La Moya, S. Modulation of ICT probability in bi(polyarene)-based O-BODIPYs: Towards the development of low-cost bright arene-BODIPY dyads. *Dalt. Trans.* **46**, 11830–11839 (2017).
4. Sánchez-Arroyo, A. J., Palao, E., Agarrabeitia, A. R., Ortiz, M. J. & García-Fresnadillo, D. (ESI)Towards improved halogenated BODIPY photosensitizers: clues on structural designs and heavy atom substitution patterns. *Phys. Chem. Chem. Phys.* **19**, 69–72 (2017).
5. Turksoy, A., Yildiz, D. & Akkaya, E. U. Photosensitization and controlled photosensitization with BODIPY dyes. *Coord. Chem. Rev.* **379**, 47–64 (2019).
6. Zhang, X. F. & Yang, X. Photosensitizer that selectively generates singlet oxygen in nonpolar environments: Photophysical mechanism and efficiency for a covalent BODIPY dimer. *J. Phys. Chem. B* **117**, 9050–9055 (2013).
7. Epelde-Elezcano, N., Palao, E., Manzano, H., Prieto-Castañeda, A., Agarrabeitia, A. R., Tabero, A., Villanueva, A., de la Moya, S., López-Arbeloa, I., Martínez-Martínez, V. & Ortiz, M. J. Rational Design of Advanced Photosensitizers Based on Orthogonal BODIPY Dimers to Finely Modulate Singlet Oxygen Generation. *Chem. - A Eur. J.* **23**, 4837–4848 (2017).
8. Measures done at UPV/EHU by R. Prieto-Montero.
9. Arbeloa, F. L., Gonzalez, I. Ll., Ojeda, P. R. & Arbeloa, I. L. Aggregate formation of rhodamine 6G in aqueous solution. *J. Chem. Soc. Faraday Trans. 2* **78**, 989 (1982).
10. Kasha, M., Rawls, H. R. & El-Bayoumi, M. A. The Exciton Model In Molecular Spectroscopy. *Pure Appl. Chem.* **11**, 371–392 (1965).
11. López Arbeloa, F., Bañuelos, J., Martínez, V., Arbeloa, T. & López Arbeloa, I. Structural, photophysical and lasing properties of pyrromethene dyes. *Int. Rev. Phys. Chem.* **24**, 339–374 (2005).
12. Berberan-Santos, M. N., Nunes Pereira, E. J. & Martinho, J. M. G. Stochastic theory of combined radiative and nonradiative transport. *J. Chem. Phys.* **107**, 10480–10484 (1997).
13. Cazes, J. *Encyclopedia of Chromatography. Florida Atlantic. University* (2005). doi:10.1081/E-ECHR.

14. Zhou, Q., Zhou, M., Wei, Y., Zhou, X., Liu, S., Zhang, S. & Zhang, B. Solvent effects on the triplet–triplet annihilation upconversion of diiodo-Bodipy and perylene. *Phys. Chem. Chem. Phys.* **19**, 1516–1525 (2017).
15. Nonell, S. & Flors, C. *Singlet Oxygen. Comprehensive Series in Photochemistry and Photobiology* vol. 1 (Royal Society of Chemistry, 2016).
16. DeRosa, M. Photosensitized singlet oxygen and its applications. *Coord. Chem. Rev.* **233–234**, 351–371 (2002).
17. Krasnovsky, A. A. Singlet molecular oxygen in photobiochemical systems: IR phosphorescence studies. *Membr. Cell Biol.* (1998).
18. Schweitzer, C. & Schmidt, R. Physical Mechanisms of Generation and Deactivation of Singlet Oxygen. *Chem. Rev.* **103**, 1685–1758 (2003).
19. Hurst, J. R. & Schuster, G. B. Nonradiative Relaxation of Singlet Oxygen in Solution. *J Am Chem Soc* **105**, 5756–5760 (1983).
20. Prieto-Montero, R., Sola-Llano, R., Montero, R., Longarte, A., Arbeloa, T., López-Arbeloa, I., Martínez-Martínez, V. & Lacombe, S. Methylthio BODIPY as a standard triplet photosensitizer for singlet oxygen production: a photophysical study. *Phys. Chem. Chem. Phys.* **21**, 20403–20414 (2019).
21. Schmidt, R., Tanielian, C., Dunsbach, R. & Wolff, C. Phenalenone, a universal reference compound for the determination of quantum yields of singlet oxygen O₂(¹Δ_g) sensitization. *J. Photochem. Photobiol. A Chem.* **79**, 11–17 (1994).

3

EXPERIMENTAL SECTION

3.1	<u>Synthesis of Multifunctional Silica Nanoparticles</u>	42
3.1.1	Synthesis of Silica Nanoparticles	42
3.1.1.1.	<i>Nonporous silica nanoparticles</i>	42
3.1.1.2.	<i>Mesoporous silica nanoparticles</i>	44
3.1.1.3.	<i>Organically modified silica nanoparticles</i>	46
3.1.2	Synthesis of Photoactive Silica Nanoparticles	47
3.1.2.1.	<i>“Core” functionalization</i>	48
3.1.2.2.	<i>“Shell” functionalization</i>	50
3.2	<u>Experimental Techniques</u>	58
3.2.1	Structural and Chemical Characterization	58
3.2.1.1.	<i>Scanning Electron Microscopy and Transmission Electron Microscopy</i>	58
3.2.1.2.	<i>Dynamic Light Scattering</i>	58
3.2.1.3.	<i>X-ray Photoelectron Spectroscopy</i>	60
3.2.1.4.	<i>Proton Nuclear Magnetic Resonance</i>	60
3.2.1.5.	<i>Infrared-Attenuated Total Reflectance</i>	61
3.2.1.6.	<i>Dye quantification</i>	61

3.2.2. Photophysical Characterization	62
3.2.2.1. <i>UV-Vis NIR-spectroscopy</i>	62
3.2.2.2. <i>Fluorescence emission, quantum yield, lifetimes and phosphorescence</i>	64
3.2.2.3. <i>Singlet oxygen emission by direct measurements</i>	65
3.2.2.4. <i>Laser flash-photolysis</i>	66
3.2.2.5. <i>Photostability measurements</i>	67
3.2.2.6. <i>Quantum mechanics calculations</i>	68
3.3. <u>In vitro HeLa cells studies</u>	68
3.3.1. Cells culture	69
3.3.2. Sample preparation	69
3.3.3. Internalization and subcellular localization	69
3.3.4. Photodynamic treatment	69
3.3.5. Cell viability (MTT) assay	71
3. 4 <u>Bibliography</u>	72

Experimental Section

Along with this chapter, the synthesis of functional nanoparticles and the required techniques used for their characterization are explained.

The first section is focused on the description of the synthesis of “core-shell” silica nanoparticles (nonporous, mesoporous and ormosil) functionalized with different groups, *i.e.* -amine, -carboxylic, -vinyl, -phenyl, etc, by using different silica source and different synthetic approaches (section 3.1.1). It is also detailed the different functionalization routes of the silica nanoparticles with compounds of interest for their potential use in biomedical applications (section 3.1.2). The functionalization is carried out by different methods; *i)* an *in situ* process where the compounds are physically embedded or chemically linked in the core of the nanoparticles and *ii)* a post-synthesis chemical modification of the external surface. This latter approach is also applied to the functionalization of laponite-clay nanoparticles.

The second section 3.2 is dedicated to the description of several techniques handled in this work to fully characterize the systems under study. Firstly, electronic microscopies, (SEM and TEM), dynamic light scattering (DLS), X-ray photoelectron spectroscopy (XPS), proton nuclear magnetic resonance ($^1\text{H-NMR}$), FTIR- and UV-Vis spectroscopies are employed to study the distribution, size, morphology, stability and chemical composition of the functionalized nanoparticles (section 3.2.1). Secondly, the most important techniques for the characterization of the photophysical properties of all these new materials and many commercial and lab-made dyes/photosensitizers in solution are detailed, which includes absorption and emission spectroscopies (steady-state and time-resolved) as well as transient absorption experiments (in nanosecond range) and photostability measurements (section 3.2.2). At the end of this section, a brief description of the quantum simulations applied for the study of organic molecules is also mentioned.

Finally, in the last section 3.3, the most remarkable aspects regarding the *in vitro* experiments carried out in HeLa cells for the most representative samples are described. Briefly, these experiments consist of the study of the cell internalization, cell localization, toxicity in dark conditions and the phototoxicity of several functionalized nanoparticles but also many commercial and lab-made photosensitizers in solution. Note here that, the latter mentioned phototoxicity experiments were

optimized in our faculty during this work to set a standardized protocol for the irradiation of the samples (section 3.3.4).

3.1 Synthesis of Multifunctional Silica Nanoparticles

In this part, the synthesis of silica nanoparticles decorated with different functional compounds for their use in biomedical applications is described. Firstly, three different synthetic approaches for silica nanoparticles are detailed, section 3.1.1. In the first case, nonporous silica nanoparticles of a diameter size of around 40-45 nm derived from the well-known Stöber method were obtained, section 3.1.1.1. In the second case, a modified Stöber method for the synthesis of mesoporous silica nanoparticles with a similar size of around 50-60 nm, is explained in section 3.1.1.2. In the third case, the synthesis of organically modified silica nanoparticles by incorporating different organo(alkoxy)silanes is also described, section 3.1.1.3. Note here that although all these types of silica nanoparticles are synthesized, the mesoporous-like were of greater interest and consequently the most employed along with this work.

Then, the functionalization of the internal and external surfaces of those nanoparticles with molecules of interest for their implementation in bioimaging and photodynamic therapy is in section 3.1.2. A fluorescent dye is physically embedded or chemically linked in the core of the nanoparticles via one-pot synthesis (section 3.1.2.1). In a second step by a post-functionalization approach, a photosensitizer, chains of polyethylene glycol and the folic acid targets are anchored at their external surface (section 3.1.2.2).

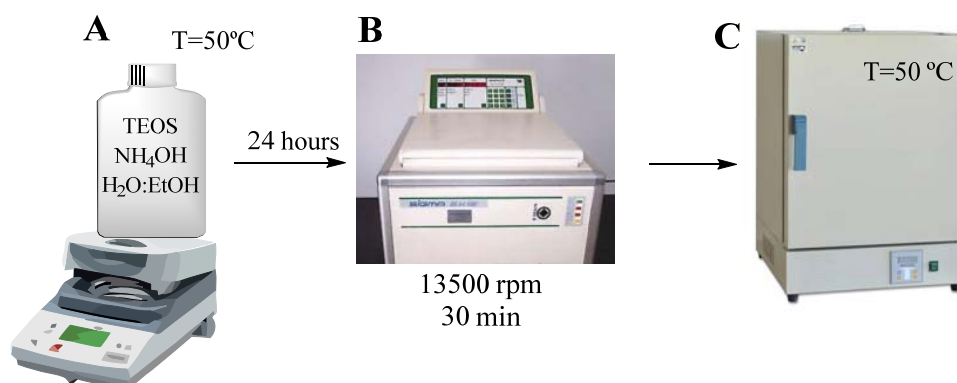
3.1.1 Synthesis of Silica Nanoparticles

3.1.1.1. Nonporous Silica Nanoparticles

Nonporous silica nanoparticles (SN) were synthesized followed the Stöber method,¹ using tetraethoxysilane (TEOS) as the main silica source and ammonium hydroxide solution (NH₄OH) as a basic catalyst in a water:ethanol mixture.

Firstly, ethanol (82 mL), Milli Q water (9.0 mL) and ammonium hydroxide solution (28% NH₃) (1.51 mL) were added in a propylene flask and stirring at 50 °C. Then, the

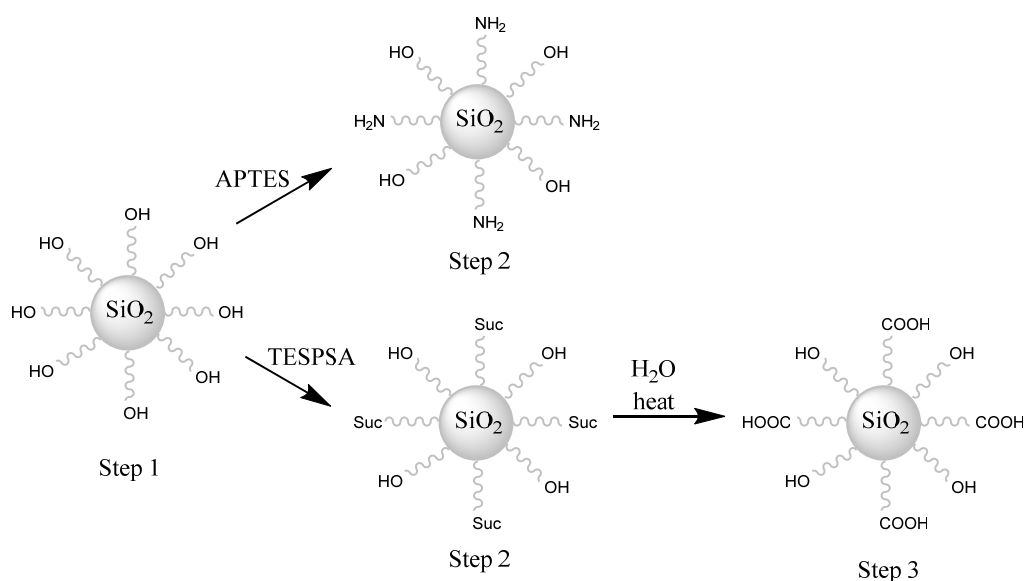
silica source TEOS was added (4.46 mL) and the mixture was stirring for 24 hours. The nanoparticles were collected by centrifugation at 13500 rpm during 30 min (B. Braun Sigma 2K15 centrifuge) and washed three times with ethanol. Finally, they were dried overnight at 50 °C. At this step, the so-called “core” is formed, Scheme 3.1. Depending on the reaction the amount of collected nanoparticles varies between 500 mg to 900 mg.



Scheme 3.1. Synthesis of Nonporous Silica Nanoparticles.

Besides the presence of the inherent hydroxyl groups in the silica, extra functional groups are added at the external surface in a second step. For that different silica sources were employed to generate a functionalized “shell” in the nanoparticles: 3-aminopropyltriethoxysilane (APTES, Sigma-Aldrich) or (3-Triethoxysilyl)propylsuccinic anhydride (TESPSA, Gelest) to include amine or succinimide groups, respectively.

Once the previously synthesized nanoparticles (400 mg) were dispersed in ethanol at a temperature of 40 °C, 25 µL of APTES or 30 µL of TESPSA were added. This amount of APTES or TESPSA was estimated to functionalize the 2 % of nanoparticle surface (see XPS results in chapter 5). After stirring for 48 hours at 40 °C, the nanoparticles were centrifuged, washed three times with ethanol and dry at 50 °C overnight. Afterward, the nanoparticles with succinimide groups were dispersed in water (40 mL) at 70° C and stirring for 6 hours to obtain the resultant carboxylic groups, Scheme 3.2.



Scheme 3.2. Functionalization of SNs shell with OH, NH₂/ Suc, and COOH groups.

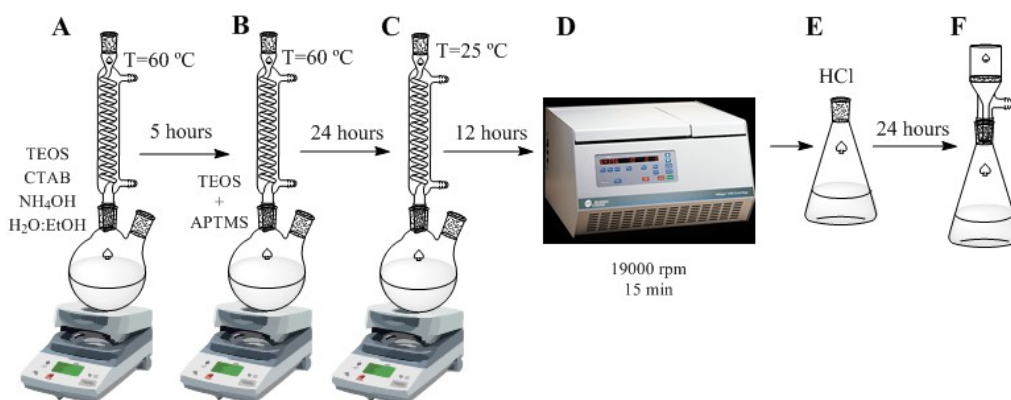
3.1.1.2. Mesoporous Silica Nanoparticles

Mesoporous Silica Nanoparticles (MSN) of 50-60 nm size were synthesized followed a modified Stöber method.¹ This synthesis is based on the previous procedure which consists in a mixture of TEOS as main silica source and NH₄OH as basic medium with ethanol as co-solvent, but adding a surfactant, hexadecyltrimethylammonium bromide (CTBA), as structure-directing agent for the formation of the long-range ordered pores with uniform size in the silica nanoparticles, Scheme 3.3.^{2,3}

In this case, the cationic surfactant, CTAB (0.1 g) was dissolved in 50 mL NH₄OH 0.13 M (pH=11) and was vigorously stirring at 60 °C, until getting a homogeneous solution. Afterward, 0.8 mL TEOS (0.2 M in ethanol) was added and it was stirring, keeping constant the temperature, during 5 hours, Scheme 3.3.A.

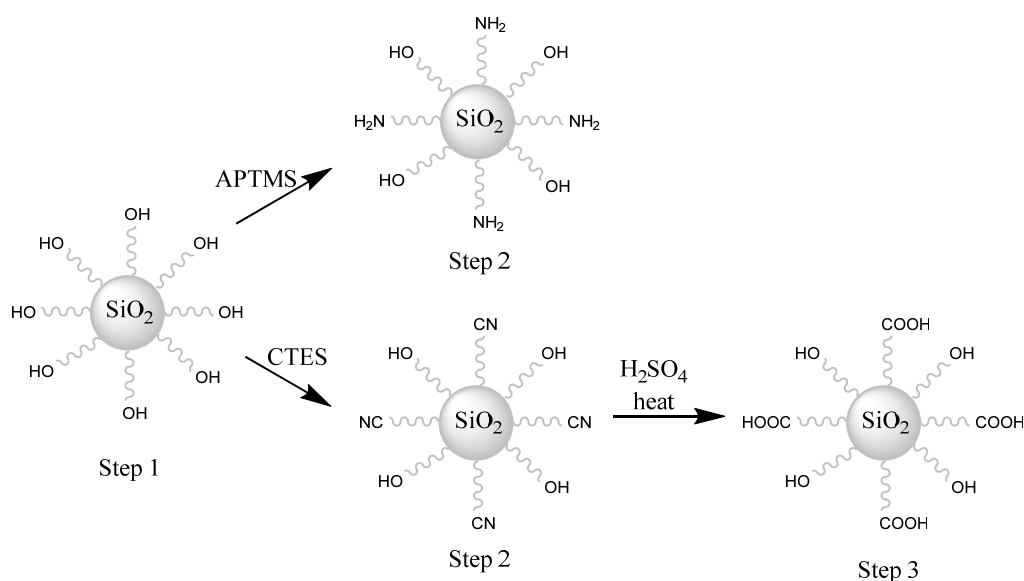
In a second step, 3-aminopropyltrimethoxysilane (APTMS, Sigma-Aldrich) or 3-cyanopropyltriethoxysilane (CTES, Sigma-Aldrich) were used as a second silica source to generate the functionalized “shell” with amine group or ciane group, respectively, Scheme 3.4.^{2,3} In the same flask, 0.8 mL of TEOS (1M in ethanol) and 0.8 mL of APTMS or CTES (12 % v) were added to the mixture, keeping under stirring for 24 hours, Scheme 3.3.B. This amount of APTMS or CTES functionalizes

the 5 % of nanoparticle surface (see XPS results in chapter 5). Subsequently, the temperature was decreased to 25 °C and it was stirred for other 12 hours, (Scheme 3.3. C). Silica nanoparticles were collected by centrifugation 19000 rpm during 15 min (Centrifuge BECKMAN COULTER model Allegra 64 R) and washed three times with ethanol:water mixture and the last one with ethanol. Then, CTAB surfactant was removed by stirring the NPs in an acidic ethanolic solution (0.2 mL of HCl (37%)) at least for 24 hours, (Scheme 3.3.D and E). Finally, the solution was filtered (Membrane Filter 0.1 μm) to obtain the nanoparticles in powder (Scheme 3.3.F). Depending on the reaction, the amount of collected nanoparticles varied between 30 mg to 50 mg.



Scheme 3.3. Synthesis of Mesoporous Silica Nanoparticles.

After adding the “shell” these MSNs have two organic groups in their external surface, NH_2 and OH or CN and OH (Scheme 3.4 step 2). Nevertheless, an extra step to convert the CN into COOH groups, more useful for grafting of interesting molecules was carried out. Thus, CN -nanoparticles were suspended in acid solution ($\text{H}_2\text{O}:\text{H}_2\text{SO}_4$ 50:50 v/v) and stirring under 140 °C for 12 hours. Then, the sample was cooled down to r.t. and kept stirring for another 24 hours. Finally, the COOH -nanoparticles were washed several times with water, until collecting neutral supernatants, step 3 in Scheme 3.4.



Scheme 3.4. Functionalization of MSNs shell with OH, NH_2 / CN and COOH groups.

3.1.1.3. Organically modified silica nanoparticles

A series of organically modified mesoporous silica nanoparticles, known as ORMOSIL-particles are also synthesized in this work. The procedure is similar to the previous synthesis for mesoporous silica nanoparticles but in this case, the common silica source TEOS was mixed with a more hydrophobic silica source, presenting organic groups. The organo(alkoxy)silanes used were triethoxymethylsilane (MTES), triethoxyvinylsilane (VTES), phenyltriethoxysilane (PTES) or triethoxy(octyl)silane (OTES),^{4,5} Figure 3.1, all purchased in Sigma-Aldrich and were used without any modifications.

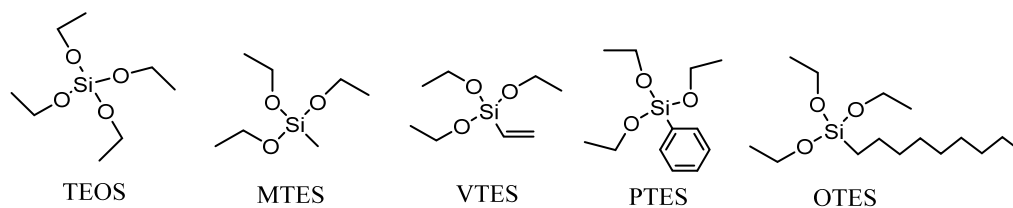


Figure 3.1 Organic structure of different silica sources.

Ormosil nanoparticles were synthesized following the modified Stöber method, previously described in section 3.1.1.2. Nonetheless, in the first step, instead of adding only TEOS, the extra silica source was also added, for instance, TEOS and MTES in ratio 1:0.1, respectively. Afterward, the mixture was stirring at 60 °C for 5 hours, subsequently, the second step shell modification was carried out, and to finalize with the cleaning and purification step, as it is explained previously for MSN synthesis. In this study, apart from using several organo(alkoxy)silane, with different organic group to tunable the hydrophobic character of the nanoparticle core, Figure 3.1, several ratios (TEOS:xTES) were also systematically tested, from 1:0.1 to 1:2, keeping constant the total concentration of silica in the solution. Otherwise, the nanoparticle size and morphology could change. These experiments were carried out in order to optimize the hydrophobic character of the core of the nanoparticles.

3.1.2 Synthesis of Photoactive Silica Nanoparticles

Silica nanoparticles were functionalized with several organic compounds following three different routes, Figure 3.2. The core was *in situ* decorated with fluorescent dyes during the synthesis for mesoporous and ormosil nanoparticles, adding the fluorophores in the synthesis gel to get them physically embedded in their pores. In the case of nonporous silica nanoparticles, the dye was chemically anchored by covalent bonding with the -OH groups present in the internal surface (section 3.1.2.1) On the other hand, the functionalization of the shell was done in a second step through a post-synthesis grafting to covalently anchor, several compounds of interest, *i.e.* fluorescence dyes, photosensitizers, polyethylene glycol chains and folic acid molecules to the different functional groups of the external surface of the silica by different reactions (section 3.1.2.2).⁶⁻⁹

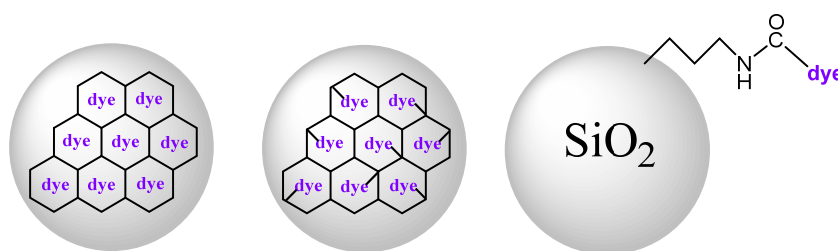


Figure 3.2. Nanoparticles functionalized with dyes following different routes; physical encapsulation, covalent occlusion and external covalent grafting.

3.1.2.1. "Core" functionalization

The core functionalization consists in the occlusion of a fluorescent dye in the inner area of the nanoparticles during their synthesis. Depending on the core structure two different procedures were carried out:

- i) For mesoporous and ormosil nanoparticles, the dye was directly added to the synthesis gel, being physically occluded in the pores when the nanoparticles were forming. To obtain a homogeneous distribution inside nanoparticles the dye was mixed with the CTAB and NH_4OH before adding the silica source. Then, the procedure previously described in section 3.1.1.2 or 3.1.1.3 was followed.⁶

As fluorescent dyes, different rhodamine-like were used. Particularly, rhodamine 6G, rhodamine 19, rhodamine 101, rhodamine 640, rhodamine 700 and rhodamine 800, Figure 3.3, with characteristic absorption and emission bands in different regions of the Visible light spectrum. The encapsulated dye loading was optimized by systematically varying the amount added to the synthesis gel from $1 \cdot 10^{-2}$ M to $5 \cdot 10^{-5}$ M to set the best conditions in terms of the final emission properties of the dye/silica nanoparticles. This optimization was carried out in the first instance for rhodamine 6G in MSN, and was extrapolated to the rest of rhodamines. Nonetheless, more accuracy study was carried out in ormosil nanoparticles with rhodamine 101, involving also changes in synthesis temperature.

- ii) Since the former physical encapsulation method could not be used for nonporous nanoparticles, the incorporation of fluorescence dyes in the inner surface of the nonporous nanoparticles was performed by a chemical reaction with the hydroxyl groups of the silica net. For that, a silylated-dye was required, which was added to the synthesis gel before starting the nonporous nanoparticles synthesis. Thus, the dye was covalently anchored as the silica nanoparticles were synthesized. Particularly, the dye used was perylenediimide derivative, Figure 3.4.¹⁰ The silylation of the perilene was performed by Carlos Baleizão *et al*, in the Centro de Química-Física Molecular of Instituto Superior Técnico at University of Lisbon, Portugal.¹¹

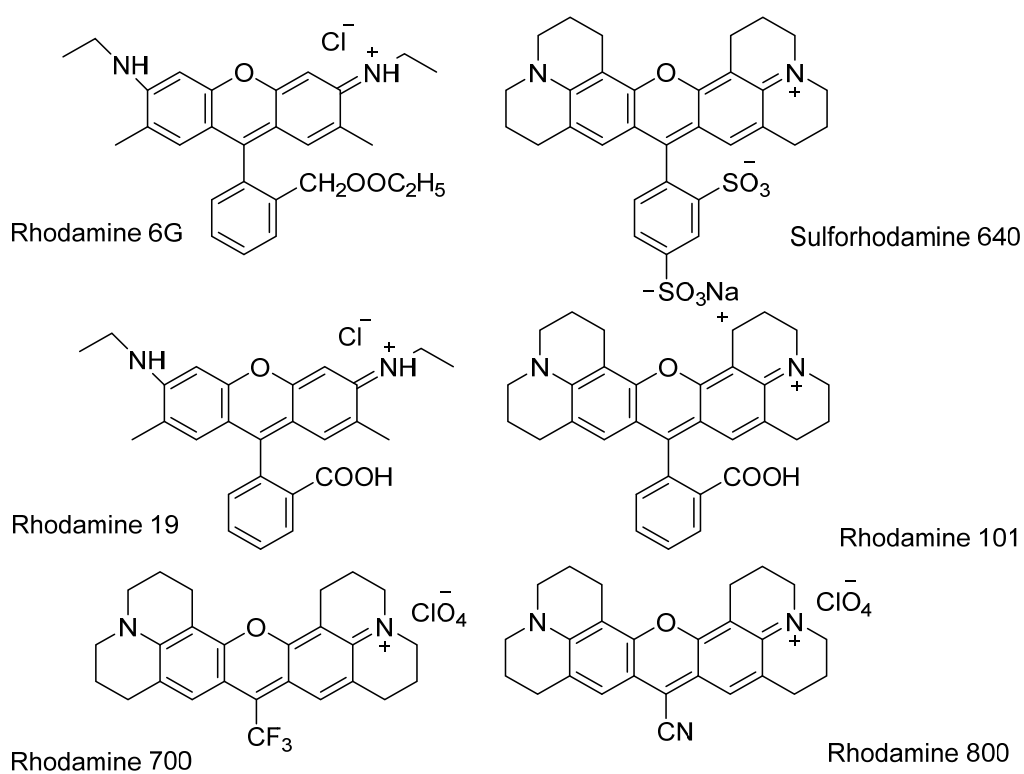


Figure 3.3. Molecular structure of the commercial rhodamine dyes used in this work.

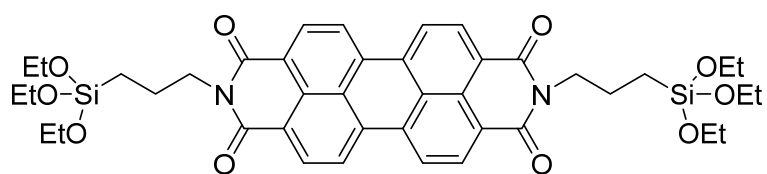


Figure 3.4. Chemical structure of perylenediimide derivative.¹⁰

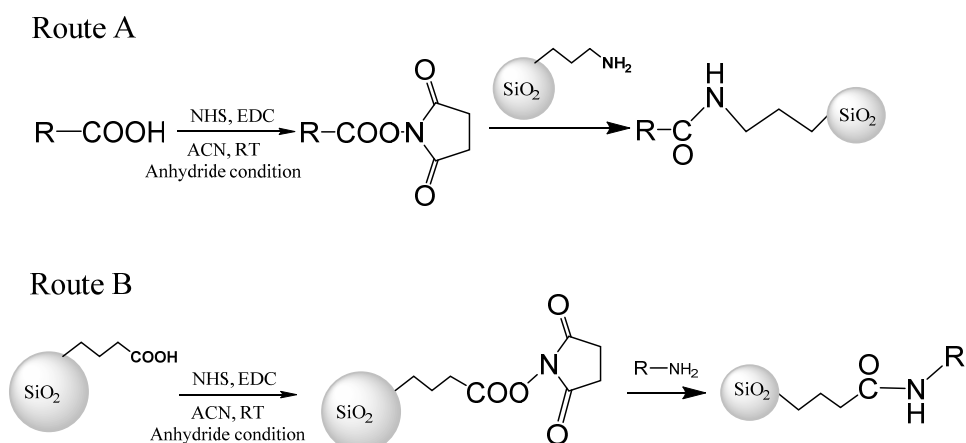
3.1.2.2. "Shell" functionalization

In this section, the post-functionalization of the external surface of the silica nanoparticles is described. Note here that in this work, nanoparticles of Laponite-clay are also functionalized to be used as an alternative nanocarrier for photodynamic treatments. In this context, the external surface of both nanocarriers was decorated with three key compounds; photosensitizer, polyethylene glycol and folic acid.^{6,8,9} However, although both nanomaterials are silica-based, their structure, composition and therefore their external surface are different. Particularly, as previously detailed in section 3.1.1, silica nanoparticles could present OH/NH₂ or OH/COOH in their external surface while laponite has only OH groups. For this reason, different approaches were followed to anchor organic molecules to NH₂, COOH or OH groups of nanoparticles, as it is detailed below.

i) *Grafting on amine or carboxylic groups*; the anchorage between amine and carboxylic groups is a common peptide reaction.¹² Silica nanoparticles with carboxylic groups or amine groups could be efficiently linked to organic compounds with amine or carboxylic groups, respectively. In both situations, the synthesis route is alike.

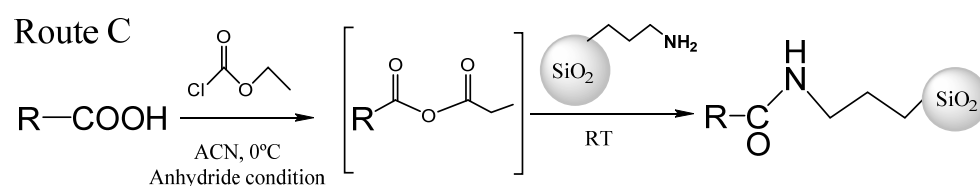
Firstly, the compound (route A in Scheme 3.5) or nanoparticle (route B in Scheme 3.5) with carboxylic group were dissolved or suspended in dry acetonitrile (20 mL) under inert atmosphere (Argon). Then, N-Hydroxysuccinimide (NHS) and N-(3-(dimethylaminopropyl)-N'-ethylcarbodiimide (EDC), both from Sigma-Aldrich, were added to activate the carboxylic groups in equimolar concentration respect to the graftable organic molecule (estimated $7 \cdot 10^{-2}$ mmol for 20 mg of nanoparticles).^{2,12,13} After 30 minutes of stirring, the nanoparticles (route A in Scheme 3.5) or the organic molecule (route B in Scheme 3.5) with amine groups were added to the synthesis and was kept under stirring for 3 hours. Finally, the synthesized nanoparticles were washed several times and collected by filtration.¹³⁻¹⁵

Note here that depending on the graftable organic compounds other conditions were also used. For instance, the thionine photosensitizer is not soluble in ACN, so in this case, dry methanol was used.



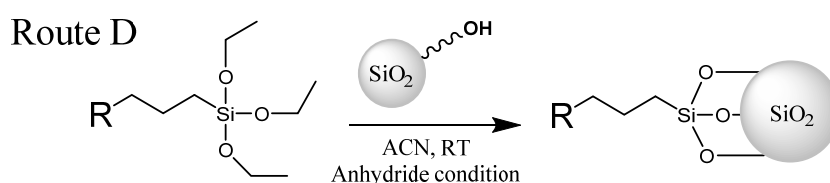
Scheme 3.5. Common peptide reaction between R-COOH and NP-NH₂ (Route A) or NP-COOH and R-NH₂ (Route B).

However, an alternative route was performed for the tethering of lab-made BODIPYs since they were decomposed under these aggressive conditions. In those cases, the organic compound with COOH group (in particular BODIPY-COOH) was dissolved in ACN anhydride (20 mL) at 0 °C. Then, ethyl chloroformate (Acros) and Triethylamine (TEA, Sigma-Aldrich) was added dropwise in equimolar concentration respect to the R-COOH. The system was vigorously stirred for 30 minutes. Then, the NH₂-nanoparticles were added at r.t. and stirred for 30 minutes.⁶ Finally, the functionalized nanoparticles were washed with ethanol until a colorless supernatant was obtained. BODIPY/nanoparticles were collected by filtration, (Route C, Scheme 3.6).



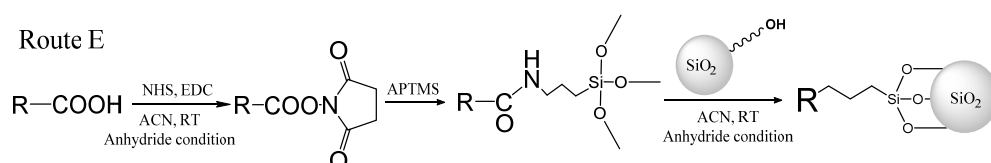
Scheme 3.6. Alternative grafting route for BODIPY-COOH and NP-NH₂ (Route C).

ii) *Grafting on nanoparticle hydroxyl groups*; the above procedures were carried out for silica nanoparticles with NH_2 or COOH functional groups at the external surface. However, silica nanoparticles have also, in a higher extension, hydroxyl groups at their surface. Moreover, for laponite nanoparticles OH is the only functional group present on their external surface. Thus, they were functionalized by the following route. The easier way to covalently attach organic molecules to the external OH groups of the nanocarriers (laponite and silica nanoparticles) is by a direct condensation reaction, (Route D). For that the compounds should be silylated, *i.e.* R-Si(OEt)_3 . The procedure consisted of dissolving the silylated compound (approx. $7 \cdot 10^{-2}$ mmol) in dry acetonitrile (20 mL) under inert atmosphere (Argon). They were under stirring for complete dissolution, approximately for 15 minutes, and then the nanoparticles (20 mg) were added. The mixture was stirring for 3 hours, Scheme 3.7. Finally, the nanoparticles were collected by filtration and washed with ethanol until the supernatant was completely clean.¹³



Scheme 3.7. R-Si(OEt)_3 grafting synthesis on nanoparticle hydroxyl groups, (Route D).

However, it is also possible to efficiently anchor compounds with $-\text{COOH}$ function to the OH groups of nanoparticles, by previously transforming the COOH groups into succinimide groups, (Scheme 3.8, Route E), following the previously described reaction. Then an equimolar concentration of APTMS (amine-functionalized silica source) was added to render the (alkoxy)silane derivatives. In the last step, the nanoparticles were added and the direct condensation reaction takes place (Scheme 3.8).^{6,16}



Scheme 3.8. Synthesis of silylated derivative and its grafting on OH groups of NPs, route E.

It is outstanding that the grafting reactions not only depend on the external functional groups of nanocarriers but also on the graftable groups available in the molecular structure of the selected organic compound; *i)* fluorescence dyes, *ii)* photosensitizers, *iii)* polyethylene glycol and *iv)* folic acid.

i) Fluorescence dyes, particularly two commercial rhodamines, 19 and 101 (Figure 3.3), were tethered at the external surface of the silica nanoparticles. Both of these rhodamines have a carboxylic group in their structure and route A (Scheme 3.5), was used to link them to the NH₂-nanoparticles.

ii) Photosensitizers (PS). In this case, compounds from different families were studied, *i.e.* commercial PSs such as Rose Bengal (RB), Chlorin e6 and Thionine, from Sigma-Aldrich (Table 3.1) and others lab-made PSs (BODIPY-derivatives, Table 3.2) were tethered to the external surface of silica nanoparticles. Rose Bengal and Chlorin e6 have carboxylic groups in their molecular structure while Thionine dye presents amine groups. Moreover, the lab-made photosensitizers (supplied by Prof. M.J. Ortiz *et al.* from Universidad Complutense de Madrid, Spain) were rationally designed with carboxylic or alkoxide groups.

Table 3.1. Molecular structure of commercial photosensitizers grafted to nanoparticles

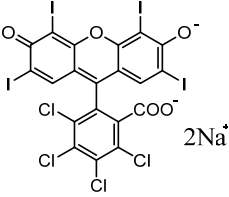
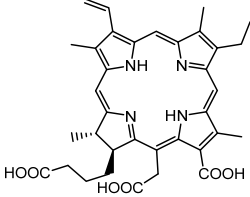
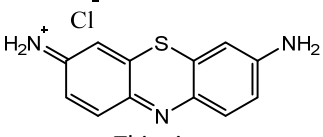
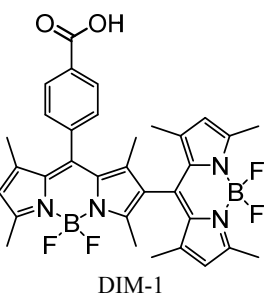
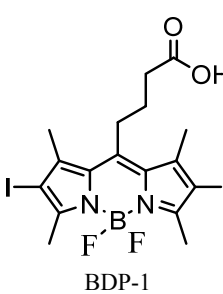
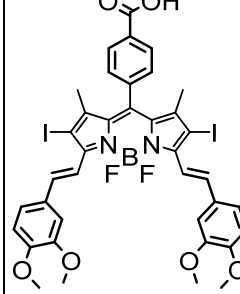
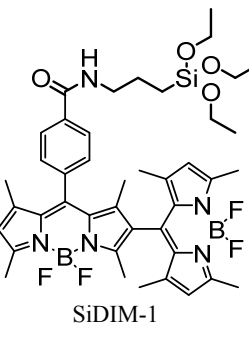
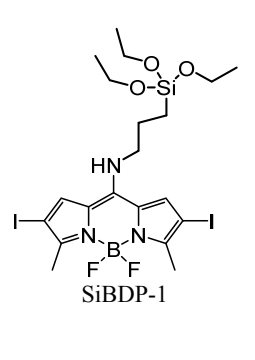
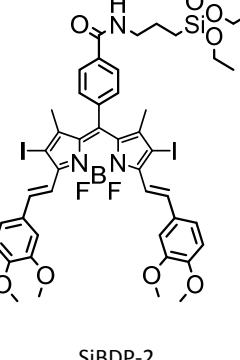
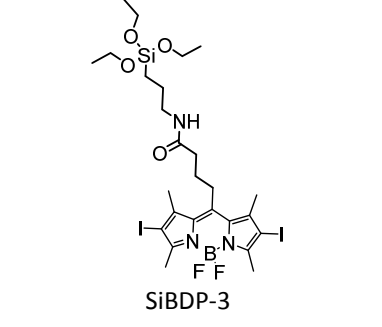
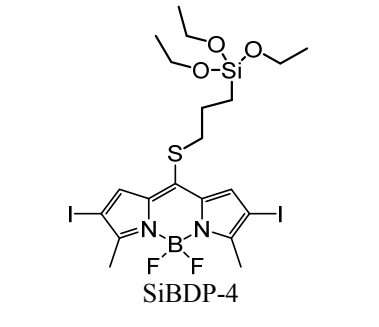
-COOH	 <p>Rose Bengal</p>	 <p>Chlorin e6</p>
-NH₂	 <p>Thionine</p>	

Table 3.2. Molecular structure of lab-made BODIPY photosensitizers grafted to nanoparticles

-COOH	 <p style="text-align: center;">DIM-1</p>	 <p style="text-align: center;">BDP-1</p>	 <p style="text-align: center;">BDP-2</p>
Si(OEt)₃	 <p style="text-align: center;">SiDIM-1</p>	 <p style="text-align: center;">SiBDP-1</p>	 <p style="text-align: center;">SiBDP-2</p>
	 <p style="text-align: center;">SiBDP-3</p>	 <p style="text-align: center;">SiBDP-4</p>	

In this context, RB and Chlorin e6 were attached to NH₂- (according to route A, Scheme 3.5) while the thionine was linked to COOH- of the external surface of nanoparticles, (route B, Scheme 3.5). Moreover, RB was also attached to external OH- groups of the silica and Laponite nanoparticles (following the reaction E,

Scheme 3.8). Regarding the lad-made BODIPYs, were synthesized with different graftable groups, and those which are silylated were directly attached to the OH- (approach D, Scheme 3.7) and those with a carboxylic function were tethered to the NH₂- groups of the external surface of the silica nanoparticles, (reaction A, Scheme 3.5).

iii) Polyethylene glycol (PEG), was anchored in the external surface of nanoparticles to obtain stable nanoparticle in suspension, as well as to improve the lifetime of the nanoparticles in blood.^{17,18} In this case, two optimizations were done. Firstly, the different length of the PEG chain was tested (750 Da, 2000 Da and 5000 Da). Secondly, the covalent anchorage of the PEG was also performed at different functional groups of the nanoparticles. For that, two PEG derivative with different graftable groups was used: PEG with a succinimide group (NHS-PEG) and PEG with silyl group (Si-PEG) at one end of the chain (Figure 3.5), both supplied by Iris BIOTECH GMBH. The NHS-PEG was anchored to NH₂-nanoparticles and Si-PEG was tethered to -OH groups according to route A and D, respectively (Scheme 3.5 and 3.7). Note that, the study of the chain length was carried out only for the NHS-PEG derivative (750 Da and 2000 Da, supplied by Iris BIOTECH GMBH and 5000 Da by Sigma-Aldrich).

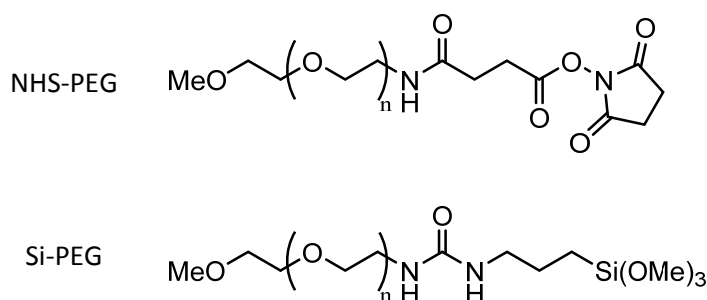


Figure 3.5. Molecular structure of two PEG derivatives anchored to NPs

iv) Folic acid (FA) is needed at the external surface of the nanoparticles to act as a selective target to cancer cells, which have usually overexpressed folate receptors at their membrane.⁹ This molecule was always attached to the external surface in the last step (after PS and PEG). This order is set to ensure a more external

distribution on the surface of the nanoparticles, to avoid being covered by the long chains of PEG, and therefore allowing its communications with the cell receptors. The folic acid has a carboxylic group in its molecular structure, Figure 3.6, and was attached to the NH_2 - of the silica nanoparticles (approach A, Scheme 3.5) or to the OH - groups of laponite nanoparticles (route E, Scheme 3.8). Nonetheless, an extra modification was required to tether the folic acid to $-\text{COOH}$ silica nanoparticles (Figure 3.6). Firstly, the folic acid was anchored with N-Boc-1.6-hecanediamine (Boc-HDA) after that, the Boc group was removed to obtain the amine groups (FA-HDA).

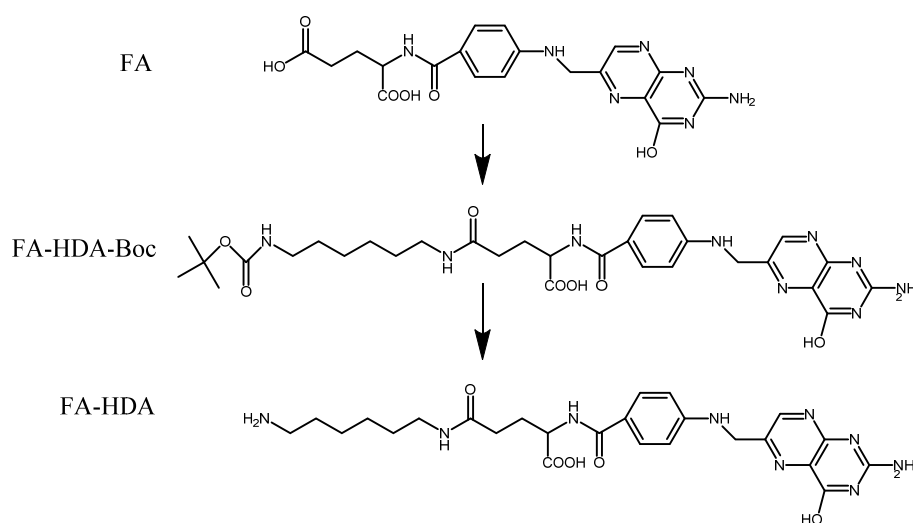
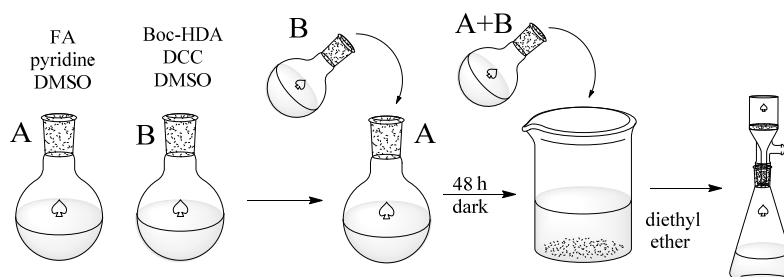


Figure 3.6. Folic acid (FA) structure and their derivate FA-HDA-Boc and FA-HDA

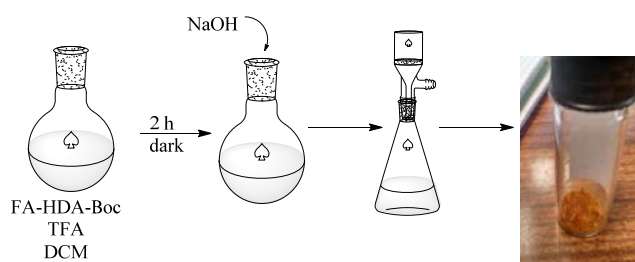
To derivate the folic acid, two solutions were prepared; A and B (Scheme 3.9). Solution A contains folic acid in dry DMSO (6 mL) and pyridine (3 mL) under inert condition and solution B, Boc-HDA (0.112 g) and DCC (0.213 g) in dry DMSO (5 mL). Then solution B was added dropwise to solution A and the mixture was under stirring for 48 hours at 30 °C in dark. The resultant solution was added to diethyl ether (2 L) in order to precipitate the compound. The yellow powder was filter and dry in vacuum; (FA-HDA-Boc),⁹ Scheme 3.9.

For the deprotection of Boc, the yellow compound was dissolved in dichloromethane (5 mL), and trifluoroacetic acid (TFA) (2 mL) was added. The

mixture was stirring for 2 hours in dark. Afterward, NaOH (1 M) was added to neutralize TFA. Finally, the solution was filtered and the powder was dried in vacuum,⁹ Scheme 3.10. Now, the transformed folic acid presents an elongated hydrocarbon chain with a free NH₂-group able to react with the COOH- groups disposed at the external surface of the silica nanoparticles.



Scheme 3.9. Synthesis of folic acid derivative FA-HDA-Boc



Scheme 3.10. Deprotection of FA-HDA-Boc to obtain FA-HDA

As it is described in this section, there are many possibilities to anchor different organic molecules of interest to the different functional groups of the nanoparticles. Along with this work, the resultant hybrid systems will be characterized and studied to elucidate the best systems to be implemented in the biomedicine field.

3.2 Experimental techniques

3.2.1. Structural and Chemical Characterization

The structure, size distribution and chemical composition of synthesized nanomaterials were characterized by several techniques. Their size distribution and morphology were measured by scanning electron microscopy (SEM), transmission electron microscopy (TEM) and dynamic light scatter (DLS). Their external chemical composition was analyzed by photoelectron spectroscopy (XPS), proton nuclear magnetic resonance ($^1\text{H-NMR}$) and Infrared-ATR (ATR). The dye quantification was performed by a photometric method (UV-Vis absorption spectroscopy). All these techniques are described below.

3.2.1.1. Scanning Electron Microscopy and Transmission Electron Microscopy

The size and morphology of the silica nanoparticles were characterized by electronic microscopies, SEM and TEM from SGIKER at the University of the Basque Country. Electron microscopy produces high-resolution images by scanning the surface of the sample with an electron beam. The image was generated by the detection of secondary electrons for SEM and transmitted electrons through the sample for TEM.

SEM analyses were carried out by JEOL JSM-7000F, with Schottky field emission, in powder metalized with copper at 20 kV with magnifications (x10000, x 25000, and x100000).

TEM analysis was performed by Philips SuperTwin, CM200 at 200 kV, with LaB_6 filament applying different magnifications. Samples were dispersed in acetonitrile or ethanol after stirring at least for 24 hours.

3.2.1.2. Dynamic Light Scattering

The measurements were recorded by Malvem Zetasizer Nano ZS, which has Helio-Neon ($\lambda = 633 \text{ nm}$) laser, available in Inorganic Chemistry Department at the University of the Basque Country. DLS technique characterizes the hydrodynamic diameter and the Zeta potential of the nanoparticles.

The dynamic light scattering (DLS) is used to determine the size distribution of small particles in suspension. A laser illuminates the sample and the scattered light is collected by a photomultiplier. The interferences of the diffracted light from all of the nanoparticles are analyzed by means of the intensity correlation function that compares the intensity of light over time.

In this way, DLS estimates the average of whole nanoparticles size in suspension. A narrow distribution is obtained for homogeneous suspension, while several peaks will be derived in a suspension with nanoparticles of heterogeneous size distribution.

On the other hand, zeta potential is a key indicator of the stability of colloidal dispersions. The magnitude of the zeta potential indicates the degree of electrostatic repulsion between charged particles in the suspension. A high zeta potential (negative or positive) indicates good stability and conversely, if the value is small is indicative of the attractive forces exceed the repulsion and the nanoparticles will aggregate and consequently flocculate,¹⁹ (see Table 3.3). The obtained value is always absolute; the sign shows the nanoparticle charge.

NP was studied in Milli-Q water, in a concentration of 0.1 mg/mL, previously stirred for 1 day, in disposable cuvettes of 1 cm optical path for DLS and in specific cuvettes for zeta potential (Figure 3.7).

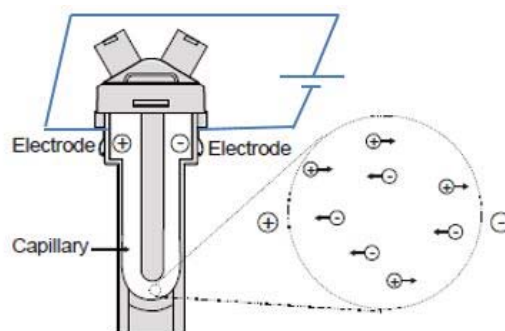


Figure 3.7. Disposable cuvettes for the measurement of zeta potential: Dispersion is introduced into this cell which contains two electrodes. When an electrical field is applied to the electrodes, the particles with a net charge, or more strictly a net zeta potential, migrate towards the oppositely charged electrode with a velocity, known as the mobility that is related to their zeta potential.

Table 3.3 Zeta potential value and the suspension stability²⁰

Zeta potential (mV)	Stability
0-5	Fast flocculation
10-30	Instable
30-40	Moderate stability
40-60	Good stability
>60	Excellent stability

3.2.1.3. X-ray Photoelectron Spectroscopy

In order to analyze the elements at the sub-surface of the mesoporous silica nanoparticles, X-ray Photoelectron Spectroscopy (XPS) SPECS system (Berlin, Germany) with a Phoibos 150 1D-DLD analyzer and Al K α (1486.7 eV) as monochromatic radiation was used, in SGIKER facilities at the University of the Basque country. The XPS is a non-destructive technique that gets information about elements present on the NP surface (around 5 nm), on its oxidation state and/or environmental situations (coordination).

Firstly an initial analysis was carried out to determine the elements present in the sample (wide scan: step energy 1 eV, dwell time 0.1 s, pass energy 80 eV). Then, a deep analysis of detected elements was realized (detail scan: step energy 0.08 eV, dwell time 0.1 s, pass energy 30 eV) with an electron exit angle of 90 °. The spectrometer was previously calibrated with Ag (Ag 3d5/2, 368.26 eV).

The spectra were adjusted using the software CasaXPS 2.3.16 which models the Gauss-Lorentzian contributions after background subtraction (Shirley). The concentrations were calculated correcting the values with relative atomic sensitivity factors (Scofield).

3.2.1.4. Proton Nuclear Magnetic Resonance

Proton nuclear magnetic resonance (¹H-NMR) characterization was carried out at Centro de Química-Física Molecular of Instituto Superior Técnico at the University of Lisbon, Portugal.

$^1\text{H-NMR}$ data in solution were collected on AMX-400 Bruker spectrometer (Bruker, MA, EE.UU) operating at 400 MHz. This technique is used to identify the presence of functional groups at the nanoparticles and the different organic molecules grafted at the external surface.

Samples were prepared by dispersing 5 mg of silica nanoparticles in 500 μL NaOH solution in D_2O (pH 13). NMR tube with the dispersed silica nanoparticles was sonicated for 1 hour and then the $^1\text{H-NMR}$ measurement was performed. The results were processed by MestReNova Software.

3.2.1.5. Infrared-Attenuated total reflectance

FTIR technique is employed to analyze the presence of the different molecules in the nanoparticles after the grafting process of the organic compounds. Particularly, Infrared-Attenuated total reflectance (IR-ATR) is used to collect the FTIR spectra of the silica nanoparticles directly in power. ATR technique is based on the total internal reflection. When the infrared light passes through a crystal of high refractive index which is in direct contact with the sample undergoes multiple internal reflections. The reflection forms an evanescent wave with a penetration depth in the samples of around one micrometer,

An ATR accessory with a diamond as ATR material is mounted in an IRAffinity-1S Shimadzu spectrometer in a 4000-600 cm^{-1} range. The IR Affinity-1S has a high S/N ratio (30000:1, 1-minute accumulation, neighborhood of 2100 cm^{-1} , peak-to-peak), a maximum resolution of 0.5 cm^{-1} , and compact dimensions.

3.2.1.6. Dye quantification

The amount of uptake dye in the core or the grafted dye at the external surface of the nanoparticles was spectrometrically quantified, following two different methods:

- i) Based on the silica matrix dissolution; 2 mg of the sample powder was dissolved in NaOH (1M, 3 ml). Then the absorption spectra of the samples are compared with the spectra of standard solutions prepared from known concentrations of the dyes in analogous conditions. Note that this method should provide more accurate information. However, there are some dyes, *i.e.* BODIPYs, which are not

chemically stable in such a basic environment. For those dyes method ii) was applied.

ii) Based on the reading of absorbance value of a previously weighted amount of nanoparticles in a stable suspension and assuming that the molar extinction coefficient of the dye is the same in solution as being occluded inside or grafted at the nanoparticles.

All those absorption spectra were recorded with a UV-Vis spectrophotometer (Varian, model Cary 7000), described later in detail in section 3.2.2.1.

3.2.2. Photophysical Characterization

In this section, the experimental techniques used to characterize the photophysical properties of fluorescence dyes, photosensitizers (PS) and dye doped nanocarriers are detailed including spectrophotometry (UV-Vis) and spectrofluorimetry (steady-state and time-correlated).

Generally, samples, for the conventional photophysical characterization (absorption and emission spectra and fluorescence lifetimes), are measured in diluted solution ($3\text{-}5\cdot 10^{-6}$ M) or stable suspensions of spectroscopic solvents and in quartz cuvettes of 1 cm optical pathway.

For the quantification of the singlet oxygen quantum yield, samples are measured in quartz cuvettes of 1 cm, in a range of concentrations from 10^{-6} M to 10^{-4} M. For the triplet states characterization samples with an absorbance between 0.3-0.5, in its excitation wavelength, were used in specific quartz cuvettes for degasification.

To perform photophysical studies with the dye concentration, from 10^{-6} M - 10^{-3} M different optical paths were used to avoid undesirable effects (*i.e.* inner filters: cuvettes of optical path of 1cm for diluted concentration (10^{-6} M - 10^{-5} M), of 1 mm for concentrations from 10^{-5} M to $1\cdot 10^{-4}$ M and 0.1 mm for concentrations $> 1\cdot 10^{-4}$ M).

3.2.2.1. UV-Vis-NIR spectroscopy

Absorption spectra were recorded on a double beam UV-Vis-NIR Spectroscopy (Cary 7000). The spectrophotometer has two lamps; halogen lamp (Vis-IR region) and deuterium lamp (UV region), which are exchanged at 350 nm. The Cary 7000 has a double monochromator (Littrow) and double diffraction grating of 1200 lines/mm.

The absorption spectra for dye solutions were recorded in transmittance from 250 nm to 800 nm at 600 nm min^{-1} and slits width of 1 nm. The signal was corrected for sample in solution with solvent in the reference beam.

For nanoparticles in suspension, the measurements were recorded in an integrating sphere (Internal DRA 900), in which the reflected light is detected, in order to eliminate the scattering contribution of the nanoparticles to the absorption spectra. In this context, the integrating sphere is not used in reflectance mode but in transmittance mode, Figure 3.8.

In this way, the geometry of the integrating sphere has the ability to collect most reflected or transmitted radiation, removing any directional preferences. Therefore, it can collect a great proportion of the scattered radiation transmitted by the sample reducing its contribution to the absorption spectra and therefore minimizing the sloping baseline and increasing signal-to-noise ratio, Figure 3.8.

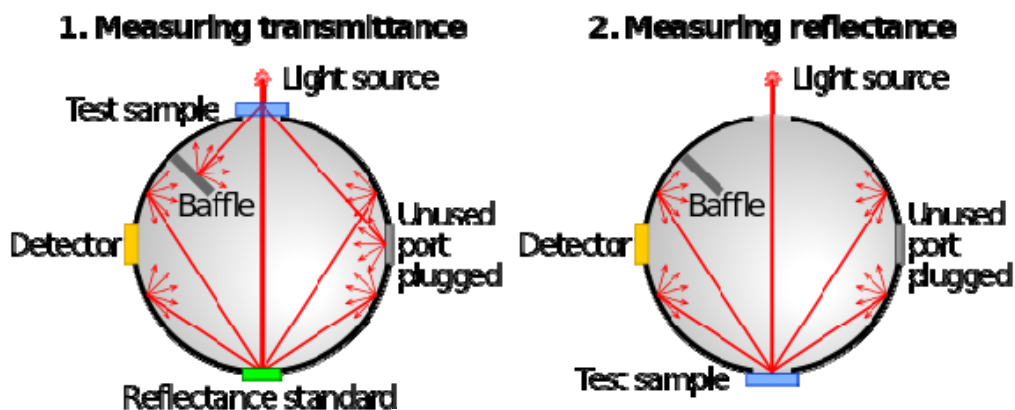


Figure 3.8. Scheme of the use of an integrating sphere to measure the transmittance and reflectance of a sample.

3.2.2.2. Fluorescence emission, quantum yield, lifetimes and phosphorescence

Fluorescence emission and lifetime decay curve were recorded in an Edinburgh Instruments Spectrofluorimeter; model FLSP920, Figure 3.9.

The Edinburgh Spectrofluorimeter has a continuous xenon flash lamp 450 W as excitation source (model Xe900). The fluorescence spectra were corrected from the wavelength dependence on the detector sensibility.

Two different methods were used to obtain the fluorescence quantum yield: the absolute method and the relative method (see chapter 2, section 2.2.1). For the relative method, different standard samples depending on the spectral region, were used: coumarin 152 ($\phi_{\text{fl}}^{\text{r}} = 0.19$ in ethanol) for the blue region,²¹ PM546 ($\phi_{\text{fl}}^{\text{r}} = 0.91$ in cyclohexane, $\phi_{\text{fl}}^{\text{r}} = 0.85$ in ethanol),^{22,23} PM567 ($\phi_{\text{fl}}^{\text{r}} = 0.84$ in ethanol)²⁴ and PM597 ($\phi_{\text{fl}}^{\text{r}} = 0.44$ in acetone)²⁵ for the green and cresyl violet ($\phi_{\text{fl}}^{\text{r}} = 0.54$ in methanol)²⁶ and zinc phthalocyanine ($\phi_{\text{fl}}^{\text{r}} = 0.30$ in 1% pyridine in toluene)²⁷ for the red-Visible region.

On the other hand, the absolute method was applied to some chromophores through the use of an integrating sphere coupled to the spectrofluorimeter and using the solvent as reference.

Radiative decay curves were recorded in the same Edinburgh Instrument by *Time-Correlated Single-Photon Counting Technique (TC-SPC)*, using a microchannel plate detector (Hamamatsu C4878) with picoseconds time resolution (~ 20 ps). Fluorescence decay curves were monitored at the maximum emission wavelength after excitation by means of a titanium supercontinuous wavelength tunable-laser with 150 ps FWHM pulses, Figure 3.9.



Figure 3.9. Spectrofluorimeter Edinburgh (FLSP920 model).

Fluorescence lifetimes (τ_{fl}) were obtained from the slope of the decay after the deconvolution of the instrumental response signal from the recorded decay curves by means of an iterative method by the FAST software (Fluorescent Analysis Software Technology). The goodness of the exponential fit was controlled by statistical parameters; chi-square (χ^2) and residuals analysis.

Some samples can show multiexponential kinetics in the deactivation of their excited-state. In those cases, the decay curves are adjusted to a sum of exponential decays by means of:

$$I_{fl}(t) = \sum_i A_i e^{(-t/\tau_i)} \quad \text{eq. 3.1}$$

where A_i are the pre-exponential factors related to the statistical weights of each exponential, and τ_i are the fluorescence lifetimes of each exponential decay.

Phosphorescence spectra were recorded also in Edinburgh Instrument in low temperature (77 K) by an Optisa DN cryostat and ITC 601 external temperature controller (Oxford Instruments).

Finally, the phosphorescence lifetime (τ_{ph}) was measured by the time-resolved decay of the phosphorescence signal at low temperatures. These long decay curves were measured similarly, in the same spectrofluorimeter, but exciting the sample with a 60W pulsed xenon flashlamp (model μ F920H, Edinburgh Instruments), recording the emission at the maximum emission peak and accumulating 5000 counts at the maximum channel. The phosphorescence lifetimes were obtained from the slope following a tail fitting by means of an iterative method by the FAST software, as it was described for fluorescence lifetime.

3.2.2.3. Singlet oxygen emission by direct measurements.

The singlet oxygen (1O_2) production was determined by direct measurement of their phosphorescence^{28,29} at 1276 nm by means of NIR detector (InGaAs detector, Hamamatsu G8605-23), integrated into the same Edinburgh spectrofluorimeter upon continuous monochromatic excitation (450 W Xenon lamp) of the sample.

The singlet oxygen signal was recorded in front configuration (front face), 40° and 50° to the excitation and emission beams, respectively and leaned 30° to the plane formed by the direction of incidence, in 1 cm cuvettes. The signal was filtered by a

low cut-off of 850 nm and at least 5 different concentrations between $2 \cdot 10^{-6}$ M and $1 \cdot 10^{-4}$ M have been measured for every photosensitizer and 3 different measurements were done for the nanoparticle suspensions.

Singlet oxygen quantum yields ($\Phi_{\Delta}^{\text{PS}}$) is calculated by a relative method in a similar way as the fluorescence quantum yield, comparing the singlet oxygen signal of photosensitizer with the signal (in the same solvent and experimental conditions) obtained for a reference (Φ_{Δ}^{R}) whose singlet oxygen quantum yields is known, following the equation 2.18 depicted in chapter 2 section 2.2.5.2.

The commercial photosensitizers used as references are phenalenone (PN) for PSs which absorption band is in UV-blue region,^{30,31} Rose Bengal (RB) for green region, and a new standard proposed during this thesis, based on BODIPY (MeSBDP, CAS-1835282-63-7) was used for UV-blue and green region.³² Finally, New Methylene Blue (NMB) was employed for red region.

The lifetime of singlet oxygen in different solvents was measured by the time-resolved decay of the phosphorescence signal at 1276 nm in Edinburgh Instruments, using the above mentioned pulsed flash lamp 60W (μF920) as excitation and recording 5000 counts in the emission channel. The singlet oxygen lifetimes (τ_{Δ}) were obtained from the slope by means of an iterative method by the FAST software likewise it was explained before.

3.2.2.4. Laser flash-photolysis

Laser Flash Photolysis (LP980, Edinburgh Instruments) was used to record transient absorption spectra in the nanosecond range and to characterize the lifetime of triplet states ($^3\text{PS}^*$). Samples were excited at different wavelengths with a computer-controlled Nd:YAG laser coupled to OPO system from LOTIS TII (laser model), Figure 3.10.

Time-resolved transient spectra were registered with a PMT detector (Hamamatsu R928), recording the decay curves as a function of the emission wavelength (wavelength increment of 2 nm).

The transient spectra at different times after excitation were obtained by averaging the integrated intensity.

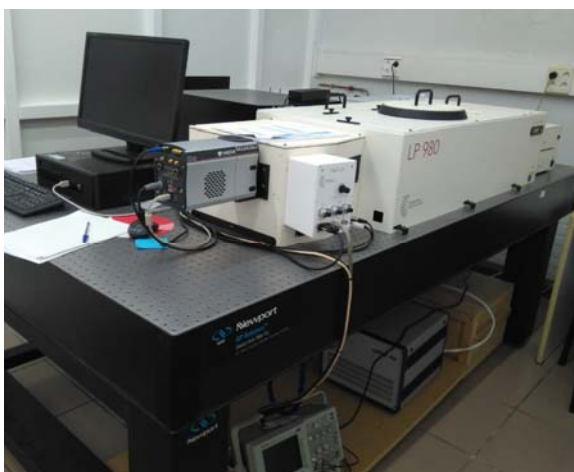


Figure 3.10. LP980 Spectrometer; Edinburgh Instruments

The rate constants for oxygen quenching of the triplet state (k_{q,O_2}^T) were determined by measuring the decay of triplet-triplet absorption at the absorption maximum in the presence and absence of oxygen (nitrogen, air and oxygen saturated solutions). The pseudo-first order decay constant in air-saturated solution is given by the Stern-Volmer equation 3.2.

$$\frac{1}{\tau^T} - \frac{1}{\tau_0^T} = k_{q,O_2}^T [O_2] \quad \text{eq.3.2}$$

3.2.2.5. Photostability measurements

The photosensitizer photostability was measured in the flash photolysis instrument, using a 1 cm cuvette in acetonitrile. The samples were irradiated by LOTIS TII (laser model) and their absorption bands were recorded after pumping the samples at different times.

3.2.2.6. Quantum mechanics calculation

Quantum mechanics calculations were performed in the Molecular Spectroscopy group by Dr. Jorge Bañuelos and Ainhoa Oriden at the University of Basque Country, using the Gaussian 09 and Gaussian 16 software as implemented in the computational cluster “Arina” of the at University of Basque Country (UPV/EHU). Ground state

geometries were optimized at the B3LYP and wB97XD hybrid method using the double valence basis set (6-31g) for enamines (chapter 4, section 4.4.2.2) and the triplet valence basis set with polarization and diffuse functions (6-311 + G*) for soluble BODIPY (chapter 4, section 4.1.1) and bodipy-binol series (chapter 4 section 4.4.2.1). The energy minimization was carried out without any geometrical constraints and the geometries were considered as energy minimum when the corresponding frequency analysis did not give any negative value. The electronic charge distribution was simulated by the CHelpG method (chapter 4, enamine-based BODIPYs; section 4.2.2.2)

3.3 In vitro HeLa cells studies

The most part of *in vitro* experiments done in human cervix adenocarcinoma (HeLa) cells were carried out in collaboration with Dr. Alberto Katsumiti at the University of Basque Country, in order to test the internalization, subcellular localization, cytotoxicity and the capability of PSs and nanoparticles to be used in PDT (phototoxicity), as it is explained below.

On the other hand, similar *in vitro* experiments were also carried out by the group of Prof. Angeles Villanueva *et al.* at Universidad Autónoma de Madrid (UAM) for some photosensitizers (chapter 4, enamine-based BODIPYs; section 4.2.2.2). Finally, other *in vitro* studies carried for some fluorophores (chapter 4, BODIPYs for fluorescence bioimaging; section 4.1.) were done by Dr. Maria D. Chiara *et al.* at University of Oviedo and Asturias Central Hospital in SCC38 cells (derived from human larynx squamous cell carcinoma)

3.3.1 Cells culture

Human cervix adenocarcinoma cells obtained from ATCC were grown in Dulbecco's modified Eagle's medium (DMEM) supplemented with 10 % (v/v) fetal bovine serum (FSB) and 50 U/mL penicillin and 50 mg/mL streptomycin, in a humidified 5% CO₂ cells incubator at 37 °C. For the cell viability assays, cells were grown to monolayer confluency in 96-well microplates. For internalization and subcellular localization studies, cells were seeded in glass-bottom 35 mm petri dishes and subconfluent monolayers were used.

3.3.2 Sample preparation

The sample preparation for in vitro experiments depends on their solubility in water. In the case of photosensitizers, the initial solutions were prepared in DMSO ($1 \cdot 10^{-3}$ M), assuring that the amount of DMSO in the medium does not exceed the 1% due to its associate toxic effects for the cell. Regarding the nanoparticles, they were prepared directly in PBS buffer ($1 \cdot 10^{-4}$ M) suspension and stirring for at least 24 hours. Nevertheless, in some samples of nanoparticles, the amount of powder was not enough to prepare such a high concentration and the initial suspensions in PBS were prepared as concentrated as possible.

3.3.3 Internalization and subcellular localization

Cells were incubated for 24h with 1, 10 and $100 \cdot 10^{-7}$ M of photosensitizer or photosensitizer-nanoparticle complex in 10% FBS culture medium. Unexposed cells were used as control. Internalization and subcellular localization of photosensitizer or photosensitizer-nanoparticle complex in HeLa cells were assessed through fluorescence microscopy analysis. After incubation, cells were washed three times with culture medium and incubated for 30 min with 50 nM LysoTrackerTM Deep Red (Invitrogen, Paisley, UK) in order to label cell's lysosomes, and fixed with 0.4% paraformaldehyde for 10 min at 4 °C. Cells were then washed three times with culture medium without FBS and observed under an Olympus Fluorview FV500 confocal microscope (Hamburg, Germany). Images were edited using Fiji software (ImageJ 1.49a, National Institutes of Health, Bethesda, MD, USA).

3.3.4 Photodynamic treatments

Cells were incubated for 24 h with 1, 5, 10, 50 and $100 \cdot 10^{-7}$ M of each photosensitizer or photosensitizer-nanoparticle complex in 10% FBS cell culture medium. After 24 h exposure, cells were washed three times with culture medium without FBS and maintained in the culture medium during irradiation and post-treatment time (24h). Irradiations were performed using a light-emitting diode (LED) device (LED Par 64 Short Q4-18, Showtec, Burgebrach, Holland) at blue (λ_{ab} 455 nm), green (λ_{ab} 518 nm), red (λ_{ab} 630 nm) or white, using a total light dosage between 10 and 30 Jcm^{-2} , equation 3.3. Irradiations were also performed at λ_{ab} 655 nm (deep-red) using a different red

LED device (LED 36 W from KINGBO LED). Parallel experiments were carried out by incubating the cells with each photosensitizer or nanoparticle without irradiation to test their dark toxicity. Unexposed cells and cells exposed to 1% DMSO and nanoparticles alone were used as controls. Four replicates of each treatment were used, and experiments were repeated three times.

Lamps characteristics were tested before the experiments; spectra were measured by optical fiber VIS-NIR connected to miniature spectrometer both from OCEANOPTICS and the power was checked by a power meter (Nova handheld laser power and energy meter of OPHIR), Table 3.4 and Figure 3.11. The total light dose was regulated by the time of exposure (eq. 3.3).

$$\text{Total Light dose (J/cm}^2\text{)} = \text{fluence rate (mW/cm}^2\text{)} \times \text{treatment time (s)} \quad \text{eq. 3.3}$$

The different LEDs were chosen depending on the main absorption band of each sample.

Table 3.4. Irradiation source properties, absorption wavelength, power, fluence rate and time of exposure for 10 J/cm² doses

Region	LED	λ_{ab} (nm)	Power (mW)	Fluence rate (mW/cm²)	Time (min) doses= 10 J/cm²
Blue	blue	455	22.5	16.9	10
Green	green	518	11.5	8.6	20
Red	red	630	15.0	11.3	15
Deep-red	red	655	12.0	9.0	19
White	Blue	455	64.0	48.1	5
	green	518			
	red	630			

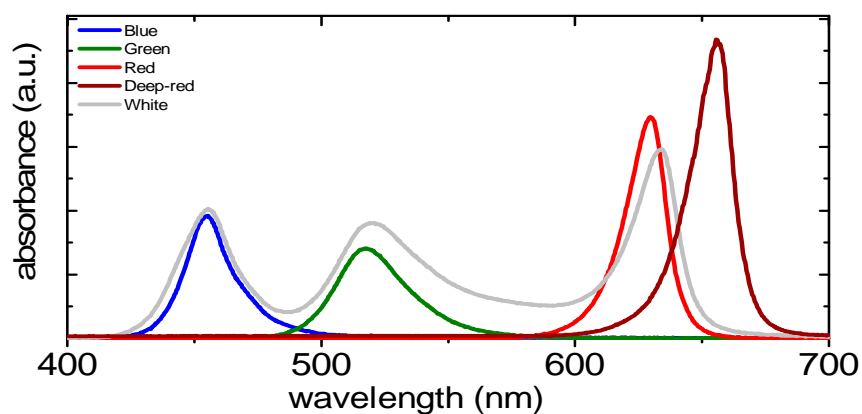


Figure 3.11. Spectra of the irradiation sources.

3.3.5 Cell viability (MTT) assay

Dark- and phototoxicity were assessed in HeLa cells using the thiazolyl blue tetrazolium bromide (MTT) assay following the manufacturer's instructions. After exposures, cells were incubated with a 50 mg/ml MTT for 3h at 37 °C. Then, reduced formazan product was extracted from cells with DMSO and the absorbance was measured at 570 nm in a Biotek EL 312 microplate spectrophotometer reader (Winooski, USA). Cell viability was expressed as the percentage respect to control cells. Differences between control and treated cells were analyzed through the Kruskal-Wallis test followed by Dunn's post hoc test using the SPSS 23.0 software (Chicago, USA). Significance level was globally established at 5% ($p < 0.05$).

3.4 Bibliography

1. Stöber, W., Fink, A. & Bohn, E. Controlled growth of monodisperse silica spheres in the micron size range. *J. Colloid Interface Sci.* **26**, 62–69 (1968).
2. Cheng, S.-H., Lee, C.-H., Yang, C.-S., Tseng, F.-G., Mou, C.-Y. & Lo, L.-W. Mesoporous silica nanoparticles functionalized with an oxygen-sensing probe for cell photodynamic therapy: potential cancer theranostics. *J. Mater. Chem.* **19**, 1252 (2009).
3. Lin, Y.-S. & Haynes, C. L. Impacts of Mesoporous Silica Nanoparticle Size, Pore Ordering, and Pore Integrity on Hemolytic Activity. *J Am Chem Soc* **132**, 4834–4842 (2010).
4. Sanchez, C., Julián, B., Belleville, P. & Popall, M. Applications of hybrid organic-inorganic nanocomposites. *J. Mater. Chem.* **15**, 3559–3592 (2005).
5. Tapeç, R., Zhao, X. J. & Tan, W. Development of organic dye-doped silica nanoparticles for bioanalysis and biosensors. *J Nanosci Nanotechnol* **2**, 405–409 (2002).
6. Epelde-Elezcano, N., Prieto-Montero, R., Martínez-Martínez, V., Ortiz, M. J., Prieto-Castañeda, A., Peña-Cabrera, E., Belmonte-Vázquez, J. L., López-Arbeloa, I., Brown, R. & Lacombe, S. Adapting BODIPYs to singlet oxygen production on silica nanoparticles. *Phys. Chem. Chem. Phys.* **19**, 13746–13755 (2017).
7. He, Q., Shi, J., Cui, X., Zhao, J., Chen, Y. & Zhou, J. Rhodamine B-co-condensed spherical SBA-15 nanoparticles: facile co-condensation synthesis and excellent fluorescence features. *J. Mater. Chem.* **19**, 3395–3403 (2009).
8. Vallet-Regí, M., Colilla, M., Izquierdo-Barba, I. & Manzano, M. Mesoporous silica nanoparticles for drug delivery: Current insights. *Molecules* **23**, 1–19 (2018).
9. Santiago, A. M., Ribeiro, T., Rodrigues, A. S., Ribeiro, B., Frade, R. F. M., Baleizão, C. & Farinha, J. P. S. Multifunctional Hybrid Silica Nanoparticles with a Fluorescent Core and Active Targeting Shell for Fluorescence Imaging Biodiagnostic Applications. *Eur. J. Inorg. Chem.* **2015**, 4579–4587 (2015).
10. Ribeiro, T., Baleizão, C. & Farinha, J. P. S. Synthesis and characterization of perylenediimide labeled core-shell hybrid silica-polymer nanoparticles. *J. Phys. Chem. C* **113**, 18082–18090 (2009).
11. Ribeiro, T., Raja, S., Rodrigues, A. S., Fernandes, F., Farinha, J. P. S. & Baleizão, C. High performance NIR fluorescent silica nanoparticles for bioimaging. *RSC Adv.* **3**, 9171 (2013).
12. Conde, J., Dias, J. T., Grazú, V., Moros, M., Baptista, P. V. & de la Fuente, J.

- M. Revisiting 30 years of biofunctionalization and surface chemistry of inorganic nanoparticles for nanomedicine. *Front. Chem.* **2**, (2014).
13. Ronzani, F., Costarramone, N., Blanc, S., Benabbou, A. K., Behec, M. Le, Pigot, T., Oelgemöller, M. & Lacombe, S. Visible-light photosensitized oxidation of α -terpinene using novel silica-supported sensitizers: Photooxygenation vs. photodehydrogenation. *J. Catal.* **303**, 164–174 (2013).
 14. Hamley, I. W. PEG-peptide conjugates. *Biomacromolecules* **15**, 1543–1559 (2014).
 15. Freitas, L. B. de O., Bravo, I. J. G., Macedo, W. A. de A. & de Sousa, E. M. B. Mesoporous silica materials functionalized with folic acid: preparation, characterization and release profile study with methotrexate. *J. Sol-Gel Sci. Technol.* **77**, 186–204 (2016).
 16. Liu, S., Zhao, J., Zhang, K., Yang, L., Sun, M., Yu, H., Yan, Y., Zhang, Y., Wu, L.-J. & Wang, S. Dual-emissive fluorescence measurements of hydroxyl radicals using a coumarin-activated silica nanohybrid probe. *Analyst* **141**, 2296–2302 (2016).
 17. Dawidczyk, C. M., Kim, C., Park, J. H., Russell, L. M., Lee, K. H., Pomper, M. G. & Searson, P. C. State-of-the-art in design rules for drug delivery platforms: Lessons learned from FDA-approved nanomedicines. *J. Control. Release* **187**, 133–144 (2014).
 18. Manzano, M. & Vallet-Regí, M. Mesoporous Silica Nanoparticles for Drug Delivery. *Adv. Funct. Mater.* **30**, 1902634 (2020).
 19. Brinker, C. J. & Scherer, G. W. Particulate Sols and Gels. in *Sol-Gel Science* 234–301 (Elsevier, 1990). doi:10.1016/B978-0-08-057103-4.50009-X.
 20. Arulprakasajothi, M., Elangovan, K., Chandrasekhar, U. & Suresh, S. Performance Study of Conical Strip Inserts in Tube Heat. *Therm. Sci.* **22**, 477–485 (2018).
 21. Nad, S., Kumbhakar, M. & Pal, H. Photophysical Properties of Coumarin-152 and Coumarin-481 Dyes: Unusual Behavior in Nonpolar and in Higher Polarity Solvents. *J. Phys. Chem. A* 4808–4816 (2003).
 22. Epelde-Elezcano, N., Palao, E., Manzano, H., Prieto-Castañeda, A., Agarrabeitia, A. R., Tabero, A., Villanueva, A., de la Moya, S., López-Arbeloa, I., Martínez-Martínez, V. & Ortiz, M. J. Rational Design of Advanced Photosensitizers Based on Orthogonal BODIPY Dimers to Finely Modulate Singlet Oxygen Generation. *Chem. - A Eur. J.* **23**, 4837–4848 (2017).
 23. Gómez-Infante, A. de J., Bañuelos, J., Valois-Escamilla, I., Cruz-Cruz, D., Prieto-Montero, R., López-Arbeloa, I., Arbeloa, T. & Peña-Cabrera, E. Synthesis, Properties, and Functionalization of Nonsymmetric 8-

- MethylthioBODIPYs. *European J. Org. Chem.* **2016**, 5009–5023 (2016).
24. López Arbeloa, F., López Arbeloa, T., López Arbeloa, I., García-Moreno, I., Costela, A., Sastre, R. & Amat-Guerri, F. Photophysical and lasing properties of pyrromethene 567 dye in liquid solution.: Environment effects. *Chem. Phys.* **236**, 331–341 (1998).
 25. Prieto, J. B., Arbeloa, F. L., Martínez, V. M., López, T. A. & Arbeloa, I. L. Photophysical properties of the pyrromethene 597 dye: Solvent effect. *J. Phys. Chem. A* **108**, 5503–5508 (2004).
 26. Magde, D., Brannon, J. H., Cremers, T. L. & Olmsted, J. Absolute luminescence yield of cresyl violet. A standard for the red. *J. Phys. Chem.* **83**, 696–699 (1979).
 27. Vincett, P. S., Voigt, E. M. & Rieckhoff, K. E. Phosphorescence and Fluorescence of Phthalocyanines. *J. Chem. Phys.* **55**, 4131–4140 (1971).
 28. Martí, C., Jürgens, O., Cuenca, O., Casals, M. & Nonell, S. Aromatic ketones as standards for singlet molecular oxygen $O_2(^1\Delta_g)$ photosensitization. Time-resolved photoacoustic and near-IR emission studies. *J. Photochem. Photobiol. A Chem.* **97**, 11–18 (1996).
 29. Braun, A. M. & Oliveros, E. Applications of singlet oxygen reactions: mechanistic and kinetic investigations. *Pure Appl. Chem.* **62**, 1467–1476 (1990).
 30. Schmidt, R., Tanielian, C., Dunsbach, R. & Wolff, C. Phenalenone, a universal reference compound for the determination of quantum yields of singlet oxygen $O_2(^1\Delta_g)$ sensitization. *J. Photochem. Photobiol. A Chem.* **79**, 11–17 (1994).
 31. Martí, C., Jürgens, O., Cuenca, O., Casals, M. & Nonell, S. Aromatic ketones as standards for singlet molecular oxygen photosensitization. Time-resolved photoacoustic and near-IR emission studies. *J. Photochem. Photobiol. A Chem.* **97**, 11–18 (1996).
 32. Prieto-Montero, R., Sola-Llano, R., Montero, R., Longarte, A., Arbeloa, T., López-Arbeloa, I., Martínez-Martínez, V. & Lacombe, S. Methylthio BODIPY as a standard triplet photosensitizer for singlet oxygen production: a photophysical study. *Phys. Chem. Chem. Phys.* **21**, 20403–20414 (2019).

4

New BODIPY-based dyes for bioimaging and Photodynamic Therapy

4.1 <u>BODIPYs for fluorescence bioimaging</u>	83
4.1.1 Soluble BODIPYs in aqueous media	84
<i>4.1.1.1 Photophysical properties and discussion</i>	87
<i>4.1.1.2 Live cells imaging</i>	94
<i>4.1.1.3 Conclusions</i>	95
4.1.2 carnitine-BODIPY probes as mitotrackers	96
<i>4.1.2.1 Photophysical properties and discussion</i>	97
<i>4.1.2.2 Live cells imaging studies</i>	99
<i>4.1.2.3 Conclusions</i>	101
4.2 <u>BODIPYs for Photodynamic Therapy</u>	102
4.2.1. Halogen BODIPYs	104
<i>4.2.1.1 MethylThio-BODIPY as standard reference</i>	104
<i>4.2.1.2 Iodinated-BODIPYs in the red region</i>	
<i>4.2.1.3 Conclusions</i>	119
4.2.2. Halogen-free BODIPY	130
<i>4.2.2.1 Binol BODIPYs</i>	130
<i>4.2.2.2 Enamine-based BODIPYs</i>	
<i>4.2.2.3 Conclusions</i>	142
4.3 <u>Bibliography</u>	156

New BODIPY-based dyes for bioimaging and photodynamic therapy

Cancer is the second cause of human death worldwide, being 13% of the total deaths and it is expected to increase in the following years. Generally, the disease is characterized by uncontrolled cell multiplication and a deficiency of cell death, caused by mutations in some specific genes. Early diagnosis of the disease is often the key to an effective treatment to ensure patient survival. The most used imaging techniques are Computed Tomography (CT), Magnetic Resonance Image (MRI), and Positron Emission Tomography (PET).^{1,2}

These scan techniques are based on different sources such as X-ray (CT), high magnetic field (MRI) or radioactive substances as tracers (PET), which could generate secondary effects in the patients; hair loss, nausea and/or respiratory problems. Moreover, these detection methods are not selectivity for tumor cells. In addition, healthy cells may suffer the consequences of the irradiation or magnetic fields, and sometimes to improve the contrast in the image several scans are required, increasing the exposition of the patients to the damage sources. Finally, these techniques are quite expensive and consequently are not easily accessible.

For that, an alternative or complementary detection technique “*fluorescence microscopy*” is in expansion in the last decades. Fluorescence microscopy is experienced great development in terms of the improvement of its sensitivity and its resolution limit (previously conditioned by the diffraction limit, $\lambda/2$). An example of this is the Nobel Prize in Chemistry corresponding to the year 2014 (Profs. S. Hell, E. Betzig and W. Moerner) closely related to this multidisciplinary research field, that thanks to joining efforts of scientists from various disciplines the so-called nanoscopy has been developed. Nowadays confocal fluorescence microscopy has become a versatile platform, less invasive, with safe detection and high resolution for studying structural and molecular dynamics in biological systems. It enables the direct imaging of fluorophores *in vitro* or *in vivo* experiments. The fluorophore is a selective fluorescent dye specifically designed to track a certain biological activity. For instance, the fluorescent probes can label different cell organelles (nuclei, mitochondria, lysosomes..) or other specific cellular structures such as actin fibers in mammalian cells. In this way, fluorescence microscopy can provide information about

the localization and quantity of the molecules of interest enabling the detection of several diseases (osteoporosis, cancer, Alzheimer)³⁻⁵

In this context, there are many commercial fluorescent dyes, which can be chemically linked to a molecule of interest to target a certain activity. Generally speaking, a good fluorophore should fulfill several requirements; *i*) high molar extinction coefficients (ϵ), *ii*) high fluorescence quantum yields (Φ_f) and narrow emission spectra, *iii*) low tendency to aggregate, *iv*) high Stokes shift in order to prevent reabsorption-reemission process and *v*) high chemical- thermal and photostability. Although there are several kinds of commercial dyes, the most of them present some limitations to be used in biomedical fields; low biocompatibility, poor solubility in aqueous media, non-specificity for any organelle or their absorption band is not located in phototherapeutic window⁶ (630-850 nm) to enhance penetration depth, Figure 4.1. For all of these, the design of new fluorophores is necessary in order to overcome these drawbacks and adapt them as potential biomarkers for bioimaging.⁷

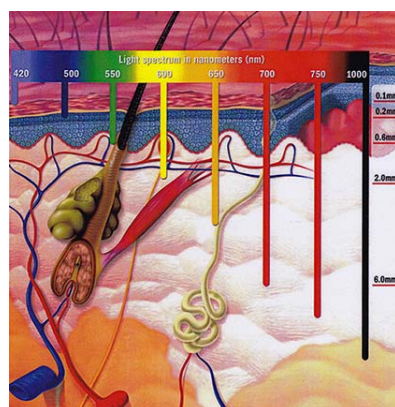


Figure 4.1. schematic illustration of the light penetration depth in human skin

After the diagnosis of any cancer, the diseases have to be treated. Currently, the most common procedures against cancer are radiotherapy and chemotherapy. In both cases, healthy cells are also being damaged either by the X-ray radiation applied or by the chemo-drugs required to kill tumor cells. As a consequence of the application of these techniques, the patient presents important secondary effects such as nausea, vomits, respiratory problems, changes in the skin, loss hair, etc. Note that many of these effects could not disappear with time.

In this thesis, the *photodynamic therapy* (PDT) is studied as a complementary treatment for cancer, in order to reduce the drawbacks of conventional methods. PDT is a minimally invasive procedure that involves the use of light, a sensitive drug, denoted photosensitizer (PS), and environmental oxygen. In a few words, under suitable light irradiation, the PS is activated and generates ROS (Reactive Oxygen Species) mainly singlet oxygen, a cytotoxic species able to damage nearby cells, Figure 4.2.

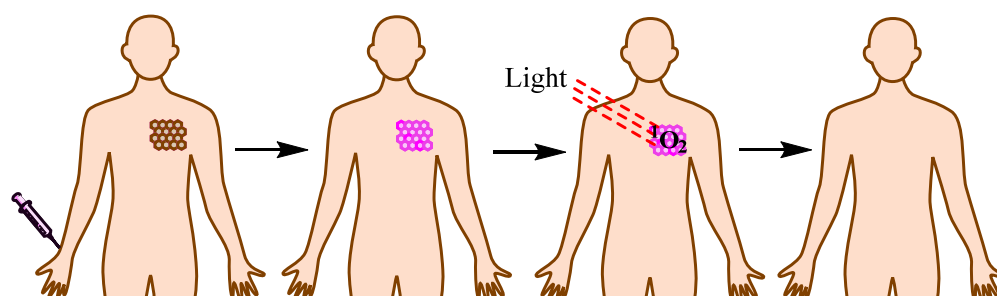


Figure 4.2. Scheme of different steps in photodynamic therapy

Generally, a photosensitizer is also a dye which has to fulfill some requirements to be used as efficient singlet oxygen generator; *i)* high absorption coefficient in the spectral region of the excitation light; *ii)* high intersystem crossing (ISC) quantum yield, *iii)* long triplet lifetimes, *iv)* triplet energy higher than the energy gap between the ground O_2 ($^3\Sigma_g$) and the first excited O_2 ($^1\Delta_g$) states (94.2 kJ/mol), *v)* high quantum yield of singlet oxygen production Φ_Δ , preferably independent of media parameters such as solvent polarity, *vi)* thermal and photochemical stability, *vii)* low reaction rate of the PS itself with singlet oxygen to minimize the quantum yield dependence on the sensitizer concentration.

Moreover, to use a PS as a photoactive drug for PDT has to meet extra conditions: *viii)* non-toxic in dark conditions, *ix)* selectivity accumulation in cancer tissues, *x)* limited stability in vivo in order to be removed after the irradiation, *xi)* high molar absorption coefficient ($\epsilon \geq 50000 \text{ M}^{-1}\text{cm}^{-1}$) preferentially in the phototherapeutic window⁶ (630-850 nm) and finally, *xii)* a significant solubility in water together with a hydrophobic part to facilitate the cell membrane crossing.⁸ At the moment, few PSs

fulfill these requirements and new molecular designs are demanded in order to improve their current limitations.

To sum up, the main objectives of this thesis are the study of new dyes (fluorophores and photosensitizers) for their implementation in bioimaging and photodynamic therapy or in the best of the cases, with a dual activity able to track and treat simultaneously, what is known as *theragnostic agents*. In this context, theragnosis offers an increase in the success of the therapy by the *in-situ* visualization of the tissue to be treated.

Particularly, this chapter is based on the design of new dyes, based on BODIPY chromophore, and to study their chemical-physical properties for their potential use in biomedical applications.

In few words, BODIPY chromophore or 4,4-difluoro-4-boro-3a,4a-diaza-s-indacene is a family of fluorophore,⁹ which has attracted significant attention due to their chemical-physical features which fulfill the most requirements of fluorescent dyes; *i*) high absorption coefficient, *ii*) high thermos- and photo-stability, *iii*) good solubility in a wide range of solvents and *iv*) high fluorescence quantum yield.^{10,11,12} Its chromophoric core consists of two pyrroles linked by methylene groups, allowing the π electron density delocalization between two rings, anchoring by BF_2 which does not take place in the delocalization but gives rigidity to the molecular structure, Figure 4.3.

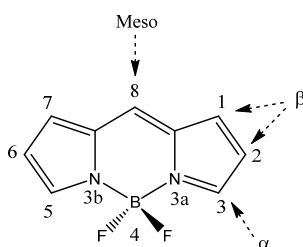


Figure 4.3. General BODIPY structure. The different positions in the core are indicated and numbered according to the IUPAC system.¹²

The absorption spectrum of the naked BODIPY (without any substitutions in the chromophore core) consists in a main band around 500 nm with high intensity ($\epsilon_{\text{max}} \sim 7 \cdot 10^4 \text{ M}^{-1} \text{ cm}^{-1}$), as the result of electron transition from HOMO orbital to the LUMO ($S_0 \rightarrow S_1$). Besides, this band presents a vibronic shoulder in higher energies, which is

attributed to out of plane vibrations of the C-H bonds of the aromatic system. In the near UV region, a weak band appears as a consequence of transition between ground state (S_0) and more energetic excited state (S_i), Figure 4.4A.

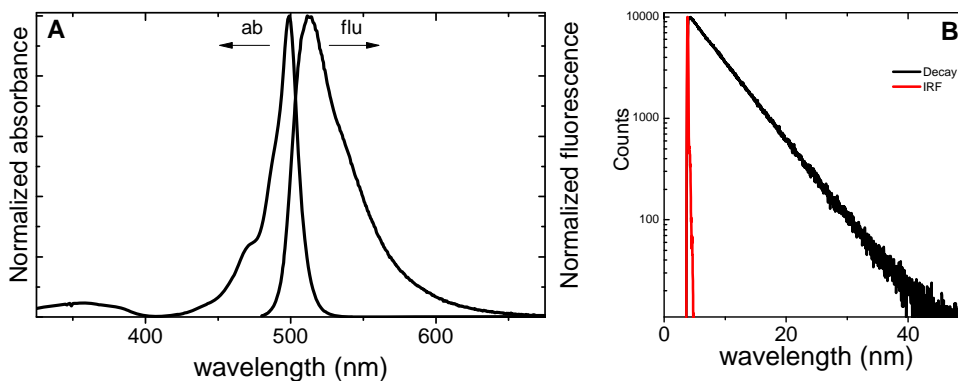


Figure 4.4. (A) UV/ Vis absorption and emission spectra and (B) lifetime decay curve of BDP546 in chloroform

The emission band is located at around 510 nm and the shape tends to be the mirror image of the absorption spectrum, Figure 4.4 A, since the geometry and vibrational levels of ground and excited state are similar.¹³ Note that these dyes could achieve a fluorescence quantum yield near to 100 % in apolar medium.¹⁴ This high fluorescence efficiency is due to the BODIPY structure guarantees a low probability of non-radiative deactivation because i) BF_2 bond confers structural rigidity to the system reducing the internal conversion process¹⁵ and ii) BF_2 bond does not contribute to the π electron delocalization, decreasing the spin-orbit coupling and consequently the intersystem crossing to the triplet state. This type of chromophore is characterized by short Stokes shifts (300 cm^{-1}).¹⁴ The fluorescence decay curve of BODIPYs, it is usually monoexponential, (Figure 4.4.B), being the lifetimes of around 6 ns.¹⁴

Apart from the excellent photophysical properties of BODIPYs, another great characteristic of these compounds is the chemical versatility, which allows the tuning of their photophysical properties by modifying their structure in a straightforward way. The chemico-physical properties and in particular the photophysical features of the BODIPY can be modulated by the incorporation of varied groups at different positions by several approaches, see Figure 4.5.¹⁶⁻²⁰

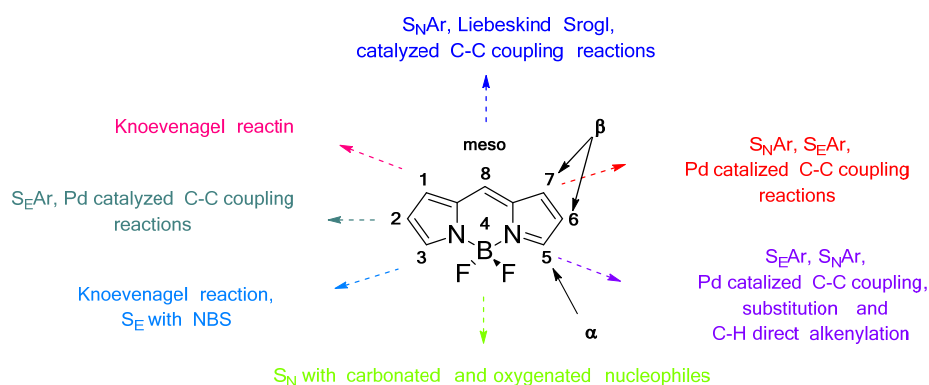


Figure 4.5. BODIPY core reactivity

This chapter 4 is dedicated to the study of new BODIPY dyes and the results are divided into two main sections: fluorescent BODIPYs derivatives for bioimaging (section 4.1) and new BODIPY as photosensitizers for photodynamic therapy (section 4.2). Briefly, the first section, 4.1 is focused on BODIPY dyes to be used as fluorescent biotrackers. Two different examples of BODIPY functionalization are shown, in which molecular modification strategies were destined to overcome two of the BODIPY limitations as biomarkers; *i*) increase their solubility in aqueous media and *ii*) enhance their selectivity to a particular organelle cell, *i.e.* mitochondria. The photophysical properties of these new BODIPY were characterized in our lab and analyzed in this section. Furthermore, *in vitro* experiments are presented to test their applicability in human larynx squamous cell carcinoma (SCC38). The second section 4.2 is focused on the modification of the BODIPY chromophore to obtain improved photosensitizers with high singlet oxygen production. Different approaches were employed: *i*) the tethering of heavy atoms to BODIPY core to improve the intersystem crossing by spin-orbit mechanism; *ii*) the addition of electron-donating groups to induce an intracharge transfer (ICT) states, responsible of the population of the triplet state. The photophysical properties of these compounds, and in particular the singlet oxygen generation and the triplet states were characterized. *In vitro* experiments were also carried out in Human cervix epithelial carcinoma (HeLa) cells for the most representative BODIPY as PS in order to test their efficacy in photodynamic therapy. The results are compared with commercial PS such as Rose Bengal, Thionine and Chlorine e6.

4.1 BODIPYs for Fluorescence bioimaging

Nowadays, there are a great number of commercial fluorophores with different structural and photophysical features. For instance; coumarins or perylene in the blue region, xanthenes derivate (rhodamines or fluorescein) and BODIPY in the green-yellow region and oxazines (cresyl violet) and phthalocyanines in the red region, Figure 4.6. Although these fluorescent dyes could be applied in several areas such as medicine, laser dyes, antenna systems or chemical sensors (polarity, viscosity, pH), this work is focused on their use in the bioimaging field as biotrackers.

In this field, the most typical fluorophores used are Alexa or ATTO dyes, commercializing by Life Technologies or ATTO-TEC, respectively. They usually offer high molar extinction coefficients (ϵ), good photostability, high fluorescence quantum yields (Φ_f), and narrow emission spectra. These commercially available dyes have functional groups of interest (amine, thiols, NHS-esters, and maleimides, or even streptavidin and biotin) for labeling of DNA, RNA or proteins. However, for biomedical research, these fluorophores present common limitations, such as low biocompatibility, poor solubility in water and poor-specificity. Besides, they are also quite expensive.

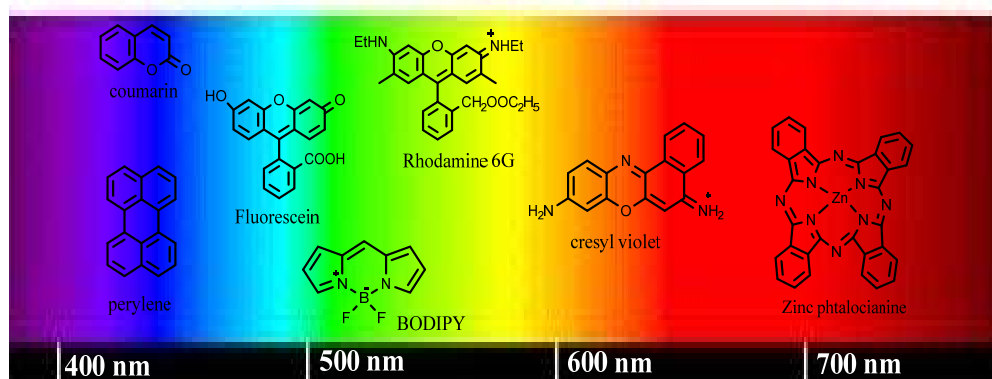


Figure 4.5. Structures of different fluorophores in the electromagnetic spectrum

Particularly, new fluorescent dyes are carefully designed by combining BODIPY chromophore with hydrophilic groups or biomolecules to enhance their solubility in aqueous media and the selectivity for the required tissue, respectively

The new lab-made compounds are mainly derivatives of the BODIPY 546 and BODIPY 567 structures, Figure 4.7. In these compounds hydrophilic groups; tetra-, octaethylene glycol and sulfobetaine chains were anchored to increase the dye solubility and biocompatibility (section 4.1.1) or biomolecules such as L-carnitine to act as a mitochondrial target (section 4.1.2). The results of both studies are shown below. Note here that the syntheses of these new compounds were carried out by D. J.L.Chicara *et al* at Institute of General Organic Chemistry (IQOG-CSIC, Madrid).

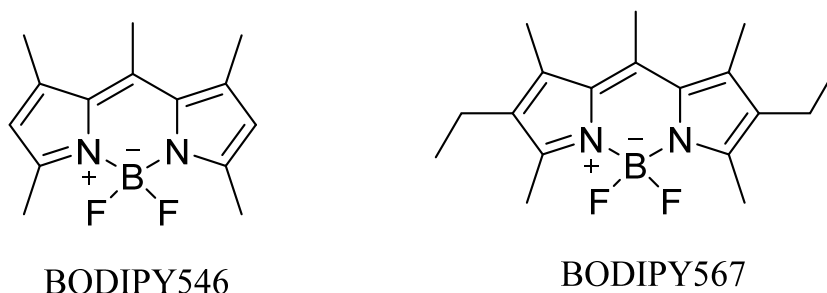


Figure 4.7. Commercial BODIPY 546 and 567 molecular structures.

4.1.1 BODIPYs soluble in water

Despite the fact that BODIPY has excellent chemical, electronic and photophysical features its inherent hydrophobic nature presents a serious drawback for its application in biological research. They show a low solubility and a high tendency to aggregate in aqueous media. Indeed, BODIPY is a neutral molecule with a zwitterionic nature, characterized by a negative charge in boron atom and a positive one in nitrogen atom, although the positive charge could be delocalized through the π electronic system, and the resonance forms “a” and “d” could be considered like extreme structures, Figure 4.8.

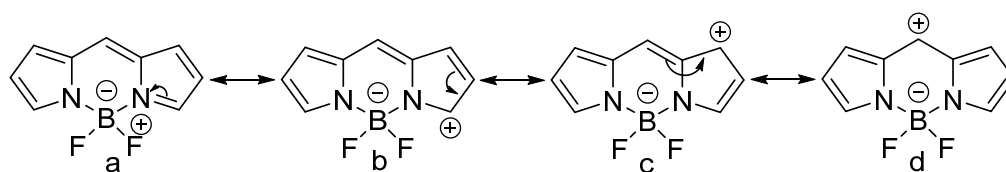
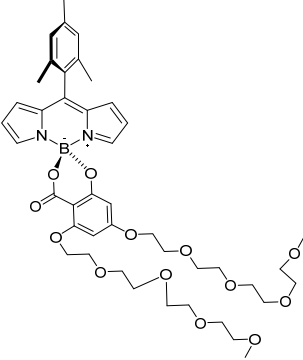
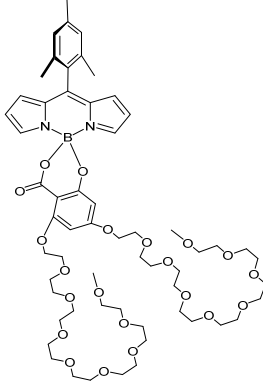
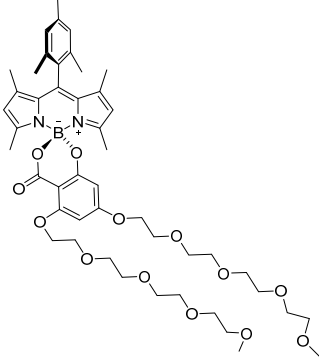
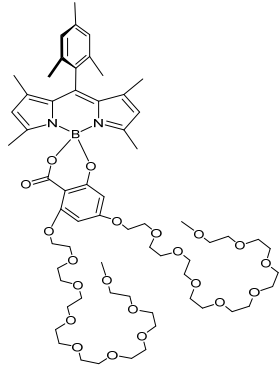
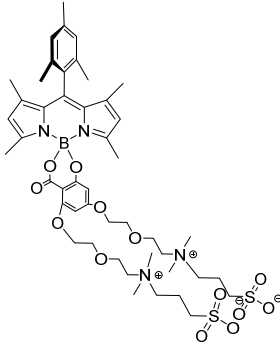
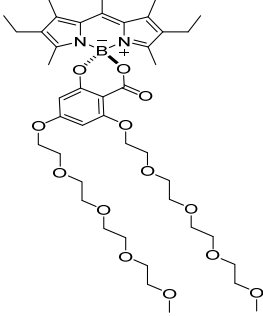
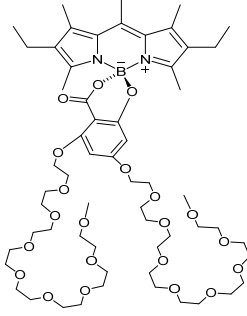
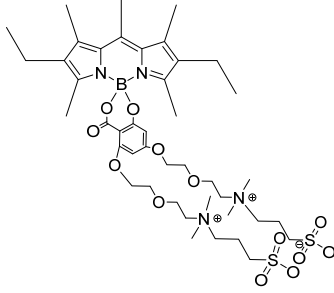


Figure 4.8. Resonance structures of BODIPY.¹²

As a result, these fluorophores demonstrate partition into lipophilic compartments of cells resulting in nonspecific staining of cell organelles. Likewise, they also tend to embed into hydrophobic pockets.^{19,21–23} For these reason, different approaches have been developed along the last decade to enhance water solubility and minimize molecular aggregation. The structure is being modified by grafting to the fluorophore ionizable groups or hydrophilic (bio)/mono-/oligo-/polymers; such as phosphonic, sulfonic acid salts, ammonium groups, zwitterionic sulfobetaines, carbohydrates, peptides, oligonucleotides, or mono-/oligoethylene glycols.^{24–28} However, although these changes improved significantly the water solubility, the ionic character and/or large size of the solubilizing groups often impair membrane permeability, which limits the practical application of the fluorescent to tag live-cells for *in vivo* imaging. Moreover, most of these approaches implement multistep synthetic routes making the process quite complex.

In this work, eight different compounds were synthesized adding at the boron atom either neutral (tetra- and octaethylene glycol chains) or zwitterionic (sulfobetaine) hydrophilic tags in the molecule (Table 4.1). The synthesis was performed following a new efficient one-step strategy.²⁹ The original protocol allows the direct modification of known F-BODIPY dyes at the boron atom via an efficient F-to-O exchange reaction that uses simple reagents and conditions, providing easy access to diversely functionalized mono- and bichromophoric O-BODIPYs.^{30,31} In addition, substitution at boron usually has a minimal effect on the photophysical properties of the BODIPY chromophore. For more details of the synthesis see Blazquez-Moraleja et al. *Dyes and Pigments* 170 (2019) 107547.²⁹

Table 4.1. New soluble BODIPY structures, with different hydrophilic groups; tetra- and octaethylene glycol and sulfobetaine.

Tetraethylene glycol	Octaethylene glycol	Sulfobetaine
 <p data-bbox="284 763 416 797">SoBDP-1a</p>	 <p data-bbox="627 775 759 808">SoBDP-1b</p>	-
 <p data-bbox="284 1227 416 1261">SoBDP-2a</p>	 <p data-bbox="627 1227 759 1261">SoBDP-2b</p>	 <p data-bbox="978 1216 1110 1249">SoBDP-2c</p>
 <p data-bbox="284 1637 416 1671">SoBDP-3a</p>	 <p data-bbox="627 1630 759 1664">SoBDP-3b</p>	 <p data-bbox="978 1624 1110 1657">SoBDP-3c</p>

4.1.1.1 Photophysical properties and discussion

Firstly, the solubility-tagged tethered to the boron atom of the BODIPY core should not significantly affect their photophysics. Indeed, the presence of different spiranic rings centered at the boron bridge in O-BODIPY do not usually alter neither their absorption nor the fluorescence, following a similar photophysical behavior to their respective F-BODIPY precursors.^{30,32,33}

On the other hand, hydrophilic chains should not alter their inherent solvent dependence properties, which typically consist of a reduction of the molar extinction coefficient and a gradual hypsochromic shift of the absorption maxima as the solvent polarity increase.^{30,32,33} Nevertheless, in some cases, in particular, SoBDP-**1a** and SoBDP-**1b**, the incorporation of these chains have induced a dramatic effect on the fluorescence of the new dyes in any solvent, behavior that does not show in the others derivatives, SoBDP-**2** and SoBDP-**3c** (Table 4.2).

The low emission efficiency of dyes SoBDP-**1a** and SoBDP-**1b** could not be attributed to the molecular flexibility of the 8-aryl substituent since these values are far from the typical values of homologous 8-mesityl substituted F-BODIPYs.³⁴ The SoBDP-**1** behavior may hypothetically be related to the high electron density of the substituent grafted at the boron center (a phenyl group decorated with three electron-donor oxygen atoms). Dramatic fluorescence quenching in O-BODIPYs has been already reported upon the introduction of a spiranic ring at the boron bridge (*e.g.* binol). Such derivatives are weakly emissive due to the activation of intramolecular charge transfer (ICT) processes, which could eventually evolve into a photoinduced electron transfer (PET) as the main non-radiative deactivation channel.³⁵ Trying to confirm this hypothesis, atomistic simulations (B3LYP/6-311 + G*) of dye SoBDP-**1a** and its methylated analog SoBDP-**2a** as representative compounds were carried out, Figure 4.9.

Table 4.2. Photophysical properties of SoBDP in chloroform, ethanol and water: absorption (λ_{ab}), molar absorption (ϵ), fluorescence wavelength (λ_{fl}) fluorescence yield (Φ_{fl}) and fluorescence lifetime (τ).

Dye	Solvent	λ_{ab} (nm)	ϵ_{max} ($10^4 M^{-1} cm^{-1}$)	λ_{fl} (nm)	Φ_{fl}	τ (ns)
SoBDP-1a	CHCl ₃	507.0	4.8	520.0	0.17	0.45
	EtOH	504.0	4.4	518.0	0.03	<0.15
	H ₂ O	503.0	3.2	515.0	<0.02	<0.15
SoBDP-1b	CHCl ₃	507.0	5.8	521.0	0.06	0.49
	EtOH	505.0	5.1	514.5	0.02	0.11
	H ₂ O	503.0	4.0	514.0	<0.01	<0.15
SoBDP-2a	CHCl ₃	507.0	7.6	516.0	0.88	6.04
	EtOH	504.0	7.9	512.5	0.85	6.58
	H ₂ O	501.0	4.0	512.5	0.66	6.86
SoBDP-2b	CHCl ₃	507.0	7.8	515.5	0.86	5.82
	EtOH	504.0	6.9	514.5	0.79	6.60
	H ₂ O	502.0	4.2	511.5	0.78	6.40
SoBDP-2c	CHCl ₃	507.0	8.1	517.0	0.71	5.72
	EtOH	504.0	6.5	514.5	0.84	5.99
	H ₂ O	501.0	6.4	510.5	0.85	6.31
SoBDP-3a	CHCl ₃	527.0	6.3	548.5	0.72	6.99
	EtOH	523.0	6.2	546.0	0.75	7.42
	H ₂ O	519.0	4.1	540.5	0.71	7.55
SoBDP-3b	CHCl ₃	527.0	6.2	547.0	0.73	6.85
	EtOH	523.0	4.5	545.5	0.72	7.28
	H ₂ O	520.0	4.9	540.0	0.71	7.77
SoBDP-3c	CHCl ₃	528.0	4.6	546.0	0.72	6.87
	EtOH	523.0	5.5	543.0	0.76	7.39
	H ₂ O	519.0	4.5	538.0	0.78	7.50

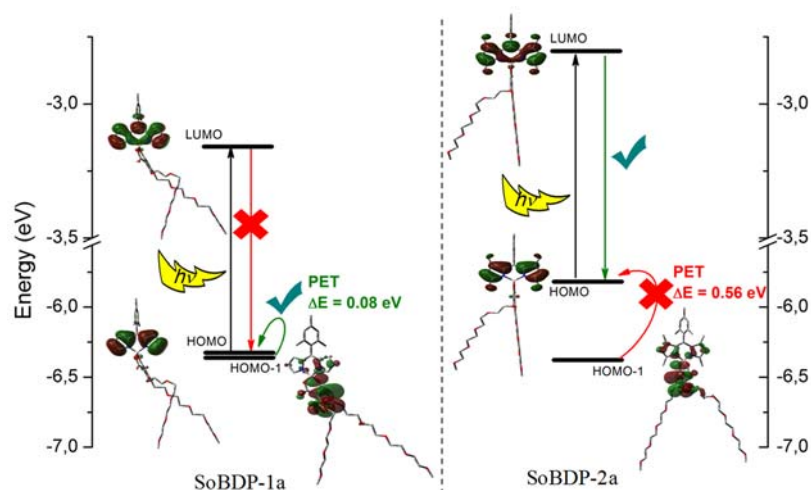


Figure 4.9. Calculated (B3LYP/6-311 +G *) energy arrangements of the frontier molecular orbitals of the non-methylated BODIPY SoBDP-**1a** and its tetramethylated analog SoBDP-**2a**.²⁹

The HOMO-1 of SoBDP-**1a**, almost entirely located on the pendant aromatic moiety grafted at the boron atom, is energetically very close to the HOMO (just 0.08 eV below), which is completely located on the dipyrroin system. Such energetic distribution of molecular orbitals enables a reductive photoinduced electron transfer (PET) upon excitation. Thus, upon the photoinduced promotion of an electron from the HOMO to the LUMO, an electron transfer from the low-lying HOMO-1 to the semi-vacant HOMO is thermodynamically feasible. Such a reductive PET from the spiranic group grafted at boron to the BODIPY core avoids radiative deactivation from the LUMO back to the HOMO, thus explaining the almost negligible fluorescence emission of SoBDP-**1a**. The presence of methyl groups at C-1, C-3, C-5 and C-7 positions on the chromophoric core of SoBDP-**2a**, drastically changes the energetic arrangement of the molecular orbitals. The inductive electron-donor ability of the methyl groups in SoBDP-**2a** increases the energy of the HOMO and LUMO orbitals with respect to dye SoBDP-**1a**, without energetically altering the HOMO-1. Consequently, the energy gap between the frontier orbitals HOMO-1 and HOMO (0.58 eV) becomes 7-fold higher than in the non-methylated counterpart SoBDP-**1a**, thus hampering an effective PET process and thereby allowing the fluorescence emission of the BODIPY. Therefore, tetramethylation of the BODIPY scaffold reduces the electron-acceptor character of the chromophoric core making

thermodynamically unfeasible any PET or ICT process from the functionalized group at its boron bridge to the BODIPY core. Thus, the bright fluorescence emission and long excited-state lifetimes of typical BODIPYs are recovered in dyes SoBDP-2 (Table 4.2).^{30,32-34} In the same way, the electron-donor character of the ethyl groups additionally grafted at the C-2 and C-6 positions of SoBDP-3a-c reduces the probability of an PET or ICT process, allowing these dyes to emit highly efficient fluorescence with elongated lifetimes regardless of the length and nature of the hydrophilic chains and the solvent polarity (Table 4.2).²⁹

The alkyl substituents on the BODIPY core may also play a major role in controlling intermolecular interactions. The capability of the new dyes to avoid non-fluorescent aggregation in water would impel their application in biological settings since fluorescent probes are typically used in concentrations higher than 2 μM . To understand the intermolecular interactions of dyes SoBDP-2 and SoBDP-3 in aqueous media, the photophysical studies were also performed at different increasing concentrations of dye in water, Tables 4.3-4.4.

Table 4.3. Dependence of the fluorescence quantum yield^a and lifetime of synthesized dyes derived from BODIPY skeleton 2 on the dye concentration in water.

[c] $\times 10^4$ (M)	SoBDP-2a			SoBDP-2b			SoBDP-2c		
	$\Phi_{\text{fl}}^{\text{b}}$	$\Phi_{\text{fl}}^{\text{c}}$	τ^{b} (ns)	$\Phi_{\text{fl}}^{\text{b}}$	$\Phi_{\text{fl}}^{\text{c}}$	τ^{b} (ns)	$\Phi_{\text{fl}}^{\text{b}}$	$\Phi_{\text{fl}}^{\text{c}}$	τ^{b} (ns)
0.02	-	-	-	0.78	-	6.30	0.85	-	5.89
0.05	-	-	-	0.78	-	6.40	0.85	-	6.09
0.06	0.66	-	6.06	0.78	-	6.40	0.85	-	6.20
0.1	-	-	-	0.78	-	6.59	0.86	-	6.20
0.2	0.66	-	6.14	-	-	-	0.85	-	6.36
0.3	0.64	-	6.14	-	-	-	0.83	-	-
0.7	0.63	-	6.17	0.76	-	7.35	0.87	-	-
0.95	0.60	-	6.22	0.75	-	-	0.85	-	-
1.2	0.57	0.58	6.29	0.42	0.55	7.79	0.45	0.58	6.81
3.0	0.38	0.45	6.41	-	-	-	0.19	-	-
5.0	0.19	0.20	6.41	0.14	0.20	-	-	-	-
7.0	<0.1	<0.1	6.45	0.05	-	-	-	-	-

^aUpon excitation at 490 nm using PM546 ($\Phi_{\text{fl}} = 0.91$) in cyclohexane as reference

^{b,c}Evaluated under front-face configuration, using 1 and 0.1 mm optical pathway cuvette, respectively.

Table 4.4. Dependence of the fluorescence quantum yield^a and lifetime of synthesized dyes derived from BODIPY skeleton **3** on the dye concentration in water.

[c]×10 ⁴ (M)	SoBDP3a		SoBDP3b				SoBDP3c			
	Φ ^b _{fl}	τ ^b (ns)	Φ ^b _{fl}	Φ ^c _{fl}	τ ^b (ns)	τ ^c (ns)	Φ ^b _{fl}	Φ ^c _{fl}	τ ^b (ns)	τ ^c (ns)
0.02	-	-	0.72	-	7.52	-	0.78	-	7.25	-
0.05	0.71	7.30	-	-	-	-	0.78	-	7.27	-
0.06	0.71	7.33	-	-	-	-	-	-	-	-
0.1	0.71	7.42	0.72	-	7.58	-	0.78	-	7.36	-
0.2	0.73	7.44	0.73	-	7.78	-	0.76	-	7.44	-
0.3	0.72	7.47	0.75	-	7.81	-	0.78	-	-	-
0.5	0.33	-	0.74	-	8.03	-	0.68	0.77	7.88	-
0.9 ^d	-	-	-	-	-	-	0.63	0.75	-	-
1.3	-	-	0.65	0.75	8.22	7.67	0.35	0.48	8.22	7.48
2.5	-	-	0.31	0.57	7.85	7.42	0.22	0.34	8.24	7.47
3.6	-	-	0.17	0.55	7.52	7.39	0.06	0.24	7.83	7.21
5.5	-	-	0.08	0.33	7.53	7.42	0.01	0.09	-	-

^aUpon excitation at 490 nm and using PM567 (Φ_{fl} = 0.84) in ethanol as reference, ^{b,c} Evaluated under front-face configuration using a 1 and 0.1 mm optical pathway cuvette, respectively.

^dSoBDP-3c not soluble beyond this concentration.

The fluorescence quantum yields of SoBDP-2 and SoBDP-3 were not significantly affected by augmenting dye concentration from $2 \cdot 10^{-6}$ M to 10^{-4} M, which emphasized the absence of aggregates and enhanced the water solubility of the new BODIPY derivatives. A further increase in concentration led to the gradual quenching of the emission efficiency, which could be ascribed, at least to some extent, to the reabsorption/reemission processes. In addition, growing concentrations markedly changed the spectral profiles depending on the substitution pattern of the chromophoric backbone. In the case of SoBDP-2, an increase of dye concentration in water produced a gradual broadening and a slight red-shift of the absorption spectra, without involving neither the growth of vibronic shoulders nor the appearance of new bands, until $1.7 \cdot 10^{-4}$ M (Figure 4.10).²⁹ Likewise, in the emission spectra, the intensity of the long-wavelength shoulder increases with dye concentration (Figure 4.10 blue and grey spectra) until reaching or even exceeding the intensity of the main fluorescence band. This spectral behavior is a fingerprint of short-range intermolecular interactions, likely excimer-like species and/or J-type aggregates.³⁰

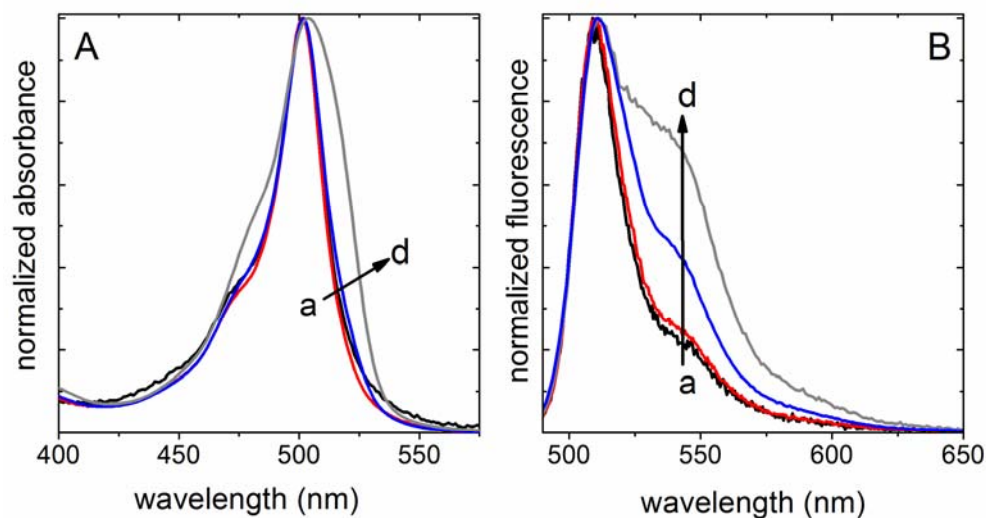


Figure 4.10. (A) Height-normalized absorption and (B) emission spectra of compound SoBDP-2c in water at different concentrations: a) $2.0 \cdot 10^{-6}$ M (1 cm-optical path); b) $1.0 \cdot 10^{-5}$ M (1 mm-optical path); c) $1.7 \cdot 10^{-4}$ M (0.1 mm-optical path); d) $3.4 \cdot 10^{-4}$ M (0.1 mm-optical path).

In contrast to SoBDP-2 compounds, the absorption spectra of SoBDP-3 are strongly dependent on dye concentration ($> 10^{-4}$ M), and the vibronic shoulder placed at 490 nm is gradually growing with concentration until reaching the intensity of the main absorption band centered at 520 nm (Figure 4.11). Conversely, the emission spectral profile of dyes SoBDP-3 remained roughly unchanged except for a decrease of the fluorescent intensity and a slight red-shift of the main fluorescence band. This photophysical behavior (Table 4.4) is indicative of not emissive H-type intermolecular interactions, which efficiently quench the fluorescence emission. The more planar structure of the boradiazaindacene unit in dyes SoBDP-3 allows an effective intermolecular π -stacking arrangement of the chromophores at high concentrations favored by the low steric hindrance of the 8-methyl group as compared to the orthogonally oriented 8-mesityl group in dyes SoBDP-2. Thus, compounds SoBDP-2 displayed higher fluorescence quantum yields and shorter lifetimes than dyes SoBDP-3 regardless of dye concentration and solvent polarity.²⁹

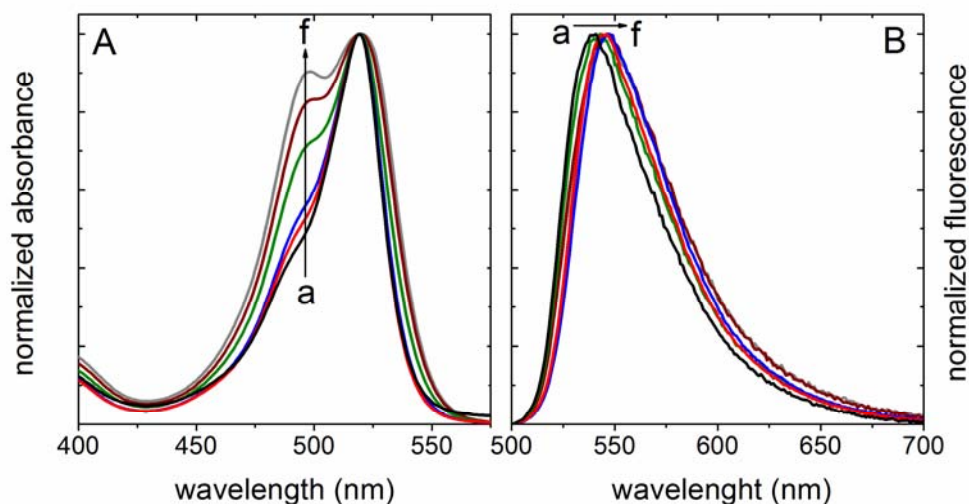


Figure 4.11. (A) Height-normalized absorption and (B) emission spectra for compound SoBDP-3c in water at different concentrations: a) $2.2 \cdot 10^{-5}$ M; b) $1.6 \cdot 10^{-4}$ M, recorded in 1 mm-optical path cuvette; c) $2.3 \cdot 10^{-4}$ M; d) $3.9 \cdot 10^{-4}$ M; e) $6.8 \cdot 10^{-4}$ M; f) $7.4 \cdot 10^{-4}$ M, recorded in 0.1 mm-optical path cuvette.

For the intention to use these new dyes in live-cell imaging, their solubility and stability in water, as well as their lipophilicity, were studied. All these compounds were completely soluble in water at 10^{-4} M which is above the maximum concentration typically required for cell microscopy studies. The evolution of the stability of SoBDP dyes was determined by recording their absorption spectra with the time.

For their intended application in cell microscopy, it was studied the stability under simulated physiological conditions (cell culture medium with 10% fetal bovine serum, pH 7.4) and phosphate-buffered saline solution at pH 6.0 and 8.0, at room temperature, using SoBDP-3b as a representative example. No changes in absorbance nor shape in the band were observed in the UV-visible spectra of the corresponding solutions after monitoring the sample for 7 days (see Figure 4.12 for PBS pH= 6 as an example).²⁹

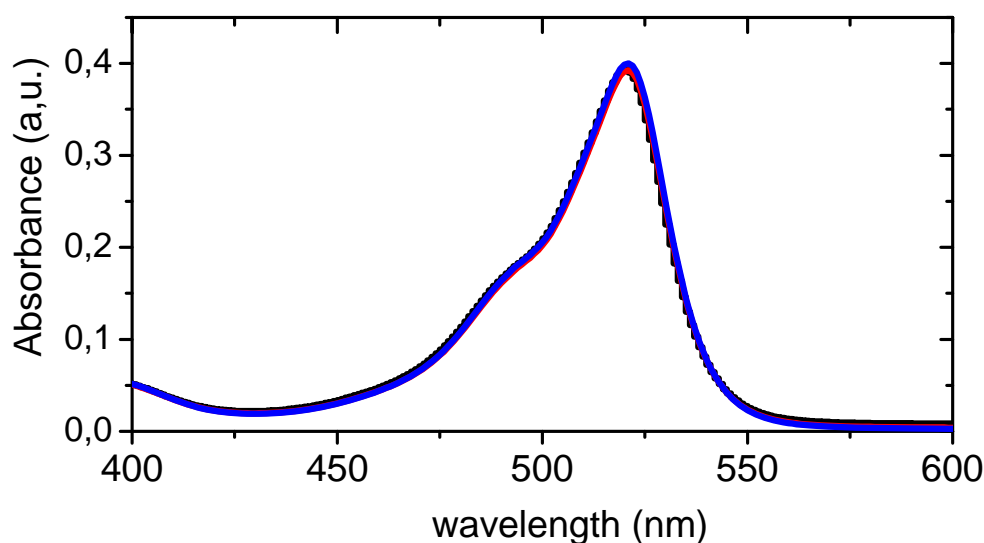


Figure 4.12. Time-dependent absorption spectra of SoBDP-**3b** ($8 \cdot 10^{-5}$ M) in pH 6.0 phosphate buffered saline solution at room temperature in 0.1 cm cuvette. Time zero (black), after 1 day (red) and 7 days (blue).

4.1.1.2 Live cell imaging studies

The behavior of new dyes, where the lipophilic and aggregation have been ameliorated with respect to commercial BODIPYs, was studied by microscopy in SCC38 cells by Dr. M. Chiara *et al.* at Hospital Central de Asturias, Oviedo), to assess their potential use in biological applications.

For the same solubility module, fluorescence brightness decreased in the order **2a** > **2b** > **3a** > **3b** > **1a** > **1b**, corresponding with the same order that it was obtained for photophysical study in water solution, Figure 4.13. Indeed, fluorescence staining with SoBDP-1 was too weak for practical use even though their concentration assays were increased. Respect to compounds with sulfobetaines (SoBDP-**2c** and **3c**) groups tethered, no staining was observed attributed to their inability to cross the cell membrane even after prolonged incubation time. This effect was observed also for other dyes with similar sulfobetaine substituents.³⁶

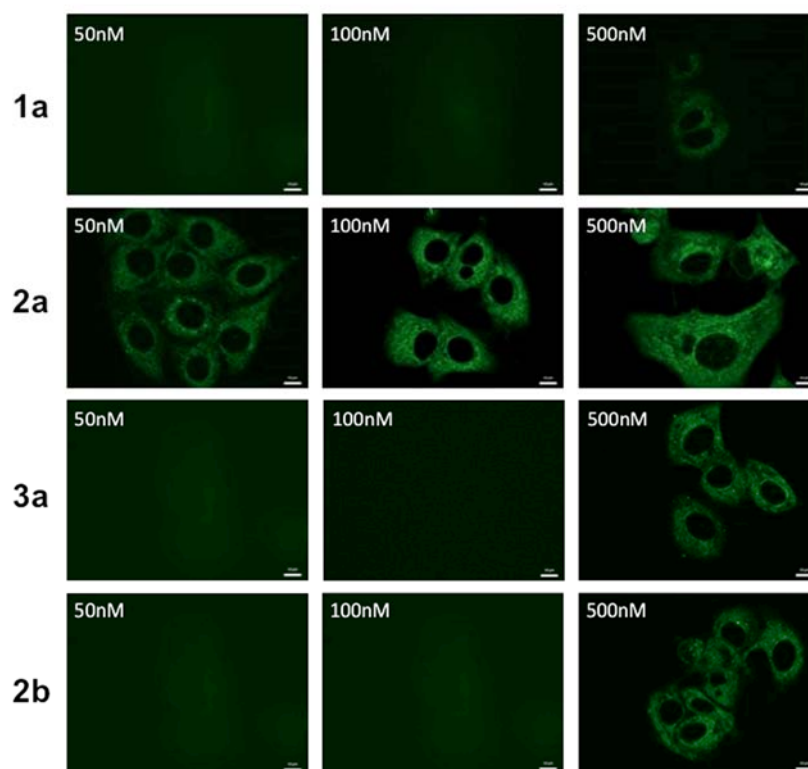


Figure 4.13. Representative fluorescence images of live SCC38 cells incubated with the indicated concentrations of the new BODIPYs for 30 min at 37 °C before washing and microscopic analysis. To compare fluorescence intensities for the different dyes and concentrations, all images were taken with the same exposure time (200 ns) on the same day. Scale bar 10 μm .²⁹

4.1.1.3 Conclusions

In this study a modular one-pot synthetic strategy for the direct post-functionalization of F-BODIPYs was developed, to tune their solubility properties. The covalent attachment has a minimal effect on the absorption properties, while its effect on the fluorescence emission properties depends on the degree of alkylation of the chromophoric system. Thus, for non-alkylated chromophores, SoBDP-1, low fluorescence quantum yield was observed due to their deactivation by PET process as predicted by DFT atomistic simulations. In the case of alkylation BODIPYs this phenomenon was thermodynamically unfeasible, and as a result, SoBDP-2 and SoBDP-3 present a highly efficient fluorescence. Regarding the solubility in water of

new O-BODIPYs containing either neutral (tetra- and octaethylene glycol chains) or zwitterionic (sulfobetaine) tags were highly stable under the most common aqueous conditions used in biological settings (pH 6-8). The live-cell studies of the SoBDP chromophores shown that the cell membrane permeability depends on the nature and size of the chemical tags decreasing in the order tetraethylene glycol > octaethylene glycol >> sulfobetaine. Here it is shown a good example of how straightforward one-step chemical modification of the BODIPY core consisting in the incorporation of short glycol chains attached at the Boron-atom has increased the solubility in aqueous media, allowing its use as stains of cells at high concentrations.²⁹

4.1.2 Carnitine BODIPY probes as mitotrackers

However, as the majority of the BODIPY chromophores, the former examples do not present an inherent selectivity for a specific organelle. Nevertheless, their synthetic versatility can allow the anchorage of biotargeting elements of interest for this propose. In this case, a carnitine molecule, selective as a biotarget for mitochondria is tethered, in a similar way as the former example, through the boron atom forming a B-spiro system, being both units orthogonally disposed. This new fluorescent compound is readily prepared in one-step from free carnitine and the corresponding F-BODIPY, Figure 4.14.³¹ For more details of the synthesis see Blazquez-Moraleja *et al.* Chemical Science (2020) doi:10.1039/C9SC04852A.³⁷

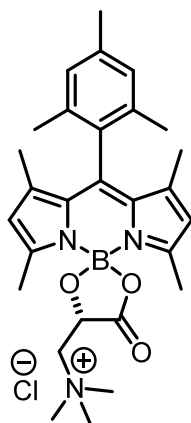


Figure 4.14. Carnitine BODIPY (BDP-C) molecular structure

Mitochondria is an organelle responsible for the production of energy in the form of ATP in eukaryotic cells through aerobic respiration. The inner membrane is highly impermeable to most molecules and contains among others, the proteins involved in oxidative phosphorylation and proteins involved in the mitochondrial carries systems, responsible for regulating the transfer of small molecules between the matrix and the cytosol. Consequently, mitochondria have an extraordinary capability to precisely regulate cell chemistry. Besides cellular respiration, it is responsible for other processes including calcium homeostasis, production of reactive oxygen species (ROS), the metabolism of heme groups, nucleotides, amino acids and phospholipids, inflammation, cell proliferation, and apoptosis. Thus, it fulfills an essential role in cell survival. The damage or deregulation of these mechanisms implicates great numerous pathological processes, either directly, as in mitochondrial genetic diseases, or secondarily related to neurodegenerative, inflammatory, and cardiovascular diseases, as well as in some metabolic syndromes.^{38,39} Therefore, mitochondria are an interesting organelle to study due to many details of their functions and basic activities are still unknown.

In this work, the carnitine system was chosen, because it facilitates the transport of long-chain fatty acids through the mitochondrial membranes into the matrix for β -oxidation.⁴⁰ A key protein of the carnitine system is the carnitine/acylcarnitine translocase (CACT), which is an antiporter carrier that transfers the fatty acids in the form of acylcarnitines across the inner mitochondrial membrane into the matrix.^{37,41-43}

4.1.2.1 Photophysical properties and discussion

First at all, although BDP-Carnitine (BDP-C) was designed for live-cell fluorescent staining, their photophysical properties were characterized in several solvents at low concentrations (approx. $5 \cdot 10^{-6}$ M); chloroform, acetone, acetonitrile, ethanol, and water in order to fully characterize the probe. As it is shown in Figure 4.15, no aggregation band could be detected in the UV-visible and emission spectra, and it does not show any dependence on the solvent polarity. Indeed, a high molar absorption coefficient ($3.8 \cdot 10^4 \text{ M}^{-1} \text{ cm}^{-1}$ at 499 nm) and an efficient fluorescent emission peaked at 511 nm with a quantum yield higher than 80 % were obtained in water. The photophysical properties are quite similar in the rest of the solvents, Table 4.5.

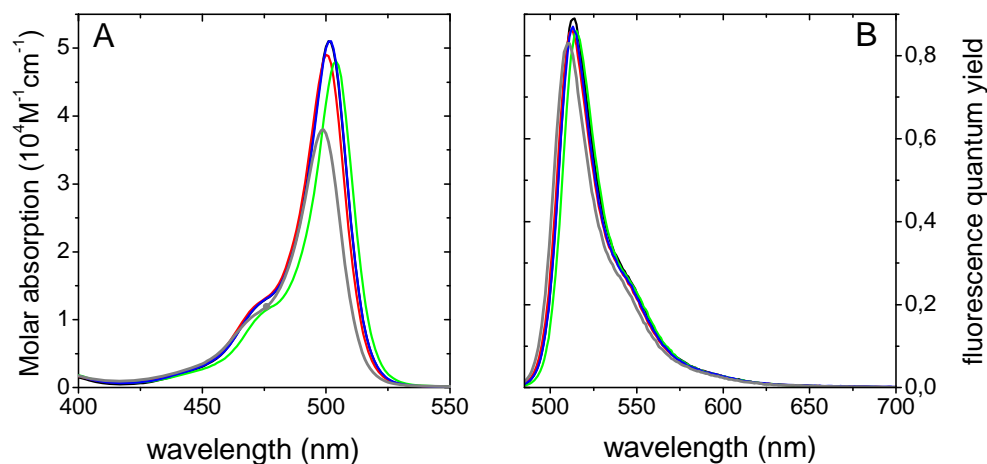


Figure 4.15. (A) Molar absorption-normalized and (B) quantum yield fluorescence-normalized spectra of BDP-C in different solvents; chloroform (green), acetone (black), acetonitrile (red), ethanol (blue) and water (grey). Reference PM546 ($\Phi_{fl} = 0.87$) in ethanol.

Table 4.5. Photophysical properties of BDP-C in chloroform, acetone, acetonitrile ethanol and water: absorption (λ_{ab}), molar absorption (ϵ), fluorescence wavelength (λ_{fl}), Stokes shift ($\Delta\nu$) fluorescence yield (Φ_{fl}) and fluorescence lifetime (τ).

Solvent	λ_{ab} (nm)	ϵ_{max} ($10^4 \text{ M}^{-1} \text{ cm}^{-1}$)	λ_{fl} (nm)	$\Delta\nu$ (cm^{-1})	Φ_{fl}	τ (ns)
Chloroform	504	4.8	514	424	0.86	6.32
Acetone	501	5.1	514	504	0.89	7.00
Acetonitrile	500	4.9	512	469	0.86	7.12
Ethanol	502	5.1	513	427	0.87	7.10
Water	499	3.8	511	470	0.83	7.30

The high fluorescence emission demonstrated is related to the low probability of non-radiative processes attributed to rigid and constrained molecular structure design resultant from the ring grafted at the *meso* position and at the boron atom together with the 1,3,5,7-tetrametylation of the chromophore scaffold.³⁷

On the other hand, the study of the stability in water of the new BDP-C is of importance for its use as a fluorescent probe for bioimaging. Although by ^1H NMR, a slow hydrolysis of BDP-C was observed, it did not result in a significant change of the overall fluorescence emission, (Table 4.6).³⁷ In fact, its fluorescence quantum yield remained unchanged after 7 hours so the hydrolysis may not significantly affect the fluorescence performance, which is a favorable factor for the probe. Note that, the fluorescence capacity started to decrease after 24 hours reaching 65 %.

Table 4.6. Temporal evolution of photophysical properties of BDP-C in water

Time (hour:min)	λ_{ab} (nm)	ϵ_{max} ($10^4 \text{ M}^{-1}\text{cm}^{-1}$)	λ_{fl} (nm)	Φ_{fl}	τ_{fl} (ns)	k_{fl} (10^8 s^{-1})	k_{nr} (10^8 s^{-1})
00:00	499	3.8	511	0.83	7.30	1.14	0.23
00:10	498	3.8	511	0.82	7.25	1.14	0.24
00:25	498	3.8	511	0.82	7.20	1.14	0.25
00:50	498	3.8	509	0.83	7.15	1.16	0.24
01:20	498	3.8	509	0.83	7.05	1.17	0.25
02:00	497	3.8	509	0.83	7.00	1.18	0.25
04:00	497	3.8	509	0.82	6.90	1.19	0.26
07:00	496	3.8	508	0.83	6.70	1.23	0.26
24:00	496	3.7	507	0.65	6.50	1.03	0.54

4.1.2.2 Live cell imaging

The ability of compound BDP-C for mitochondrial staining was assessed in live SCC38 cells (derived from human larynx squamous cell carcinoma) by Dr. M. Chiara *et al.* Different concentration of BDP in water (50, 100 and 500 nM) were tested, being the lowest concentration (50 nM) the optimal to obtain a bright staining without causing any cytotoxicity, Figure 4.16.³⁷ The localization of BDP-C in live cells was studied by co-staining experiments with commercially available Mito Tracker Red CMXRos. As shown in Figure 4.17, the green fluorescence from BDP-C colocalized

well with the red fluorescence from the Mito Tracker dye. These data revealed that BDP-carnitine acts as an organelle-specific probe that targets mitochondria and is retained within the organelle like the commercial Mitotracker dye. Nevertheless, it was observed that the mechanisms of transport were different. After some tests *in vitro* it was observed that Mito Tracker dye is dependent on the mitochondrial membrane potential, in contrasts of BDP-carnitine. These observations could be indicative that BDP-C was internalized into mitochondria via an active transport system while Mito Tracker did it by passive electrophoretically-driven diffusion. For more details see other *in vitro* experiments detailed in the article Blazquez-Moraleja *et al.* Chemical Science (2020) doi:10.1039/C9SC04852A.³⁷

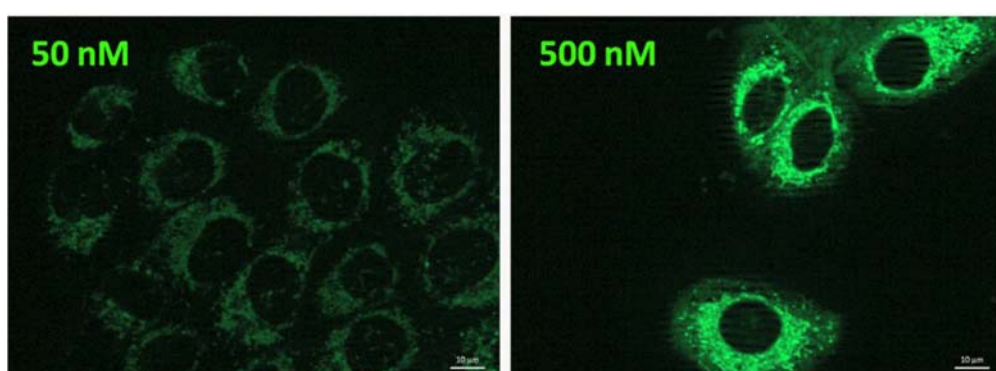


Figure 4.16. Dose-dependent cellular distribution of BDP-C. Representative fluorescence images of live SCC38 cells incubated with the indicated concentration for 30 min before washing and microscopic analysis. Scale bars 10 µm.³⁷

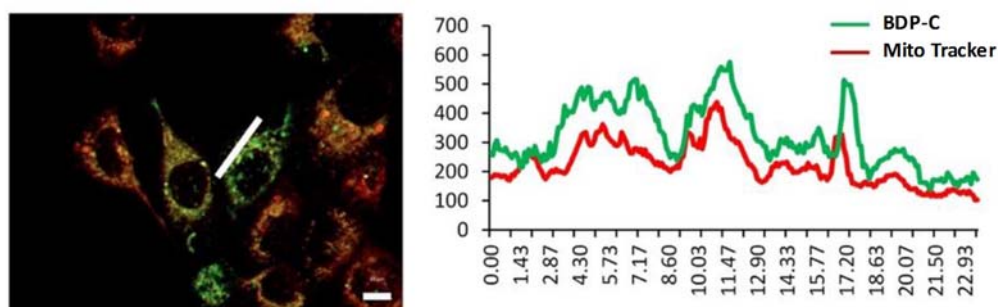


Figure 4.17. Colocalization of BDP-C and Mito Tracker Red CMXRos fluorescence signals in SCC38 cells (left). Graphic shows the fluorescence intensity profiles or the region of interest indicated with a white line in the panel (right). Scale bar 10 µm.³⁷

4.1.2.3 Conclusions

BDP-carnitine compound is the first fluorescent probes that are actively channeled into the mitochondrial matrix by specific mitochondrial membrane transport in living cells. This is another example of the rational design of a probe with minimalist structural features. It has been prepared in one-step by the reaction of carnitine as a biotargeting unit with a photostable F-BODIPY through the boron atom forming a B-spiro system. In contrast to most commonly used mitochondrial specific dyes, BDP-C enters mitochondria in a time-dependent way (data not shown), regardless of the mitochondrial membrane potential. Besides, this simple design could be extended for other F-BODIPY to obtain chromophores with different photophysical properties with wavelength emission along the visible and NIR region.³⁷

4.2 BODIPYs for Photodynamic Therapy

As briefly described above, Photodynamic therapy (PDT), involved three main components, a photosensitizer (PS), light and environmental oxygen, and when the PS is irradiated with suitable light it is able to generate singlet oxygen species from the molecular oxygen dissolved in the media, which is a cytotoxic species able to destroy any nearby tissue. This treatment could be combined with traditional cancer treatments in order to reduce the drawbacks of conventional methods since is a treatment able to cause local damages, focused on the irradiated area. Indeed, the clinical PDT has existed already for 30 years. Currently, a huge effort is devoted to making this treatment more effective. On the one hand, nowadays it is being improved the technology dedicated to developing irradiation sources to be implemented in PDT studies and particularly in clinic cases. On the other hand, many efforts are also focused on the synthesis of better PSs. In this line, although there are a wide variety of families of PSs; xanthenes-type dyes, anthracenes, porphyrins, anthraquinone derivatives, benzophenones, metal-bases complexes and fullerenes, Figure 4.18,⁸ few of them have been approved for clinical use by the Food and Drug Administration (FDA).

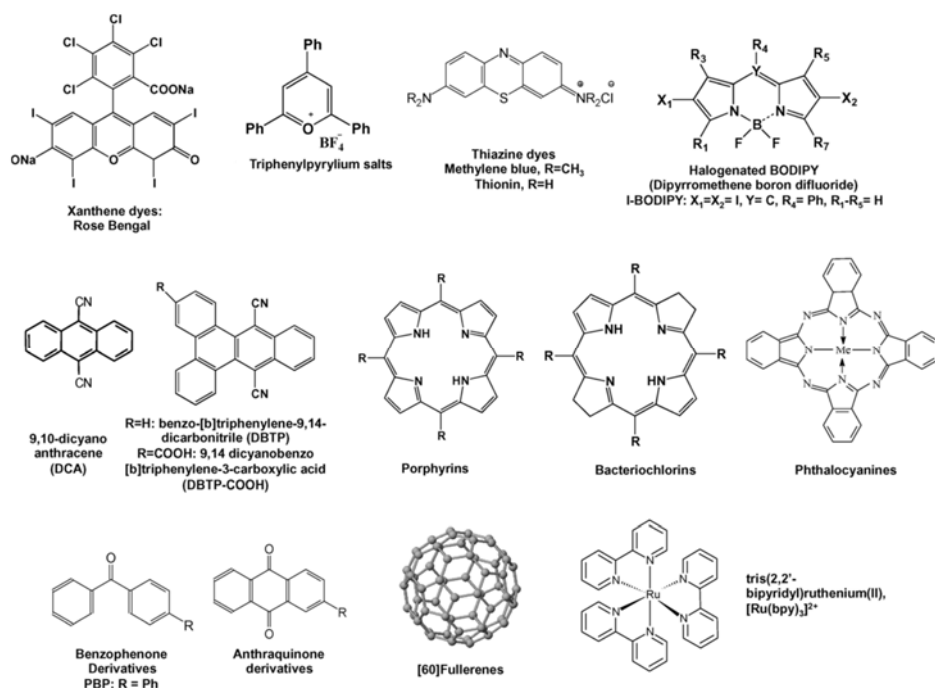


Figure 4.18. Molecular structure of photosensitizers for singlet oxygen production⁶

The most of the current PSs approved belong to porphyrin-like family such as Photofrin, Visudyne or Levulan. Indeed, the Hematoporphyrin derivative (HpD) was the first useful PS in clinical with patients who suffered primary or secondary skin cancers. HpD or Photofrin (HpD purified) belongs to the first generation of PSs, and although it is efficient destroying cancer cells, this compound has a lack of tumor selectivity and low absorption coefficient ($\epsilon = 3 \cdot 10^4 \text{ M}^{-1} \text{ cm}^{-1}$ at 630 nm), so large amount of the PS is required. Therefore, a second generation of PSs was developed (Levulan or Visudyne) which presents better antitumor effects than HpD because of their higher singlet oxygen quantum yield and shorter tissue accumulation time. Nonetheless, their selectivity has not improved, though apparently, most of PS are hydrophobic and their solubility problems in aqueous media generate molecular aggregation, decreasing their effectiveness. For these reasons, a third generation of PSs are development in order to improve tumor specificity, by adding biologic molecules to the molecular structure of PSs or by encapsulating them in delivery carriers.⁴⁴⁻⁴⁶

In this thesis, new PSs designed based on the modification of the BODIPY structure were studied. Although BODIPY is often characterized by a poor triplet state formation, changes in their structure give the opportunity to tune their photophysical properties. In this sense, there are several strategies to increase the populating of the triplet state and consequently the singlet oxygen production. In general, the increase of the intersystem crossing (ISC) to the triplet excited state can be obtained by involving heavy atoms in the dye skeleton or by incorporation electron donor groups.^{18,47}

The first part of this section (4.2.1) is dedicated to the study of new PSs with heavy atoms, *i.e.* halogenated-BODIPY. Firstly, it is proposed a di-iodinated-BODIPY, (supplied by Cuántico de México) as a new universal standard reference for singlet oxygen (4.2.1.1), in which a wide study about their photophysical behavior and singlet oxygen production in several solvents, together with the dynamics of its excited states and triplet states are detailed. Secondly, several iodinated-BODIPY are rationally-design for their implementation in PDT. In this contest, the absorption band is shifted into the clinic window ($> 650 \text{ nm}$) by adding π -extended functionalization are described (4.2.1.2). The viability of these photosensitizers for PDT was tested in vitro in HeLa cells. These compounds were synthesized by Dr. M. J. Ortiz *et al.* from Universidad Complutense de Madrid.

Nevertheless, although, currently there are many examples of halogenated-BODIPY dyes with high singlet oxygen production, particularly, iodinate ones,⁴⁸⁻⁵⁰ the presence of these heavy atoms could promote dark toxicity, which is a shortcoming for their implementation as clinic photosensitizers in PDT. For these reasons, the second section 4.2.2 is focused on the design and study of new halogen-free-BODIPY photosensitizers. It is described how intersystem crossing to the triplet state is modulated by adding different electron-donor moieties to the BODIPY skeleton, *i.e.* binol (4.2.2.1) or enamine (4.2.2.2). Besides, the characterization of photophysical properties and singlet oxygen production, *in vitro* experiments in HeLa cells are also performed for the most representative BODIPY-PS for PDT. Note here that binolated BODIPYs were synthesized by D. Santiago de la Moya *et al.* and the enamine-based BODIPYs by Dr. M. J. Ortiz *et al.*, both from Universidad Complutense de Madrid.

4.2.1. Halogen BODIPY

4.2.1.1 MeSBDP as standard reference

As it is explained previously in theoretical bases (chapter 2), the quantification of singlet oxygen production can be performed by an indirect method using a probe or by a more straightforward and accurate direct method. The latter approach is based on the recording of singlet oxygen photoluminescence at 1276 nm and the determination always require the comparison of Φ_{Δ} of the new PS with that of a reference sensitizer with known singlet oxygen quantum yield ($\Phi_{\Delta}^{\text{ref}}$) under similar conditions (same solvent, irradiation wavelength and similar absorbance, equation 2.29 in chapter 2). Until now, there are some commercial photosensitizers used as references: Phenalenone (PN) with absorption band in the UV-blue region, Rose Bengal for the green region and New Methylene Blue (NMB) for the red region, Figure 4.19.

Apparently, these three PSs are able to cover the whole UV-visible region for the determination of the singlet oxygen quantum yield of new compounds. Nevertheless, they have several drawbacks.

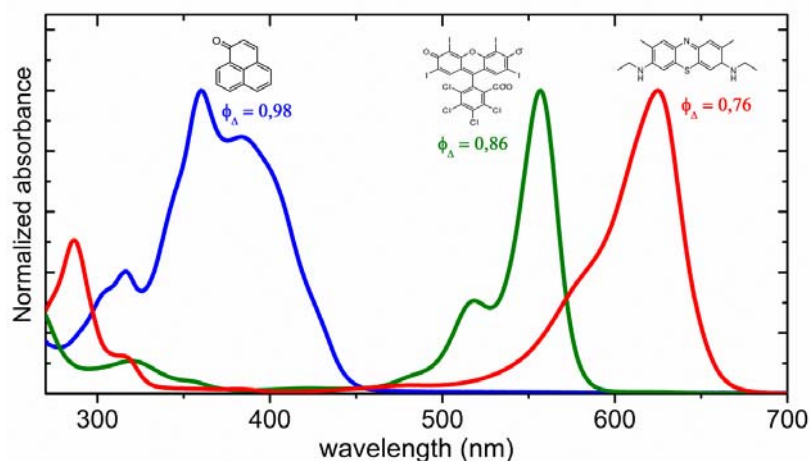


Figure 4.19. Molecular structures, absorption spectra and singlet oxygen quantum yield in MeOD for commercial references phenalenone (blue), rose Bengal (green) and new methylene blue (red).

For instance, Phenalenone is considered as the universal standard reference owing its solubility in both polar and non-polar solvents with singlet oxygen quantum yield close to 1, mostly independent of the solvent, but it can be only used under UV light irradiation.⁵¹ In contrast, Rose Bengal and New Methylene Blue have their absorption band, with moderate oxygen quantum yields values ($\Phi_{\Delta}=0.5-0.8$), in the Visible region. Nonetheless, they are mainly soluble in polar solvents, which presents a huge limitation. Moreover, both PSs, RB and NMB, have a high tendency to form molecular aggregates (H-type dimers and higher-order aggregates) impairing the production of singlet oxygen at relatively low concentrations. Additionally, they are known to photobleach easily.

For these reasons, in this thesis, it is proposed a new compound, based on BODIPY structure, 8-methyltio-2,6-diiodo-BODIPY, MeSBDP, (CAS-1835282-63-7), Figure 4.20, as a suitable universal standard reference, able to be irradiated under UV and Visible light and soluble in a wide range of solvents. The selection of this compound was based on a previous study related to halogen-free analogs MeSBDP dyes, which have revealed that they showed an intense and broad S_0-S_1 absorption band located in the green-orange region together with a relatively intense S_0-S_2 band centered in the UV region.⁵² Furthermore, previous studies, also performed in the group, demonstrated that the substitution of different halide atoms (Br or I) at 2 and 6 positions of the BODIPY skeleton induced high singlet oxygen quantum.¹⁷ For all

these reason, the selected MeSBDP compound is considered a promising PS to become into universal standard reference.

In this section, a completed photophysical study in a broad range of solvents including methanol-water mixtures is detailed. It includes absorption and fluorescence properties, triplet state energy by recording its phosphorescence emission at 77 K, the quantum yield of singlet oxygen production by recording the photoluminescence of singlet oxygen and the determination of the rate constant quenching by MeSBDP itself. Moreover, the quenching of the triplet state by molecular oxygen or by β -carotene is studied by nanosecond transient absorption spectroscopy. Finally, the photostability of MeSBDP and Rose Bengal was compared. With all these data, it is intended to demonstrate that MeSBDP can be excellent triplet-triplet sensitizer for singlet oxygen production.¹⁰

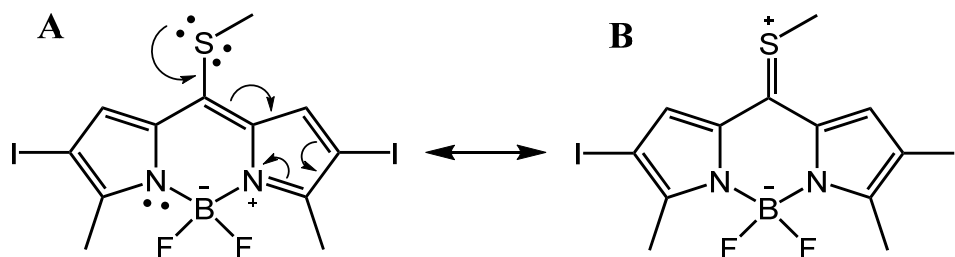


Figure 4.20. Different resonance structures of the BODIPY chromophore upon electronic coupling with a methylthio group at *meso* position; A) hemicyanine-like form and B) cyanine-like form^{17,52,53}

i) Photophysical results and discussion

The photophysical properties of MeSBDP in various solvents, together with its quantum yields of singlet oxygen production, are displayed in Table 4.7. Moreover, the absorption and fluorescence spectra in the most representative solvents of different polarity are shown in Figure 4.21.

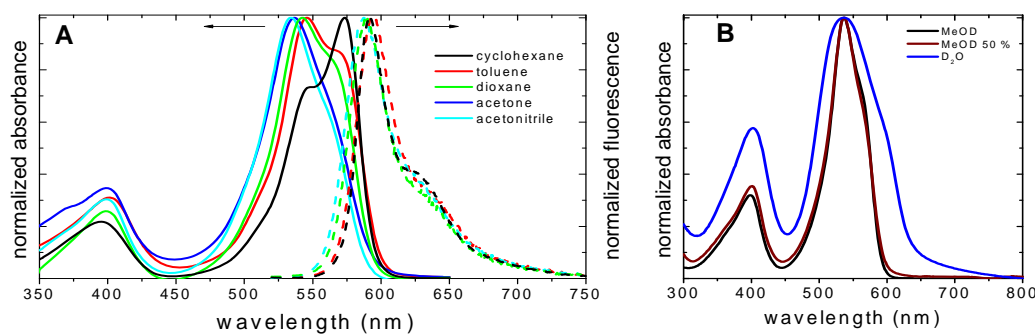


Figure 4.21. (A) Normalized absorption and normalized emission spectra of MeSBDP in various representative solvents and (B) height-normalized absorption spectra of different solutions MeOD (black), D₂O (blue) and MeOD:D₂O 50/50 % v (brown).

As expected, an important change in the shape of the absorption band was observed with the polarity of the solvent. The characteristic intense and sharp absorption band, centered at 573 nm, with a vibronic shoulder, typical of BODIPYS was only observed in the most apolar solvent, cyclohexane.^{50,54} However, in a slightly more polar solvent, *i.e.* toluene, the main band was shifted to shorter wavelengths, now centered at around 545 nm, close to the position of the vibronic shoulder observed in cyclohexane (Figure 4.21). This effect is attributed to the different contribution of the main resonance forms depending on the solvent polarity:¹⁶ the less energetic form A (cyanine-like with a more delocalized π -system, Figure 4.20) is favored in an apolar solvent such as cyclohexane while in more polar solvents the resonance form B (hemicyanine-like) has a higher contribution, leading to a blue-shift of the main absorption band. This result was also demonstrated in a series of halogen-free BODIPYS with methylthio patterns at the *meso* position.⁵² This effect was even more pronounced for functional groups with higher electronegative atoms such as amino or methoxy groups tethered at that *meso* position.^{16,17} On the other hand, the absorption spectra of MeSBDP in D₂O, even at low concentration ($5.6 \cdot 10^{-6}$ M) shows a poor solubility. Indeed, the low absorption coefficient and the broader absorption band in D₂O recorded respect to methanol indicates the formation of molecular aggregates. Alternatively, MeSBDP in different MeOD:D₂O mixtures (80:20, 50:50 v/v, with two drops of DMSO in the latter case) does not show any evidence of aggregation according to its absorption spectra, similar to those obtained for other polar solvents, Figure 4.21.B.¹⁰

Table 4.7. Photophysical parameters and singlet oxygen quantum yields of MeSBDP in various solvents; absorption maxima (λ_{\max}), molar absorption coefficient (ϵ_{\max}), fluorescence maxima (λ_{fl}), fluorescence quantum yield (Φ_{fl}), fluorescence lifetime (τ_{fl}), rate constant of fluorescence (k_{fl}), non-radiative rate constant (k_{nr}^S), singlet oxygen quantum yield (Φ_{Δ}) and rate constant of singlet oxygen quenching by MeSBDP itself (k_t^{PS}).

Solvent	$E_T(30)^1$	λ_{\max} nm	ϵ_{\max} $10^4 \text{ M}^{-1}\text{cm}^{-1}$	λ_{fl} nm	Φ_{fl}	τ_{fl}^2 ns	k_{fl} 10^9 s^{-1}	k_{nr}^S 10^9 s^{-1}	Φ_{Δ}^3	k_t^{PS} $\text{M}^{-1}\text{s}^{-1}$
C-hexane	30.9	573.0	4.6	590.5	0.06	0.70	0.09	1.3	0.87	$\leq 4.3 \cdot 10^7$
Toluene	33.9	546.0	4.4	592.0	0.06	0.53	0.11	1.8	$\frac{0.89^4}{0.95^4}$	$\leq 8.2 \cdot 10^7$
Dioxane	36.0	543.0	4.5	589.0	0.04	0.57	0.07	1.6	0.96	$\leq 4.5 \cdot 10^7$
CHCl ₃	39.1	547.0	4.7	592.0	0.06	0.58	0.10	1.6	0.91	$\leq 1.3 \cdot 10^7$
CH ₂ Cl ₂	40.7	543.0	4.9	591.0	0.06	0.54	0.11	1.7	0.87	$\leq 1.6 \cdot 10^7$
Acetone	42.2	536.0	4.8	590.5	0.03	0.39	0.08	2.5	0.94	$\leq 4.5 \cdot 10^7$
CH ₃ CN	45.6	533.0	4.3	588.0	0.04	0.40	0.10	2.5	0.95	$\leq 2.7 \cdot 10^7$
EtOH	51.9	539.0	4.6	591.0	0.04	0.42	0.10	2.3	0.98	$\leq 9.4 \cdot 10^7$
MeOH	55.6	537.0	4.5	587.5	0.03	0.40	0.08	2.4	0.98	$\leq 3.8 \cdot 10^7$
MeOD	55.6	537.0	4.5	588.5	0.04	0.40	0.10	2.4	0.98	$\leq 1.1 \cdot 10^8$
D ₂ O	63.1	526.0	1.65 ⁵	-	-	-	-	-	n.d.	-
D ₂ O:MeOD	-	537.0	2.6	588.0	0.02	n.d.	n.d.	n.d.	0.86	$\leq 3.8 \cdot 10^7$

¹ $E_T(30)$ is the Reichardt parameter of solvents polarity; ²Decay curves at the emission maxima. The decays are monoexponential ($\chi^2 < 1.3$). These lifetimes do not change under N₂ or O₂ saturated, tested in chloroform and acetonitrile as representative solvents; ³Values relative to phenalenone singlet oxygen quantum yields ($\Phi_{\Delta}^{PS_{\text{Ref}}}$) took from literature and detailed in Table 4.8); ⁴Depending on the $\Phi_{\Delta}^{PS_{\text{Ref}}}$ value of the phenalenone in toluene (0.92⁵⁵ or 0.97⁵⁶); ⁵Low absorption coefficient due to the lower solubility of MeSBDP in water.

* Photophysical errors are 5 %

In contrast to the absorption features, MeSBDP showed a fluorescence emission band practically independent of the solvent, and only a slight blue-shift is recorded as the polarity of the solvent increase, a typical behavior for BODIPY dyes. The wavelengths displayed in Table 4.7 reflect an energy of around 2.10 eV (202 kJ mol⁻¹) for the first excited singlet state. Moreover, the fluorescence quantum yields, Φ_{fl} is quite low (≤ 0.06) for every solvent, in agreement with previous results reported on halogenated-Bodipys.¹⁹ From the fluorescence decay curves, fitted as monoexponential ($\chi^2 < 1.3$), a fluorescence lifetimes, τ_{fl} , between 400 and 700

picoseconds is obtained (Table 4.7). This fluorescence lifetime was demonstrated to be independent of the oxygen concentration (lifetimes measured under nitrogen-, air- and oxygen- saturated chloroform and acetonitrile), indicating no interaction between the PS excited singlet state and molecular oxygen.

Regarding the singlet oxygen quantum yield, it was determined in every solvent using as standard, the universal reference phenalenone, Table 4.8, under strictly similar conditions. As cited before, despite the main S_0 - S_1 absorption band of MeSBPD located in the Visible range (500-600 nm), it shows a relatively intense S_0 - S_2 band at higher energies ($\lambda_{\max} \sim 400$ nm), Figure 4.21 A, overlapping with the absorption band (350-420 nm) of phenalenone Figure 4.19. For that reason, the obtained singlet oxygen quantum yields for MeSBPD in any of the studied solvents can be considered very reliable values. The values of singlet oxygen quantum yields of MeSBPD were high ($0.86 \leq \Phi_{\Delta}^{PS} \leq 0.98$) and practically independent of the solvent (Table 4.7).¹⁰

In fact, the sum of the quantum yields of fluorescence and of singlet oxygen production of MeSBPD are close to unity ($\Phi_{fl} + \Phi_{\Delta} \sim 1$) in any solvent (Table 4.7). It can thus be assumed in a first step that the non-radiative internal conversion processes (k_{ic}) are practically negligible and the intersystem crossing, k_{isc} , is the main non-radiative process to depopulate the S_1 excited state ($k_{nr}^S = k_{ic} + k_{isc} \sim k_{isc}$, chapter 2 section 2.2.5). The result $k_{nr}^S \gg k_{fl}$ (Table 4.7), and the insensitivity of k_{fl} to oxygen also lead to the postulation of MeSBPD as a good triplet-triplet photosensitizer for singlet oxygen production.

Additionally, taking advantage of MeSBPD as an effective PS for singlet oxygen production in any solvent, the different singlet oxygen lifetimes and their respective rate constants of quenching by the solvent were determined and compared with the values found in the literature (values in brackets), Table 4.8. The obtained lifetime values are in good agreement with those already determined in reference;⁵⁵

Table 4.8: Phenalenone singlet oxygen quantum yield ($\Phi_{\Delta}^{\text{Phe}}$) from literature (except otherwise stated), singlet oxygen lifetimes (τ_{Δ}), rate constant of singlet oxygen quenching by the solvent (k_d).

Solvent	$\Phi_{\Delta}^{\text{Phe}}$	τ_{Δ}^{***} (μs)	k_d (s^{-1})
c-hexane	0.92 ⁵⁶	27 (21±4)	3.70·10 ⁴
Toluene	0.92 ⁵⁵	27 (27±2)	3.70·10 ⁴
Dioxane	0.99 ⁵⁷	30 (n.d.)	3.33·10 ⁴
Chloroform	0.98 ⁵⁶	201 (235±30)	4.98·10 ³
Dichloromethane	0.96 ⁵⁵	97 (101±39)	1.03·10 ⁴
Acetone	1*	58 (50.5±4)	1.72·10 ⁴
Acetonitrile	1 ⁵⁵	81(66.7±13.5)	1.23·10 ⁴
EtOH	0.92 ⁵⁵	18(15.5±3.5)	5.56·10 ⁴
MeOD	0.98**	37 (n.d.)	2.70·10 ⁴
MeOH	0.98 ⁵⁶	10(9.9±0.5)	9.09·10 ⁴
D ₂ O:MeOD (1:1)	1*	45(n.d.)	2.22·10 ⁴
D ₂ O	0.97 ⁵⁵	n.d.	n.d.

*we have used 1 for acetone and D₂O:MeOD (1:1) as there is not any value in the literature

**we have used the same values as MeOH as there is not any value in the literature

*** Between brackets are the singlet oxygen lifetime values found in the literature⁵⁷

ii) Nanosecond transient absorption spectroscopy

To get information about the triplet state of MeSBDP, transient absorption (ns-TA) spectra of MeSBDP were measured in nitrogen-, air- or oxygen-saturated toluene, chloroform, acetonitrile, and methanol under 530 nm excitation wavelength. The spectra, very similar in all the studied solvents, recall those observed on -bromine or -iodine BODIPYs derivatives.⁵⁸ According to these previous investigations, the negative contribution placed between 500-600 nm is assigned to the ground state bleaching (GSB) associated with the S₀-S₁ absorption. The positive transient absorption bands in the range of 410-450 nm and 620-700 nm are attributed to the triplet absorption. This latter assignation is confirmed by their fast quenching by oxygen. Indeed, their lifetimes in oxygen absence (τ_T^0) are in the range of 12-34 μs , drastically change to tens of nanoseconds in oxygen-saturated samples occurs (Figure 4.22 and Table 4.9).⁵⁹

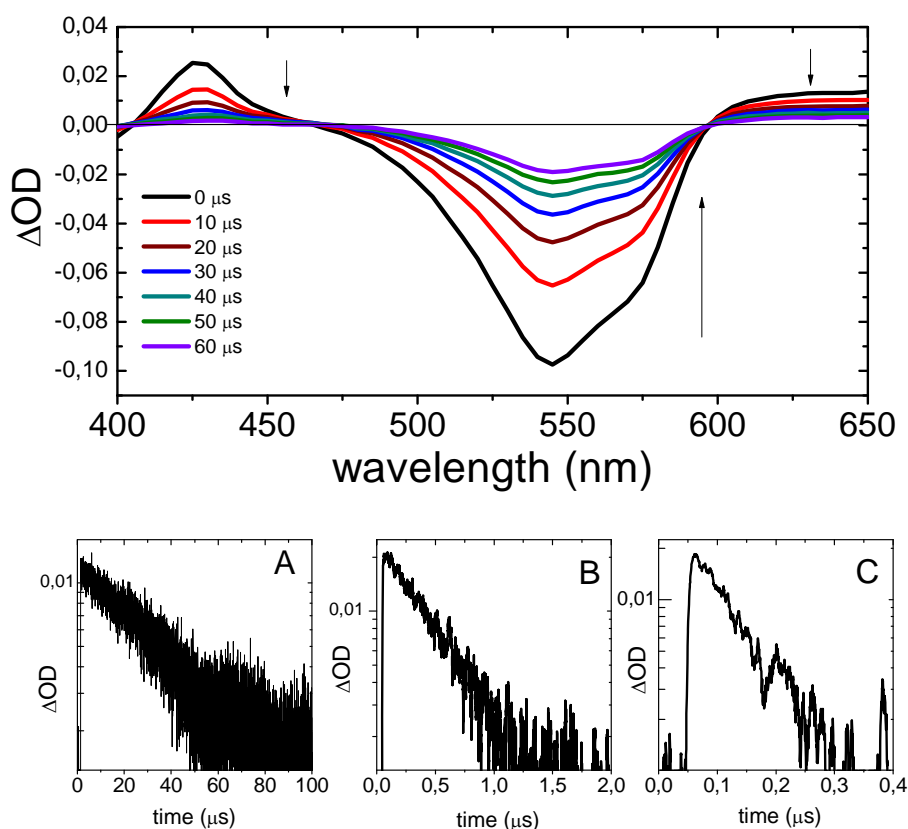


Figure 4.22. (top) Transient absorption spectra of MeSBDP in CHCl_3 ($\lambda_{\text{ex}} = 530 \text{ nm}$) in nitrogen at different times after the excitation pulse of $^3\text{MeSBDP}^*$; (Bottom) triplet lifetime under nitrogen (A), air (B) or oxygen (C) saturated CHCl_3 , recorded at 425 nm under 530 nm excitation.

The bimolecular rate constants of triplet quenching by molecular oxygen (k_{q,O_2}^T) at room temperature could be determined through recording the triplet lifetime in the different conditions (following equation 3.2 in experimental chapter 3). The k_{q,O_2}^T values are in the range $1.00\text{-}1.80 \cdot 10^9 \text{ M}^{-1} \text{ s}^{-1}$ (Table 4.9, Figure 4.23), depending on the solvent. Following equation 2.28 described in chapter 2, the fraction of triplet $^3\text{MeSBDP}^*$ quenched by oxygen ($P_{O_2}^T$) of near the unity in every investigated solvent were obtained (Table 4.9), indicating that the short-range energy transfer process from the triplet state of MeSBDP to the molecular oxygen is totally effective.¹⁰

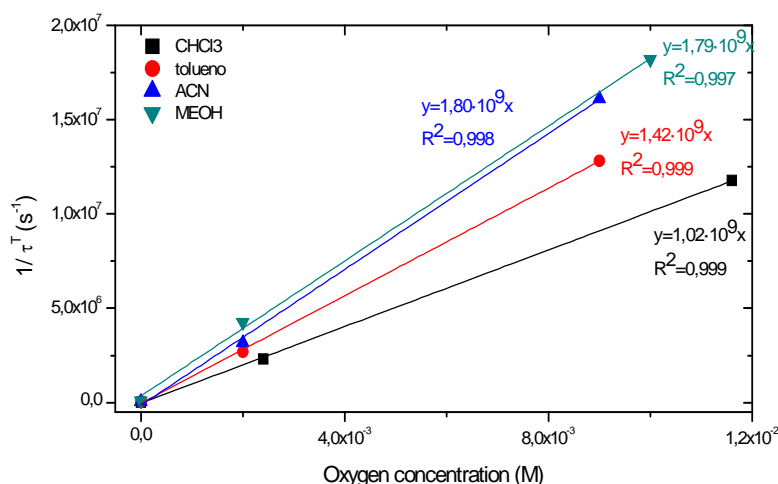


Figure 4.23. Determination of the bimolecular rate constants of triplet quenching of MeSBDP by molecular oxygen (k_{q,O_2}^T) at room temperature in chloroform (black square), toluene (red circle), acetonitrile (blue triangle) and methanol (green triangle).

Concerning the quantum yield of the triplet state production was estimated by two different approximations. The simplest approach is assuming that the sum of the $\Phi_T + \Phi_{\text{fl}}$ should be 1, by considering negligible the internal conversion process. In this way, using the fluorescence quantum yield values recorded in the different solvents (Table 4.7), intersystem crossing yield values between 0.94 and 0.97 are derived (Table 4.9). The second method is based on equations 2.21 and 2.23 detailed in chapter 2, where Φ_{Δ} and $P_{O_2}^T$ has been determined experimentally (Table 4.7 and Table 4.9, respectively). Then, assuming that the singlet oxygen generation is under diffusion-controlled conditions f_{Δ}^T should be 1, or in other words, all the triplet excited states of MeSBDP quenched by O_2 yields 1O_2 . Indeed, the values calculated for the bimolecular rate constants of triplet quenching by molecular oxygen, k_{q,O_2}^T , (Table 4.9 and Figure 4.23) of around 1/9 of the diffusion constant, $k_{diff} \sim 3 \cdot 10^9 \text{ M}^{-1} \text{ s}^{-1}$ in most organic solvents,⁵⁵ supports this assumption ($f_{\Delta}^T = 1$). Therefore, triplet quantum yields values derived from the second method are between 0.92 and 1.00 (Table 4.9 values in brackets), which are in accordance with the values obtained from the first approach. Therefore, it is confirmed that the quantum yield of triplet formation Φ_T is close to Φ_{Δ} being internal conversion process practically negligible ($k_{nr}^S = k_{ic} + k_{isc} \sim k_{isc}$).

Table 4.9: Triplet ³MeSBDP* T–T absorption maxima (λ_{max}^T), lifetime in nitrogen- (τ_0^T), air- (τ_{air}^T), or oxygen- ($\tau_{\text{O}_2}^T$) saturated samples, bimolecular rate constants of triplet quenching by molecular oxygen (k_{q,O_2}^T), fraction of triplet excited state quenched by O₂, $P_{\text{O}_2}^T$, triplet quantum yield Φ_T in four different solvents by two different approaches, and rate constants of triplet quenching by β -carotene ($k_{q,\text{car}}^T$) in chloroform.

Solvent	λ_{max}^T (nm)	τ_0^T (μs)	τ_{air}^T (ns)	$\tau_{\text{O}_2}^T$ (ns)	k_{q,O_2}^T $10^{-9}\text{M}^{-1}\text{s}^{-1}$	$P_{\text{O}_2}^T$	Φ_T	$k_{q,\text{car}}^T$ $10^9\text{M}^{-1}\text{s}^{-1}$
Toluene	426	23.6	370	78	1.43	0.99	0.94 ^a (0.96) ^b	-
Chloroform	426	34.3	430	85	1.02	0.99	0.94 ^a (0.92) ^b	12.6
Acetonitrile	426	15.0	315	62	1.80	0.98	0.96 ^a (0.97) ^b	-
Methanol	426	12.2	235	55	1.74	0.98	0.97 ^a (1.00) ^b	-

^a derived from the equation $\Phi_T + \Phi_{\text{H}} = 1$ ^b derived from the equation $\Phi_{\Delta} = \Phi_T P_{\text{O}_2}^T f_{\Delta}^T$

In order to prove that the MeSBDP is a potential standard reference for singlet oxygen, its singlet oxygen quantum yield, triplet lifetimes, triplet energy and rate constants of quenching by O₂ were compared to those of the widely used standard phenalenone ($\Phi_{\Delta} \geq 0.92$, $\tau_0^T \sim 34 \mu\text{s}$ in methanol, E_T 176-182 kJ mol⁻¹ in ethanol and $k_{q,\text{O}_2}^T \sim 1.3\text{-}3.2 \cdot 10^9 \text{M}^{-1} \text{s}^{-1}$).^{55,59} With no doubt, these parameters are in the same order of magnitudes as those obtained for MeSBDP in a variety of solvents ($\Phi_{\Delta} \geq 0.87$, $\tau_0^T \sim 12\text{-}34 \mu\text{s}$, $E_T = 1.48 \text{eV}$ and $k_{q,\text{O}_2}^T \sim 1\text{-}1.7 \cdot 10^9 \text{M}^{-1} \text{s}^{-1}$, Table 4.9).

Moreover, the rate constants of quenching of singlet oxygen by MeSBDP itself, k_t^{PS} , were determined in all the solvents by varying the PS concentration relative to the reference phenalenone (Figure 4.24). In any solvent, the independence of the ratio of the ¹O₂ signals for MeSBDP and phenalenone, corrected by the absorption factors with respect to MeSBDP concentration, is indicative of the absence of self-quenching of singlet oxygen by MeSBDP itself. The lack of deactivation of singlet oxygen when increasing MeSBDP concentration leads to regularly low values of rate constant of singlet oxygen quenching by MeSBDP itself; $k_t^{PS} (< 10^8 \text{M}^{-1} \text{s}^{-1})$, Table 4.7). These values confirm that $k_t^{PS}[\text{PS}] \ll k_d$, where k_d is the rate constant of singlet oxygen deactivation in a given solvent, Table 4.8.¹⁰

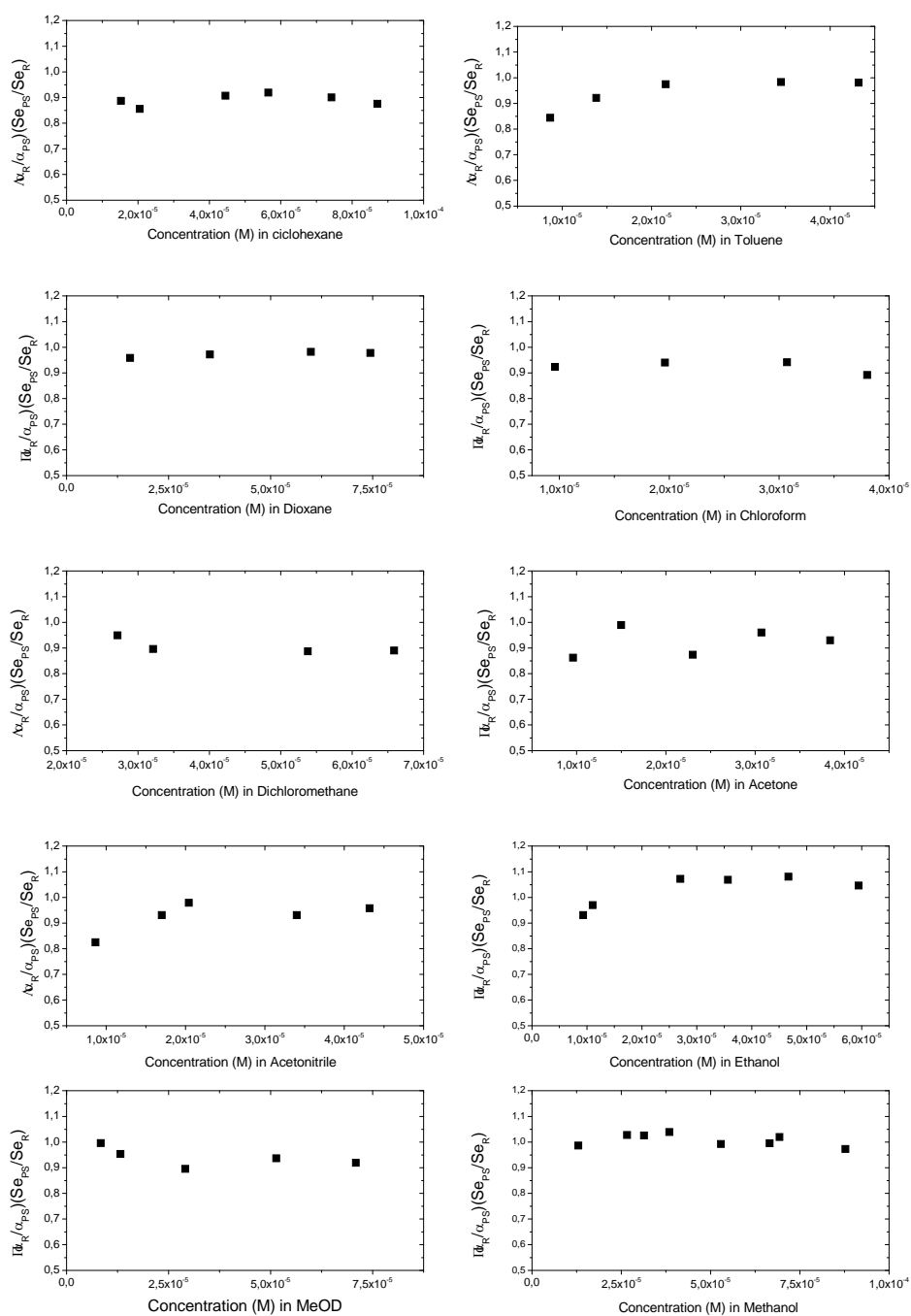


Figure 4.24. Variation of the ratio $(S_{0,PS_{Ref}}/S_{0,PS})(\alpha_{PS}/\alpha_{PS_{Ref}})$ of singlet oxygen emission signal for MeSBDP as a function of MeSBDP concentration in representative solvents at room temperature. Error: approx. 10%.¹⁰

iii) Phosphorescence spectra at 77 K

The phosphorescence signal and the lifetime of MeSBDP was recorded at 77 K in EtOH:MeOH (4:1 glassy mixture) (Figure 4.25). The band was placed at 835 nm, leading to an energy of its lower triplet state (E_T) of 1.48 eV (142.8 kJ mol⁻¹), in good agreement with the triplet state energy of other halogenated BODIPYS previously reported (values between 1.50 and 1.74 eV).⁶⁰⁻⁶² This low lying triplet energy is actually higher than the energy gap between the ground state O_2 ($^3\Sigma_g$) and first singlet excited state O_2 ($^1\Delta_g$) of oxygen (94.2 kJ mol⁻¹), fulfilling the necessary condition to generate singlet oxygen by type-II energy transfer mechanism. On the other hand, the energy difference between the first excited singlet (202 kJ mol⁻¹) and triplet state (148 kJ mol⁻¹) of MeSBDP* is $E_{S1}-E_{T1} \sim 54$ kJ mol⁻¹, being much lower than the energy of O_2 ($^1\Delta_g$) (94.2 kJ mol⁻¹), what rules out any production of singlet oxygen from the singlet state $^1\text{MeSBDP}^*$ and therefore it cannot be considered as an ST photosensitizer.⁵⁹ This last statement is confirmed by its insensitivity of τ_{fl} to oxygen.

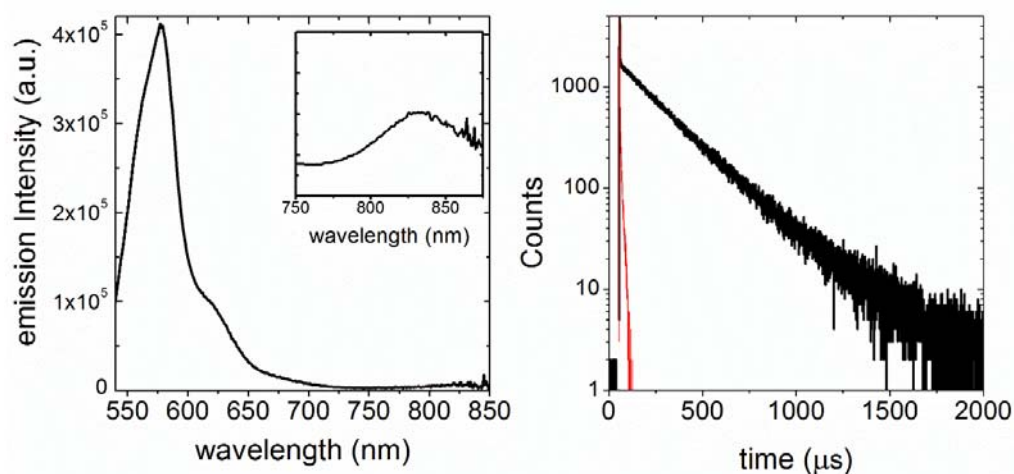


Figure 4.25. (left) Emission spectra and (right) phosphorescence decay curve at 835 nm of MeSBDP in EtOH: MeOH (4:1) mixture at 77K.

The phosphorescence shows a characteristic lifetime of $\tau_{ph} = 245$ μ s, typical from the deactivation of triplet states, which are much longer than that registered for the singlet state, $\tau_{fl} = 0.61$ ns, in the nanosecond range. From these lifetimes values, the

physical deactivation rates (without considering bimolecular processes) of singlet ($k^{S,0} = k_{nr}^{S,0} + k_{fl}^{S,0}$) and triplet ($k^{T,0} = k_{nr}^{T,0} + k_r^{T,0}$) states of MeSBDP of $1.64 \cdot 10^9 \text{ s}^{-1}$ and $4.10 \cdot 10^3 \text{ s}^{-1}$, respectively, are derived at 77 K.

iv) *Triplet-triplet energy transfer*

Since MeSBDP has also a long triplet lifetime at room temperature ($\tau_T = 34 \mu\text{s}$ in chloroform, Table 4.9), a triplet-triplet energy transfer (TTET) process between the photosensitizer and a triplet acceptor should be possible. β -carotene was chosen here as a triplet acceptor because its absorption band does not overlap with that of MeSBDP at 570 nm (Figure 4.26A), it has a lower triplet energy (0.91 eV) than MeSBDP (1.48 eV) and both compounds are soluble in chloroform. Different solutions were prepared, keeping constant the MeSBDP concentration ($1.0 \cdot 10^{-5} \text{ M}$) and varying β -carotene concentration (0, $2.4 \cdot 10^{-6}$, $1.6 \cdot 10^{-5}$, $2.4 \cdot 10^{-5} \text{ M}$). The triplet state transient absorption bands and lifetimes of MeSBDP were thus modified depending on the β -carotene acceptor concentration (Figure 4.26 B).

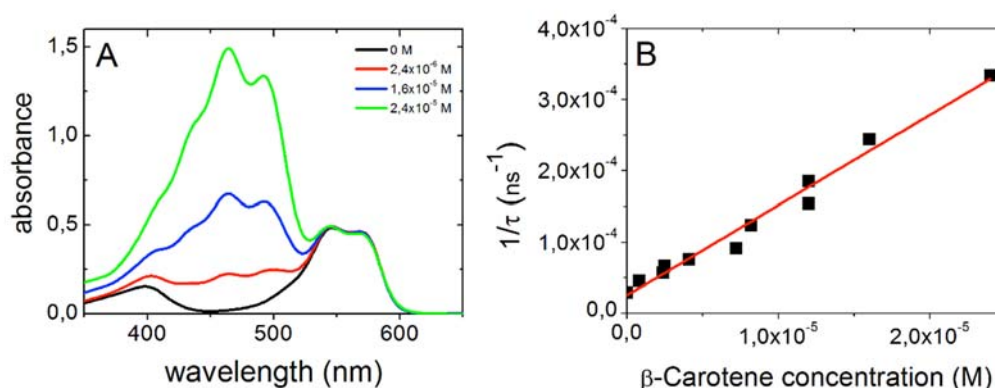


Figure 4.26. (A) Absorption spectra of a mixture of 10^{-5} M MeSBDP and different concentration of β -carotene (0, $2.4 \cdot 10^{-6}$, $1.6 \cdot 10^{-5}$, $2.4 \cdot 10^{-5} \text{ M}$) in chloroform and (B) Stern-Volmer plot generated from the triplet state quenching of $^3\text{MeSBDP}^*$ in the presence of β -carotene in N_2 degassed chloroform ($\lambda_{\text{ex}} = 570 \text{ nm}$).

The calculation of the bimolecular quenching rate constant of MeSBDP triplet state by β -carotene relies on the Stern-Volmer equation (equation 3.2 experimental section) The value obtained $k_{q,\text{car}}^T = 12.6 \cdot 10^9 \text{ M}^{-1} \text{ s}^{-1}$ was found in the same range as the

diffusion rate constant in chloroform ($k_{\text{dif}} = 12 \cdot 10^9 \text{ M}^{-1} \text{ s}^{-1}$, equation 2.19 theoretical bases chapter).^{58,63} The fact that both constants are very close implies that the TTET between the photosensitizer and the acceptor is a dynamic process controlled by diffusion.

v) *Photodegradation study*

As claimed in the introduction, it is also important that an efficient photosensitizer be photostable. We thus compared the photostability of MeSBDP and Rose Bengal under similar irradiation conditions in acetonitrile, Figure 4.27, (see experimental section 3.2.21 Photostability measurements).¹⁰

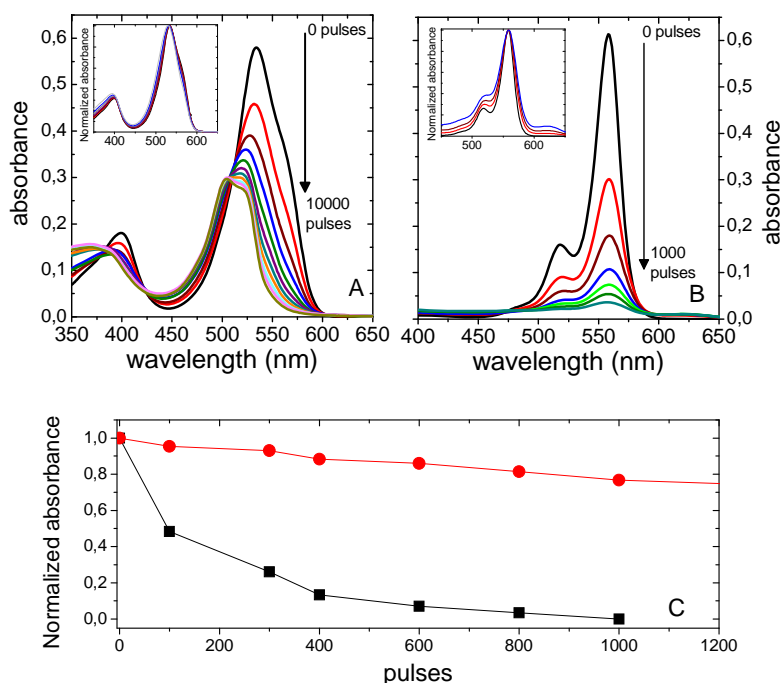


Figure 4.27. (A) Evolution of the absorption spectra of MeSBDP with the irradiation time, every 1000 pulses up to 10000 pulses), under 550 nm excitation and 9.8 mJ power; Inset the normalized absorption spectra every 100 pulses for the first 1000 pulses. (B) Evolution of the absorption spectra of RB with irradiation time every 100 pulses up to 1000 pulses under 550 nm excitation and 9.8 mJ power. Inset the normalized absorption spectra from 0 to 600 pulses and (C) evolution of the absorbance at their respective absorption maxima, 535 nm (red circles) for MeSBDP and at 550 nm for RB (black squares) in acetonitrile with the number of pulses

Following 100 irradiation pulses (10 seconds of irradiation at 10 Hz of repetition rate), approximately half of the initial Rose Bengal concentration was lost, whereas only 3% of the initial MeSBDP were photodegraded. Indeed, after 1000 pulses (100 seconds at 10 Hz of repetition rate), the absorbance of MeSBDP has decreased by 20%. Interestingly, when the solution of MeSBDP was kept pumped, a gradual change in the shape was observed. Particularly, the main absorption band progressively shifted to the blue giving rise an isosbestic point at 508 nm. This new absorption band registered after 10000 pulses, centered at 505 nm and with a pronounced shoulder around 525 nm, agrees well with the homologous non-iodinated BODIPY.⁵²

vi) Conclusions

It was demonstrated that MeSBDP is an efficient triplet photosensitizer for singlet oxygen production in a large range of solvents. Actually, the energy of its low-lying triplet state was experimentally determined to be 1.48 eV, higher than the energy gap between ground-state O₂ (³Σ_g) and the first excited state O₂ (¹Δ_g) of oxygen, and its triplet lifetime was sufficiently long (12-34 μs) to allow the generation of singlet oxygen by energy collisional transfer process. It shows an efficient ISC process, confirmed by fluorescence and by triplet quenching experiments, leading to high triplet quantum yields $\Phi_T \geq 0.92$ and to $P_{O_2}^T$ (fraction of triplet state quenched by oxygen) close to 1. Moreover, the quenching of the first triplet excited state of MeSBDP by β-carotene was also a very efficient and diffusion-controlled process.

MeSBDP can thus be considered as a universal standard for the measurement of singlet oxygen quantum yields in the UV and visible range in various solvents. It can be used instead of the widely documented Rose Bengal or phenalenone for the following reasons:

- i) High and solvent-independent singlet oxygen quantum yields ($\phi_\Delta \geq 0.87$) in a wide range of apolar and polar solvents, except for pure aqueous solutions. This inconvenient can be solved by using D₂O:MeOD mixtures (50:50 or 80:20) with also high singlet oxygen quantum yields
- ii) Negligible quenching of singlet oxygen by MeSBDP itself was observed in any solvent, allowing its use in a large range of concentrations.

- iii) MeSBDP shows a broad excitation spectral range with two possibilities, either in the UV (350-400 nm) or in the visible (500-600 nm), contrary to phenalenone (300-450 nm) or to Rose Bengal (500-600 nm).
- iv) It exhibits a much higher photostability (> 10 times) with respect to the Rose Bengal, more prone to photobleaching.

4.2.1.2 Iodinated-BODIPY in the red region

As cited previously, typical BODIPY dyes have intense absorption and emission bands in the green part of the electromagnetic spectrum. On the one hand, a rational molecular design is proposed to shift their absorption band into the clinic window (650-850 nm) to increase the penetration of the irradiation inside the tissues (Figure 4.1). Nevertheless, the most common commercial available irradiation sources are center in the 630-670 nm and from 750 nm to NIR, existing a gap around 700 nm. Moreover, the available NIR light sources usually do not achieve the required energy to properly excite PS.^{45,64} On the other hand, their photophysical properties should be also tuned to increase the population of the triplet state in detriment of the emission of the singlet state. In this section, the increase of the intersystem crossing (ISC) to the triplet excited state is obtained by involving heavy atoms in the dye skeleton.

New four BODIPY derivatives with high singlet oxygen generation have been designated to gain the far-red region or covering the Visible spectra with pantochromic action. In this regard, the design of photosensitizers with the capability to efficiently produce singlet oxygen by absorbing white light is of special interest, particularly for dermatological treatment because they could be activated by sunlight.

The molecular design strategy is based on the following modification in the BODIPY skeleton (Figure 4.28):

- i) Incorporation of iodine atoms at 2 and 6 positions (Figure 4.3). These positions have been demonstrated to be the most effective for the population of the triplet states and consequently a high production of singlet oxygen.¹⁷ Indeed, in a previous study was observed that the increase in the number of heavy atoms attached at the BODIPY core does not necessarily increase ¹O₂ production. Indeed, the highest ¹O₂ production was reached when the halogen atoms are attached to the 2 and 6 BODIPY positions whereas extra halogenation at 3 and/or 5 does not produce a significant increase. These results demonstrated the importance of controlling the

position of the halogen substitution for the designing of potential PDT PSs based on BODIPY.⁵⁴

- ii) Although there are several strategies to shift the absorption band into the therapeutic window, such as aza-substituted BODIPY at *meso* position⁶⁵ or the fusion of extra aromatic rings attached to 2,6, positions,^{66,67} in this work π -conjugated systems, particularly, styryl groups were incorporated at 3 and 5 positions.⁶⁸ This approach has already shown a very effective ability to shift the absorption band to the red region in fluorescent BODIPYs.⁶⁹ Moreover, the incorporation of electron donor-groups, *i.e.* methoxy groups or dimethylamino groups in *para* position of phenyl, induced a larger red-shift of the absorption band.⁷⁰⁻⁷²
- iii) Varying the *meso* substitution of the chromophore with electron-withdrawing groups (nitrophenyl) or electron-donating (aminophenyl or methoxy-styryl) in order to study their photophysical effect both in absorption and fluorescence emission and singlet oxygen generation. Moreover, the addition of such polar groups (MeO-, NH₂-, or NO₂-) to the molecular structure, can modify their lipophilicity/hydrophilicity and solubility, which will influence the cell membrane permeability.^{73,74} Indeed, some compounds enter and diffuse into cells, *i.e.* throughout the cytosol or into particular organelles, whereas similar ones not, what reflect the importance of the molecular design of the new dyes, and their testing into cells.⁷⁴

The structures of new photosensitizers synthesized by Dr. M. J. Ortiz *et al* are shown in Figure 4.28. Their photophysical results are displayed and discussed below.

The results of these four iodinated-red-BODIPYs will be compared with those obtained for chlorin e6, a porphyrin-like system, which has been reported as a photodynamic drug, Figure 4.29.^{75,76} Chlorin e6 is a second generation and clinically-used photosensitizer, characterized by high sensitizing efficacy and rapid elimination from the body. Chlorin e6 has intense absorption in the range of 650-680 nm ($\lambda_{\text{abs}} = 664$ nm, $\epsilon = 4.5 \cdot 10^4$ M⁻¹ cm⁻¹), where biological tissues are transparent to a larger extent than in case of porphyrins (610-620 nm). Furthermore, this region match well with the commercially available red light sources for clinical use, mainly centered at 660nm.⁶⁴ Promising clinical benefits have been obtained applying PDT with Chlorin e6 in the treatment of lung, bladder, skin, and head and neck cancers.^{77,78}

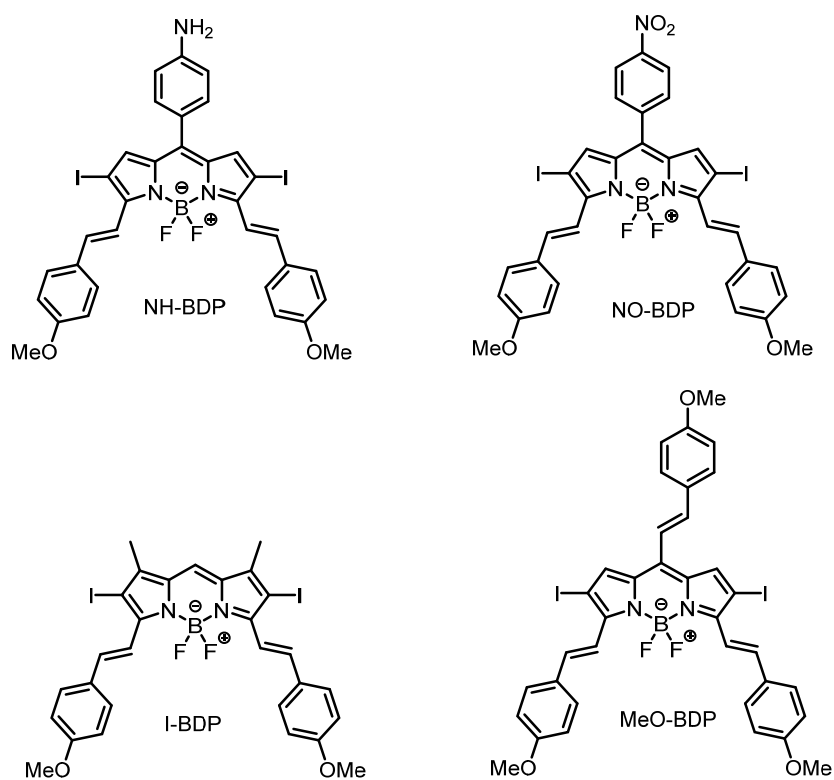


Figure 4.28. New photosensitizers based on 2,6-iodinated-BODIPY with styryl groups at 3 and 5 position and different substitution patterns in *meso*.

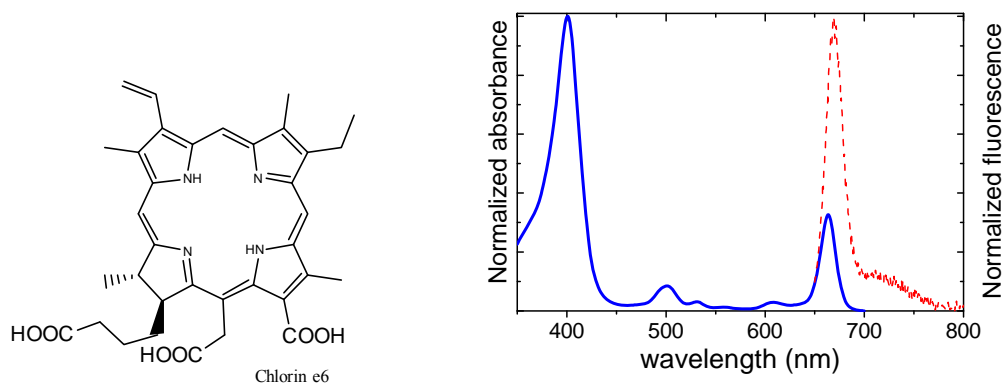


Figure 4.29. Molecular structure of Chlorin e6 (left) and normalized absorption (blue curve) and fluorescence spectra of Chlorin e6 in acetone (right).

i) *Photophysical characterization and discussion*

The photophysical properties of these PSs were carried out only in chloroform, considered an excellent solvent thanks to its high singlet oxygen lifetime (Table 4.8), and it has been demonstrated that the hydrophobic domains of the intracellular environment are alike to the chloroform polarity.⁷⁹ All these results are recorded in Table 4.10 and Figure 4.30.

All the iodinated-BODIPY dyes with styryl groups incorporated into 3 and 5 positions, exhibit intense absorption bands centered into the clinic window (> 650 nm). Particularly, the compound **NO-BDP**, with electro withdrawing group in its *meso* position (p-nitrophenyl) presents an absorption band centered in 705 nm with a high absorption coefficient ($\epsilon = 8.1 \cdot 10^4 \text{ M}^{-1} \text{ cm}^{-1}$). Moreover, this compound shows a good balance between its oxygen production (52%) and its fluorescence quantum yield (22%), which makes it a potential theragnostic system to be implemented in PDT allowing also optical imaging (Table 4.10).

Table 4.10: Photophysical parameters and singlet oxygen quantum yields for iodinated-BODIPY in chloroform; absorption maxima (λ_{ab}), molar absorption coefficient (ϵ_{max}), fluorescence maxima (λ_{fl}), fluorescence quantum yield (Φ_{fl}) and singlet oxygen quantum yield (Φ_{Δ}), different references used in brackets.

Compounds	λ_{abs} nm	ϵ_{max} 10^4 $\text{M}^{-1}\text{cm}^{-1}$	λ_{flu} nm	Φ_{fl}	Φ_{Δ}
NO-BDP	705.0	8.1	762.0	0.22	0.56 (NMB)
NH-BDP	380.0	2.0	701.5	0.30	0.43(MeSBDP)
	509.0	1.4			0.41(MeSBDP)
	677.0	4.1			0.41(MeSBDP)
MeO-BDP	388.0	2.3	780.0	0.02	0.70 (PN)
	535.0	3.1			0.72 (MeSBDP)
	708.0	5.2			0.70 (NMB)
I-BDP	675.0	8.0	699.0	0.46	0.40 (MeSBDP)
Chlorin e6	401.0	13.7	669.5	0.16	0.80 (MeSBDP)
	501.0	1.2			
	664.0	4.5			

Note here that despite the absorption band of **NO-BDP** is placed into the therapeutic window, proper studies cannot be made at this moment, because of the lack of commercial light sources centered at 700 nm (Figure 4.30).⁶⁴

Regarding the homologous compound but with an electron-donor group (*p*-aminophenyl) at *meso* position, **NH-BDP**, shows a less intense absorption band, with a molar extinction coefficient half of the former compound, $\epsilon = 4.1 \cdot 10^4 \text{ M}^{-1} \text{ cm}^{-1}$ at its maximum ($\lambda_{\text{abs}} = 677 \text{ nm}$). However, this compound also shows two more complementary absorption bands, strategically located at UV ($\lambda_{\text{abs}} = 380 \text{ nm}$, $\epsilon = 2.0 \cdot 10^4 \text{ M}^{-1} \text{ cm}^{-1}$) and green region ($\lambda_{\text{abs}} = 509 \text{ nm}$, $\epsilon = 1.4 \cdot 10^4 \text{ M}^{-1} \text{ cm}^{-1}$), offering a potential compound with panchromatic action, able to take advantage of natural irradiation. Indeed, **NH-BDP**, similarly to **NO-BDP**, shows also good balance between its fluorescence efficiency (30%) and its capacity to generate singlet oxygen (40%), features that are independent of the excitation wavelength (Table 4.10).

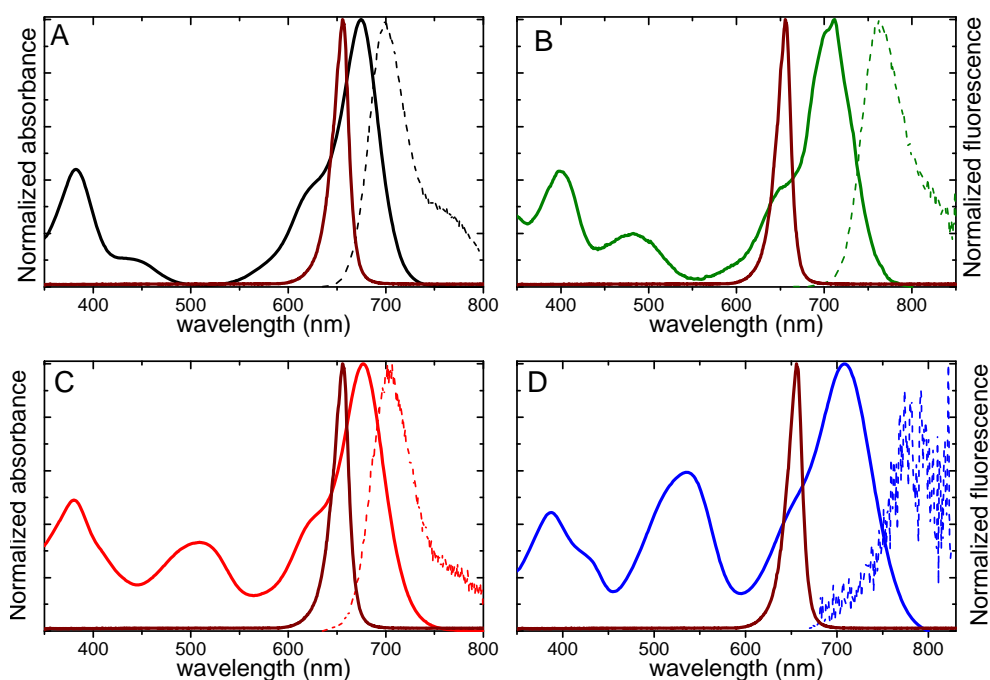


Figure 4.30. The absorption and emission normalized spectra in chloroform for **I-BDP** (A), **NO-BDP** (B), **NH-BDP** (C) and **MeO-BDP** (D). It is included in all the graphs the peak of the deep-red illumination source (brown)

Similarly to **NH-BDP**, the compound **MeO-BDP**, with 3 *p*-methoxystyryl groups in 3, 5 and 8 positions, also offers three main absorption bands centered at UV ($\lambda_{\text{abs}} = 388 \text{ nm}$, $\epsilon = 2.3 \cdot 10^4 \text{ M}^{-1} \text{ cm}^{-1}$), green ($\lambda_{\text{abs}} = 535 \text{ nm}$, $\epsilon = 3.1 \cdot 10^4 \text{ M}^{-1} \text{ cm}^{-1}$) and red ($\lambda_{\text{abs}} = 708 \text{ nm}$, $\epsilon = 5.2 \cdot 10^4 \text{ M}^{-1} \text{ cm}^{-1}$) region of the visible spectra which are slightly more intense than those registered for **NH-BDP**. Although this compound shows the highest singlet oxygen quantum yield of this series of iodinated- BODIPY PSs (70%), independent of the excitation wavelength with practically a null fluorescence (2 %), the irradiation with the available red lights (centered at 630-680 nm) will be not very efficient (Figure 4.30). Finally, compound **I-BDP** despite being the most simple structure, without any substitution at *meso* position, it shows also an intense absorption band in the red region ($\lambda_{\text{abs}} = 675 \text{ nm}$, $\epsilon = 8.0 \cdot 10^4 \text{ M}^{-1} \text{ cm}^{-1}$), together with a good balance of its singlet oxygen quantum yield (40%) and fluorescence quantum yield (46%), offering an additional potential theragnostic agent.

As a general trend, the substitution of electron-donating groups at the *meso* position (**NH-BDP** and **MeO-BDP**) induce a less intense absorption band in the red-region respect to not-substituted *meso* (**I-BDP**) or substituted by electron-withdrawing groups (**NO-BDP**), but at the same time, new bands at UV-blue and green regions are prompted, which could be interesting for PDT-PS under white light irradiation. Indeed, these photosensitizers, **NH-BDP** and **MeO-BDP**, are able to generate singlet oxygen independently of the excitation wavelength (blue, green or red region) giving the opportunity to irradiate the sample in the whole visible spectrum.

On the other hand, the compounds **NO-BDP** and **I-BDP** are interesting PSs for biomedical applications because of their intense absorption ($\epsilon \geq 8.0 \cdot 10^4 \text{ M}^{-1} \text{ cm}^{-1}$) into the therapeutic window ($\lambda_{\text{abs}} \geq 650 \text{ nm}$), both endowed with dual-action (fluorescence + singlet oxygen), promising properties for theranostic applications in biomedicine research. Thus, these four compounds could have interesting properties to be successfully used in photodynamic therapy and, in exception of **MeO-BDP**, also allow imaging. Now, the most relevant results of in vitro experiments in HeLa cells are described and compared with those obtained for Chlorin e6.

ii) In vitro experiments with HeLa cells

The four BODIPY-based photosensitizers and chlorin e6 for comparison were irradiated under deep red (655 nm) light for 30 minutes (doses= 15 J/cm², Figure 4.31-Figure 4.32), and in case of the panchromatic compound **NH-BDP** was also irradiated under white light for 30 minutes (doses = 60 J/cm², Figure 4.33). Moreover, the internalization inside the HeLa cells was studied by fluorescence microscopy for the two fluorescent chromophores **NO-BDP** and **NH-BDP**, Figure 4.34.

According to MMT assays, none of the compounds show any cytotoxic effect under dark conditions, showing a cell viability without irradiation of 100 %. As regards compound **MeO-BDP**, the in vitro experiments reflect a very low phototoxicity action despite having the highest singlet oxygen quantum yield in this series of compounds (Figure 4.31 D). Similarly, the compound **NO-BDP** barely caused damage to the HeLa cells (Figure 4.31 B). Indeed, it is needed a high amount of PS (10 µM) to induce a cellular death of 40 % and 60 % under deep-red irradiation (655 nm at 15 J/cm²) for **NO-BDP** and **MeO-BDP**, respectively. These poor results were primarily attributed to a not good matching between the absorption spectra of **NO-BDP** and **MeO-BDP**, located at 705 nm and 708 nm respectively, Table 4.10, and the standard red-irradiation lights (peak centered at around 660 nm) commercially available for clinical applications.⁶⁴

On the contrast, the absorption bands of compounds **I-BDP** and **NH-BDP**, at 675 nm and 677 nm, Table 4.10, respectively, much near to the peak of the deep-red irradiation light, show a higher photoactivity action even at submicromolar concentrations, *i.e.* a cellular death of 75 % and 90 % were produced at 0.5 µM by **I-BDP** and **NH-BDP**, respectively (Figure 4.31 A & C).

Surprisingly, the compound **NH-BDP** shows a higher sensitizing efficacy than that obtained for **I-BDP**, which kills the 65% of the cell population at 0.1 µM. This result is against the photophysical features previously recorded for these compounds, since for absorption bands being practically centered at the same position, the absorption coefficient of **I-BDP** ($\epsilon = 8.0 \cdot 10^4 \text{ M}^{-1} \text{ cm}^{-1}$), is double with respect to that obtained for **NH-BDP** ($\epsilon = 4.0 \cdot 10^4 \text{ M}^{-1} \text{ cm}^{-1}$), for the same singlet oxygen production ($\phi_{\Delta} \sim 0.40$). The reason should be attributed to a better internalization into the cell by the **NH-BDP** with respect to **I-BDP**.

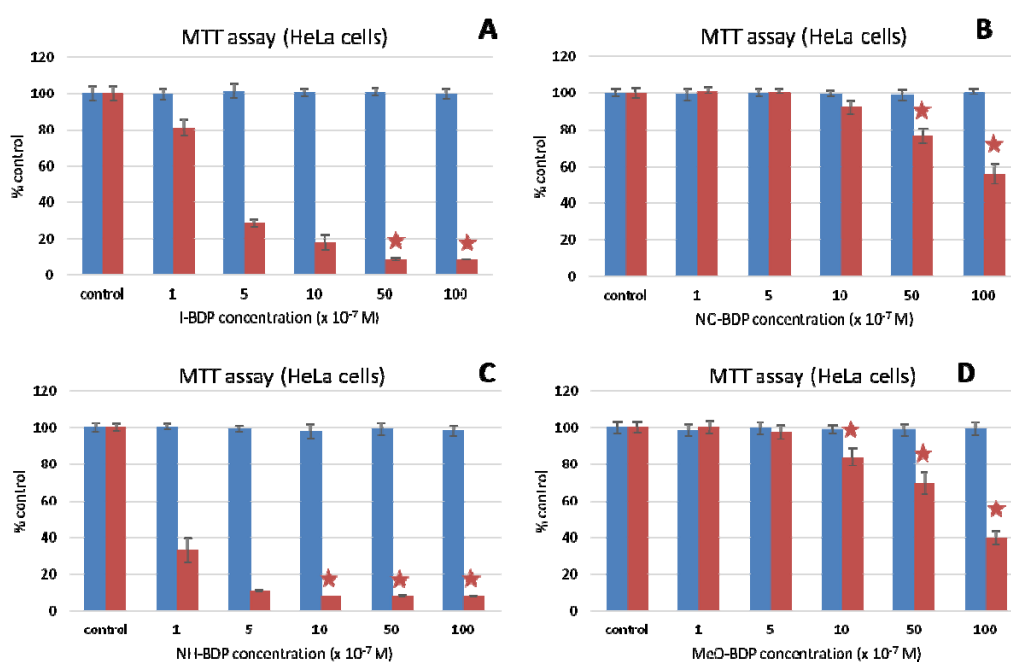


Figure 4.31. MTT results of photosensitizer **I-BDP** (A), **NO-BDP** (B), **NH-BDP** (C) and **MeO-BDP** (D) in dark condition (blue) and after 30 minutes irradiation (red) under deep-red light. *Significant differences with respect to controls according to the Kruskal Wallis test followed by the Dunn's test or Mann-Whitney's test ($p < 0.05$). Statistical analyses were conducted using the statistical package SPSS v.25 (SPSS Inc., IBM Company, Chicago, USA).

Importantly, the photoactivity of these two new iodinated red BODIPYs under irradiation at 655 nm, is much higher than that observed for wide-used commercial PS chlorine e6, Figure 4.32. Although the chlorin e6 shows a higher singlet oxygen production ($\phi_{\Delta} = 0.80$, Table 4.10) and its absorption band ($\lambda_{\max} = 664.0$ nm) also matches well with the red illumination peak (Figure 4.32.B) only shows a relevant photoactivity at 5 and 10 μM . However, at those concentrations, it also causes cytotoxic effects in dark. At lower concentrations, *i.e.* 1 μM , although no cytotoxicity was detected in dark, the phototoxicity action is much lower (cell survival of around 60%) than that of **I-BDP** and **NH-BDP**, which only have left a fraction of cell survival of 20% and 10%, respectively. These results indicate that **I-BDP** and **NH-BDP** could be very promising PSs to be implemented in PDT.

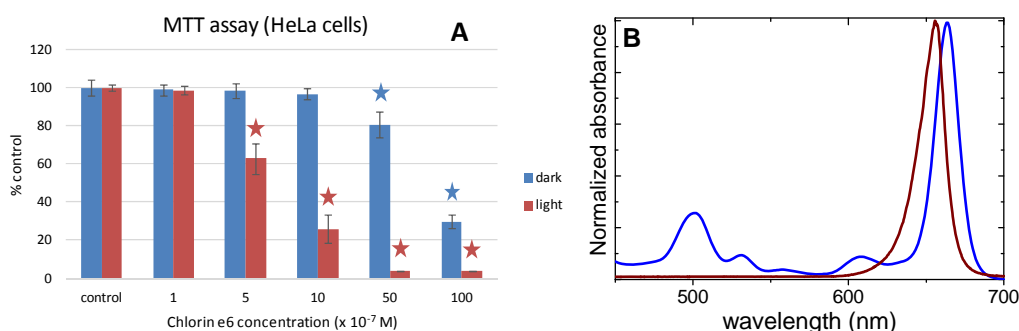


Figure 4.32. (A) MTT assay results of photosensitizer Chlorin e6 in dark condition (blue) and after 30 minutes irradiation (red) under deep-red light and (B) normalized absorption spectra of chlorin e6 (blue) and deep-red light (brown). *Significant differences with respect to controls according to the Kruskal Wallis test followed by the Dunn's test or Mann-Whitney's test ($p < 0.05$). Statistical analyses were conducted using the statistical package SPSS v.25 (SPSS Inc., IBM Company, Chicago, USA).

The phototoxicity effect of compound **NH-BDP** was also studied under white light irradiation, Figure 4.33. MTTs assays indicated a similar cellular death to that found deep-red light (90% at 0.5 μM and 55% at 0.1 μM) despite the light doses are very different (60 J/cm^2 for white light and 15 J/cm^2 for deep-red light). This fact is attributed to the light doses for white light is counted by the intensity of three peaks centered at 455 nm (blue, which corresponds to a doses of 30 J/cm^2 for 30 min of irradiation time), 518 nm (green, 15 J/cm^2 for 30 min) and 630 nm (red, 20 J/cm^2 for 30 min), according to the Table 3.4 in chapter 3. However, the green irradiation is the only peak that fits relatively well with the absorption spectra of the compound **NH-BDP**, while the two other illuminations show only a partial overlapping (see Figure 4.33 B). Indeed, the photoactivity obtained for **NH-BDP** under 30 min or 60 J/cm^2 of white irradiation could be normalized to a green light dose of 15 J/cm^2 , showing also a good photodynamic effect under this illumination source.

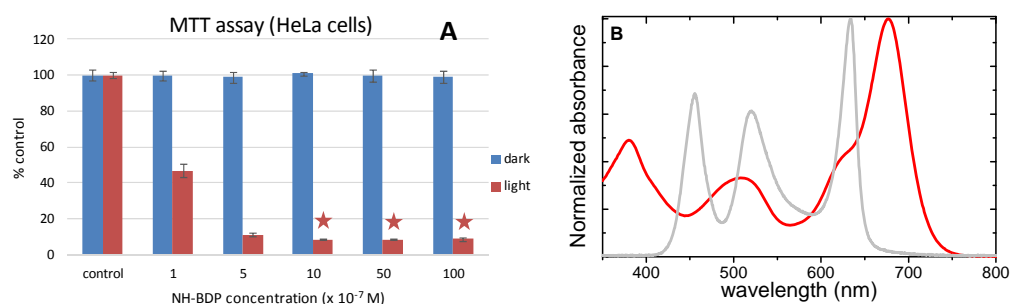


Figure 4.33. (A) MTT results of photosensitizer **NH-BDP** in dark condition (blue) and after 30 minutes irradiation (red) under white light, and (B) normalized absorption spectra of **NH-BDP** (red) and white light (grey). *Significant differences with respect to controls according to the Kruskal Wallis test followed by the Dunn's test or Mann-Whitney's test ($p < 0.05$). Statistical analyses were conducted using the statistical package SPSS v.25 (SPSS Inc., IBM Company, Chicago, USA).

On the other hand, fluorescence microscopy imaging has been performed for **NO-BDP** and **NH-BDP** as it is shown in Figure 4.34. The fluorescence images show significant differences between both PSs. The compound **NO-BDP**, which has demonstrated low phototoxicity, is visualized in an aggregated appearance, forming spicule-shape structures even at low concentration (1 μ M), while **NH-BDP** is homogeneously accumulated inside the cells (with the exception of the nucleus). Therefore, a second and possibly a more important reason for the low phototoxic activity of **NO-BDP** is its poor solubility in the culture media and consequently its low internalization inside the cells. That behavior might be extended to its analog **MEO-BDP**, which also has demonstrated a poor phototoxicity action, but cannot be tested because its practically null fluorescence.

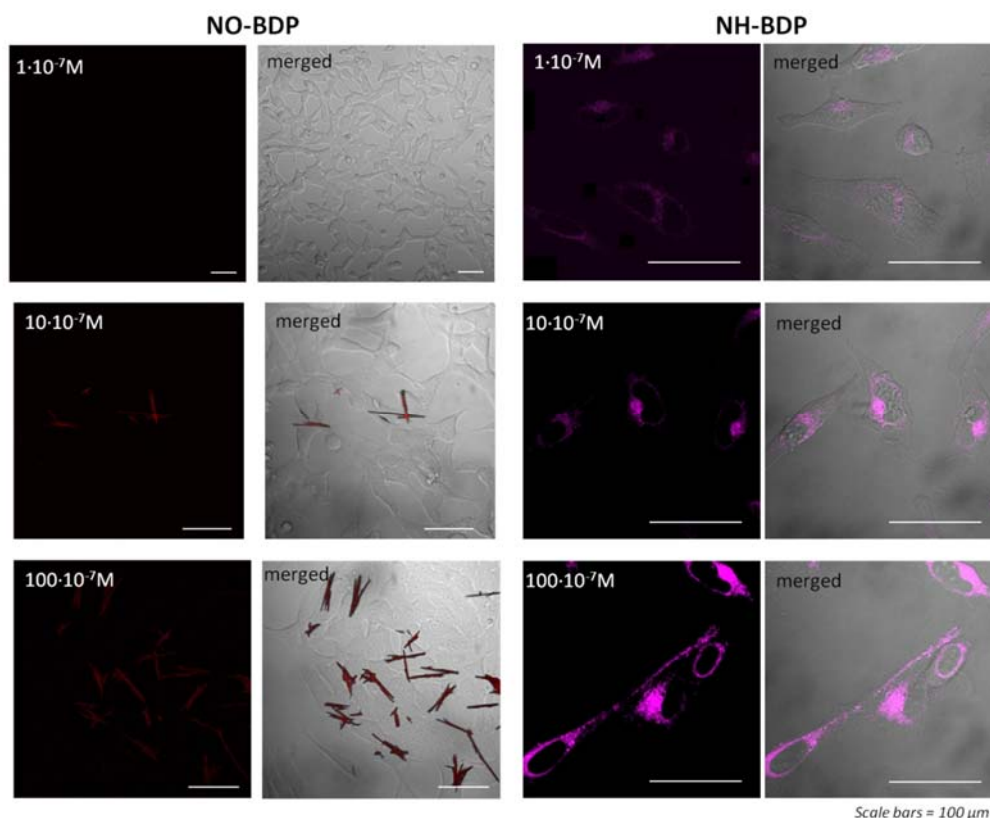


Figure 4.34. Fluorescence microscopy images of compounds **NO-BDP** (left) and **NH-BDP** (right), incubated in HeLa cells at different concentrations ($1 \cdot 10^{-7} \text{M}$, $10 \cdot 10^{-7} \text{M}$ and $100 \cdot 10^{-7} \text{M}$). The scale bars are equal to 100 μm .

iii) Conclusions

Four photosensitizers based on the BODIPY chromophore were strategically designed to fulfill some of the desirable properties in order to use them in photodynamic therapy. All the studied compounds have reached the following requirements; *i*) high singlet oxygen generation, $\geq 40 \%$, as a consequence of the iodine substitution attached to the position 2 and 6 of the BODIPY core, and *ii*) and intense absorption bands in the red region of the electromagnetic spectra ($> 650 \text{ nm}$) by tethering methoxystyryl groups at position 3 and 5 positions, which allows a deeper light penetration in the tissues.

Furthermore, the different *meso* substitution, *i.e.* with electron donor or withdrawing compounds, also modifies the BODIPY photophysical properties. Thus, by varying

the substitution pattern at their meso position, BODIPYS with a suitable balance between fluorescence and singlet oxygen (**NO-BDP** and **I-BDP**), or with panchromatic action (**MeO-BDP**), or even both features, panchromatic compounds with dual activity (**NH-BDP**) are obtained.

In vitro studies in HeLa cells indicates that none of them are cytotoxic under dark condition but they show very different phototoxicity effects following the tendency **NH-BDP** > **I-BDP** > **MeO-BDP** ≥ **NO-BDP**. On the one hand, the incapability of **NO-BDP** and **MeO-BDP** to effectively damage cells can be related to their low efficacy to absorb photons due to the mismatch between their absorption bands and the commercial illumination sources in the red used, but a likely more important reason, probed by confocal imaging for the fluorescent **NO-BDP**, is a poor solubility in culture media impeding the internalization into the cells. Thus, it is expected that enhancing the solubility, *i.e.* via pegylation process which not only provides water solubility but also prolongs its circulation time, reducing renal clearance and enhancing the protection against degradation.

Finally, the compounds **I-BDP** and **NH-BDP** have demonstrated efficient phototoxicities, being able to induce cellular death under red irradiation (655 nm) at low concentrations (even in the submicromolar range). The phototoxic effect is higher than that obtained for the commercial PS chlorine e6, one of the most studied and used photosensitizers in PDT in many countries worldwide until now. Adding, **NH-BDP** not only is an excellent PS under red irradiation but also under white light. Furthermore, both compounds (**I-BDP** and **NH-BDP**) present also a dual activity allowing imaging by optical microscopy.

4.2.2. Halogen-free BODIPY

4.4.2.1 Binol BODIPY

In the former section, some of the iodinated BODIPY derivatives have shown dual activity; fluorescence and singlet oxygen properties. Nonetheless, these two properties are antagonistic to each other, a chromophore with high fluorescence involves low singlet oxygen and *vice versa*, (Figure 2.1 chapter 2). Indeed, combining diagnosis and therapy in a single system is not an easy task but is very advantageous for biomedical

researches. Consequently, both properties need to be properly balanced in the molecular design to reach an efficient theragnostic action.

The most common strategy to synthesize this kind of chromophores is selecting a fluorescent dye (in this case BODIPY) and chemically attaching heavy atoms (as it has done in the previous section). However, the presence of heavy atoms can increase the toxicity of the molecule and diminishing its biocompatibility.⁸⁰ As a consequence, different strategies to generate singlet oxygen were required to design new photosensitizers. Nowadays, it is known that an efficient population of a charge-transfer state (CTS) could pave the way to an effective intersystem crossing (ISC) process and being able to generate singlet oxygen, although the origin of this mechanism is still controversial.⁸¹ Therefore, manipulating the CTSs could allow the developing of new heavy-atom free photosensitizers with fluorescent capability.

In previous studies³⁵ it has been demonstrated that the functionalization of BODIPYs at the boron atoms with BINOL moieties can tune the photonic properties of the BODIPY. Briefly, it is demonstrated that the electron-donor capability of the involved binol moiety switches on a non-emissive intramolecular charge transfer (ICT) state, which restricts the fluorescence efficiency of the dyad. Interestingly, such CT can be efficiently tuned by manipulating the substitution pattern in the BODIPY-BINOL system, particularly by diminishing the electron-donating capability of the BINOL moiety (using bromine as electron-withdrawing substituent at BINOL), or by enhancing the electron-acceptor ability of the BODIPY core (*e.g.*, by diminishing the number of alkyl groups at BODIPY).

Therefore, four accessible and highly fluorescent F-BODIPY precursors were selected (BDP **1-4** in Figure 4.35) and were chemically manipulated to tune their ability to populate CTSs upon excitation. Then, they were photophysically characterized to study their capability to act as fluorescent ROS-PSs.

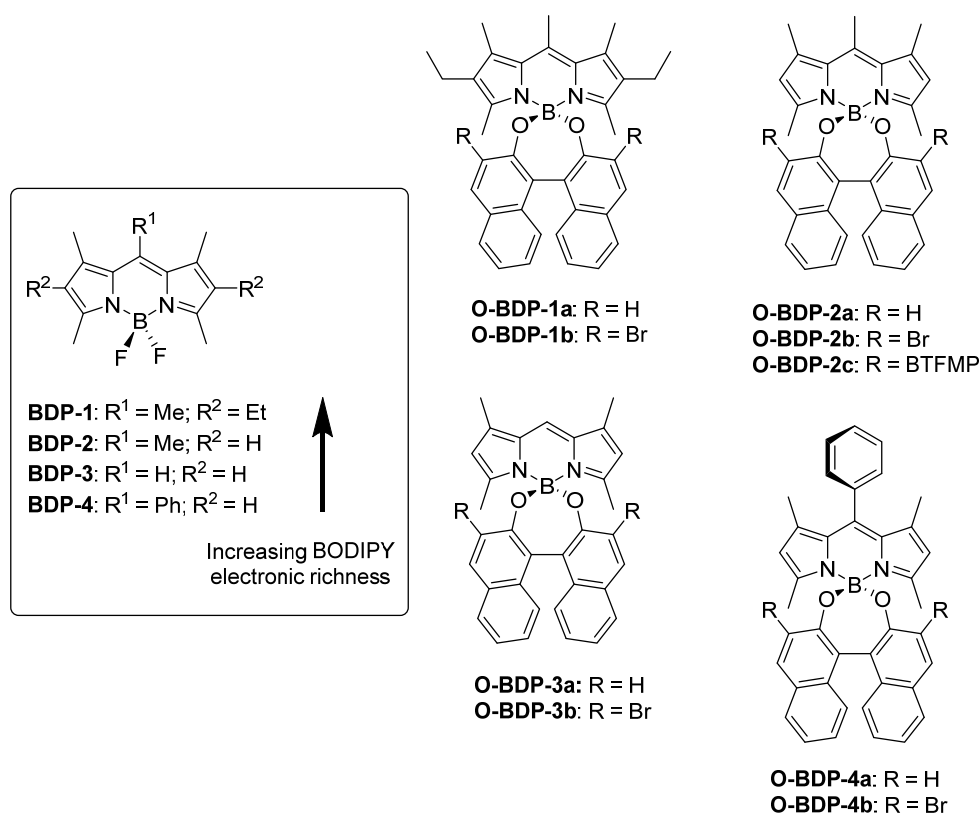


Figure 4.35. BINOL-based O-BODIPYs, as well as parent F-BODIPYs (inset). BTFMP: 3,5-bis(trifluoromethyl)phenyl.

The synthetically route to obtain these new BINOL-based O-BODIPY compounds, consisted on covalently linking the oxygen atoms of a binol (1,1'-binaphth-2-ol) or bromobinol (3,3'-dibromobinol) moiety to the boron atom of BDP-1-4 (substitution of the fluorines by a binol moiety), to generate the corresponding binolated (O-BDP-1a-4a) or 3,3'-dibromobinolated (O-BDP-1b-4b) O-BODIPY dyes (Figure 4.35). This simple chemical transformation was selected due to the known differential ability of BODIPYs BPD-1, O-BDP-1a and O-BDP-1b, previously studied, to undergo charge transfer (CT) upon excitation, Figure 4.35.^{35,82}

These compounds were synthesized by Prof. S. de la Moya *et al* at Universidad Complutense de Madrid, and their photophysical results are detailed below.

i) Photophysical characterization and discussion

The new synthesized compounds O-BDP-**2a-4a** were expected to populate the CTSs with higher probability than their analog bromobinol (O-BDP-**2b-4b**), Figure 4.35. This assumption is based on the higher push-pull character induced by binol group (more electron donor) than bromobinol groups (less electron donor), on the BODIPY chromophore, as it occurred in the couple O-BDP-**1a/1b**, studied previously.³⁵ Accordingly, O-BDP-**1b** should exhibit the lowest probability to populate CTS upon excitation since it is based on electron-poor bromobinol and the electron-richest BODIPY core among the selected ones (note peralkylation injecting electronic density into the BODIPY core of O-BDP-**1b**). Oppositely, O-BDP-**4a**, based on electron-rich binol and the electron-poorest BODIPY core among the selected ones (note the lower degree of BODIPY alkylation joint to the presence of an orthogonal, electron-withdrawing, phenyl group), should exhibit the highest CT probability.

To test the different abilities of new compounds O-BDP-**2-4** to undergo CT, the influence of the solvent polarity in its fluorescence was studied, Table 4.11. Moreover, a completed photophysical characterization is shown in Table 4.12, in chloroform as representative solvent, together with the singlet oxygen generation in this solvent (Φ_{Δ}).

Table 4.11. Fluorescence quantum yield (Φ_f) of BDP-**2/4** and O-BDP-**2/4** in different solvents; cyclohexane, chloroform, acetone and acetonitrile.

solvent	2	2a	2b	2c	3	3a	3b	4	4a	4b
c-hex	0.91	0.05	0.69	0.70	0.99	0.02	0.51	0.41	0.01	0.22
CHCl ₃	0.90	0.06	0.62	0.43	0.90	0.11	0.27	0.60	0.01	0.16
Acetone	0.84	0.02	0.30	0.07	0.72	0.02	0.05	0.44	0.01	0.03
ACN	0.83	0.02	0.10	0.02	0.81	0.02	0.02	0.47	0.01	0.01

As occurred when transforming parent BDP-1 in their derivatives O-BDP-1a and 1b,³⁵ the high fluorescence efficiency of parent BDP-2 and parent BDP-3 (around 90 % in chloroform) was deeply affected upon the substitution of their fluorine atoms by a binol or bromobinol moiety (Table 4.11). A similar effect was found in the derivative of BDP-4 although its fluorescence is lower (60%).

However, the extension of this quenching is not the same for all these chromophores. Thus, the loss of fluorescence efficiency with respect to the corresponding parent *F*-BODIPYs is significantly less pronounced in O-BDP-1b-4b, (bromobinol is less electron-rich), than in binol based O-BDP-1a-4a, see Table 4.12. Besides, this fluorescence loss follows the tendency $1 < 2 < 3 < 4$, both for the binol series and the respective bromobinol series, agreeing with the expected probability of undergoing CT.

These results support that the fluorescence quenching CT is significantly working in the selected *O*-BODIPYs and the fluorescence efficiency can be finely modulated in these new compounds manipulating the push-pull character adding binol or bromobinol groups to different BODIPY core. Then, as it was predicted O-BDP-2b with the lowest probability to undergo CT, presented the less decrease in fluorescence quantum yield (Table 4.11). In contrast, for O-BDP-4a the highest probability to populate CT is expected, undergoing a great diminishing of fluorescence (until 1 % for O-BDP-4a Table 4.11). Nonetheless, most of the BINOL-BODIPY derivatives (series O-BDP-a) show a quantum yield almost null in every solvent (Table 4.12). In order to explain this behavior computational simulations were done (Figure 4.36).

The simulations revealed that a photoinduced electron transfer (PET) is taken place, being responsible for the non-radiative deactivation in these derivatives, Figure 4.36. Thus, the conducted computations (DFT wB97XD/LanL2DZ; see experimental chapter 3, section 3.2.2.7 for details) demonstrate that the electronic transitions occur from its HOMO-1 to its LUMO, being these orbitals mainly located at the BODIPY core, Figure 4.36. The calculations also show that upon such electronic transitions a PET from the HOMO (mainly located at the binol) to the generated low-lying semi-vacant HOMO-1 is thermodynamically feasible. This PET explains the dramatic loss of fluorescence observed for the series O-BDP-a in all the studied solvents, Table 4.11. Therefore, the enabled PET competes with the probability of undergoing CT and fluorescence emission.

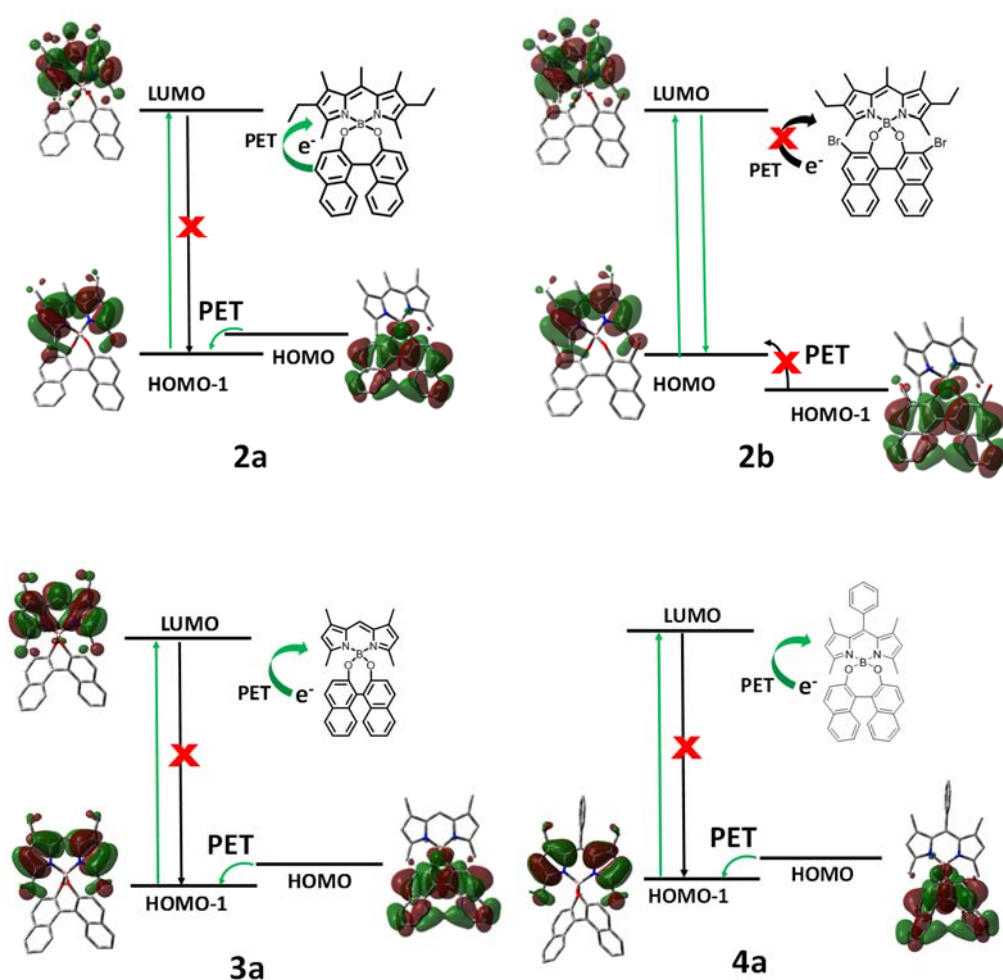


Figure 4.36. Computed differential photonic behavior of O-BDP-**2a** and **2b** (top) **3a** and **4a** (bottom) Reductive PET, turning off the expected CT due to binol-BODIPY push-pull, is feasible in binol derivative (**2a**, **3a** and **4a**) but not in their respective bromobinol **2b** as an example

Nonetheless, in the case of bromobinol O-BDP-**b** series, a process PET is not possible (see example O-BDP-**2b** in Figure 4.36). That is because the visible light absorption computed for this compound O-BDP-**2b** implies an electron promotion from HOMO to LUMO, being these orbitals localized at the BODIPY core Figure 4.31, and the gap between the low-lying HOMO-1 and the HOMO is not thermodynamically feasible at room temperature (the energy gap is very high: 150 meV, Figure 4.36). Therefore, the expected CT is not turned off by PET and it is also

confirmed by the fluorescence dependency on those bromobinol-BDPs with the polarity of the solvent, Table 4.11.

Regarding the singlet oxygen production, the *F*-BODIPY chromophores did not show $^1\text{O}_2$ photogeneration (Φ_{Δ} is null in chloroform, Table 4.12), as it is expected. Additionally, when these compounds were binolated, only the O-BDP-**1a** was able to generate singlet oxygen, because in the rest of the compounds (O-BDP-**2a-4a**) the PET process is the main deactivation path. Therefore, with the aim of searching for theranostic agents PET phenomenon should be avoided.

However, the introduction of bromines in the binol structure (O-BDP-**1b-4b**), enhances the $^1\text{O}_2$ photoproduction by increasing the CT probability, at least in chloroform. This generation must not only be ascribed to a possible direct $\text{S}_1 \rightarrow \text{T}_1$ ISC promoted by heavy atom effect, but also to the additional key participation of a properly stabilized CTS as intermediate to achieve the ISC, ascribed to the electronic effect exerted by the bromine atoms on the push-pull character of the involved BODIPY-BINOL dyad. Actually, these compounds present a significant difference in the production of singlet oxygen despite involving the same number of bromine atoms in their respective structures. For instance, O-BDP-**2b** and O-BDP-**4b** show six-fold higher singlet oxygen production under the same experimental conditions than that for O-BDP-**1b** in chloroform (Table 4.12).

The results presented support the idea of how the CT probability can modulate the triplet population, and its usefulness for designing theranostic agents with fluorescence and singlet oxygen capability; for example the compound O-BDP-**2b** show a suitable balance between its fluorescence and singlet oxygen ability in chloroform ($\Phi_{\text{f}}=0.62$ and $\Phi_{\Delta}=0.32$, Table 4.12).

To support the possibility of the design of heavy-atom-free agents based on by the modulation of their CT probability, and to give more evidence of how CTS is able to populate triplet state, heavy-atom-free O-BDP-**2c** was synthesized, Figure 4.35. In this case, the binol is 3,3'-disubstituted with 3,5-bis(trifluoromethyl)phenyl (BTFMP) groups, which should have a halfway behavior between O-BDP-**2a** (non-substituted binol) and O-BDP-**2b** (bromobinol), due to their electron-withdrawing capacity ($\text{H} < \text{BTFMP} < \text{Br}$). This hypothesis was confirmed after experimental measurements, Table 4.11-12, offering O-BDP-**2c** an intermediate behavior with a fluorescence quantum yield of 43 % and a singlet oxygen quantum yield 7 % in chloroform.

Table 4.12. Photophysical parameters and singlet oxygen quantum yields for O-BDP in chloroform; absorption maxima (λ_{ab}), molar absorption coefficient (ϵ_{max}), fluorescence maxima (λ_{fl}), fluorescence quantum yield (Φ_{fl}), fluorescence lifetime (τ_{fl}), singlet oxygen quantum yield (Φ_{Δ}) and as if it suffers PET phenomenon.

Compound	λ_{ab} (nm)	ϵ_{max} 10^{-4} ($M^{-1} cm^{-1}$)	λ_{fl} (nm)	Φ_{fl}	τ_{fl} (ns)	Φ_{Δ}	PET
BDP-1	523.0	8.3	539.0	0.89	6.15	0.00	NO
O-BDP-1a	525.0	6.0	550.0	0.47	5.84	0.05	NO
O-BDP-1b	527.0	7.4	547.0	0.69	6.56	0.11	NO
BDP-2	499.0	8.4	511.5	0.90	5.63	0.00	NO
O-BDP-2a	501.0	4.1	533.0	0.06	1.19 (11%) 3.58 (89%)	0.00	YES
O-BDP-2b	503.0	6.6	527.5	0.62	4.26	0.32	NO
O-BDP-2c	501.0	7.3	518.0	0.43	3.22	0.07	NO
BDP-3	509.0	7.3	514.0	0.90	5.48	0.00	NO
O-BDP-3a	510.0	6.4	515.0	0.11	5.00	0.04	YES
O-BDP-3b	512.0	7.9	519.0	0.27	1.61 (96%) 4.39 (4%)	0.20	NO
BDP-4	503.0	8.3	513.5	0.60	3.57	0.00	NO
O-BDP-4a	504.0	6.0	513.5	0.01	<0.15(62%) 3.08 (38%)	0.00	YES
O-BDP-4b	507.0	7.2	519.0	0.16	1.05 (97%) 2.67 (3%)	0.32	NO

Finally, in order to characterize the promoted triplet states, dyes with $\Phi_{\Delta} > 5\%$ (O-BDP-**2b**, **2c**, **3b**, and **4b**) were studied by nanosecond transient spectroscopy, Figure 4.37. The recorded spectra were similar for all the studied compounds and comparable to those previously registered for BODIPYs enabling efficient triplet state

population.^{18,58,83} According to previous investigations, the positive band at around 400-450 nm is attributed to the absorption of the T_1 state. The intense and negative contribution in the 500-550 nm range corresponds to the ground state bleaching (GSB) associated with the $S_0 \rightarrow S_1$ transition. Finally, the weak and broad contribution at >550 nm is also attributed to triplet absorption.⁸⁴

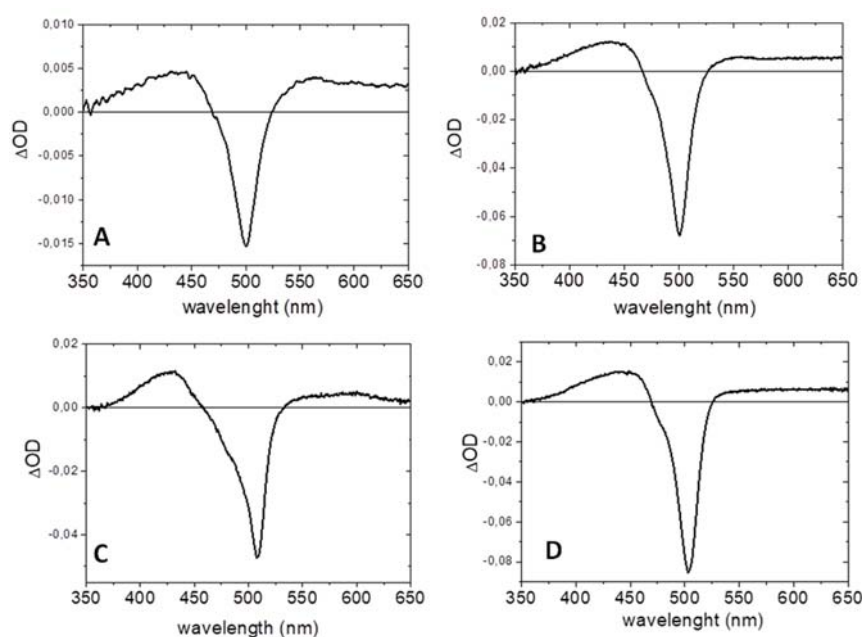


Figure 4.37. ns-TAS of O-BDP-2b (A), O-BDP-2c (B), O-BDP-3b (C) and O-BDP-4b (D) in deaerated chloroform

The assignment of the absorption of triplet states is also confirmed by its fast quenching by oxygen (see the temporal evolution of the 440 nm triplet bands in Figure 4.38). Indeed, triplet lifetimes in deaerated solution, τ_{T_0} , are found to be higher than 100 μs , long enough for an efficient quenching by oxygen, which drastically changes to hundreds of nanoseconds in air-saturated samples (Table 4.13). Besides, all the $P_{O_2}^T$ fractions are almost unity (Table 4.13), indicating that most of the generated triplets are efficiently quenched by molecular oxygen. Moreover, the found k_{q,O_2}^T values at room temperature stand into the $0.8 \cdot 10^9 - 1.0 \cdot 10^9 \text{ M}^{-1} \text{ s}^{-1}$ interval, which are in the range of the 1/9 diffusion constant in chloroform ($k_{diff} = 12 \cdot 10^9 \text{ M}^{-1} \text{ s}^{-1}$).

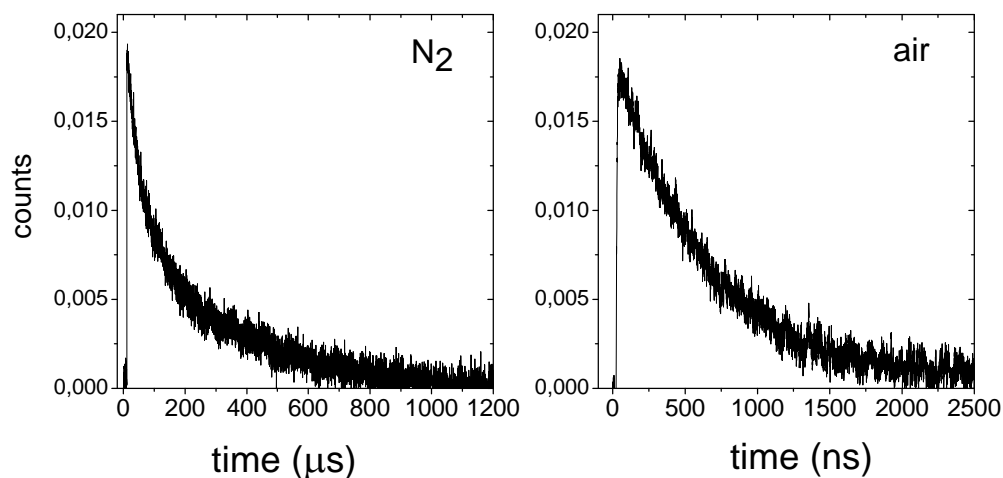


Figure 4.38. Decay curve of transient triplet band of O-BDP-4b under nitrogen and air-saturated CHCl_3 , recorded at 440 nm upon excitation of 507 nm.

Table 4.13. Triplet lifetime in nitrogen- and air-saturated samples ($\tau_{\text{N}_2}^T$ and τ_{air}^T , respectively), the fraction of triplet excited states quenched by O_2 ($P_{\text{O}_2}^T$) and the second-order rate constants of the bimolecular quenching k_{q,O_2}^T of the triplet by O_2 . For the calculation of $P_{\text{O}_2}^T$ and k_{q,O_2}^T , see section 2.2.5.1. in chapter 2

BODIPY	$\tau_{\text{N}_2}^T$ (μs)	τ_{air}^T (μs)	$P_{\text{O}_2}^T$	k_{q,O_2}^T ($10^9 \text{M}^{-1} \text{s}^{-1}$)
O-BDP-1b	168	0.462	0.997	0.96
O-BDP-2b	238	0.430	0.998	1.02
O-BDP-2c	116	0.535	0.995	0.78
O-BDP-3b	114	0.483	0.996	0.74
O-BDP-4b	101	0.612	0.994	0.88

Remarkably for PDT application, all the studied dyes showed a relatively long triplet lifetimes in the absence of oxygen ($\tau_{\text{N}_2}^T > 100 \mu\text{s}$), being these values significantly longer than those exhibited by previous heavy-atom-functionalized BODIPYs.^{18,83} This reason is that heavy atoms usually lead to efficient $\text{S}_1 \rightarrow \text{T}_1$ but also

to a fast $T_1 \rightarrow S_0$ ISC, showing relatively short-lived triplet states, which limits their use in PDT.

ii) *In vitro* experiments in HeLa cells

After the promising photophysical results obtained, the compound with a better balance between its fluorescence efficiency and singlet oxygen production, O-BDP-**2b** was tested *in vitro* in HeLa cells. In this experiment, the internalization and subcellular localizations were studied, together with its MTT assay, Figure 4.39 and Figure 4.40. The sample was irradiated under green light for 40 minutes (20 J/cm^2).

The MTT assay for compound O-BDP-**2b** displays almost null cytotoxicity under dark conditions while it is able to induce a cellular death under green irradiation, killing 60% of the HeLa cells at $1 \mu\text{M}$ and more than the 80% at $5 \mu\text{M}$ (Figure 4.39). It shows a good capability to be internalized inside the HeLa cells even at low concentrations ($0.1 \mu\text{M}$) being widespread in the cytoplasm of the cells with the exception of the nucleus (Figure 4.40).

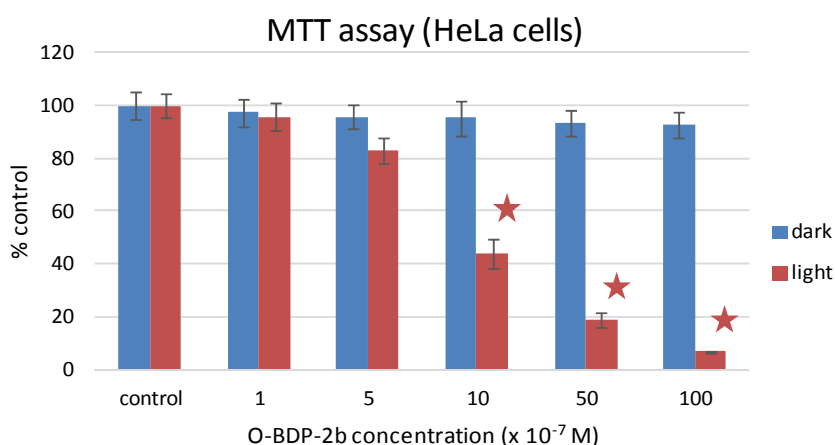


Figure 4.39. MTT result of O-BDP-**2b** incubated a different concentration under green irradiation. *Significant differences with respect to controls according to the Kruskal Wallis test followed by the Dunn's test or Mann-Whitney's test ($p < 0.05$). Statistical analyses were conducted using the statistical package SPSS v.25 (SPSS Inc., IBM Company, Chicago, USA).

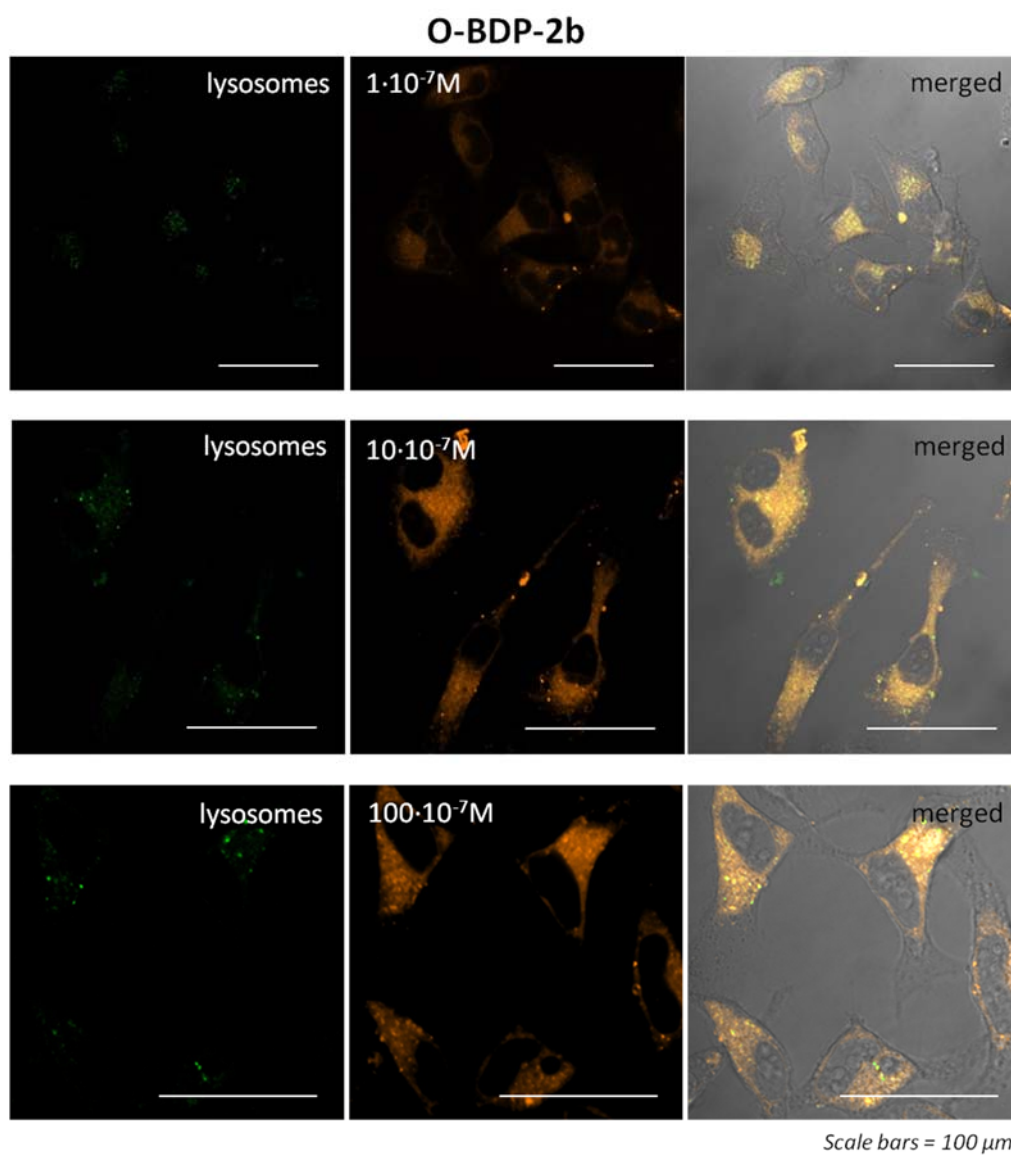


Figure 4.40. Fluorescence microscopy images of O-BDP-2b, incubated in HeLa cells at different concentrations ($1 \cdot 10^{-7} \text{ M}$, $10 \cdot 10^{-7} \text{ M}$ and $100 \cdot 10^{-7} \text{ M}$), together with lysosome tracker (left). The scale bars are equal to $100 \mu\text{m}$.

iii) Conclusions

This approach demonstrates the usefulness of manipulating CTSs to balance fluorescence vs. singlet-oxygen production in organic chromophores. This can be easily done by chemically tuning the probability of undergoing CT upon the excitation, and constitutes a valuable tool to take into account when developing triplet PSs from bright fluorophores, without heavy atoms. This presents a great advantage because reduces the inherent toxicity of halogen-photosensitizers, offering also higher triplet lifetimes which increase their performance in PDT applications. Besides, this strategy could be easily extended to other organic chromophores, by using different CT-tuning approaches. This fact opens up new perspectives for the rapid development of smarter, less toxic and more efficient, PDT agents, as well as new triplet PSs for demanded applications beyond ROS production. Furthermore, as supports the *in vitro* assays these molecules show an excellent capability to stain cells at low concentrations and induce cellular death only under irradiation.

4.4.2.1 Enamine-BODIPY derivatives

As demonstrated in the previous section, inducing charge-transfer character could be useful to enhance the singlet oxygen generation in purely organic photosensitizers, avoiding the use of heavy atoms. In this section, different halogen-free BODIPYs based on the incorporation of an electron-donor group, but in this case at their *meso* position, with the aim of inducing CTS, and consequently singlet oxygen production. Generally speaking, the presence of any substitution at the *meso* position of the BODIPY usually causes a great impact on its photophysics. Actually, the *meso* position is considered as the most sensitive one to substituent effects due to the marked change of the electronic density upon excitation (Figure 4.41). For instance, the substitutions of electron-donor groups usually cause a blue shift of the absorption maximum,^{14,85} while electron-withdrawing groups cause red-shift.⁸⁶

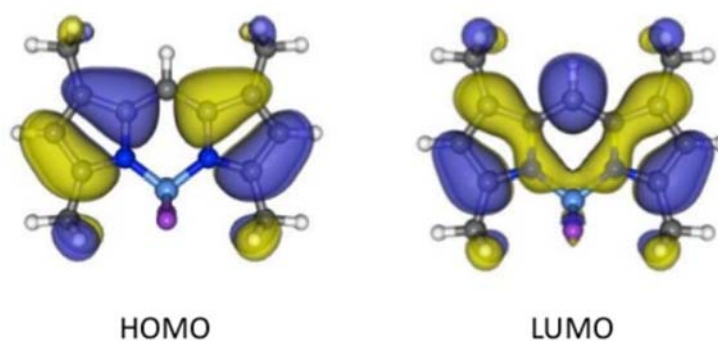


Figure 4.41. Computationally explained on the basis of the differential stabilization of the frontiers orbitals involved in the electronic transition (HOMO and LUMO) of BODIPYs.

Note here that the effect from electron-donor substituents is larger than that of electron-acceptors^{87–89} and affects photophysical properties to a higher extent. Indeed, very recently, different heavy-atom free BODIPYs have been proposed as potential photosensitizers by doping the *meso* position with electron-donating groups,^{47,90–93} while electron-withdrawing groups do not mediate excited triplet state formation.⁹⁴ The design of those halogen-free PSs was based on the covalent *meso*-aryl derivatives (phenyl, naphthyl, anthryl, or pyrenyl with different substituted groups) as electron donors to effectively induce the formation of the excited triplet state and singlet oxygen (Figure 4.42).

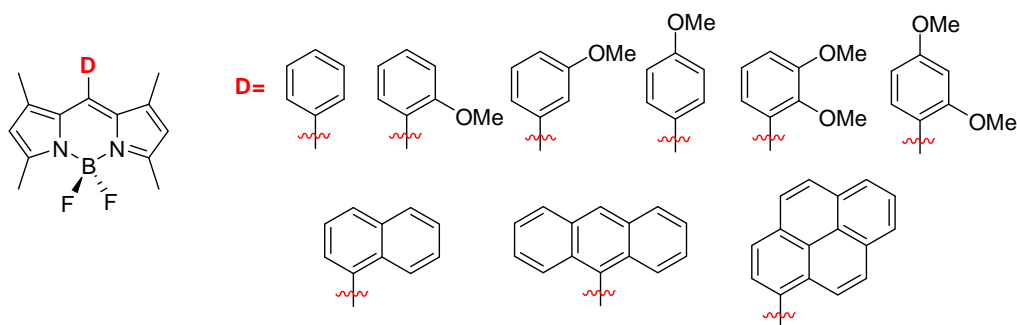


Figure 4.42. Some examples of BODIPY with donor-groups at *meso* position, structures were taken from pigments *Dyes and Pigments* 164 (2019) 139–147, and from *Chem. Asian J.* 2017, 12, 2447–2456; Red line indicates the linking position to BODIPY pigments.^{93,95}

In this line, the control of Vilsmeier-Haack reaction in BODIPYs has opened a selective generation of *meso*-enamines BODIPYs, showing a new family of structurally-simple and easily-accessible compounds with push-pull character.⁹⁶ Now in this section, the photophysical properties and the capability to generate singlet oxygen of a series of *meso*-enamine-BODIPYs (previously synthesized in ref⁹⁶ and new ones, see Figure 4.43) are described.

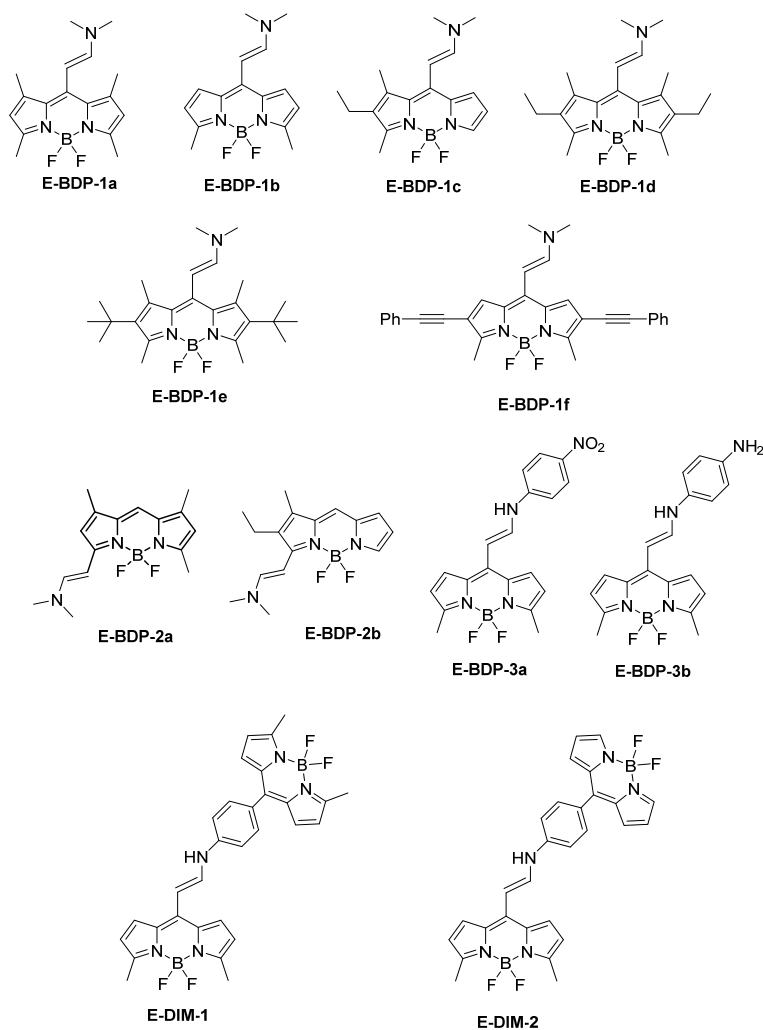


Figure 4.43. Molecular structures of the different Enamine-BODIPY derivatives

Firstly, the photophysical effects induced by different locations of the enamine substitution (at α - and *meso*- positions) on the BODIPY core are studied (E-BDP-**1a** vs E-BDP-**2a** and E-BDP-**1c** vs E-BDP-**2b** in Figure 4.43). Then, several *meso*-enamines-BODIPYs with different alkylated BODIPY parents are proposed (E-BDP-**1a-1e**, Figure 4.43) to test their capacity to modulate the ICT character. Moreover, the dimethylamino-based enamine group is further derivate with an electron-acceptor or electron-donating groups (*i.e.* incorporation of *p*-nitro aniline and *p*-amino aniline, compounds E-BDP-**3a** and E-BDP-**3b** in Figure 4.43, respectively) to check if any of these changes induce a positive effect on the generation of singlet oxygen. The best compound of the above series in terms of singlet oxygen quantum production was then chemically modified to extend its π -conjugation by adding ethynyl phenyl groups at 2, 6 positions with the aim of red-shifting the absorption band (E-BDP-**1f** in Figure 4.43). Finally, two non-orthogonal dimers derived from the monomer E-BDP-**3b** and varying the alkylation pattern of the second BODIPY monomer unit (E-DIM-**1-2**, Figure 4.43), were synthesized and photophysically described.

These compounds were synthesized and provided by Dr. M.J Ortiz *et al* at the Universidad Complutense de Madrid.

i) Photophysical characterization

The photophysical characterization and the singlet oxygen production were carried out in chloroform. For the most representative enamine-BODIPYs were also studied in toluene. Adding, theoretical simulations are performed in some compounds in order to support the experimental results.

Firstly, the highest differences regarding their photophysical features are found based on the enamine-BODIPYs substituted in *meso* or in 3 positions, Figure 4.44 and Table 4.14 (E-BDP-**1a** and E-BDP-**1c** vs E-BDP-**2a** and E-BDP-**2b**). As expected, the substitution in *meso* does not produce a bathochromic shift, as occurs when the enamine is tethered at C3 due to increasing the resonance conjugation, but hypsochromic shift (Figure 4.44, Table 4.14). It brings an important difference in the location of their respective spectroscopic bands (absorption and fluorescence) of around 80 nm and 60 nm for E-BDP-**1a** vs E-BDP-**2a** and BDP-**1c** vs E-BDP-**2b**, respectively. This hypsochromic effect is typically found when electron donor groups are anchored in *meso* position, especially for amine groups, assigned to the generation

of a new resonance form, hemicyanine-like, characterized by shorter delocalization system that competes with the typical cyanine form of BODIPY.^{16,97}

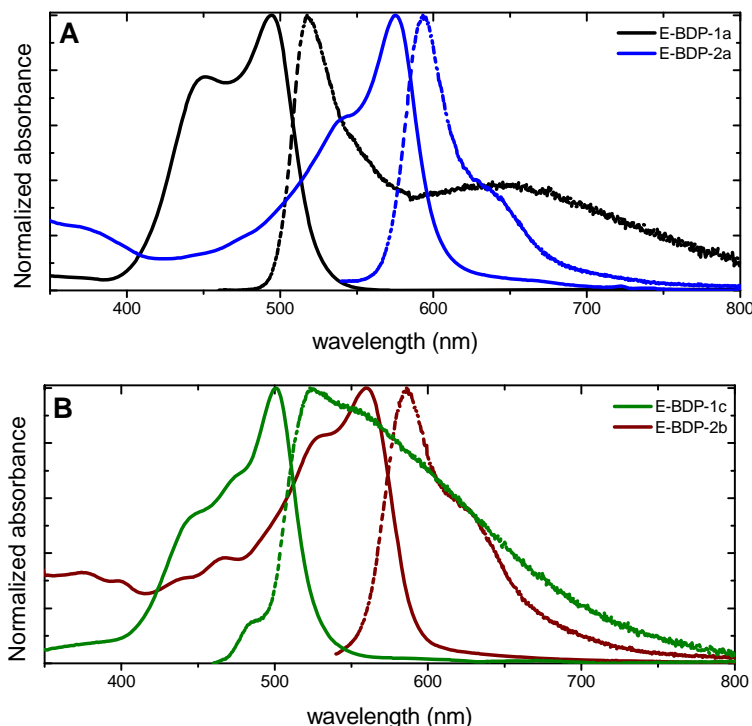


Figure 4.44. Normalized absorption and emission spectra in chloroform for E-BDP-1a (black) vs E-BDP-2a (blue) (A) and E-BDP-1c (green) vs E-BDP-2b (brown) (B).

Apart from the different shifts found in the absorption and emission bands, the position of the enamine in the BODIPY core has also a great influence on the fluorescence efficiency of these compounds. Indeed, the enamine at *meso* position induces a drastic fluorescence emission quenching (fluorescence efficiency tends to 0 % and shortens their lifetimes, Table 4.14). In this regard, the presence of the *meso*-enamine moiety enhances different non-radiative deactivation pathways. On the one hand, the internal conversion probability is increased due to the theoretically predicted loss of planarity of the BODIPY in the excited state.^{98–101} On the other hand, the strong electron-donating character of the enamine group at the more sensitive *meso* position activates an ICT state switching off the S_1 emission.^{96,102} For that reason, the *meso*-enamine-BODIPYs E-BDP-1a, and E-BDP-1c show a practically null emission ($\Phi_f \leq$

0.02) with respect to their homologous compounds with enamine groups at C3, E-BDP-2a and E-BDP-2b demonstrating a relatively high efficient fluorescence ($\Phi_{\text{fl}} \geq 0.60$, Table 4.14). Note here that although the compounds E-BDP-2a and E-BDP-2b cannot be promising PSs because of emission capacity, they could be used as fluorescence probes in bioimaging.

Table 4.14. Photophysical properties and singlet oxygen quantum yield in chloroform for E-BDP compounds; absorption maxima (λ_{ab}), molar absorption coefficient (ϵ_{max}), fluorescence maxima (λ_{fl}), fluorescence quantum yield (Φ_{fl}), fluorescence lifetime (τ_{fl}) and singlet oxygen quantum yield (Φ_{Δ}).

Compound	λ_{ab} (nm)	ϵ_{max} 10 ⁻⁴ (M ⁻¹ cm ⁻¹)	λ_{fl} (nm)	Φ_{fl}	τ_{fl} (ns)	Φ_{Δ}
E-BDP-1a	494.0	5.7	517.5	<0.01	-	0.04
E-BDP-1b	496.0	6.6	529.0	0.04	0.92 (97%) 5.29 (3%)	0.20
E-BDP-1c	501.0	5.6	523.0	0.02	0.51 (49%) 5.32 (51%)	0.10
E-BDP-1d	464.0	3.3	543.0	<0.01	-	0
E-BDP-1e	469.0	2.5	547.5	<0.01	-	0
E-BDP-2a	575.0	4.3	593.0	0.60	0.69 (10%) 4.04 (90%)	-
E-BDP-2b	560.0	2.8	586.0	0.64	4.02	0.07
E-BDP-3a	511.0	2.8	526.0	0.05	5.61	0.21
E-BDP-3b	523.0	4.4	585.0	0.04	0.89 (98%) 1.15 (2%)	0.20
E-BDP-1f	551.0	5.7	599.0	0.42	3.23	0.31

Besides, the alkylation degree in the BODIPY skeleton has a big impact on the photophysical properties of *meso*-enamine-BODIPYs derivatives. The absorption spectra usually present two bands, as a result of the contribution of two resonance forms denote as iminium and enamine, located at high and low energies, respectively, Figure 4.45.⁹⁶ The intensity of each band depends on how much each resonance form is favored. In this regard, a higher alkylation of the BODIPY favors the iminium resonance form respect to the enamine one. For instance, the characteristic absorption band assigned to the enamine form is predominant in the compound E-BDP-1b, in which the iminium contribution appears as a shoulder in this absorption spectrum. The alkylation at positions 1 and 7, as well as at 2 and 6, enhance the resonant interaction

between the *meso*-enamine unit and the BODIPY core enhancing the contribution of an iminium-like mesomeric form (see absorption spectra of E-BDP-**1a**, E-BDP-**1d**, E-BDP-**1e** in Figure 4.45A).^{96,103} Moreover, the presence of the iminium form in the absorption band is more prominent for branched alkyls substituents (*tert*-butyl at β -positions in E-BDP-**1e**) than in linear ones (ethyl at β -positions in E-BDP-**1b**), owing to a higher donor hyperconjugative effect.

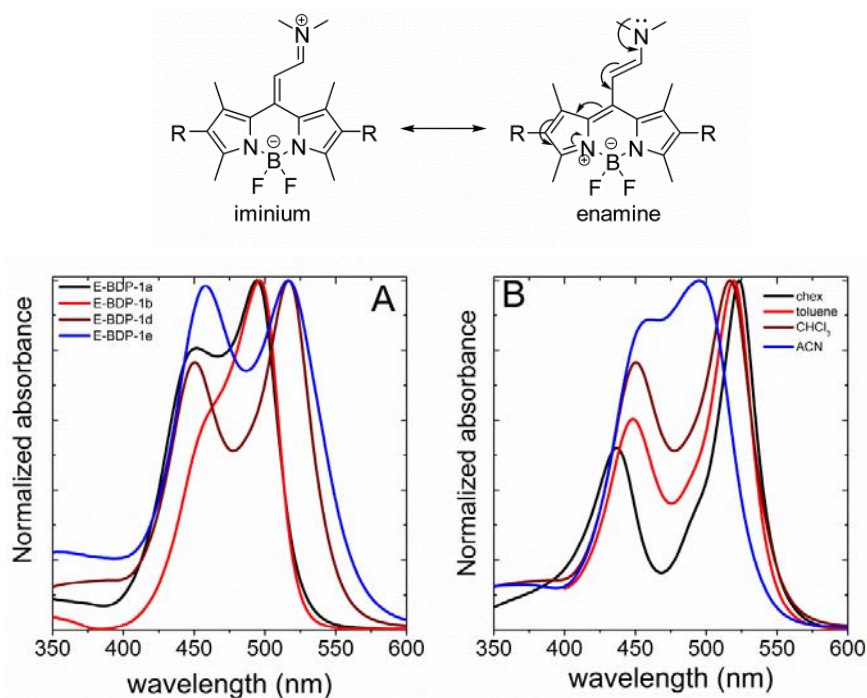


Figure 4.45. (top) An example of iminium and enamine –like structures; (bottom) Normalized absorption spectra of E-BDP-**1a**, -**1b** -**1d** and **1e** in chloroform (A) and Normalized absorption spectra for E-BDP-**1d** in different solvents: cyclohexane (black), toluene (red), chloroform (brown) and acetonitrile (blue) (B).

Note here, such delocalization has a higher push-pull nature owing to the electronic coupling of the amine with the chromophoric pyrrole through the *meso*-position. Moreover, the iminium mesomeric form presents the highest charge separation and it should be more stabilized in polar solvents, as it was tested for compound E-BDP-**1d** in solvents of different polarities (Figure 4.45.B). Decreasing the polarity of the solvent, acetonitrile > chloroform > toluene > cyclohexane, the contribution of the iminium peak in the absorption spectrum is gradually reduced and as consequence, the

absorption spectra result in two clearly distinct bands in apolar solvents (Figure 4.45.B). Note that the polarity of the media not only influences the contribution of two absorption bands but also their position; the iminium band (at low wavelengths) suffers a bathochromic shift as polarity increased, characteristic of a more polar species, while the enamine band (at high wavelengths) suffers the typical hypsochromic shift for BODIPY dyes.

The electron coupling of the *meso*-enamine with the BODIPY is computationally demonstrated by calculating the Hhelpg charges in the enamines E-BDP-1a, E-BDP-1b, E-BDP-1c, E-BDP-1d, E-BDP-1e, and E-BDP-1f. The simulations indicate that the negative charge of the nitrogen of the enamine decreases with alkylation of the BODIPY (Figure 4.46, compounds E-BDP-1a, E-BDP-1d, E-BDP-1e and E-BDP-1f), supporting the greater contribution of the iminium resonant form. In particular, the iminium form is mainly favored by the simultaneous alkylation at positions 1,7 as indicated by the lower negative charge calculated in the nitrogen of the enamine group for E-BDP-1a, E-BDP-1d, and E-BDP-1e with respect to E-BDP-1b, E-BDP-1c and E-BDP-1f, compounds without alkylation in these two positions (Figure 4.46).⁹⁶

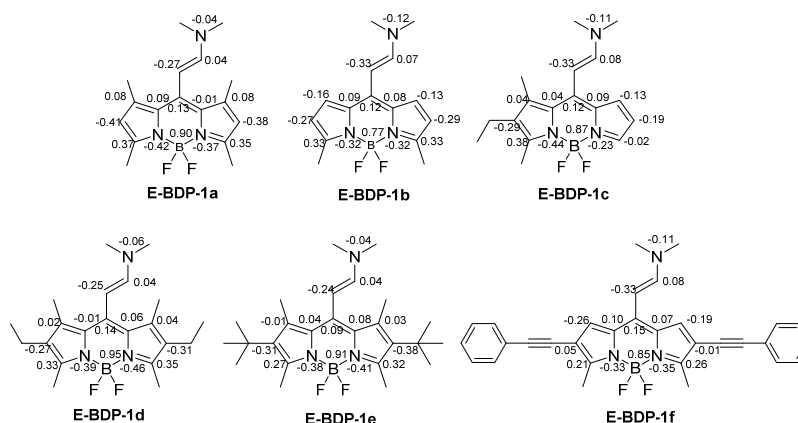


Figure 4.46. Influence of the alkylation degree in the CHelpg charge distribution at the ground state of E-BDP-1a-1f.⁹⁶

The presence of the iminium form also influences the fluorescence efficiency and more significantly the singlet oxygen generation. The compounds E-BDP-1a, -1d, and -1e, in which the iminium contribution is more important, leaving a smaller negative

charge in the nitrogen atom as computational calculation has previously demonstrated, Figure 4.46, shows a nearly null emission and singlet oxygen production (Table 4.14). Thus, the less alkylated *meso*-enamine BODIPYs, E-BDP-**1b**, shows the highest singlet oxygen quantum yield in this library of *meso*-enamine-BODIPYs, of 20% and a fluorescence efficiency of 4% (Table 4.14). In this line, the compound E-BDP-**1c**, with an extra methyl in position 1 respect to E-BDP-**1b**, displays a fluorescence and singlet oxygen quantum yields half of those recorded for E-BDP-**1b**. However, the compounds E-BDP-**3a** and -**3b**, despite the presence of electron donor or electron acceptor group (*p*-nitro aniline and *p*-amino aniline, respectively) in the enamine show a similar fluorescence and singlet oxygen quantum yields as their *meso*-enamine-BODIPY parent, E-BDP-**1b** (Table 4.14). Thus, the modification of the electron-donating ability of the enamine group does not induce any effect either on the singlet oxygen production or on the fluorescence ability.

Being E-BDP-**1b** the best compound of the above series in terms of singlet oxygen quantum production and fluorescence efficiency, a more π -conjugated *meso*-enamine BODIPY, E-BDP-**1f**, was proposed, by adding ethynyl phenyl groups at 2 and 6 positions with the aim of red-shifting the absorption band. In fact, a notable shift is reached in its respective absorption and emission bands, together with a good balance between fluorescence and singlet oxygen quantum yields ($\Phi_{\text{fl}} = 0.40$ and $\Phi_{\Delta} = 0.31$, Table 4.14). This compound could be considered as a dual purely organic agent with a promising used in theragnostic applications (bioimaging + PDT), lacking the inherent toxicity of heavy atoms in its structure.

The above results suggest that the stabilization of the iminium form, with a higher ICT character in these *meso*-enamine-BODIPYs derivatives, *i.e.* by the alkylation of the BODIPY core, hampers the formation of excited triplet states and the fluorescence radiative route, being internal conversion the main non-radiative deactivation pathway. Particularly, the methylation of position 1 and 7 C, play a critical role in this deactivation process. Moreover, the ability to generate singlet oxygen in *meso*-enamine-BODIPYs is strongly connected with their intrinsic ICT character and accordingly should be also modulated by the solvent polarity. Thus, an additional study on the photophysical properties and the singlet oxygen generation in different solvents was performed for the most interesting *meso*-enamine BODIPYs, E-BDP-**1b** and E-BDP-**1f** (Table 4.15). The fluorescence quantum yield and also the singlet oxygen quantum yield increase as the polarity of the solvent decrease with respect to chloroform (*i.e.* toluene) while the opposite behavior is recorded for more polar

solvent (acetonitrile and methanol). This result indicates that the formation of a more stabilized ICT states in polar solvents reduces the radiative deactivation of the singlet excited state as well as the singlet to triplet hopping, attaining lower emission and singlet oxygen production in polar solvents, demonstrating that the ability to generate singlet oxygen and being fluorescent is strongly connected with their intrinsic ICT character in these *meso*-eaminine-BODIPYs.

Table 4.15. Photophysical properties and singlet oxygen quantum yield in different solvents for E-BDP-1b and -1f; absorption maxima (λ_{ab}), molar absorption coefficient (ϵ_{max}), fluorescence maxima (λ_{fl}), fluorescence quantum yield (Φ_{fl}), fluorescence lifetime (τ_{fl}) and singlet oxygen quantum yield (Φ_{Δ}).

Sample	Solvent	λ_{ab} (nm)	ϵ_{max} 10^4 ($M^{-1}cm^{-1}$)	λ_{fl} (nm)	Φ_{fl}	τ_{fl} (ns)	Φ_{Δ}
E-BDP-1b	Toluene	498.0	5.2	535.5	0.22	1.83(87%) 2.94(13%)	0.37
	CHCl ₃	496.0	6.6	529.0	0.04	0.92(97%) 5.29 (3%)	0.20
	ACN ⁹⁶	487.0	5.0	506.0	<0.01	-	-
	MeOH ⁹⁶	489.0	5.6	507.5	<0.01	-	-
E-BDP-1f	Toluene	551.0	5.9	601.0	0.46	3.29	0.38
	CHCl ₃	551.0	5.7	599.0	0.42	3.23	0.31
	ACN ⁹⁶	533.0	5.6	551.0	0.04	0.43	-
	MeOH ⁹⁶	535.5	6.4	553.5	0.03	0.41	-

Finally, two dimers derived from the E-BDP-2b molecular unit, in a not orthogonal disposition, with different alkylation pattern in the other BODIPY monomer, E-DIM-1 and -2, were designed in order to enhance their molar absorption coefficient. Their photophysical properties in toluene and chloroform are recorded in Table 4.16.

Attractively, both dimers present a higher molar absorption coefficient ($\epsilon \geq 10 \cdot 10^4 M^{-1} cm^{-1}$) respect to their relative BODIPY monomers, Table 4.16, Figure 4.47. Regarding their fluorescence, they exhibit emission from the excited S₁ state and/or the characteristic broad and red-shift band of ICT state, depending on the alkylation of the second monomer unit and the solvent polarity.

Table 4.16. Photophysical properties and singlet oxygen quantum yield in different solvents for E-DIM-1 and -2; absorption maxima (λ_{ab}), molar absorption coefficient (ϵ_{max}), fluorescence maxima (λ_{fl}), fluorescence quantum yield (Φ_{fl}), fluorescence lifetime (τ_{fl}) and singlet oxygen quantum yield (Φ_{Δ}).

Sample	Solvent	λ_{ab} (nm)	ϵ_{max} 10^4 ($M^{-1} cm^{-1}$)	λ_{fl} (nm)	Φ_{flu}	τ_{fl} (ns)	Φ_{Δ}
E-DIM-1	toluene	514.0	11.2	524.0	0.21	2.08 (67%) 4.88 (33%)	0.26
	CHCl ₃	514.0	10.9	525.0 582.0	0.12	1.66 (90%) 4.97 (10%)	0.33
E-DIM-2	toluene	505.0	9.8	579.0 585.0	0.15	0.62 (83%) 4.09 (17%)	0.33
	CHCl ₃	504.0	10.1	621.0	0.08	0.85 (99%) 4.7 (1%)	0.22

Indeed, E-DIM-1 shows the common emission of the S_1 state centered at 524 nm in toluene but in a more polar solvent, chloroform, two discernible bands, at 525.0 nm and 582.0 nm, assigned to the emission of S_1 and ICT, respectively, are detected. The appearance of the ICT emission is accompanied by a reduction of the fluorescence quantum yield from 21% in toluene to 12% in chloroform (Table 4.16). Nevertheless, this diminution of fluorescence leads to an increase in singlet oxygen generation from 26% to 33%.

However, E-DIM-2, without any methylation in the second BODIPY unit, the emission spectrum in toluene already shows two emission bands, centered at 530 nm and 581 nm, likewise assigned to S_1 and ICT transition, and a singlet oxygen quantum yield identical to that registered for the former dimer in chloroform (Table 4.16). However, a further increase in the polarity of the solvent for E-DIM-2 is detrimental to both emission efficiency and singlet oxygen production as a consequence of its higher inherent ICT character. Indeed, the exclusively broad red-shifted ICT emission band registered in chloroform confirmed this assumption.

The experimental behavior found for these two dimers (E-DIM-1 and E-DIM-2) represents another example of the modulation of the ICT character and therefore the emission and the singlet oxygen production by playing with the different substitution on the BODIPY skeleton, *i.e.* by changing the alkylation, or by changing the polarity of the media.

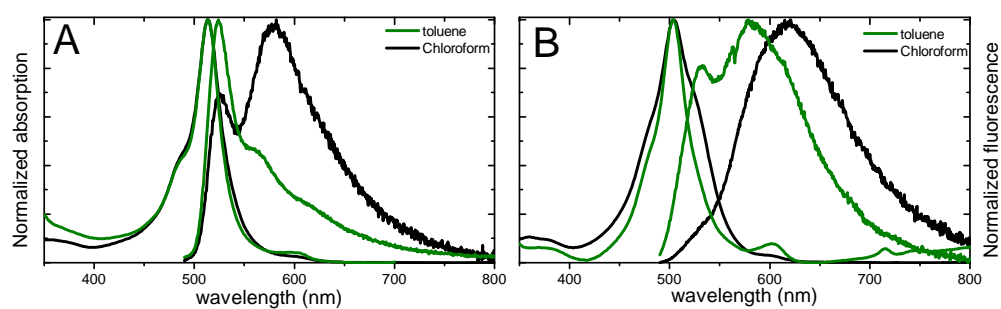


Figure 4.47. Normalized absorption and emission spectra in chloroform (black) and toluene (green) for the compounds E-DIM-1 (A) and E-DIM-2 (B).

ii) *In vitro* experiments in HeLa cells

Compounds E-BDP-1b, E-BDP-1f and E-BDP-2b are selected as the three more representative enamine-BODIPYs to be tested *in vitro* in HeLa cells. They were irradiated under green light at 10.3 J/cm^2 , the results are shown below in Figure 4.48 and 4.49.

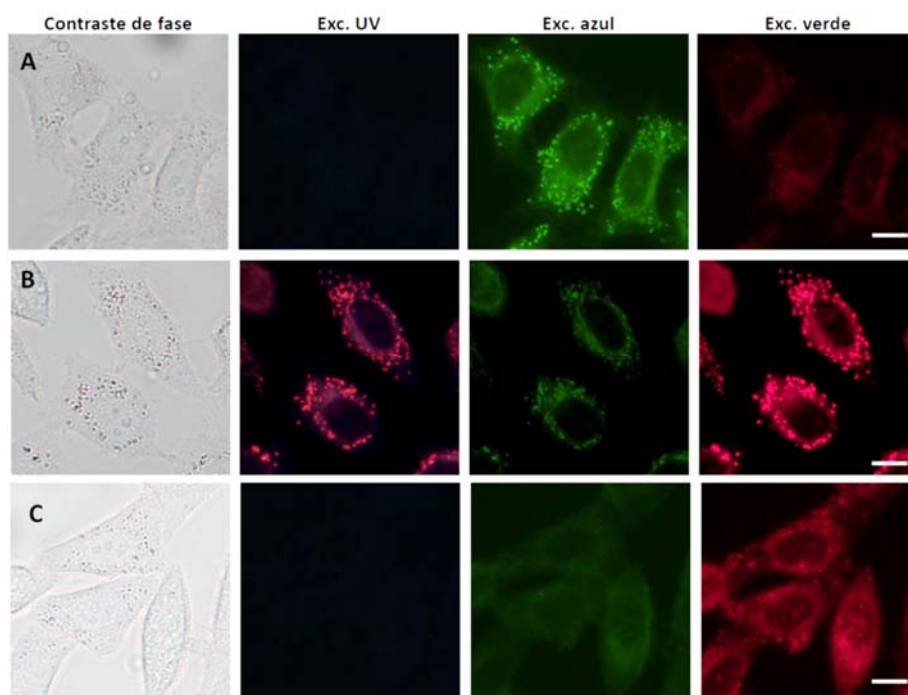


Figure 4.48. Fluorescence microscopy images of HeLa cells incubated with E-BDP-1a (A), E-BDP-1f (B) and E-BDP-2b (C). The scale bar is equal to 10 μm.

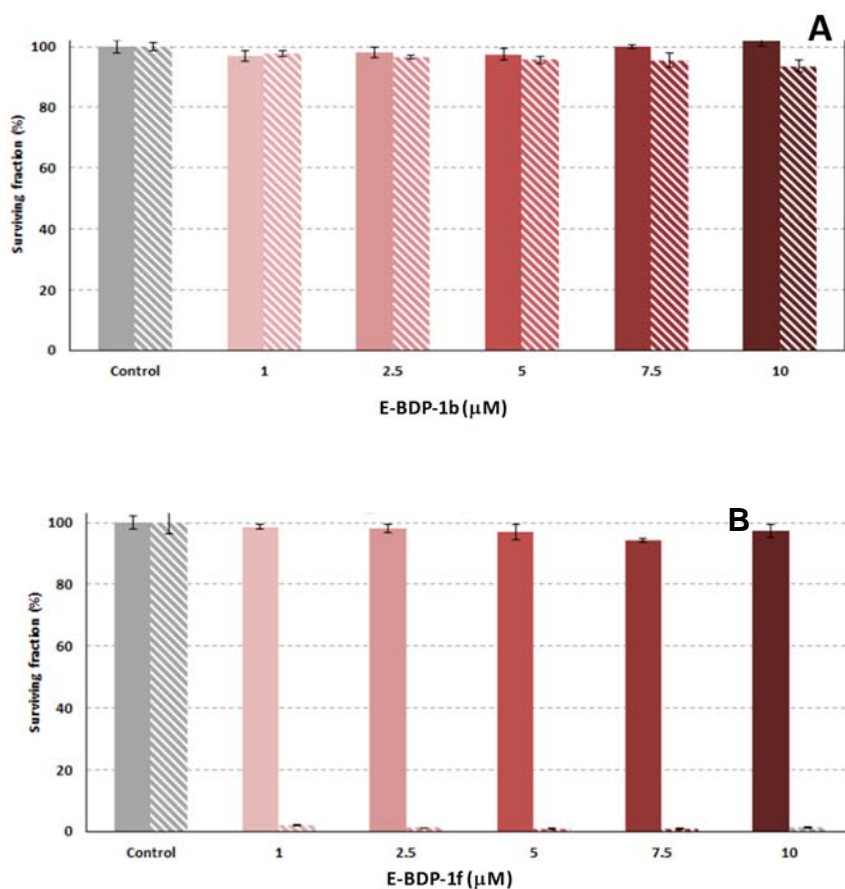


Figure 4.49. MTT assay results of E-BDP-1b (A) and E-BDP-1f (B) under green irradiation (10 J/cm²).

The *in vitro* experiments confirm that the three compounds are able to internalize inside the HeLa cells. However, only the E-BDP-1f is specifically accumulated into lipid droplets, Figure 4.48. Regarding their phototoxicity action, neither E-BDP-1b nor E-BDP-2b is capable to damage the HeLa cells even though increasing the incubated concentrations at $1 \cdot 10^{-5}$ M. The inability of E-BDP-1b to kill cells, despite its singlet oxygen quantum yield of 0.20 in chloroform, might be attributed to the small overlap between the green irradiation source ($\lambda \approx 520$ nm) and its absorption band ($\lambda = 485$ nm). Conversely, due to the low singlet oxygen generation of compound E-BDP-2b, it was not expected a great ability to damage cells, but a better

sharpness of the fluorescence image was expected, which was not the case. On the other hand, compound E-BDP-1f allows nice fluorescence imaging together with great phototoxicity, inducing a cellular death under green irradiation at low light doses (10 J/cm²) and low concentration (100% at 1 · 10⁻⁶ M), Figure 4.49.

iii) Conclusions

Meso-Enamine BODIPYs are a new family of structurally-simple and easily-accessible BODIPYs with the capability to act as halogen-free ¹O₂ photosensitizers for PDT or even for theragnosis based on PDT + fluorescence. On the other hand, both dual opposite properties, singlet oxygen production and fluorescence efficiency can be finely modulated by easy chemical modification affecting the inherent ICT character of the involved BODIPY chromophore. In fact, the methylation of positions 1 and 7 favors the iminium mesomeric form with higher ICT character and is detrimental to both fluorescence and singlet oxygen. The rational design of a *meso*-enamine BODIPY without alkylation at 1 and 7, but with extended conjugation at C2 and C6, has demonstrated its viability as biomarker of lipid droplets and photosensitizer in HeLa cells being very photoefficient under low green doses and low concentration. Moreover, the design of two different BODIPY dimers has improves the molar absorption coefficient maintaining a good balance between their fluorescence and singlet oxygen quantum yields, opening the door for advanced halogen-free new PDT-PSs.

4.3 Bibliography

1. Chaturvedi, V. K., Singh, A., Singh, V. K. & Singh, M. P. Cancer Nanotechnology: A New Revolution for Cancer Diagnosis and Therapy. *Curr. Drug Metab.* **20**, 416–429 (2018).
2. Eftekhari, A., Hasanzadeh, M., Sharifi, S., Dizaj, S. M., Khalilov, R. & Ahmadian, E. Bioassay of saliva proteins: The best alternative for conventional methods in non-invasive diagnosis of cancer. *Int. J. Biol. Macromol.* **124**, 1246–1255 (2019).
3. Robertson, T., Bunel, F. & Roberts, M. Fluorescein Derivatives in Intravital Fluorescence Imaging. *Cells* **2**, 591–606 (2013).
4. Singh, K., Rotaru, A. M. & Beharry, A. A. Fluorescent Chemosensors as Future Tools for Cancer Biology. *ACS Chem. Biol.* **13**, 1785–1798 (2018).
5. Zhu, S., Tian, R., Antaris, A. L., Chen, X. & Dai, H. Near-Infrared-II Molecular Dyes for Cancer Imaging and Surgery. *Adv. Mater.* **31**, 1–25 (2019).
6. Lacombe, S. & Pigot, T. Materials for selective photo-oxygenation vs. photocatalysis: Preparation, properties and applications in environmental and health fields. *Catal. Sci. Technol.* **6**, 1571–1592 (2016).
7. Bui, H. T., Mai, D. K., Kim, B., Choi, K.-H., Park, B. J., Kim, H.-J. & Cho, S. Effect of Substituents on the Photophysical Properties and Bioimaging Application of BODIPY Derivatives with Triphenylamine Substituents. *J. Phys. Chem. B* **123**, 5601–5607 (2019).
8. DeRosa, M. Photosensitized singlet oxygen and its applications. *Coord. Chem. Rev.* **233–234**, 351–371 (2002).
9. Treibs, Alfred, Kreuzer, F.-H. Diflourboryl-Komplexe von Di- und Tripyrrylmethene. *Justus Liebigs Ann Chem* (1968).
10. Prieto-Montero, R., Sola-Llano, R., Montero, R., Longarte, A., Arbeloa, T., López-Arbeloa, I., Martínez-Martínez, V. & Lacombe, S. Methylthio BODIPY as a standard triplet photosensitizer for singlet oxygen production: a photophysical study. *Phys. Chem. Chem. Phys.* **21**, 20403–20414 (2019).
11. López Arbeloa, F., Bañuelos, J., Martínez, V., Arbeloa, T. & López Arbeloa, I. Structural, photophysical and lasing properties of pyrromethene dyes. *Int. Rev. Phys. Chem.* **24**, 339–374 (2005).
12. Prieto, J. B., Arbeloa, F. L., Martínez, V. M., López, T. A. & Arbeloa, I. L. Photophysical properties of the pyrromethene 597 dye: Solvent effect. *J. Phys. Chem. A* **108**, 5503–5508 (2004).
13. Lakowicz, J. R. & Masters, B. R. *Principles of Fluorescence Spectroscopy, Third Edition. Journal of Biomedical Optics* (2008). doi:10.1117/1.2904580.

14. Bañuelos, J., Martín, V., Gómez-Durán, C. F. A., Córdoba, I. J. A., Peña-Cabrera, E., García-Moreno, I., Costela, Á., Pérez-Ojeda, M. E., Arbeloa, T. & Arbeloa, Í. L. New 8-Amino-BODIPY derivatives: Surpassing laser dyes at blue-edge wavelengths. *Chem. - A Eur. J.* **17**, 7261–7270 (2011).
15. Bañuelos Prieto, J., López Arbeloa, F., Martínez Martínez, V., Arbeloa López, T., Amat-Guerri, F., Liras, M. & López Arbeloa, I. Photophysical properties of a new 8-phenyl analogue of the laser dye PM567 in different solvents: Internal conversion mechanisms. *Chem. Phys. Lett.* **385**, 29–35 (2004).
16. Esnal, I., Valois-Escamilla, I., Gómez-Durán, C. F. A., Urías-Benavides, A., Betancourt-Mendiola, M. L., López-Arbeloa, I., Bañuelos, J., García-Moreno, I., Costela, A. & Peña-Cabrera, E. Blue-to-orange color-tunable laser emission from tailored boron-dipyrrromethene dyes. *ChemPhysChem* **14**, 4134–4142 (2013).
17. Epelde-Elezcano, N., Martínez-Martínez, V., Peña-Cabrera, E., Gómez-Durán, C. F. A., Arbeloa, I. L. & Lacombe, S. Modulation of singlet oxygen generation in halogenated BODIPY dyes by substitution at their *meso* position: towards a solvent-independent standard in the vis region. *RSC Adv.* **6**, 41991–41998 (2016).
18. Kamkaew, A., Lim, S. H., Lee, H. B., Kiew, L. V., Chung, L. Y. & Burgess, K. BODIPY dyes in photodynamic therapy. *Chem. Soc. Rev.* **42**, 77–88 (2013).
19. Loudet, A. & Burgess, K. BODIPY dyes and their derivatives: Syntheses and spectroscopic properties. *Chem. Rev.* **107**, 4891–4932 (2007).
20. Bessette, A. & Hanan, G. S. Design, synthesis and photophysical studies of dipyrromethene-based materials: Insights into their applications in organic photovoltaic devices. *Chem. Soc. Rev.* **43**, 3342–3405 (2014).
21. Bañuelos, J. BODIPY Dye, the Most Versatile Fluorophore Ever? *Chem. Rec.* **16**, 335–348 (2016).
22. Bergström, F., Mikhalyov, I., Hägglöf, P., Wortmann, R., Ny, T. & Johansson, L. B. . Dimers of dipyrrometheneboron difluoride (BODIPY) with light spectroscopic applications in chemistry and biology. *J. Am. Chem. Soc.* **124**, 196–204 (2002).
23. Jameson, L. P., Smith, N. W., Annunziata, O. & Dzyuba, S. V. Interaction of BODIPY dyes with bovine serum albumin: A case study on the aggregation of a click-BODIPY dye. *Phys. Chem. Chem. Phys.* **18**, 14182–14185 (2016).
24. Kowada, T., Kikuta, J., Kubo, A., Ishii, M., Maeda, H., Mizukami, S. & Kikuchi, K. In vivo fluorescence imaging of bone-resorbing osteoclasts. *J. Am. Chem. Soc.* **133**, 17772–17776 (2011).
25. Niu, S. L., Massif, C., Ulrich, G., Ziessel, R., Renard, P. Y. & Romieu, A.

- Water-solubilisation and bio-conjugation of a red-emitting BODIPY marker. *Org. Biomol. Chem.* **9**, 66–69 (2011).
26. Papalia, T., Siracusano, G., Colao, I., Barattucci, A., Aversa, M. C., Serroni, S., Zappalà, G., Campagna, S., Sciortino, M. T., Puntoriero, F. & Bonaccorsi, P. Cell internalization of BODIPY-based fluorescent dyes bearing carbohydrate residues. *Dye. Pigment.* **110**, 67–71 (2014).
 27. Liu, Y., Niu, L. Y., Chen, Y. Z. & Yang, Q. Z. A self-assembled fluorescent nanoprobe for detection of GSH and dual-channel imaging. *J. Photochem. Photobiol. A Chem.* **355**, 311–317 (2018).
 28. Atılgan, S., Ekmekci, Z., Dogan, A. L., Guc, D. & Akkaya, E. U. Water soluble distyryl-boradiazaindacenes as efficient photosensitizers for photodynamic therapy. *Chem. Commun.* 4398 (2006) doi:10.1039/b612347c.
 29. Blázquez-Moraleja, A., Álvarez-Fernández, D., Prieto Montero, R., García-Moreno, I., Martínez-Martínez, V., Bañuelos, J., Sáenz-de-Santa-María, I., Chiara, M. D. & Chiara, J. L. A general modular approach for the solubility tagging of BODIPY dyes. *Dye. Pigment.* **170**, 107545 (2019).
 30. Manzano, H., Esnal, I., Marqués-Matesanz, T., Bañuelos, J., López-Arbeloa, I., Ortiz, M. J., Cerdán, L., Costela, A., García-Moreno, I. & Chiara, J. L. Unprecedented J-Aggregated Dyes in Pure Organic Solvents. *Adv. Funct. Mater.* **26**, 2756–2769 (2016).
 31. Blázquez-Moraleja, A., Cerdán, L., García-Moreno, I., Avellanal-Zaballa, E., Bañuelos, J., Jimeno, M. L., López-Arbeloa, I. & Chiara, J. L. Stereochemical and Steric Control of Photophysical and Chiroptical Properties in Bichromophoric Systems. *Chem. - A Eur. J.* **24**, 3802–3815 (2018).
 32. Durán-Sampedro, G., Agarrabeitia, A. R., Cerdán, L., Pérez-Ojeda, M. E., Costela, A., García-Moreno, I., Esnal, I., Bañuelos, J., Arbeloa, I. L. & Ortiz, M. J. Carboxylates versus fluorines: Boosting the emission properties of commercial BODIPYs in liquid and solid media. *Adv. Funct. Mater.* **23**, 4195–4205 (2013).
 33. López Arbeloa, F., López Arbeloa, T., López Arbeloa, I., García-Moreno, I., Costela, A., Sastre, R. & Amat-Guerri, F. Photophysical and lasing properties of pyrromethene 567 dye in liquid solution.: Environment effects. *Chem. Phys.* **236**, 331–341 (1998).
 34. Kee, H. L., Kirmaier, C., Yu, L., Thamyongkit, P., Youngblood, W. J., Calder, M. E., Ramos, L., Noll, B. C., Bocian, D. F., Scheldt, W. R., Birge, R. R., Lindsey, J. S. & Holten, D. Structural control of the photodynamics of boron-dipyrin complexes. *J. Phys. Chem. B* **109**, 20433–20443 (2005).
 35. Gartzia-Rivero, L., Sánchez-Carnerero, E. M., Jiménez, J., Bañuelos, J.,

- Moreno, F., Maroto, B. L., López-Arbeloa, I. & De La Moya, S. Modulation of ICT probability in bi(polyarene)-based O-BODIPYs: Towards the development of low-cost bright arene-BODIPY dyads. *Dalt. Trans.* **46**, 11830–11839 (2017).
36. Shieh, P., Dien, V. T., Beahm, B. J., Castellano, J. M., Wyss-Coray, T. & Bertozzi, C. R. CalFluors: A Universal Motif for Fluorogenic Azide Probes across the Visible Spectrum. *J. Am. Chem. Soc.* **137**, 7145–7151 (2015).
37. Blázquez-Moraleja, A., Sáenz-de-Santa María, I., Chiara, M. D., Álvarez-Fernández, D., García-Moreno, I., Prieto-Montero, R., Martínez-Martínez, V., López Arbeloa, I. & Chiara, J. L. Shedding light on the mitochondrial matrix through a functional membrane transporter. *Chem. Sci.* **11**, 1052–1065 (2020).
38. Smith, R. A. J., Hartley, R. C., Cochemé, H. M. & Murphy, M. P. Mitochondrial pharmacology. *Trends Pharmacol. Sci.* **33**, 341–352 (2012).
39. Murphy, M. P. & Hartley, R. C. Mitochondria as a therapeutic target for common pathologies. *Nat. Rev. Drug Discov.* **17**, 865–886 (2018).
40. Adeva-Andany, M. M., Carneiro-Freire, N., Seco-Filgueira, M., Fernández-Fernández, C. & Mouriño-Bayolo, D. Mitochondrial β -oxidation of saturated fatty acids in humans. *Mitochondrion* **46**, 73–90 (2019).
41. Melone, M. A. B., Valentino, A., Margarucci, S., Galderisi, U., Giordano, A. & Peluso, G. The carnitine system and cancer metabolic plasticity review-article. *Cell Death Dis.* **9**, (2018).
42. Beloribi-Djefafli, S., Vasseur, S. & Guillaumond, F. Lipid metabolic reprogramming in cancer cells. *Oncogenesis* **5**, e189–e189 (2016).
43. Tonazzi, A., Giangregorio, N., Console, L. & Indiveri, C. Mitochondrial Carnitine/Acylcarnitine Translocase: Insights in Structure/ Function Relationships. Basis for Drug Therapy and Side Effects Prediction. *Mini-Reviews Med. Chem.* **15**, 396–405 (2015).
44. Yin, R. & Hamblin, M. Antimicrobial Photosensitizers: Drug Discovery Under the Spotlight. *Curr. Med. Chem.* **22**, 2159–2185 (2015).
45. Lucky, S. S., Soo, K. C. & Zhang, Y. Nanoparticles in Photodynamic Therapy. *Chem. Rev.* **115**, 1990–2042 (2015).
46. Huang, Z. A review of progress in clinical photodynamic therapy. *Technol. Cancer Res. Treat.* **4**, 283–293 (2005).
47. Turksoy, A., Yildiz, D. & Akkaya, E. U. Photosensitization and controlled photosensitization with BODIPY dyes. *Coord. Chem. Rev.* **379**, 47–64 (2019).
48. Zhang, X. F. & Yang, X. Photosensitizer that selectively generates singlet oxygen in nonpolar environments: Photophysical mechanism and efficiency for

- a covalent BODIPY dimer. *J. Phys. Chem. B* **117**, 9050–9055 (2013).
49. Guan, Q., Zhou, L., Li, Y. & Dong, Y. Diiodo-Bodipy-Encapsulated Nanoscale Metal–Organic Framework for pH-Driven Selective and Mitochondria Targeted Photodynamic Therapy. *Inorg. Chem.* **57**, 10137–10145 (2018).
 50. Sánchez-Arroyo, A. J., Palao, E., Agarrabeitia, A. R., Ortiz, M. J. & García-Fresnadillo, D. Towards improved halogenated BODIPY photosensitizers: clues on structural designs and heavy atom substitution patterns. *Phys. Chem. Chem. Phys.* **19**, 69–72 (2017).
 51. Martínez, C. G., Braun, A. M. & Oliveros, E. Effect of the Media on the Quantum Yield of Singlet Oxygen ($O_2(1\Delta_g)$) Production by 9H-Fluoren-9-one: Microheterogeneous Systems. *Helv. Chim. Acta* **87**, 382–393 (2004).
 52. Gómez-Infante, A. de J., Bañuelos, J., Valois-Escamilla, I., Cruz-Cruz, D., Prieto-Montero, R., López-Arbeloa, I., Arbeloa, T. & Peña-Cabrera, E. Synthesis, Properties, and Functionalization of Nonsymmetric 8-MethylthioBODIPYs. *European J. Org. Chem.* **2016**, 5009–5023 (2016).
 53. Esnal, I., Urías-Benavides, A., Gómez-Durán, C. F. A., Osorio-Martínez, C. A., García-Moreno, I., Costela, A., Bañuelos, J., Epelde, N., López Arbeloa, I., Hu, R., Tang, B. Z. & Peña-Cabrera, E. Reaction of amines with 8-methylthioBODIPY: Dramatic optical and laser response to amine substitution. *Chem. - An Asian J.* **8**, 2691–2700 (2013).
 54. Ortiz, M. J., Agarrabeitia, A. R., Duran-Sampedro, G., Bañuelos Prieto, J., Lopez, T. A., Massad, W. A., Montejano, H. A., García, N. A. & Lopez Arbeloa, I. Synthesis and functionalization of new polyhalogenated BODIPY dyes. Study of their photophysical properties and singlet oxygen generation. *Tetrahedron* **68**, 1153–1162 (2012).
 55. Martí, C., Jürgens, O., Cuenca, O., Casals, M. & Nonell, S. Aromatic ketones as standards for singlet molecular oxygen photosensitization. Time-resolved photoacoustic and near-IR emission studies. *J. Photochem. Photobiol. A Chem.* **97**, 11–18 (1996).
 56. Schmidt, R., Tanielian, C., Dunsbach, R. & Wolff, C. Phenalenone, a universal reference compound for the determination of quantum yields of singlet oxygen $O_2(1\Delta_g)$ sensitization. *J. Photochem. Photobiol. A Chem.* **79**, 11–17 (1994).
 57. Oliveros, E., Bossmann, S. H., Nonell, S., Marti, C., Heit, G., Troscher, G., Neuner, A., Martinez, C. & Brauna, A. M. Photochemistry of the singlet oxygen [$O_2(1\Delta_g)$] sensitizer perinaphthenone (phenalenone) in N, N'-dimethylacetamide and 1,4-dioxane. *New J. Chem.* **23**, 85–93 (1999).
 58. Zhou, Q., Zhou, M., Wei, Y., Zhou, X., Liu, S., Zhang, S. & Zhang, B. Solvent effects on the triplet–triplet annihilation upconversion of diiodo-Bodipy and

- perylene. *Phys. Chem. Chem. Phys.* **19**, 1516–1525 (2017).
59. Nonell, S. & Flors, C. *Singlet Oxygen, Applications in Biosciences and Nanosciences*. (Royal Society of Chemistry, 2016).
 60. Sabatini, R. P., McCormick, T. M., Lazarides, T., Wilson, K. C., Eisenberg, R. & McCamant, D. W. Intersystem crossing in halogenated Bodipy chromophores used for solar hydrogen production. *J. Phys. Chem. Lett.* **2**, 223–227 (2011).
 61. Zhang, X. F., Yang, X., Niu, K. & Geng, H. Phosphorescence of BODIPY dyes. *J. Photochem. Photobiol. A Chem.* **285**, 16–20 (2014).
 62. Rachford, A. A., Ziessel, R., Bura, T., Retailleau, P. & Castellano, F. N. Boron dipyrromethene (Bodipy) phosphorescence revealed in [Ir(ppy) 2(bpy-C - C-bodipy)]⁺. *Inorg. Chem.* **49**, 3730–3736 (2010).
 63. Cazes, J. *Encyclopedia of Chromatography*. Florida Atlantic University (2005). doi:10.1081/E-ECHR.
 64. Lin, J.-T. Progress of medical lasers: Fundamentals and Applications. *Med. Devices Diagnostic Eng.* **1**, 36–41 (2016).
 65. Jiang, X.-D., Li, S., Guan, J., Fang, T., Liu, X. & Xiao, L.-J. Recent Advances of the Near-infrared Fluorescent aza-BODIPY Dyes. *Curr. Org. Chem.* **20**, 1736–1744 (2016).
 66. Nakamura, M., Kitatsuka, M., Takahashi, K., Nagata, T., Mori, S., Kuzuhara, D., Okujima, T., Yamada, H., Nakae, T. & Uno, H. Yellow NIR dye: π -fused bisbenzoBODIPYs with electron-withdrawing groups. *Org. Biomol. Chem.* **12**, 1309–1317 (2014).
 67. Wang, D. G., Zhang, L. N., Li, Q., Yang, Y., Wu, Y., Fan, X., Song, M. & Kuang, G. C. Dimeric BODIPYs with different linkages: A systematic investigation on structure-properties relationship. *Tetrahedron* **73**, 6894–6900 (2017).
 68. Ziessel, R., Ulrich, G., Haefele, A. & Harriman, A. An artificial light-harvesting array constructed from multiple bodipy dyes. *J. Am. Chem. Soc.* **135**, 11330–11344 (2013).
 69. Ortiz, M. J., Garcia-Moreno, I., Agarrabeitia, A. R., Duran-Sampedro, G., Costela, A., Sastre, R., López Arbeloa, F., Bañuelos Prieto, J. & López Arbeloa, I. Red-edge-wavelength finely-tunable laser action from new BODIPY dyes. *Phys. Chem. Chem. Phys.* **12**, 7804–7811 (2010).
 70. Dyes, B., Thoresen, L. H., Kim, H., Welch, M. B., Burghart, A. & Burgess, K. 1276 Letters Synlett. *Synlett* 1276–1278 (1998).
 71. Burghart, A., Kim, H., Welch, M. B., Thoresen, L. H., Reibenspies, J.,

- Burgess, K., Bergström, F. & Johansson, L. B. . 3,5-diaryl-4,4-difluoro-4-bora-3a,4a-diaza-s-indacene (BODIPY) dyes: Synthesis, spectroscopic, electrochemical, and structural properties. *J. Org. Chem.* **64**, 7813–7819 (1999).
72. Tao, J., Sun, D., Sun, L., Li, Z., Fu, B., Liu, J., Zhang, L., Wang, S., Fang, Y. & Xu, H. Tuning the photo-physical properties of BODIPY dyes: Effects of 1, 3, 5, 7- substitution on their optical and electrochemical behaviours. *Dye. Pigment.* **168**, 166–174 (2019).
73. Agazzi, M. L., Ballatore, M. B., Durantini, A. M., Durantini, E. N. & Tomé, A. C. BODIPYs in antitumoral and antimicrobial photodynamic therapy: An integrating review. *J. Photochem. Photobiol. C Photochem. Rev.* **40**, 21–48 (2019).
74. Kowada, T., Maeda, H. & Kikuchi, K. BODIPY-based probes for the fluorescence imaging of biomolecules in living cells. *Chem. Soc. Rev.* **44**, 4953–4972 (2015).
75. Fernandez, J. M., Bilgin, M. D. & Grossweiner, L. I. Singlet oxygen generation by photodynamic agents. *J. Photochem. Photobiol. B Biol.* **37**, 131–140 (1997).
76. Winkler, K., Simon, C., Finke, M., Bleses, K., Birke, M., Szentmáry, N., Hüttenberger, D., Eppig, T., Stachon, T., Langenbucher, A., Foth, H. J., Herrmann, M., Seitz, B. & Bischoff, M. Photodynamic inactivation of multidrug-resistant *Staphylococcus aureus* by chlorin e6 and red light ($\lambda = 670$ nm). *J. Photochem. Photobiol. B Biol.* **162**, 340–347 (2016).
77. Triesscheijn, M., Baas, P., Schellens, J. H. M. & Stewart, F. A. Photodynamic Therapy in Oncology. *Oncologist* **11**, 1034–1044 (2006).
78. Paul, S., Heng, P. W. S. & Chan, L. W. Optimization in solvent selection for chlorin e6 in photodynamic therapy. *J. Fluoresc.* **23**, 283–291 (2013).
79. Yogo, T., Urano, Y., Mizushima, A., Sunahara, H., Inoue, T., Hirose, K., Iino, M., Kikuchi, K. & Nagano, T. Selective photoinactivation of protein function through environment-sensitive switching of singlet oxygen generation by photosensitizer. *Proc. Natl. Acad. Sci. U. S. A.* **105**, 28–32 (2008).
80. Zou, J., Yin, Z., Ding, K., Tang, Q., Li, J., Si, W., Shao, J., Zhang, Q., Huang, W. & Dong, X. BODIPY Derivatives for Photodynamic Therapy: Influence of Configuration versus Heavy Atom Effect. *ACS Appl. Mater. Interfaces* **9**, 32475–32481 (2017).
81. Turan, I. S., Gunaydin, G., Ayan, S. & Akkaya, E. U. Molecular demultiplexer as a terminator automaton. *Nat. Commun.* **9**, 1–8 (2018).
82. Jiménez, J., Moreno, F., Maroto, B. L., Cabrerós, T. A., Huy, A. S., Müller, G., Bañuelos, J. & De La Moya, S. Modulating ICT emission: A new strategy to

- manipulate the CPL sign in chiral emitters. *Chem. Commun.* **55**, 1631–1634 (2019).
83. Zhao, J., Xu, K., Yang, W., Wang, Z. & Zhong, F. The triplet excited state of Bodipy: Formation, modulation and application. *Chem. Soc. Rev.* **44**, 8904–8939 (2015).
84. Jiménez, J., Prieto-Montero, R., Maroto, B. L., Moreno, F., Ortiz, M. J., Oliden-Sánchez, A., López-Arbeloa, I., Martínez-Martínez, V. & Moya, S. Manipulating Charge Transfer States in BODIPYs: A Model Strategy to Rapidly Develop Photodynamic Theragnostic Agents. *Chem. – A Eur. J.* **26**, 601–605 (2020).
85. Goud, T. V., Tutar, A. & Biellmann, J. F. Synthesis of 8-heteroatom-substituted 4,4-difluoro-4-bora-3a,4a-diaza-s-indacene dyes (BODIPY). *Tetrahedron* **62**, 5084–5091 (2006).
86. Li, L., Nguyen, B. & Burgess, K. Functionalization of the 4,4-difluoro-4-bora-3a,4a-diaza-s-indacene (BODIPY) core. *Bioorganic Med. Chem. Lett.* **18**, 3112–3116 (2008).
87. Chen, J., Burghart, A., Derecskei-Kovacs, A. & Burgess, K. 4,4-Difluoro-4-bora-3a,4a-diaza-s-indacene (BODIPY) dyes modified for extended conjugation and restricted bond rotations. *J. Org. Chem.* **65**, 2900–2906 (2000).
88. Rihn, S., Retailleau, P., Bugsaliewicz, N., Nicola, A. De & Ziessel, R. Versatile synthetic methods for the engineering of thiophene-substituted Bodipy dyes. *Tetrahedron Lett.* **50**, 7008–7013 (2009).
89. Hall, M. J., McDonnell, S. O., Killoran, J. & O’Shea, D. F. A modular synthesis of unsymmetrical tetraarylazadipyromethenes. *J. Org. Chem.* **70**, 5571–5578 (2005).
90. Filatov, M. A., Karuthedath, S., Polestshuk, P. M., Callaghan, S., Flanagan, K. J., Wiesner, T., Laquai, F. & Senge, M. O. BODIPY-Pyrene and Perylene Dyads as Heavy-Atom-Free Singlet Oxygen Sensitizers. *ChemPhotoChem* **2**, 606–615 (2018).
91. Filatov, M. A., Karuthedath, S., Polestshuk, P. M., Savoie, H., Flanagan, K. J., Sy, C., Sitte, E., Telitchko, M., Laquai, F., Boyle, R. W. & Senge, M. O. Generation of Triplet Excited States via Photoinduced Electron Transfer in meso-anthra-BODIPY: Fluorogenic Response toward Singlet Oxygen in Solution and in Vitro. *J. Am. Chem. Soc.* **139**, 6282–6285 (2017).
92. Zhao, J., Chen, K., Hou, Y., Che, Y., Liu, L. & Jia, D. Recent progress in heavy atom-free organic compounds showing unexpected intersystem crossing (ISC) ability. *Org. Biomol. Chem.* **16**, 3692–3701 (2018).

93. Hu, W., Lin, Y., Zhang, X. F., Feng, M., Zhao, S. & Zhang, J. Heavy-atom-free charge transfer photosensitizers: Tuning the efficiency of BODIPY in singlet oxygen generation via intramolecular electron donor-acceptor interaction. *Dye. Pigment.* **164**, 139–147 (2019).
94. Liu, Y., Zhao, J., Iagatti, A., Bussotti, L., Foggi, P., Castellucci, E., Di Donato, M. & Han, K. L. A revisit to the orthogonal bodipy dimers: Experimental evidence for the symmetry breaking charge transfer-induced intersystem crossing. *J. Phys. Chem. C* **122**, 2502–2511 (2018).
95. Zhang, X. F. & Feng, N. Photoinduced Electron Transfer-based Halogen-free Photosensitizers: Covalent meso-Aryl (Phenyl, Naphthyl, Anthryl, and Pyrenyl) as Electron Donors to Effectively Induce the Formation of the Excited Triplet State and Singlet Oxygen for BODIPY Compounds. *Chem. - An Asian J.* **12**, 2447–2456 (2017).
96. Palao-Utiel, E., Montalvillo-Jiménez, L., Esnal, I., Prieto-Montero, R., Agarrabeitia, A. R., García-Moreno, I., Bañuelos, J., López-Arbeloa, I., de la Moya, S. & Ortiz, M. J. Controlling Vilsmeier-Haack processes in meso-methylBODIPYs: A new way to modulate finely photophysical properties in boron dipyrromethenes. *Dye. Pigment.* **141**, 286–298 (2017).
97. Yakubovskiy, V. P., Shandura, M. P. & Kovtun, Y. P. Boradipyrromethenecyanines derived from conformationally restricted nuclei. *Dye. Pigment.* **87**, 17–21 (2010).
98. Chibani, S., Le Guennic, B., Charaf-Eddin, A., Laurent, A. D. & Jacquemin, D. Revisiting the optical signatures of BODIPY with ab initio tools. *Chem. Sci.* **4**, 1950–1963 (2013).
99. Zhu, H., Fan, J., Li, M., Cao, J., Wang, J. & Peng, X. A ‘distorted-BODIPY’-based fluorescent probe for imaging of cellular viscosity in live cells. *Chem. - A Eur. J.* **20**, 4691–4696 (2014).
100. Lincoln, R., Greene, L. E., Bain, C., Flores-Rizo, J. O., Bohle, D. S. & Cosa, G. When Push Comes to Shove: Unravelling the Mechanism and Scope of Nonemissive meso-Unsaturated BODIPY Dyes. *J. Phys. Chem. B* **119**, 4758–4765 (2015).
101. Prlj, A., Fabrizio, A. & Corminboeuf, C. Rationalizing fluorescence quenching in meso-BODIPY dyes. *Phys. Chem. Chem. Phys.* **18**, 32668–32672 (2016).
102. Kollmannsberger, M., Rurack, K., Resch-Genger, U. & Daub, J. Ultrafast charge transfer in amino-substituted boron dipyrromethene dyes and its inhibition by cation complexation: A new design concept for highly sensitive fluorescent probes. *J. Phys. Chem. A* **102**, 10211–10220 (1998).
103. Palao, E., Prieto-Moreno, R., Prieto-Castañeda, A., Epelde-Elezcano, N.,

Agarrabeitia, A. R., Moreno, F., Maroto, B. L., Martinez-Martinez, V., de la Moya, S., Prieto-Castañeda, A. & Ortiz, M. J. Exploring BODIPY meso-enamines as singlet-oxygen photosensitizers for PDT. in *Proceedings of The 21st International Electronic Conference on Synthetic Organic Chemistry* 4785 (MDPI, 2017). doi:10.3390/ecsoc-21-04785.

5

NANOPARTICLES for Bioimaging and Photodynamic Therapy

5.1. <u>Photoactive Spherical Silica nanoparticles</u>	173
5.1.1 Structural characterization	177
5.1.1.1 <i>Nonporous nanoparticles</i>	177
5.1.1.2 <i>Mesoporous nanoparticles</i>	179
5.1.1.3 <i>Ormosil nanoparticles</i>	183
5.1.1.4 <i>Conclusions</i>	185
5.1.2 Fluorescent silica nanoparticles for bioimaging	185
5.1.2.1 <i>Dye embedded into the nanoparticles core</i>	186
5.1.2.2 <i>Dye grafted at the nanoparticles shell</i>	193
5.1.2.3 <i>In vitro experiments</i>	194
5.1.2.4 <i>Conclusions</i>	197
5.1.3 Photosensitizer-silica nanoparticles for photodynamic therapy	197
5.1.3.1 <i>Optimization of PS- silica nanoparticles with Rose Bengal</i>	198
5.1.3.2 <i>Other PS- silica nanoparticles</i>	205
5.1.3.3 <i>Conclusions</i>	214
5.2. <u>Laponite-Clay as nanocarrier for Photodynamic Therapy</u>	215
5.2.1 <i>Structural characterization</i>	217
5.2.2 <i>Rose Bengal-Laponite nanosystem for Photodynamic Therapy</i>	217
5.2.3 <i>In vitro experiments</i>	219
5.2.4 <i>Conclusions</i>	220
5.3. <u>Bibliography</u>	222

Nanoparticles for Bioimaging and Photodynamic Therapy

Nanomaterials are defined as any system in which at least one of its dimensions is in the size range of 1-100 nm, Figure 5.1.A.^{1,2} Currently, there are several types of nanoparticles, which can be categorized by their different physical properties or chemical composition. Here are divided into two main groups regarding their nature (Figure 5.1.B); *i*) organic (dendrimers, micelles, liposomes, nanogels, polymeric nanoparticles, etc) or *ii*) inorganic (Q-dots, SPIONs, silica nanoparticles, etc).³⁻¹² The nanomaterials present unique characteristics, such as high surface-to-volume ratio or size-dependent optical and magnetic properties, which are drastically different from those of their bulk material.¹ The scientific and technological interest in these nanoparticles has highly increased in the last years, owing to the multiple uses in different applications; transport, energy, environment, electronics, construction, and medicine.

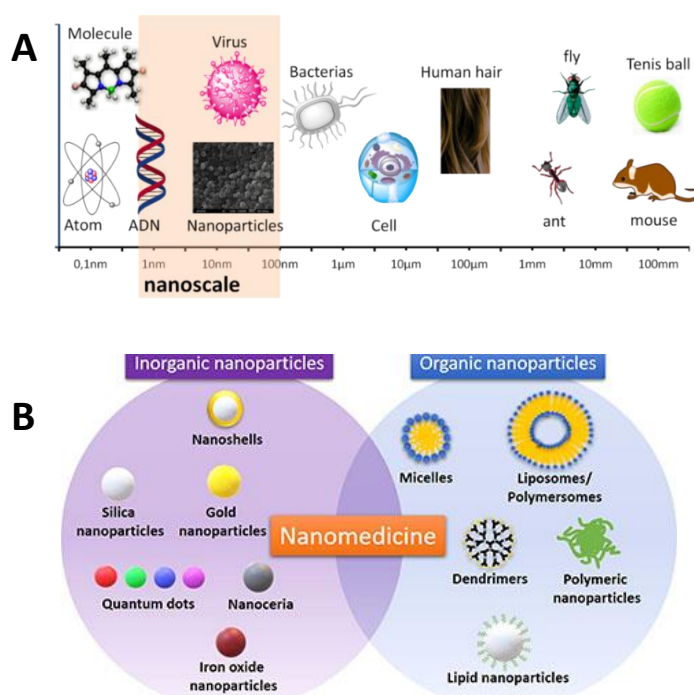


Figure 5.1. Schematic representation of the size of nanomaterials size (A), examples of different types of nanoparticles for biomedicine (B).

Despite the numerous applications fields, nanomedicine could be considered as an emerging and promising key approach in the 21st century for the diagnosis and treatment of diseases, and in particular cancer.^{3,4,7-11} The use of nanoparticles as carriers for a compound of interest, which is usually encapsulated or attached, offers many advantages: *i*) they have large surface to volume ratios which allows the administration of a high amount of drug, *ii*) prevent the degradation or inactivation of the drug by plasma components, *iii*) help to stabilize hydrophobic drugs in aqueous medium, *iv*) enhance the selective accumulation inside the tumor cells and their retention. This latter effect is known as active targeting. Commonly, nanoparticles tend to accumulate in higher extent in tumor tissues with respect to normal ones by passive targeting due to the enhanced permeability and retention (EPR) effect. Generally, tumor cells grow very fast but in a more disorganized distribution, presenting large gap junctions (between 100-600 nm) which allow the entry of nanoparticle. Thus, nanoparticles of a diameter size between 30-200 nm, are preferentially accumulated in the tumor cells, since they are unable to penetrate through tight endothelial junctions of normal blood vessels (2-20 nm). Moreover, tumors show poor lymphatic drainage, aiding longer time retention. Besides, the selectivity to cancer cells can be increased by an active targeting, consisting of the functionalization with certain ligands, such as proteins, polysaccharides, nucleic acids, peptides, and small molecules, that bind specific receptors on the cell which are overexpressed in malignant cells but not in healthy cells.

In fact, studies have indicated that drug-loaded nanocarriers combining intrinsically passive and well-designed active targeting strategies show greater *in vitro* and *in vivo* anticancer activity with lower side effects than pure drugs. In fact, pure drugs generally act on the whole organism whereas nanocarriers drive their action to a specific target increasing the therapeutic efficacy. Certainly, it is known that only around 1% of the administered chemo drugs in solution reach the tumor site.

In this context, the nanoparticles should be carefully designed balancing their stability, diffusion and targeting abilities. Currently, there are several nanosystems approved by the Food and Drug Administration (FDA). Indeed, an average of 2-3 new ones per year is being approved for specific clinical uses since 1990. Systems based on liposomes and polymeric nanoparticles were initially more dominant but nowadays the use of micellar-, metallic- or protein-based nanoparticles is more extended.^{3,7}

Therefore, nanomedicine has been attracted great interest to the scientific community in the last years with the aim of finding new nanoplatforms with improved therapeutic and imaging functions, particularly for cancer treatment, with enhanced circulation time, lower toxicity, and higher specific accumulation in targeted tissue by active transport.^{3,7} Moreover, the easy functionalization of the nanoparticles allows also the design of multifunctional nanocarriers able to combine in one single nanoplatform not only the targeting ligands but also different imaging agents and diverse active systems for complementary treatments such as hyperthermia, photodynamic therapy, and chemotherapy. However, nanoparticles also present some limitations, such as high costs, difficulties in large-scale manufacturing, and technical challenges, for instance, particle-particle aggregation.^{2,3}

In this thesis, one of the main objectives is to develop new hybrid nanosystems in order to apply them in the biomedical field to detect and treat cancer diseases.

Regarding diagnosis, the nanoparticles will be loaded with a bright fluorophore to enable fluorescence bioimaging. Although there are different molecular imaging procedures able to detect early-stage cancer and to monitor the tumor, *i.e.* positron emission tomography (PET), magnetic resonance imaging (MRI) or electron spin resonance (ESR) spectroscopy, optical imaging has some advantages such a higher sensitivity and spatial resolution, avoids the use of radioactive materials and the exposure to harmful radiation. A drawback is its low depth penetration into the tissues inherent of visible or infrared light respect to other irradiation sources. Nevertheless, although it is not much extended in clinical trials, it is widely used for *in vitro* and preclinical *in vivo* studies. Indeed, fluorescence microscopy is an economically available technique, that allows the monitoring of cellular biological processes in real-time and in an intuitive non-invasive way.

On the other hand, PDT, previously defined in chapter 4, section 4.2, is chosen as a minimally invasive and complementary cancer treatment with respect to other common procedures, radiotherapy and chemotherapy, able to exert a selective cytotoxic activity toward malignant cells by the localization of the light irradiation. In this context, the use of passive nanocarriers with active targets will improve the selective accumulation of the PS dye in the tumor region as well as provide a higher solubility in physiological media, extending its circulatory time, and protecting it for degradation. Thus, a high therapeutic action will be expected at a low PS administration dose, minimizing also possible side effects.

Although there are many different nanosystems, silica-based nanoparticles (SN) have attracted great interest as suitable carriers for drugs due to their high surface area, easy functionalization, good biocompatibility, and optically transparent properties.^{13,14} These nanoparticles will be loaded with fluorophores and/or photosensitizer dyes to be used as fluorescence-ROS generating nanoplatforms.

Note here that, these dye-nanosystems should be further functionalized with two main purposes. On the one hand, they should pass unnoticed by the immune systems. In this sense, one of the most used strategies to escape from the phagocytes cells is the coating of nanoparticles with PEG (polyethylene glycol). Moreover, the PEGylation makes the external surface of the nanoparticles more hydrophilic and minimizes their interaction with the extracellular matrix prolonging its circulatory time.¹⁵⁻¹⁸ On the other hand, folic acid (FA) is widely used as active biotarget since Folate receptors are well known to be overexpressed in tumor cells including ovarian, lung, kidney and breast cancer cells making them attractive targets for NPs via receptor-mediated endocytosis.^{19,20} In comparison with other typical active ligands, *i.e.* antibodies or transferrin, folic acid is a very low-cost, small and stable molecule. Conversely, it presents a lower specificity since FA targets are also expressed, although to less extent, in normal tissues.¹⁵⁻¹⁸

Thus, besides the PSs, the external surface of the nanoparticles will be coated by polyethylene glycol (PEG) to increase their stability in water and blood circulation time and finally functionalized with folic acid (FA) to specifically target cancer cells.

First, synthesis and characterization of three types of sphere silica nanoparticles (nonporous, mesoporous and ormosil) are described. Their morphology, size distribution and external composition were characterized by several techniques and the results are compiled in section 5.1.1. Afterward, the synthesis and characterization of different fluorescent silica nanoparticles by physical absorption or covalent grafting of fluorophores to render fluorescence nanoparticles for optical bioimaging are discussed together with *in vitro* studies in HeLa cells (section 5.1.2). Finally, section 5.1.3 is dedicated to PS-loaded-nanoparticles for photodynamic therapy, where their photophysical properties were widely characterized and the photoactivity action of the most promising systems was tested also in HeLa cells.

In section 5.2, a similar study is extended to laponite-clay nanoparticles with Rose Bengal as PS grafted at their external surface, together with PEG and folic acid. Firstly, its morphology, size distribution, and external composition were characterized

(section 5.2.1), following by their photophysical properties as well as its capability as PS-nanocarriers for PDT (section 5.2.2). Finally, their phototherapeutic efficiency was studied by *in vitro* assays in HeLa cells (section 5.2.3).

5.1. Photoactive Spherical Silica Nanoparticles

In 1968, Stöber and Fink developed an approach to control the nonporous silica nanoparticle growth, shape, and distribution, known as Stöber method.²¹ It is based on the sol-gel process, starting from an alkoxide (tetraethoxysilicate or tetramethoxysilicate or others) in a water/ethanol mixture and using ammonium hydroxide as a catalyst. As a result, monodisperse, spherical and electronically stabilized silica nanoparticles are obtained by hydrolysis and condensation reactions, Figure 5.2.

Note here that adding a cationic surfactant to the synthesis gel, mesoporous silica nanoparticles are obtained. This surfactant acts as a template and through micelle formation, pores are generated with a size range from 2 nm to 50 nm. For ormosil nanoparticles a second silica source with a more organophilic character was used. (For more details see experimental chapter 3, section 3.1.1)

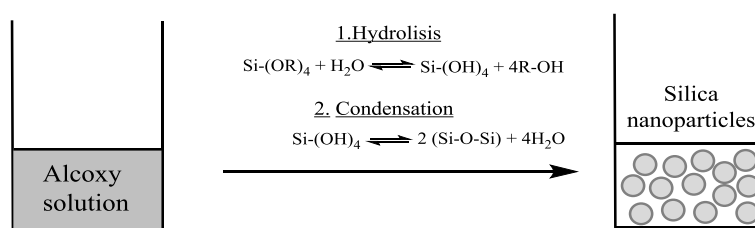


Figure 5.2. Scheme of Stöber method; hydrolysis and condensation reactions

In the bibliography, there are many different works that described the effect of changing the reaction conditions on the size, morphology and distribution of the nanoparticles. In general, five parameters are mainly considered; *i*) temperature, *ii*) pH value, *iii*) silica source concentration and nature *iv*) type of alcoholic solvent used and *v*) surfactant type and concentration, in case of mesoporous nanoparticles.²² The variations of these conditions induce a modification of the NP size from 25 nm to 2

µm. Thus, all these factors have to be taken into account in the synthesis of silica nanoparticles:

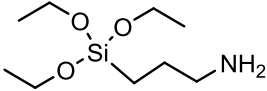
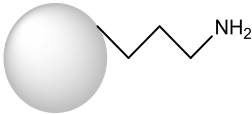
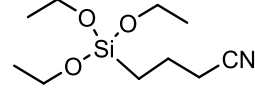
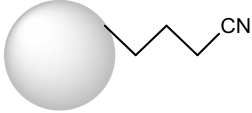
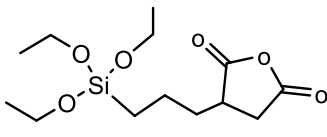
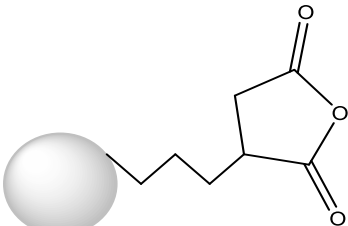
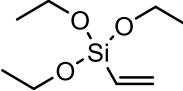
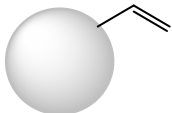
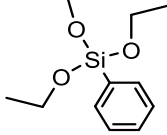
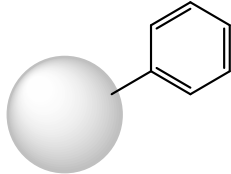
- i)* Temperature, NP size tends to decrease when the reaction temperature increased.²³
- ii)* A water/ammonia mixture (pH) usually generates spherical and larger nanoparticles. In synthesis without ammonia, nanoparticles distribution is irregular and not spherical. For that reason, the control of pH is crucial during the NP synthesis; low pH values inhibit the hydrolysis and condensation of TEOS and therefore the reaction time becomes very slow modifying the NP morphology and size.²³
- iii)* The alkoxide concentration and the size of nanoparticles are proportional, meaning that if the concentration raises the size of the nanoparticles does too.²³ In case of the silica source type, the shorter is the carbon chain the smaller is the size of the nanoparticles, attributed to a less steric effect during the nucleophilic attack by water.²²
- iv)* The presence of alcoholic as a co-solvent facilitates the alkoxide solution. Nevertheless, long-chain alcohols lead to high nanoparticles size and wider size distribution. For this reason, to obtain smaller and more homogeneous nanoparticles methanol or ethanol is convenient.²³
- v)* The surfactant concentration, in the case of mesoporous nanoparticles, results in complex interactions between the micelles and the silica oligomers formed during condensation. Particle morphologies are richer compared to the uniform nonporous Stöber silica spheres, and the particle size distribution is often broader.

In this thesis, the condition of the synthesis of silica nanoparticles was carefully considered in order to obtain nanoparticles with a narrow distribution around 40 to 60 nm (see chapter 3, section 3.1.1). It is known that the nanoparticles for *in vivo* use, have to present a uniform distribution and ideally around 50 nm; smaller nanoparticles are easily removed by the organism and while too large could provoke embolisms.^{24,15} Besides the size should optimal for a favorable clearance from the body, being possible their removal after tackling their function.¹⁶

Briefly, these nanoparticles fulfill the indispensable requirements for using in bioimaging and photodynamic therapy; *i)* they are biocompatible and nontoxic, *ii)* chemically and thermally stable, *iii)* optically transparent and *iv)* easy to synthesize

and functionalized with organic groups.^{24,25,26} To functionalize the silica external surface or for the case of mesoporous silica nanoparticles also their internal area, a second alkoxide is used. Depending on the functional groups required in the system different silica sources are added, Table 5.1. The presence of these groups gives the opportunity to chemically tether a great number of organic compounds (drugs, biomolecules, PEG), both inside in the core and outside in the shell of the nanoparticles.

Table 5.1. Different alkoxy silane sources and their corresponding organic group in NPs

Alkoxy silane source	Functionalization in nanoparticle
 <p>APTES 3-aminopropyltriethoxysilane</p>	
 <p>CTES 3-Cyanopropyltriethoxysilane</p>	
 <p>TESPSA (3-Triethoxysilyl)propylsuccinic anhydride</p>	
 <p>VTES triethoxyvinylsilane</p>	
 <p>PTES phenyltriethoxysilane</p>	

Spherical silica nanoparticles can be divided into three main types; *i*) nonporous, *ii*) mesoporous and *iii*) ormosil. Despite the fact that all of them were used in this thesis, most studies were mainly carried out in mesoporous structure.

The difference between these three nanoparticles is based on the different structure or nature of core; without porous structure (nonporous), with porous of few nanometers (mesoporous) or a more organophilic core by the combination of different silica sources (ormosil). Note here, the three types of silica nanoparticles will also contain a functionalized shell (outside), Figure 5.3.

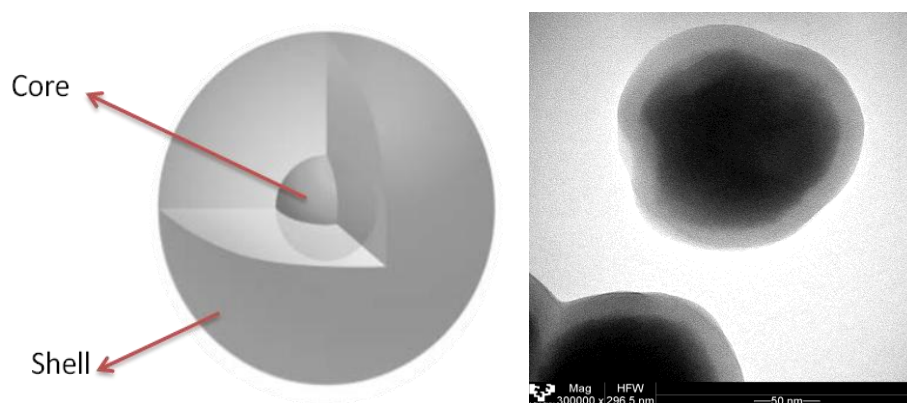


Figure 5.3. Sphere nanoparticles schematic representation of core-shell structure (left) and TEM image of silica nanoparticle (right).

Regarding the core, different organic molecules, *i.e.* fluorophores, could be physically trapped inside their pores (for mesoporous silica nanoparticles and ormosil). Nonetheless, in the case of nonporous nanoparticles, the organic compound must be chemically attached usually by direct condensation as the nanoparticles are growing. Concerning the shell all the molecules of interest will be covalently anchored following one of these two routes; *i*) direct condensation if the organic molecule contains a triethoxysilyl group or *ii*) conventional peptide coupling reaction between amine group and carboxylic group. For more details see chapter 3 section 3.1.2.

5.1.1 Structural characterization

The synthesis of all the sphere silica nanoparticles was directed to obtain silica nanoparticles of around 50 nm, which according to the size conditions mentioned before, it is an appropriate size for biomedical applications. Then, besides the inherent hydroxyl groups of the silica, the surface was further functionalized, in a second step, with additional organic groups; amine, cyano, succinimide and carboxylic. The size, morphology, distribution and the chemical composition of the silica nanoparticles were characterized by several techniques, SEM, TEM, DLS, XPS, $^1\text{H-MNR}$ and FTIR (see section 3.2.1). The results are divided into three sections: nonporous nanoparticles in section 5.1.1.1, mesoporous nanoparticles in section 5.1.1.2 and finally ormosil in section 5.1.1.3.

5.1.1.1 Nonporous nanoparticles

Nonporous nanoparticles were synthesized and externally decorated with amine group (NH-SN) and carboxylic group (COOH-SN). The carboxylic group was further modified to succinic anhydride groups (Suc-SN) based on the synthesis described of experimental chapter 3, section 3.1.1.1. The size, morphology and distribution of these sphere silica nanoparticles (SN) were studied by TEM and DLS. The presence of the different functional groups, amine, succinic anhydride and carboxylic, was characterized by XPS and $^1\text{H-MNR}$.

The nonporous nanoparticles (SN) present a spherical morphology, with a homogeneous size distribution of around 40 nm confirmed by TEM and DLS techniques (Figure 5.4).

The shell functionalization was studied by XPS and the percentage of the different atoms at the external surface is depicted in Table 5.2. The results indicate a relatively low presence of nitrogen atoms, NH-SN sample of 1.7%; for the case of Suc-SN, an increase in the carbon amount respect to SN sample is detected.

The chemical composition of the external surface of SN was also studied by $^1\text{H-RMN}$, Figure 5.5, and analyzed by MestReNova. These data were compared with theoretical bases for APTES and TESPSA. For NH-SN, three carbon denominations “a”, “b” and “c” (see Figure 5.5.A inside) at 0.36 ppm (triplet), at 1.39 ppm (quintet) and at 2.47 ppm (triplet) were identified; the peaks in 1.05 ppm and 3.55 ppm correspond to ethanol.²⁷ In the case of Suc-SN (Figure 5.5.B) only one type of carbon “a” could be

located at 0.5 ppm, which confirms the successful post-functionalization, despite the absence of the rest of the peaks, assigning to the low amount of succinic anhydride tethered. Note here that for COOH-SN, the amount of carboxylic groups was too small to be detected by $^1\text{H-NMR}$.

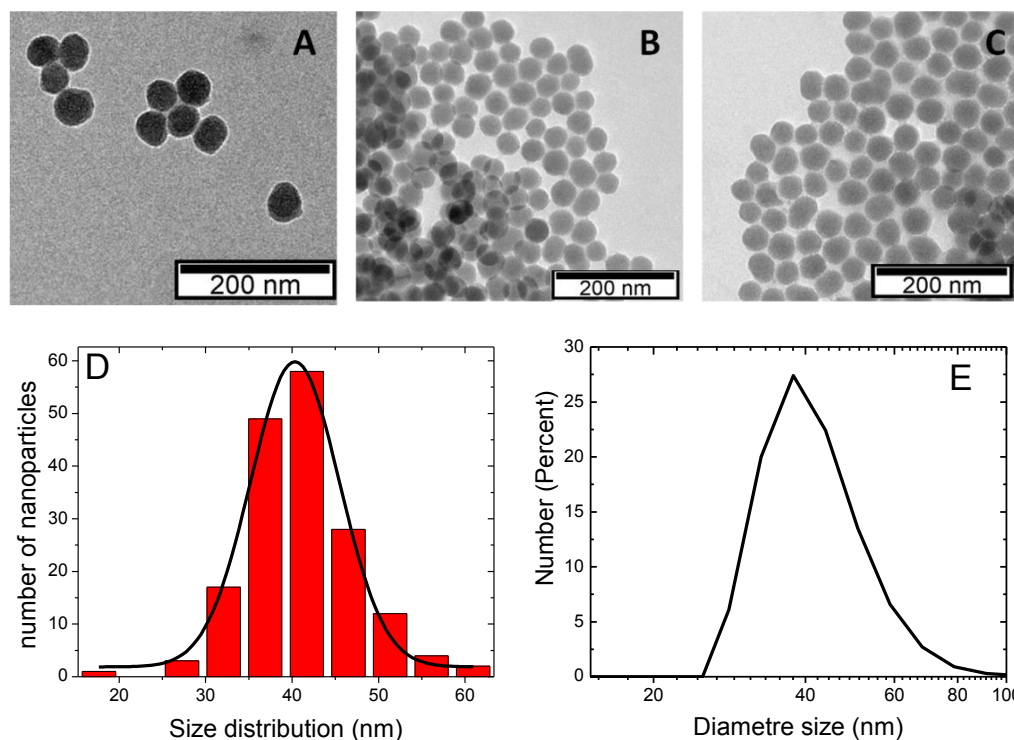


Figure 5.4. TEM image of nonporous nanoparticles (A, B and C), size distribution of image C (D) and DLS size distribution of SN nanoparticles in water (E).

Table 5.2. Silica nanoparticles synthesized and their XPS results

Name	Characteristic	Shell	XPS (% At rel)			
			C	O	Si	N
SN	Nonporous	OH	3.2	63.3	33.5	-
NH-SN	Nonporous	NH ₂ /OH	8.2	56.5	33.6	1.7
Suc-SN	Nonporous	Suc/OH	7.4	59.5	33.2	-

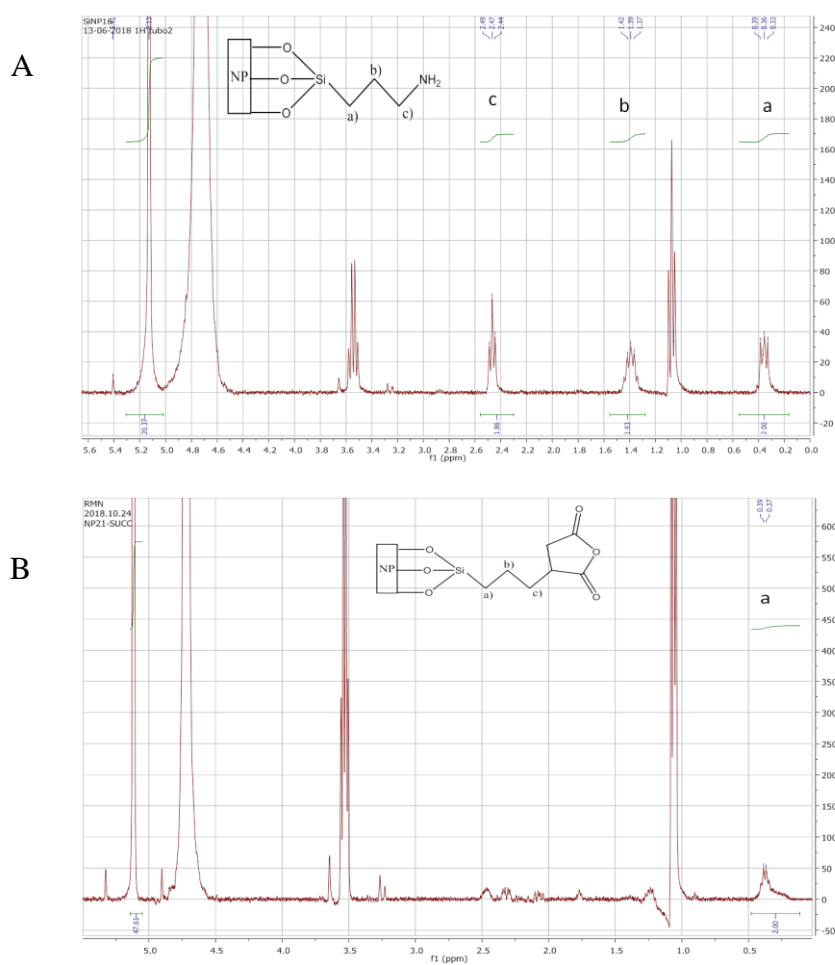


Figure 5.5. $^1\text{H-NMR}$ spectra of NH-SN (A) and Suc-SN (B) samples

5.1.1.2 Mesoporous nanoparticles

Mesoporous silica nanoparticles were analyzed by SEM, TEM, DLS, XPS and FT-IR. The external surface of mesoporous nanoparticles surface was also functionalized with amino group (NH-MSN) or carboxylic group (COOH-MSN). The carboxylic function was obtained by deriving silica nanoparticles previously functionalized with cyano groups (CN-MSN).

The nanoparticle size and distribution analyzed by SEM, TEM is shown in Figure 5.6 and Figure 5.7, respectively. The spherical nanoparticles show a size distribution of 47 ± 10 nm, by SEM.

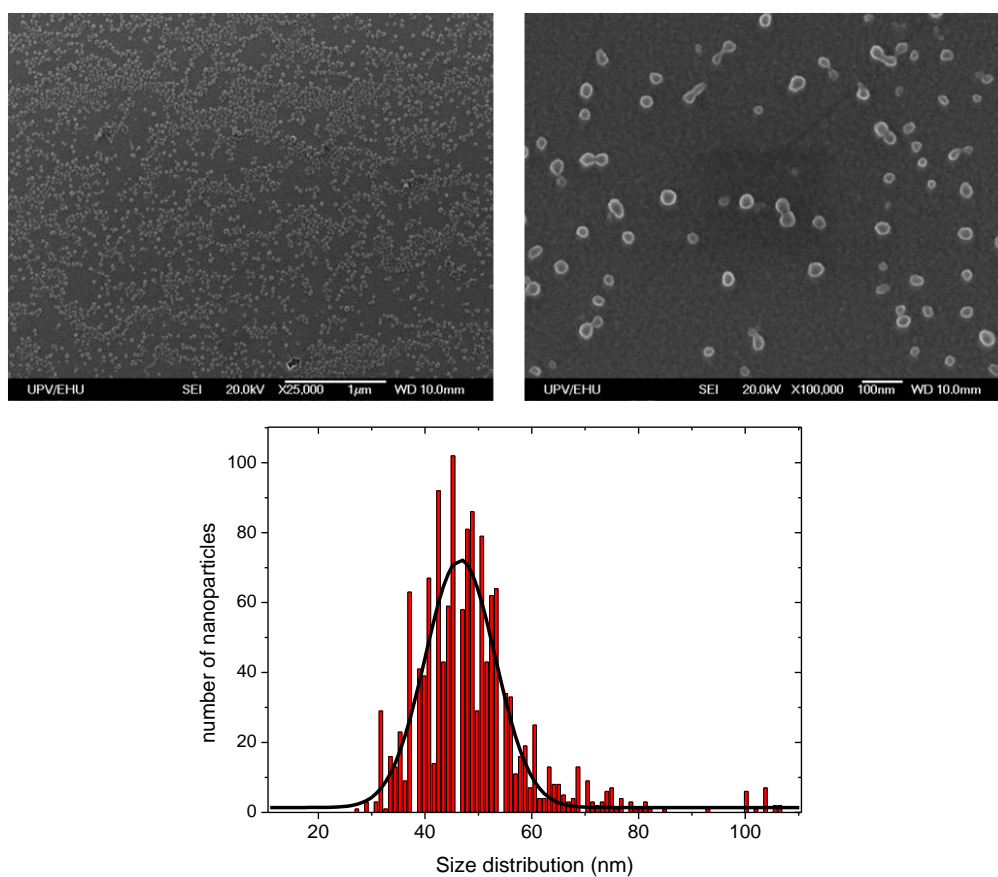


Figure 5.6 SEM images of mesoporous nanoparticles (top) and size distribution (bottom).

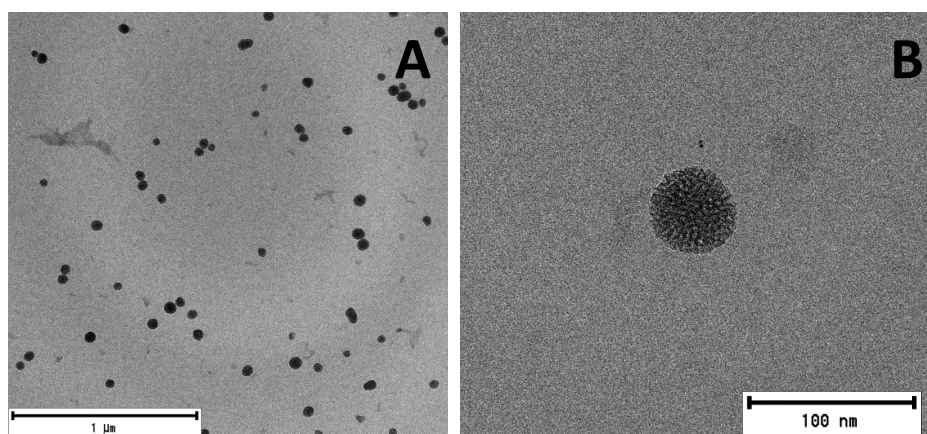


Figure 5.7. TEM image of mesoporous nanoparticles

On the other hand, the size obtained by DLS technique for the different functionalized nanoparticles (with the exception of CN-MSN) is around 60-70 nm (Table 5.3). The bigger size derived by DLS is likely explained by the fact that this technique measures the hydrodynamic ratio which depends on the surface of the nanoparticles. Note here that CN-MSN shows a much higher hydrodynamic size in water 280 nm which indicates its poor stability in water and their tendency to form aggregates.

The stability of the nanoparticles in water was studied by Zeta potential in order to test their ability as nanocarriers. NH-MSN and CN-MSN nanoparticles did not present a high Zpot value ($< \pm 25$ mV), indicating poor stability in aqueous media. However, COOH-MSN shows a high enough Zpot attributed to the presence of the carboxylic group that in aqueous media would be deprotonated (COO^-) making the system more stable by electrostatic repulsion.

To solve the stability problem, polyethylene glycol (PEG) of 2000 Da considered the optimum length as demonstrated in the experiments detailed in section 5.1.3.1, was anchored to the nanoparticles. There are a great number of publications that demonstrate the ability of PEG to stabilize nanoparticles systems or hydrophilic molecules in water. In addition, this molecule has interesting properties for in vivo experiments such as enhance the circulation time in blood and avoid the immunologic action against the nanoparticle.^{20,21,24,25}

The anchoring of PEG was done following two different procedures; *i*) PEG chain of 2000 Da with a silylated group at one end was tethered to hydroxyl groups of silica nanoparticles (PEG-OH-MSN) and *ii*) PEG chain of identical length but in this case with a succinimide group at one edge is linked to amine groups (PEG-NH-MSN), see experimental chapter 3, section 3, Figure 3.5 for more details. An increase in the Zpot values (Table 5.3) in both pegylated silica nanoparticles (*i.e.* from -3.96 mV to -46.8 mV or to -25.7 mV for PEG-OH-MSN and PEG-NH-MSN, respectively), indicates better stability of those nanosystems in water. Note here, the zeta potential of PEG-OH-MSN is larger than for PEG-NH-MSN assigned to the number of hydroxyl groups at the external surface is considerably higher than the amine groups, and consequently, more PEG molecules are linked.

Table 5.3. Mesoporous silica nanoparticles synthesized together with their DLS, Zeta potential and XPS results in water.

Name	Shell	DLS (nm)	Z pot (mV)	XPS (% At rel)			
				C	O	Si	N
NH-MSN	NH ₂ /OH	71 (98%)	-3.96	23.6	46.0	25.4	5.0
CN-MSN	CN/OH	280	-7.06	38.8	36.6	19.2	5.2
COOH-MSN	COOH/OH	66 (99%)	-39.7	25.5	50.4	24.1	-
PEG-OH-MSN	PEG/NH ₂ /OH	91 (93%)	-46.8	-	-	-	-
PEG-NH-MSN	PEG/NH ₂ /OH	89 (99%)	-25.7	-	-	-	-

Regarding the external surface, XPS (Table 5.3) indicates a presence of 5% of nitrogen atoms in the NH-MSN and CN-MSN, which agrees well with the amount of nitrogen (-NH₂ or -CN) added in the synthesis (see chapter 3 section 3.1.1.2). The absence of N atoms in the COOH-MSN suggests an effective conversion of CN into COOH groups.

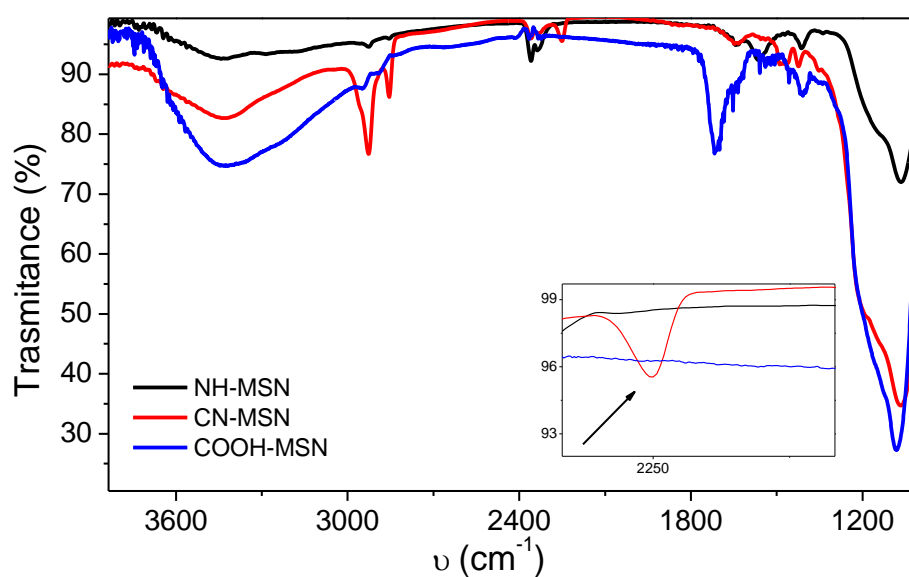


Figure 5.8. Infrared spectra of NH-MSN (black), CN-MSN (red) and COOH-MSN (blue) and from 2500 cm⁻¹ to 2150 cm⁻¹ (inset).

The three types of nanoparticles, NH-MSN, CN-MSN and COOH-MSN were also analyzed by FTIR (Figure 5.8). The most intense peak at $\nu = 1110\text{-}1000\text{ cm}^{-1}$ is assigned to Si-O-C and the broad band placed at $\nu = 3650\text{-}3200\text{ cm}^{-1}$ to the OH groups. It was not detected any indicative band for the amino group of NH-MSN nanoparticles, whereas a characteristic band of cyane group ($\text{C}\equiv\text{N}$) at $\nu = 2260\text{-}2240\text{ cm}^{-1}$ is recorded in CN-MSN. This band disappears in COOH-MSN system (Figure 5.8 blue) indicating the total conversion from $-\text{CN}$ to $-\text{COOH}$. Furthermore, the typical band of COOH group ($\text{COO-H } \nu=3550\text{-}2550\text{ cm}^{-1}$, $\text{C=O } \nu=1775\text{-}1650\text{ cm}^{-1}$) was also recorded in COOH-MSN.

5.1.1.3 Ormosil nanoparticles

The different organophilic silica source and different ratios respect to the main TEOS source are displayed in Table 5.4. Note here, the external surface of ormosil nanoparticles was functionalized with NH_2 groups, besides the intrinsic OH groups of the silica. Thus the characterization of ormosil nanoparticles is only focused on their morphologic shape and size distribution analyzed by TEM, Figure 5.9.

Table 5.4. Silica nanoparticles synthesized and their average size

Name	Characteristic	Shell	Size (nm)
M1-ON	TEOS:MTES (1:0.1)	NH_2/OH	44 ± 16
M2-ON	TEOS:MTES (1:0.5)	NH_2/OH	36 ± 7
M3-ON	TEOS:MTES (1:1)	NH_2/OH	39 ± 18
M4-ON	TEOS:MTES (1:2)	NH_2/OH	-
V1-ON	TEOS:VTES (1:0.1)	NH_2/OH	42 ± 7
V2-ON	TEOS:VTES (1:1)	NH_2/OH	40 ± 9
P1-ON	TEOS:PTES (1:01)	NH_2/OH	47 ± 10
P2-ON	TEOS:PTES (1:1)	NH_2/OH	49 ± 18
O1-ON	TEOS:OTES (1:1)	NH_2/OH	No

Firstly, different ratios were tested for TEOS:MTES (1:0.1, 1:0.5, 1:1 and 1:2) and the optimal proportion was then applied in the other synthesis. For the highest ratios of organophilic silica source nanoparticles did not form. For ratios 1:1 or lower, spherical nanoparticle with a size distribution of 50 ± 9 nm was achieved, although in some cases the size distribution is broader than the previously described MSN.

For the other silica source, VTES, PTES and OTES, ratios of 1:0.1 and 1:1 were prepared, except for OTES in which only the ratio 1:1 was studied. In the case of VTES and PTES, the obtained nanoparticles preserve the spherical shape and the size distribution of MSN, Table 5.4. Nevertheless, the synthesis with TEOS:OTES mixture was not successful.

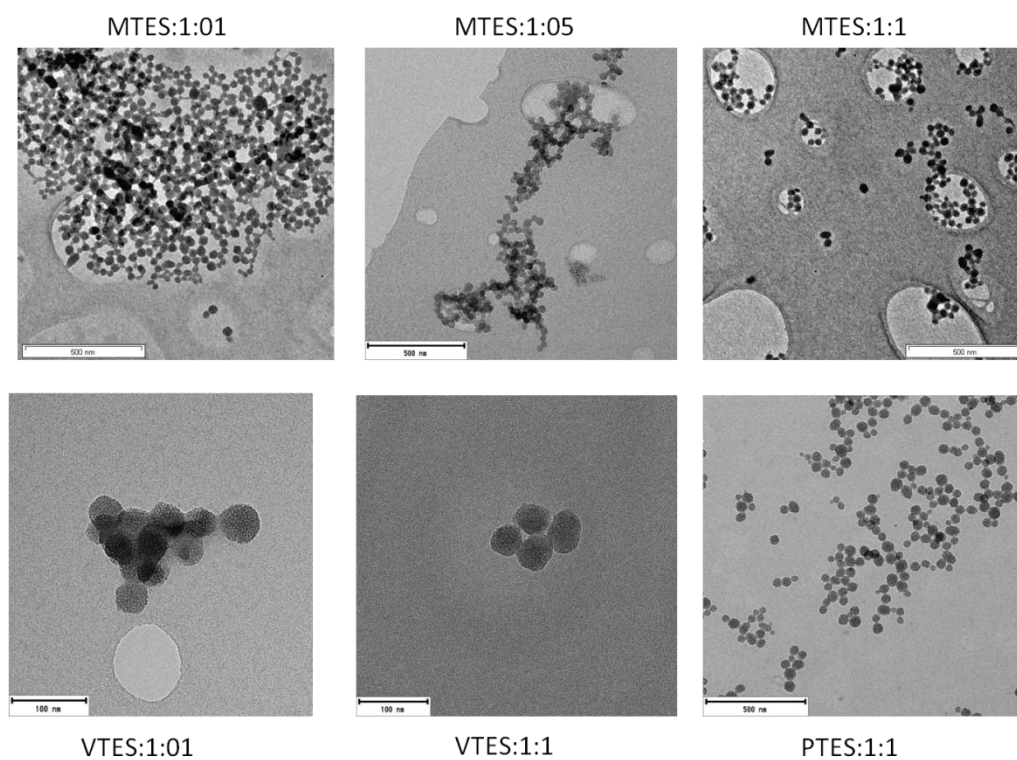


Figure 5.9. TEM images for ORMOSIL nanoparticles using different second silica source and proportions

5.1.1.4 Conclusions

The three types of silica nanoparticles (nonporous, mesoporous and ormosil) would be promising nanocarriers for fluorescence and photosensitizer dyes to be implemented in bioapplications. The shape and their size with a relatively narrow distribution, between 40 and 50 nm are suitable. Besides, these syntheses are reproducible. All the nanoparticles are synthesized with a core-shell structure, functionalizing the external surface with different groups to allow the anchorage of organic molecules of interest. In the case of nonporous and mesoporous nanoparticles, different shell compositions were produced (OH/NH₂ or OH/COOH), extending the type of organic molecules to be tethered.

For MSN nanoparticles, especially for NH-MSN the stability in water was poor and not appropriate for the biomedical field, but after tethering polyethylene glycol molecules to their external surface this problem was successfully resolved.

Regarding ormosil silica nanoparticle, synthesis with different ratios of the organophilic silica source respect to TEOS was studied. In this context, similar spherical particles of 50 nm size were reached with ratios of 1:1 or lower with a more organophilic internal surface.

5.1.2 Fluorescent silica nanoparticles for bioimaging

Different approaches were carried out to obtain fluorescence silica nanoparticles. The main results of those systems will be explained as follows: In the first part (section 5.1.2.1) different fluorescence dyes were hosted in the core of the nanoparticle. Depending on the nature of the nanoparticle core the approach used differs; *i*) for nonporous nanoparticles a fluorescent silylated dye, perylene (Figure 3.4 section 3), was covalently linked to the OH of the core of the silica nanoparticles, *ii*) for mesoporous silica nanoparticles different types of rhodamines were loaded *in situ* during the synthesis, by optimization the dye concentration added to the synthesis gel and *iii*) fluorescence ormosil nanoparticles were synthesized, encapsulating rhodamine 101 inside a more organophilic silica core and the final concentration of the loaded dye is compared with the MSN. Finally, for comparison, a rhodamine is also anchored at the external surface of the nanoparticles (section 5.1.2.2). The photophysical properties of these systems were characterized and the most interesting fluorescent nanosystems were tested in HeLa cells, (section 5.1.2.3).

5.1.2.1 Dye embedded into nanoparticles core

Fluorescence nonporous nanoparticles

The only approach to loaded fluorescent dyes into nonporous nanoparticles core is by the covalent link of the dye to the functional groups inside the nanoparticle. For that, a silylated perylene dye, Figure 3.4 in the experimental section, was directly added to the synthesis gel to be anchored to the OH groups of the silica core as the nanoparticles are forming.^{28,29} As a result, a pink powder was obtained, indicative of the presence of perylene dye trapped inside the nanoparticle (Figure 5.10). The size of nonporous nanoparticles with tethered perylene of 45 ± 11 nm (data from DLS technique) was similar to that obtained for nonporous silica nanoparticles without dye (40 nm).

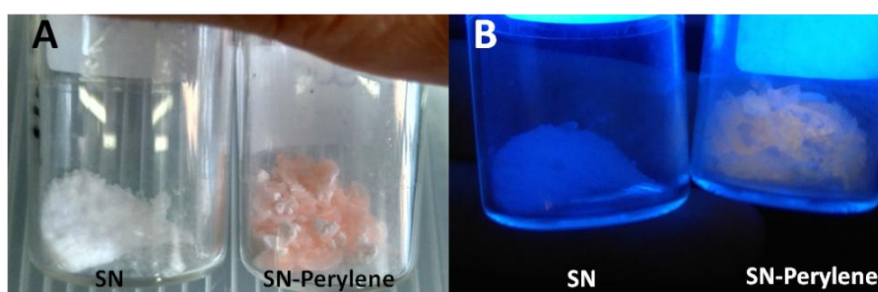


Figure 5.10. Nonporous nanoparticles in the absence (SN) and the presence of perylene inside under visible light (left) and ultraviolet light (right)

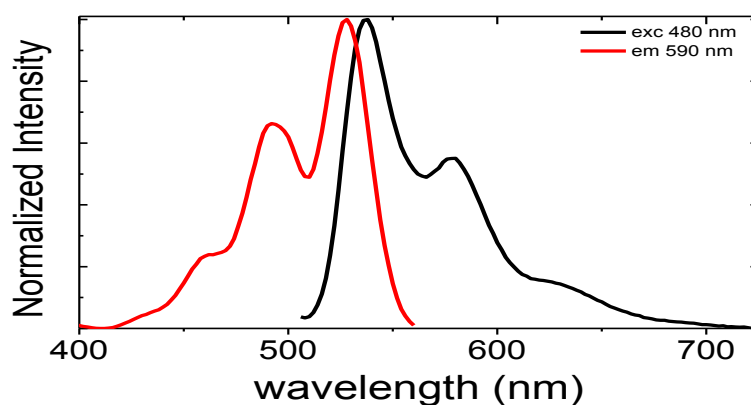


Figure 5.11. Normalized excitation (red) and emission (black) spectra of perylene nonporous nanoparticles

The photophysical properties of the perylene-loaded nanoparticles were characterized in ethanol suspension. Figure 5.11 shows similar excitation and emission spectra for the perylene inside the nanoparticles mainly centered at 522 nm and 538 nm, respectively to those recorded for perylene in solution, with absorption and fluorescence bands mainly centered at 525 nm and 538 nm, respectively.^{28–30} Note here that, although a very high concentration of dye was added in the gel a low amount was finally tethered, probably due to the poor solubility of this dye in ethanol solvent. Indeed, the characteristic absorption band of perylene was not detectable and the spectrum was dominant only by scattering signal; consequently, the dye uptake could not be quantified.

Fluorescence mesoporous nanoparticles

In this section, six different commercial rhodamines were encapsulated into the mesoporous silica nanoparticles, Figure 3.3 in experimental chapter 3, rhodamine 6G (R6G), sulforhodamine 640 (R640), rhodamine 19 (R19), rhodamine 101 (R101), rhodamine 700 (R700) and rhodamine 800 (R800). Generally, rhodamines are xanthene derivative chromophores with excellent photophysical properties (intense absorption and emission bands in the green-red region). Nevertheless, they have some drawbacks to be used as biomarkers, such as the lack of selectivity for a specific tissue or organelle and low photo- and thermo-stability.³¹ For that reason, MSN was used as potential nanocarriers for fluorescent rhodamines in order to overcome these limitations. The photophysical properties of these six compounds in ethanol are summarized in Table 5.5.

Table 5.5. Photophysical properties in ethanol for commercial rhodamines; absorption wavelength (λ_{ab}) absorption coefficient (ϵ), fluorescence wavelength (λ_{fl}), fluorescence quantum yield (Φ_{fl}) and lifetime (τ_{fl})

Dye	λ_{ab} (nm)	ϵ ($10^4 M^{-1} cm^{-1}$)	λ_{fl} (nm)	Φ_{fl}	τ_{fl} (ns)
R19	524.0	9.5	549.0	0.77	4.03
R6G	530.0	11.7	551.0	0.88	3.94
R640	575.5	3.7	595.0	0.86	4.50
R101	576.5	8.4	600.0	0.89	4.81
R700	647.0	7.3	675.0	0.17	2.68
R800	681.5	2.6	704.0	0.22	1.93

In order to optimize the amount of the occluded dye in terms of fluorescence properties of the dye-nanoparticles, different dye concentrations were added to the synthesis sol-gel, varying from $5 \cdot 10^{-5}$ M to $1 \cdot 10^{-2}$ M for R6G, Table 5.6.³² The optimization of concentration consists in reaching a relatively high loading of dye molecules inside the core without diminishing the fluorescence emission quantum yield of the hybrid nanosystem or altering the size and the morphology of the nanoparticles. In this regard, the size and morphology were analyzed by SEM, the amount of the dye was quantified dissolving the silica matrix in KOH (1M) (see section 3.2.1.6 in chapter 3), and the photophysical properties were registered in solid powder, Table 5.6.

According to the SEM images, the size, morphology, and distribution of the nanoparticles did not change when the dye was trapped inside the core, independently of the concentration added to the synthesis sol-gel, Figure 5.12.

Table 5.6. MNS-R6G characterization: initial dye concentration in the gel, occluded dye moles per gram, absorption wavelength (λ_{ab}) and fluorescence (λ_{fl}), fluorescence quantum yield (Φ_{fl}) and lifetime (τ_{fl}) measured in powder³²

Sample	[R6G] Added to the sol-gel (M)	R6G at the MSN core ($\mu\text{mol/g}$)	λ_{ab} (nm)	λ_{fl} (nm)	Φ_{fl} (%)	τ_{fl} (ns)
MSN-R6G-1	$1 \cdot 10^{-2}$	14	529.0	566.0	<1	0.44 (77%) 3.02 (23%)
MSN-R6G-2	$1 \cdot 10^{-3}$	11	525.0	553.0	3	0.76 (80%) 3.11 (20%)
MSN-R6G-3	$5 \cdot 10^{-4}$	0.67	529.0	546.0	30	3.90
MSN-R6G-4*	$1 \cdot 10^{-4}$	0.06	528.0	543.0	-	3.90
MSN-R6G-5*	$5 \cdot 10^{-5}$	-	528.0	542.0	-	-

* In this case, the encapsulated dye molecules were not enough to determinate the fluorescence quantum yield

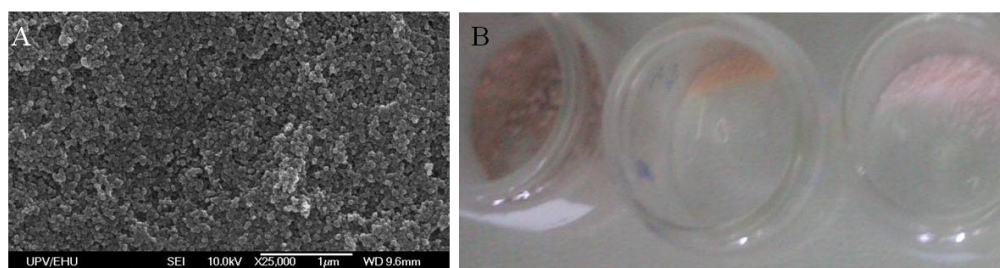


Figure 5.12. SEM image of the nanoparticles with encapsulated R6G (A) and a picture of the NP powder for different encapsulated R6G concentrations (using concentrations in synthesis gel $1 \cdot 10^{-2}$ M (left), $1 \cdot 10^{-3}$ M (middle) and $5 \cdot 10^{-4}$ M (right) (B).

According to the results depicted in Table 5.6, the amount of dye loaded into the samples MSN-R6G-4 and MSN-R6G-5 was too low. Thus, the minimum dye concentration in the gel to ensure the inclusion of rhodamine molecules inside the MSN is set at $\geq 10^{-4}$ M. On the other hand, a more intense absorption band is recorded as the amount of R6G added in the gel increases, indicating a gradual increase of dye uptake inside the nanoparticles. Indeed, the color of the powder became more intense as the amount of the dye added increased, Figure 5.12.B. Conversely, the fluorescence efficiency (define as the fluorescence intensity at the peak divided by the absorbance at the excitation wavelength) decreased with the dye loading, being maximum for a dye concentration in the gel of $5 \cdot 10^{-4}$ M (sample MSN-R6G-3, Table 5.6), with a quantum yield of 30 % measuring the power in the integrating sphere, (Figure 5.13.B and Table 5.6).^{32,33} Note here, despite the quantum yield of this sample MSN-R6G-3 is not as good as R6G in solution (88%, Table 5.5) is high enough to allow their tracking under conventional fluorescence microscopy and therefore suitable for bioimaging.³² The poor or negligible emission of samples with high dye loading (MSN-R6G-1 and MSN-R6G-2) cannot be assigned to dye molecular aggregation inside the nanoparticles since the shape of the absorption spectra did not undergo any changes and it is likely attributed to inner-filters. Indeed, the bathochromic shift registered in the fluorescence spectra of 20 nm for MSN-R6G-1 with respect to sample MSN-R6G-3 is indicative of the influence of reabsorption-reemission phenomena. On the other hand, the slight hypochromic shift in the spectroscopic bands of the R6G into the silica nanoparticles with respect to R6G in solution, Figure 5.13.C and in Table 5.5 and 5.6, was ascribed to a more hydrophobic environment as a consequence of the presence of the alkane chains of the surfactant in the silica core. Moreover, the spectra of the NP-R6G are wider relative to R6G in solution, which is a typical effect of dyes in adsorbed-state with distorted vibrational states.

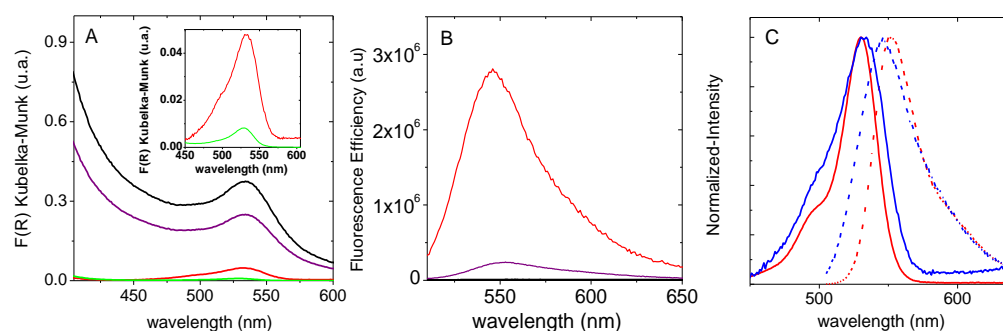


Figure 5.13. Representative absorption spectra (A), fluorescence spectra for MSN-R6G-1 (black), MSN-R6G-2 (purple), MSN-R6G-3 (red) (B) and normalized absorption and fluorescence spectra of R6G in solution (red) and in powder (blue) (C)

Occlusion of other rhodamines in the silica nanoparticles core

Other rhodamines, R640, R700, R800, and R101, were also encapsulated, applying the previously optimized dye concentration in the gel for R6G ($5 \cdot 10^{-5}$ M). These rhodamines show absorption and emission bands red-shifted with respect to R6G, being of greater interest for bioimaging.

Unfortunately, the R700 and R800 did not endure the basic conditions of the synthesis of MSN, and they were degraded before being entrapped. In contrast, the synthesis of fluorescent nanoparticles with R640 and R101 was successfully carried out and the results are showed in Table 5.7.

The amount of the dye embedded in MSN-R640 and MSN-R101 is similar to that estimated for MSN-R6G-3. Regarding their photophysical properties, in both cases, a blue shift in the absorption and fluorescence bands was registered, as in the case of MSN-R6G-3, previously ascribed to a more hydrophobic environment inside the silica core by the presence of surfactant molecules with long carbon chains. The fluorescence quantum yield values obtained for the measurements in powder for MSN-R640 and MSN-R101 systems are 52% and 32%, respectively, offering suitable nanoparticles for fluorescence bioimaging.

Table 5.7. MNS-dye characterization: moles per gram loaded in the silica core, absorption wavelength (λ_{ab}) and fluorescence (λ_{fl}), fluorescence quantum yield (Φ_{fl}) and lifetime (τ_{fl}) measured in powder.

Samples	Dye ($\mu\text{mol/g}$)	λ_{ab} (nm)	λ_{fl} (nm)	Φ_{fl} (%)	τ_{fl} (ns)
MSN-R640	1	570.0	590.0	52	4.42
MSN-R101-1	0.56	566.0	587.0	35	-

Fluorescence ormosil nanoparticles

Generally, the dye loading reached inside silica nanoparticles, in 0.5-1 $\mu\text{mol/g}$ range, is considered low. With the aim of increasing the dye uptake, several fluorescent ormosil silica nanoparticles with different organic groups were synthesized (Figure 3.1 section 3.1.1.3) in order to modify the porous environment and size. These experiments were carried out with R101 using the previously optimized dye concentration of $5 \cdot 10^{-4}$ M in the sol-gel.

Table 5.8 shows the main results of the different synthesis carried out for fluorescent ormosil silica nanoparticles. The occluded dye amount in the ormosil silica nanoparticles has slightly increased but the size of the nanoparticles tended to be smaller. Note here that the fluorescence quantum yields, now recorded in acetonitrile, selected as the best solvent to get stable suspensions of these particles, according to previous studies (data obtained via DLS),³² are larger than those derived from the measure in powder, likely ascribed to a reduction of inner-filter effects in comparison to measurement in bulk powder.

In order to increase the amount of the dye inside but keeping constant the size of the nanoparticles, the syntheses, instead of at 60 °C were repeated at 70°C and at 80°C, using a dye concentration in the gel of $2.5 \cdot 10^{-4}$ M (Table 5.9) and $5 \cdot 10^{-4}$ M, respectively. At 70°C, the amount of R101 loaded dye has considerably enhanced with a suitable particle size of around 60 nm in all the cases (Table 5.9). Conversely, the synthesis performed at 80 °C ($5 \cdot 10^{-4}$ M) led to a huge increase in nanoparticles size obtained particles of around 500 nm, not suitable for biomedical application (data not shown).

Table 5.8. Synthesis at 60 °C of different ormosil silica nanoparticles with an initial concentration of R101 in the sol-gel of $5 \cdot 10^{-4}$ M, the amount of loaded dye inside the nanoparticles, the average size by TEM and the fluorescence quantum yield in acetonitrile suspensions.

Sample	Mixture	Ratio	Dye ($\mu\text{mol/g}$)	Size (nm)	Φ_f (%)
MSN-R101-1	TEOS	1:0	0.56	47 \pm 9	70
M-ON-R101-1	TEOS:MTES	1:1	0.81	54 \pm 8	50
V-ON-R101-1	TEOS:VTES	1:1	0.96	29 \pm 5	75
P-ON-R101-1	TEOS:PTES	1:1	0.94	39 \pm 7	45

Table 5.9. Synthesis at 70°C with the initial concentration of R101 in the sol-gel of $2.5 \cdot 10^{-4}$ M, amount of occluded dye inside the nanoparticles and the average size of the nanoparticles by TEM.

Sample	Mixture	Ratio	Dye ($\mu\text{mol/g}$)	Size (nm)
MSN-R101-2	TEOS	1:0	9.98	60 \pm 9
M-ONR101-2	TEOS:MTES	1:1	7.54	58 \pm 11
V-ON-R101-2	TEOS:VTES	1:1	3.64	63 \pm 14
P-ON-R101-2*	TEOS:PTES	1:1	-	-

* In this case, the nanoparticles did not form completely

Indeed, the highest dye loading inside the nanoparticles was reached for “common” MSN with only TEOS as silica surface (sample MSN-R101-2 in Table 5.9) at 70°C, and a dye concentration in the sol-gel of $2.5 \cdot 10^{-4}$ M. Thus, this sample is considered optimum and will be further tested in HeLa cells.

5.1.2.2 Dye grafted at the nanoparticles shell

Another approach to obtain fluorescence nanoparticles is by tethering of fluorophores at the external surface of the nanoparticles, *i.e.* by carbodiimide method, detailed in section 3.1.2.2, Scheme 3.5. In this case, only rhodamines with a carboxylic group could be anchored to the external amine group of MSN, such as R19 and R101, Figure 3.3.

However, only R101 was successfully linked to the external surface of the silica nanoparticles, since R19 in basic conditions form a non-fluorescent intramolecular spirolactone (Figure 5.14.C). Indeed, when an aprotic solvent is used, *i.e.* acetonitrile, the zwitterionic form (Figure 5.14.B) is not stable and as a consequence, the lactone is formed. Nevertheless, the formation of the lactone ring is less favorable in R101 due to steric hindrance.^{34–36} For that reason, R101 is successfully anchored to the amine groups of the silica external surface (MSN-S-R101) but not R19. In fact, the estimated amount of the R101 tethered outside, by dissolving the silica matrix (section 3.2.1.6 in chapter 3), is 22 $\mu\text{mol/g}$, considerably higher than the dye embedded inside the core, Table 5.7.

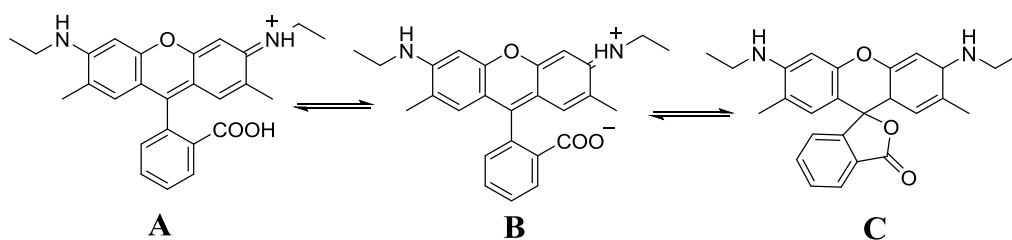


Figure 5.14. Molecular structures of Rhodamine 19 in equilibrium: cationic (A), zwitterionic (B) and lactone (C)

The photophysical properties of MSN-S-R101 were first characterized in acetonitrile. The absorption and emission spectra are shown in Figure 5.15. The respective bands are broader and blue-shift respect to those in ethanolic solution, a similar effect as for the rhodamines inside the core (Figure 5.15 blue). Regarding fluorescence quantum yield, only 8 % is recorded. However, in chloroform, a higher fluorescence of 55 % is attained, ascribed to better stability of the chloroform suspension compared to acetonitrile. Probably, the own presence of the dye at the

external surface induce a more hydrophobic shell and consequently, the nanoparticles are more stabilized in a less polar solvent, chloroform as it has demonstrated in previous work for rose bengal linked in the external surface of these nanoparticles.³² It is thus of crucial importance to obtain stable nanoparticle suspensions to obtain good emission ability for future implementation.

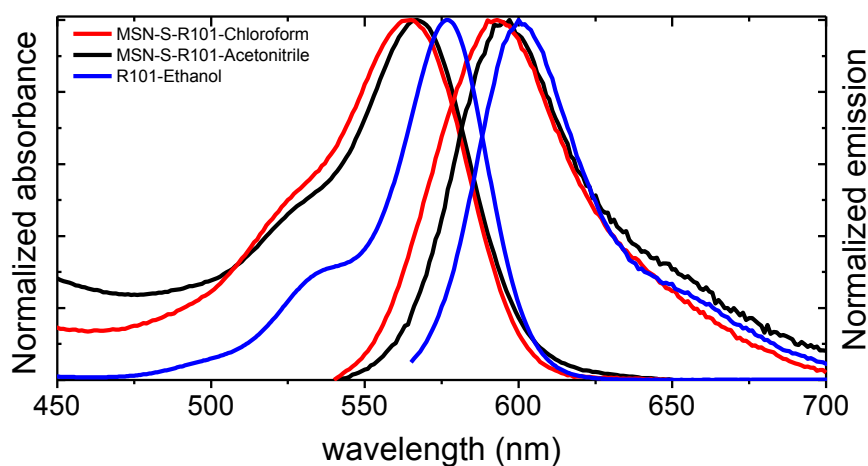


Figure 5.15. Normalized absorption and emission spectra of MSN-S-R101 in chloroform (red) and acetonitrile (black) together with rhodamine 101 in ethanol (blue).

5.1.2.3 *In vitro* experiments

After the previous study to design the fluorescence nanoparticles able to be used in fluorescence bioimaging, the two most promising hybrid nanosystems, MSN-R101-2 and MSN-S-R101 (R101 embedded in the core vs R101 grafted in the shell) were chosen in order to test *in vitro* their cytotoxicity and capability to be internalized inside the HeLa cells.

As has been mentioned above, these systems do not show good stability in aqueous media. For that reason, PEG (2000 Da) was anchored to the external hydroxyl groups of the silica nanoparticle shell, which confers good stability in water (see previous results in Table 5.3). The DLS results related to the hydrodynamic ratio and zeta potential together with the photophysical properties of the pegylated nanoparticles, MSN-R101-2-PEG and MSN-S-R101-PEG, characterized in water, are shown in Table 5.10.

Table 5.10. Hydrodynamic diameter (in nm), zeta potential (in mV), absorption peak (λ_{ab} in nm) fluorescence peak (λ_{fl} in nm) and fluorescence quantum yield (Φ_{fl}) of samples MSN-R101-2-PEG and MSN-S-R101-PEG in water.

Sample	DLS (nm)	Z pot (mV)	λ_{ab} (nm)	λ_{fl} (nm)	Φ_{fl}^a
MSN-R101-2-PEG	69	-21	572.0	594.0	0.51
MSN-S-R101-PEG	64	-23	571.0	595.0	0.25

^a Reference R101 in water $\Phi_{fl} = 0.77$

After the pegylation of the external surface, both nanosystems are stable in water, as confirmed by the Z pot values. Furthermore, the quantum yield obtained in water is relatively high, especially for the MSN-R101-2-PEG. Note here that the amount of the dye in MSN-S-R101 is more than double with respect to MSN-R101-2 (22 $\mu\text{mol/g}$ vs 10 $\mu\text{mol/g}$, respectively) and reabsorption-reemission processes and/or molecular aggregation process might have effect reducing its fluorescence.

First of all, the cytotoxicity at different incubated concentrations (0.1 -1000 $\mu\text{g/mL}$) of both systems was tested in HeLa cells (Figure 5.16). Sample MSN-R101-2-PEG shows a higher cytotoxic effect in comparison with MSN-S-R101, killing 20 % of the HeLa cells at 1 $\mu\text{g/mL}$ while MSN-S-R101-PEG did not show any cytotoxicity till a concentration of 100 $\mu\text{g/mL}$. This difference is attributed to the possible realize of the surfactant CTAB from the core of sample MSN-R101-2-PEG, used as the template in the synthesis of the mesoporous nanoparticles, which has been proved to be toxic to many types of cells.³⁷⁻⁴⁰ The surfactant was removed before the R101 anchorage in sample MSN-S-R101, whereas this process cannot be undertaken in sample MSN-R101-2 since it would affect also R101 dye inside the pores.

Interestingly, the nanoparticles were internalized in the cells and they were specifically accumulated into the lysosomes as supported by the co-localization experiments shown in Figure 5.17, where the lysotracker (green) and the nanoparticles (red) perfectly merged. Note that the nanoparticles offer a sharper quality of the lysosomes bioimaging with respect to commercial lysotrakers.

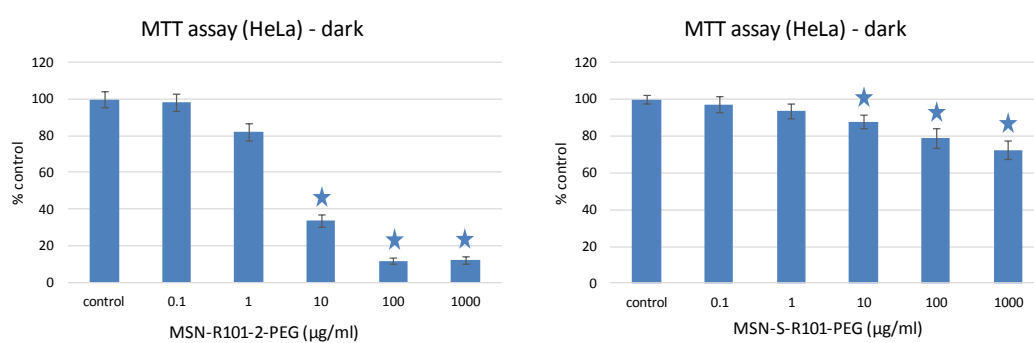
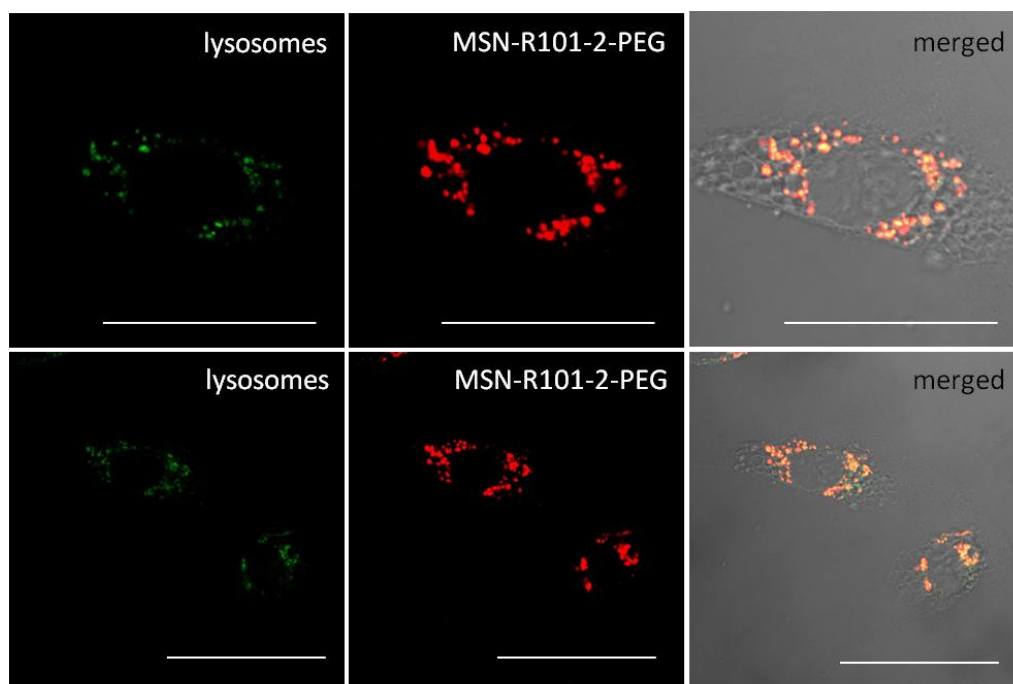


Figure 5.16. Results of MTT assay for MSN-R101-2-PEG (left) and MSN-S-R101-PEG (right). *Significant differences with respect to controls according to the Kruskal Wallis test followed by the Dunn's test or Mann-Whitney's test ($p < 0.05$). Statistical analyses were conducted using the statistical package SPSS v.25 (SPSS Inc., IBM Company, Chicago, USA).



Scale bars = 100 μm

Figure 5.17. Fluorescence images of MSN-R101-2-PEG in HeLa cells at 1 $\mu\text{g/mL}$; colocalization in lysosomes (green-left), rhodamine 101 (red-middle) and merged (right). Scale bar 100 μm

Thus, by fluorescence imaging is demonstrated that pegylated silica nanoparticles systems are internalized into the cells and specifically accumulated into the lysosomes. This is valuable information, which will be extended for the nanosystems described in the next section, consisting of silica nanoparticles with different PSs grafted at the external surface. In fact, there are many of the PS-silica nanosystems which are not fluorescent and consequently cannot be tracked by optical microscopy. Nevertheless, the above-demonstrated cell internalization and cell distribution will be assumed for all the new systems, designed to be implemented in PDT, of the following section 5.1.3.

5.1.2.4 Conclusions

It is demonstrated the capability of the different types of silica nanoparticles to embedded fluorescent dyes for bioimaging purposes. In this context, a silylated fluorophore is needed to be trapped into the core of the nonporous nanoparticles while dyes were successfully embedded in mesoporous nanoparticles without any chemical modifications even to a higher extent. Indeed, the use of ormosil nanoparticles did not markedly increase the amount of loaded dye. After the optimization of the dye occlusion process into the mesoporous silica nanoparticles core (70°C with an initial dye at the sol-gel of $2.5 \cdot 10^{-4}$ M), promising fluorescent nanosystems are achieved, able to internalize and localize in the lysosomes of HeLa cells, which provides high-quality images with respect to commercial lysotracker dyes in solutions. As a disadvantage, these nanosystems show cytotoxic effects at incubated concentrations ≥ 1 $\mu\text{g/mL}$, assigned to the possible leaking of toxic surfactant molecules³⁷⁻⁴⁰ in the nanoparticle core. To solve this drawback the dye can be anchored at the external surface after removing the surfactant.⁴¹

5.1.3 Photosensitizer Mesoporous silica nanoparticles for photodynamic therapy

In the previous chapter 4, several new PSs were proposed as PDT agents and they were tested in HeLa cells. The main goal in this section is the use of silica nanoparticles as nanocarriers of PSs to improve their therapeutic action by increasing their solubility in aqueous media together with the selectivity to tumor cells. For that, the photosensitizers should present organic groups susceptible to be tethered to the

functionalized external surface of the silica nanoparticle. Firstly, this approach is optimized with the commercial PS, Rose Bengal (section 5.1.3.1), where different possibilities to anchor PS, polyethylene glycol and folic acid are explored.^{32,42–45} Then, in section 5.1.3.2, the optimized synthesis is applied to other commercial PSs (Chlorine e6 and thionine, see Table 3.1 in experimental chapter 3) and to new lab-made based on BODIPY structure photosensitizers (see Table 3.2 in experimental chapter 3).^{24–26,46–48} Note here, that some of the new BODIPY-based PSs, detailed in chapter 4, section 4.2.1.2 have demonstrated poor internalization into the HeLa cell as a consequence of their lack of solubility in physiological media. Finally, the phototoxic action of the new PS-silica nanohybrid systems was tested in HeLa cells and compared to the homologous PS in solution.

5.1.3.1 Optimization of PS- silica nanoparticles with Rose Bengal

Different PS-loaded silica nanoparticles with rose bengal covalently linked by its carboxylic function to amine groups and to intrinsic hydroxyl groups of the external surface of MSN (following the synthesis route depicted in scheme 3.5 and 3.8, respectively) were synthesized. Besides rose bengal (RB), polyethylene glycol (PEG), necessary to avoid the flocculation of the nanoparticles in aqueous media, is also anchored at the external surface. Indeed, in previous work,³² MSN with RB grafted at the external NH_2 or OH showed instantaneous flocculation in water media and their stability only enhanced in less polar solvents such as chloroform. The presence of the organic dye at the surface of the silica nanoparticles induces an interparticle aggregation process (detected by Visible spectra) even in acetonitrile as solvent. This particle-particle aggregation is detrimental to singlet oxygen production. Thus, stable nanoparticle suspension in water is crucial to obtain competitive hybrid nanocarriers for PDT.³²

In this section, different combinations for the anchorage of RB and PEG are synthesized and characterized. First of all, several PEG molecules with different chain length (750 Da, 2000 Da and 5000 Da), were linked to the amine groups of the silica and RB to the OH-group (samples G1a, G1b and G1c in Table 5.11)

Table 5.11. Different MSN synthesized and the results obtained the amount of RB tethered in the shell, the nanoparticle size by DLS in water and their Zeta potential

System	Characteristic	PEG length (Da)	DLS size (nm)	Zpot (mV)	[RB] ($\mu\text{mol/g}$)
G1a	RB-OH-MSN PEG-NH ₂ -MSN	750	130	-4.3	-
G1b	RB-OH-MSN PEG-NH ₂ -MSN	2000	99	-25.0	20
G1c	RB-OH-MSN PEG-NH ₂ -MSN	5000	114	-25.0	20
G2	RB-NH ₂ -MSN PEG-OH-MSN	2000	95	-29.0	10
G3	RB-OH-MSN PEG-OH-MSN	2000	88	-31.0	20

The low zeta potential registered for sample G1a indicates that attaching the shorter PEG derivative of 750 Da (Table 5.11) does not improve the stability in water for RB-silica nanoparticles. Indeed, the value of around -4 mV is similar to that derived for naked NH-MSN without RB (Table 5.3). On the contrast, PEG of higher molecular weight, 2000 Da and 5000 Da (samples G1b and G1c in Table 5.11) have led to Zpot values of -25 mV, indicating better stability of these nanosystems in water. Since too long PEG chains can impede the internalization into the cells, PEG of 2000 Da was selected as the most suitable chain. Thus, 2000-PEG was also tethered to the OH-groups of their external surface (samples G2 and G3 in Table 5.11), leading to even higher Zpot values and smaller hydrodynamic size respect to samples G3, offering nanosystems with improved suspensions in water. This fact is likely assigned to a higher presence of PEG at the external surface when is linked to the majority OH-groups of the silica external surface respect to the NH₂-groups.

The absorption spectra were recorded for every RB-MSN-PEG system in water (Figure 5.18), except G1a owing to its poor stability, after stirring for at least 24 hours. Generally, the main band is hypochromic shifted and broader than that of RB in water solution, likewise as the previous fluorescent MSN. However, important

differences are found in the shape of the main absorption band of the nanosystems. G1b and G1c show more prominent shoulders at both sides of the main absorption band indicating a higher dye aggregation tendency. Indeed, according to the absorption spectra, the dye aggregation follows the tendency $G1b \sim G1c > G3 > G2$. Because of the estimated quantity of grafted RB at the OH groups of the external surface of silica nanoparticles is equal (see samples G1b, G1c and G3 in Table 5.11), the dye aggregation can be considered as an interparticle process. This process is likely mediated by the fewer presence of the PEG molecules at the external surface when are linked to the NH_2 groups respect to the intrinsic OH-functional groups of the silica, as previously confirmed by DLS results. Accordingly, the estimated RB amount tethered at external NH_2 is also smaller, around half of the load obtained for the RB at the OH-groups (Table 5.11). From these results, sample G3, with PS and PEG at OH-groups, is expected to be the best nanosystems for PDT in terms of maximized PS loading with good stability in aqueous media.

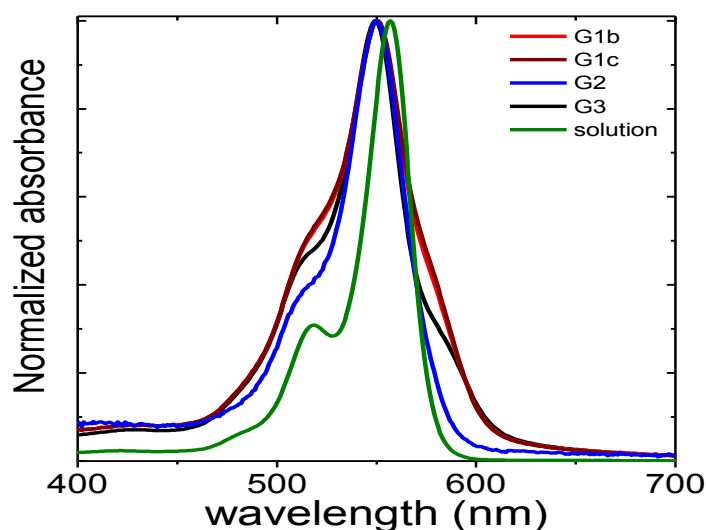


Figure 5.18. Normalized absorption spectra of PS-MSN-PEG G1b (red), G1c (brown) G3 (black), G2 (blue), and rose bengal in water solution (green).

Interestingly, all the RB-MSN-PEG systems, except for G1a, show similar singlet oxygen quantum yield, with values around $\Phi_{\Delta} \sim 0.80-0.85$, in deuterated methanol, MeOD, similar to that registered for RB in the same solvent ($\Phi_{\Delta}=0.86$). The fact that RB grafted to MSN is able to generate singlet oxygen as efficiently as the RB in solution is a good indicator for the potential use of these nanosystems in PDT.^{32,42,49}

The phototoxicity efficiency of the most representative nanosystems, G1b, G2, and G3, was tested *in vitro* in HeLa cells. The three carriers pegylated with PEG-2000 Da, but the grafting of PEG and RB to the available functional groups of the silica nanoparticle (NH_2 or OH) are different from sample to sample (Table 5.11).

Importantly, none of the three nanosystems show any cytotoxicity under dark conditions, confirming the biocompatibility of the silica nanocarriers (Figure 5.19). However, under green light irradiation (5.2 J/cm^2), they show differences in their ability to kill cells. According to MTT assays, G1b does not show any ability to damage cells even at the highest normalized RB concentration in the MNS of $1 \cdot 10^{-5} \text{ M}$ while G2 and G3 induce a cellular death of around 85% and 60%, respectively. The significant differences in the phototoxicity action between G1b respect to G2 and G3 can be explained in terms of the less quantity of PEG anchored to amine groups, which might lead to nanoparticle aggregation in culture media, likely impeding their internalization into the cells. Contrary, G1 and G2, both samples pegylated at their respective OH-groups of the external surface display phototoxic effects. Although G2 shows a higher cell killing action under irradiation, the fact that the PS-loaded in sample G2 is half than G3 compels to use a double amount of nanoparticles, which under a practical point of view for the implementation of PDT could be disadvantageous. Indeed, at the same amount of nanoparticles incubated in the cell of G2 and G3, a much higher therapeutic effect would expect for G3.

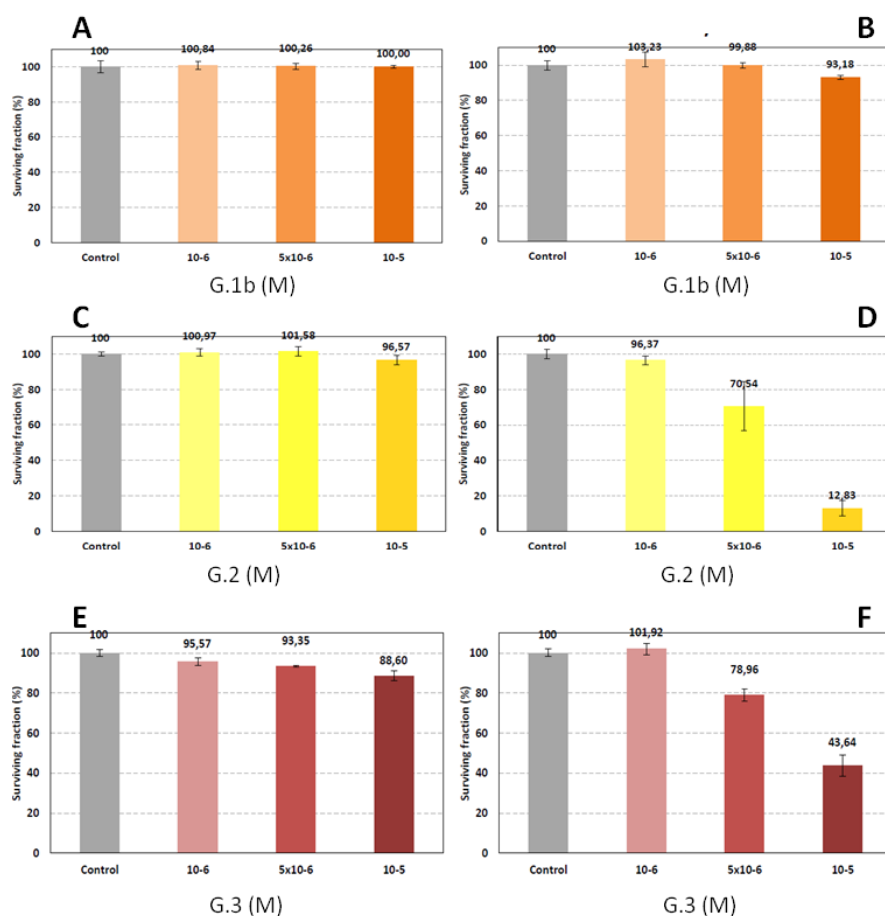


Figure 5.19. MTT assays for G1b (orange) and G2 (yellow) G3 (red) in dark condition (A, C and E) and under green irradiation 5.2 J/cm^2 (B, D and F) normalized to RB concentration

A step further for the optimization of the system for being applied as potential nanoacarrriers in PDT applications is the use of a biotarget molecule for selective delivery of the system to the tumor. As it was described above, folic acid (FA) has a high affinity for the folate receptor proteins (FR), which are commonly overexpressed in the membranes of many human cancer cells (*i.e.* ovarian, endometrial and kidney cancer)^{18,48,50} favoring a cellular uptake via endocytosis.

In sample G3 (in which RB and PEG are simultaneously grafted at the OH), considered as the most interesting system, the folic acid molecule was anchored (G3-FA) through its carboxylic function to the NH_2 of the external surface of the silica

via carbodiimide method (Scheme 3.5 B in chapter 3). The presence of FA at the silica nanoparticles was verified by absorption spectroscopy (Figure 5.20), where the characteristic band of the FA, centered at 355 nm⁵¹ was detected together with the main band of rose bengal at 557 nm. However, the quantification of the amount of FA at the external surface was not a trivial task since the position of its band lies into the region of the scattering contribution of the nanoparticles (Figure 5.20)

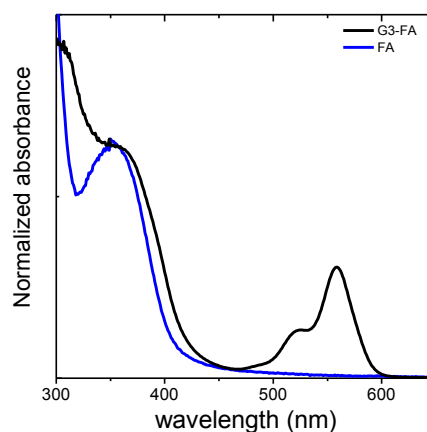


Figure 5.20. Normalized absorption spectra of folic acid (blue), G3 (brown) and G3-FA (black).

In vitro experiments in HeLa cells are now carried for G3-FA (Figure 5.21.A) to be compared with the previous results derived for G3 (Figure 5.19.F) to study the effect of the FA at the external surface. Besides, RB in solution is also tested (Figure 5.21.B) for comparison. Importantly, the G3-FA system shows a much greater ability to kill cells under green irradiation respect to G3, endorsing the positive effect of FA for the internalization into HeLa cells. Moreover, the photoactivity of G3-FA is also higher than the RB in solution at the same concentration (Figure 5.21). For instance, a cell survival of 55% vs 75 % is obtained for G3-FA and RB in solution at a normalized RB concentration of 0.5 μM , or in the case of 1 μM , the fraction of cellular death is already 80% for G3-FA, while a 50% is reached for RB in solution.

Although with a modest quantum yield ($\Phi_{\text{R}}=0.10$ in MeOH), RB can be tracked by fluorescence microscopy, Figure 5.22. The images clearly show a much higher internalization for G3-FA respect to RB in solution at the same RB concentration (1 μM), a crucial factor for resultant greater phototoxicity.

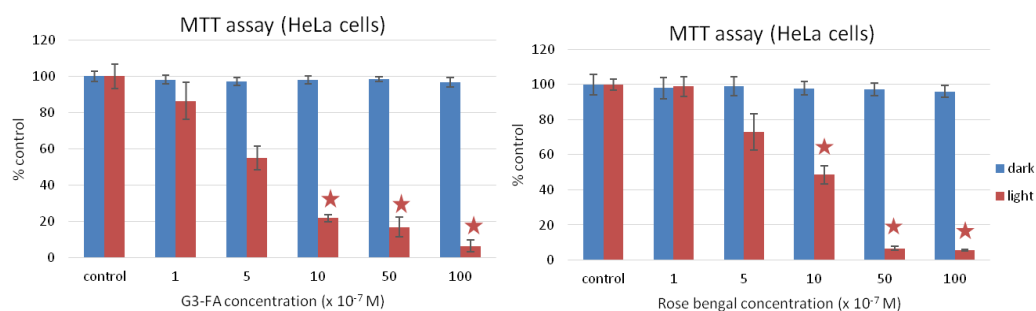


Figure 5.21. MTT assay results for G3-FA system (left) and rose bengal in solution (right) under dark conditions (blue values) and green irradiation at 518 nm 10 J/cm² (red values), normalized to rose bengal concentration.*Significant differences with respect to controls according to the Kruskal Wallis test followed by the Dunn's test or Mann-Witney's test ($p < 0.05$). Statistical analyses were conducted using the statistical package SPSS v.25 (SPSS Inc., IBM Company, Chicago, USA).

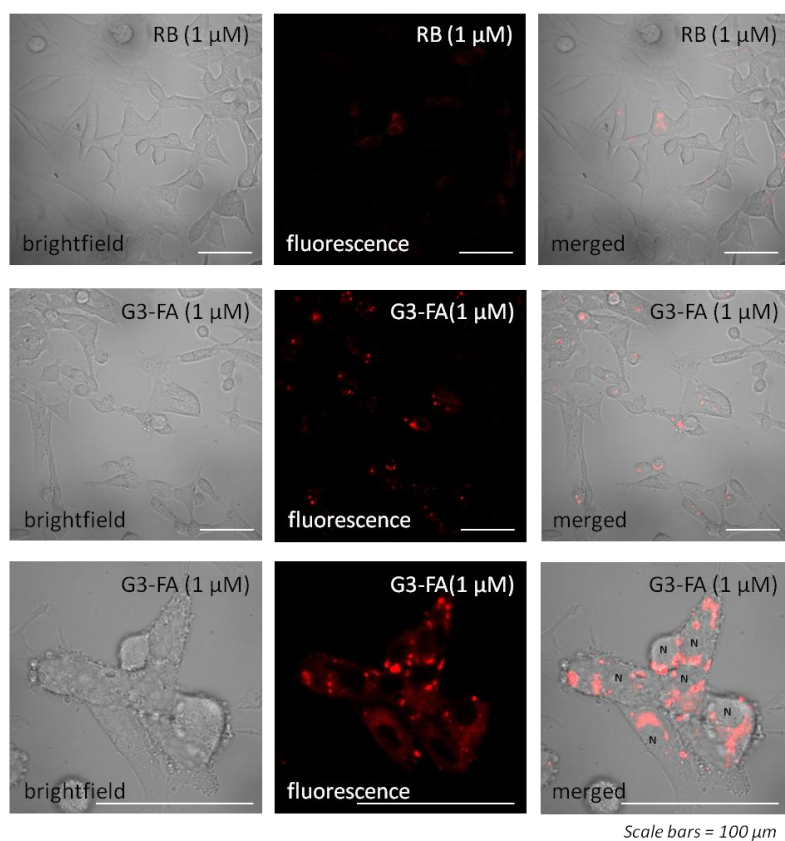


Figure 5.22 Fluorescence microscopy images of rose bengal in solution (top) and G3-FA (middle and bottom), in both case the rose bengal concentration was 1 μM. Scale bars 100 μm.

Thus, it can be concluded that G3-FA is the optimum system to enhance the activity of the photosensitizers by overcoming some of the limitations of RB such as the poor solubility in aqueous media and selectivity for target tissues. This design is now used for other photosensitizers which results are recorded in the following sections.

5.1.3.2 Other PSs silica nanoparticles

Different PSs, commercial and new lab-made based on BODIPY structure, see experimental chapter 3, section 3.1.2.2 *Shell functionalization*, Table 3.1 and 3.2, are now loaded at the external silica surface. The photophysical features, the singlet oxygen production and the phototoxicity action in HeLa cells are compared with their homologous PSs in solution.

The PSs are divided depending on their graftable groups; *i*) carboxylic (chlorin e6, I-BDP-1, I-BDP-2 and DIM), *ii*) silylated (SiBDP-1, SiBDP-2, SiBDP-3, SiBDP-4 and SiDIM) and *iii*) amine group (thionine). Thus, PSs with carboxylic groups were linked to the amine groups of nanoparticles, silylated ones to the hydroxyl groups and those with amine groups to the carboxylic groups of the external surface of MSN. After anchoring the PS in MSN, PEG molecules were tethered at the hydroxyl groups of MSN. Finally, the folic acid was linked to the amine groups, except for the nanoparticles functionalized with COOH to anchored *i.e.* thionine, in this case, a modified folic acid, FA-HDA (see Figure 3.6) was tethered to the carboxylic groups.

The photophysical results of the commercial and lab-made photosensitizers with graftable groups are recorded in chloroform, with the exception of thionine and chlorin e6, which were characterized in methanol and acetone respectively, owing to their lack of solubility in the former solvent (Table 5.12.). These photosensitizers have characteristic absorption bands centred in different regions; in the blue, green and red region of the visible spectra. For instance, the main absorption band of SiBDP-1, is located at 447 nm, SiDIM, DIM, SiBDP-3 and I-BDP-1 display absorption bands in the green region with maxima between 510-540 nm and the absorption of SiBDP-2 and I-BDP-2 in the red region, centered at 675 nm. The two commercial photosensitizers, thionine and Chlorine e6 have their respective absorption maxima at 600 nm and 664 nm, respectively. Importantly, most of the graftable PSs present a high singlet oxygen quantum yield $\geq 80\%$, with the exception of red-PS, with $\Phi_{\Delta} \sim 0.45$, high enough for PDT. However, the high singlet oxygen production hampers

their fluorescence ability ($\Phi_{\text{fl}} \leq 0.03$), except for SiBDP-2 and I-BDP-2 and Chlorin e6 with fluorescence quantum yield of around 20 % (Table 5.12)

On the other hand, the main parameters for the resultant hybrid PS-silica nanoparticles are displayed in Table 5.13. The different color of nanoparticles in suspension is depicted in Figure 5.23.

Table 5.12. Photophysical parameters and singlet oxygen quantum yields for graftable-PSs; absorption maxima (λ_{ab}), molar absorption coefficient (ϵ_{max}), fluorescence maxima (λ_{fl}), fluorescence quantum yield (Φ_{fl}), fluorescence lifetime (τ_{fl}) and singlet oxygen quantum yield (Φ_{Δ}).

Compound	λ_{ab} (nm)	ϵ_{max} 10^{-4} ($\text{M}^{-1} \text{cm}^{-1}$)	λ_{fl} (nm)	Φ_{fl}	τ_{fl} (ns)	Φ_{Δ}
SiBDP-1	447.0	4.3	513.5	0.01	0.21	0.79
SiDIM	511.0	15.22	532.0	0.02	0.02 (97%) 3.88 (3%)	0.84
DIM	511.0	10.34	526.0	0.02	0.03 (94%) 3.57 (6%)	0.77
SiBDP-3	534.0	7.1	547.0	0.03	0.28	0.93
I-BDP-1	535.0	5.3	549.0	0.03	0.28 (99%) 1.00 (1%)	0.98
SiBDP-4	571.0	2.4	595.0	0.02	0.36(35%) 0.65 (65%)	0.86
Thionine	600.0	3.3	621.0	0.06	0.50	0.79
SiBDP-2	675.0	7.9	715.0	0.21	2.05	0.46
I-BDP-2	675.0	4.2	709.0	0.20	2.04	0.44
Chlorin e6	401.0 501.0 664.0	13.7 1.2 4.5	669.5	0.16	4.89	0.80

Table 5.13. Different hybrid PS-MSN synthesized: amount of the photosensitizer tethered, the absorption maxima (λ_{ab}) and the singlet oxygen quantum yield in MeOD (Φ_{Δ}).

System	Characteristic	[PS] ($\mu\text{mol/g}$)	λ_{ab} (nm)	Φ_{Δ}
G4	SiBDP-1-OH-MSN PEG-OH-MSN FA-NH ₂ -MNS	30	435.0	0.62
G5	SiDIM-OH-MSN PEG-OH-MSN FA-NH ₂ -MNS	10	511.0	0.30
G6	DIM-NH ₂ -MSN PEG-OH-MSN FA-NH ₂ -MNS	4	513.0	0.81
G7	I-BDP-1-NH ₂ -MSN PEG-OH-MSN FA-NH ₂ -MNS	3	527.0	-
G8	SiBDP-3-OH-MSN PEG-OH-MSN FA-NH ₂ -MNS	40	528.0	0.69
G9	Th-COOH-MSN PEG-OH-MSN FA-HDA-COOH-MNS	15	599.0	0.84
G10	SiBDP-2-OH-MSN PEG-OH-MSN FA-NH ₂ -MNS	3	635.0	-
G11	Ce6-NH ₂ -MSN PEG-OH-MSN FA-NH ₂ -MNS	6	662.0	0.82
G12	I-BDP-2-NH ₂ -MSN PEG-OH-MSN FA-NH ₂ -MNS	7	670.0	0.50



Figure 5.23. Nanoparticles suspension in MeOD after stirring 24 hours. From left to right; G6, G9, G12, G7, G5, G8, G4 and G10.

The absorption spectra of the PS-MSN are recorded in MeOD after stirring the suspensions for 24 hours. The amount of the anchored photosensitizer is characterized by the absorbance at the maximum of the suspension (see chapter 3, section 3.2.1.6). The presence of the FA was also checked by its characteristic band at 350 nm,⁵¹ although was not possible to quantify because the scatter contribution in this region is too important. The nanosystems demonstrated good stability and low aggregation as a consequence of the PEG-2000 at the external surface (Figure 5.24). Moreover, the singlet oxygen quantum yield of these suspensions were successfully characterized in MeOD, Table 5.13, and compared with the PSs in solutions (see Table 5.12).

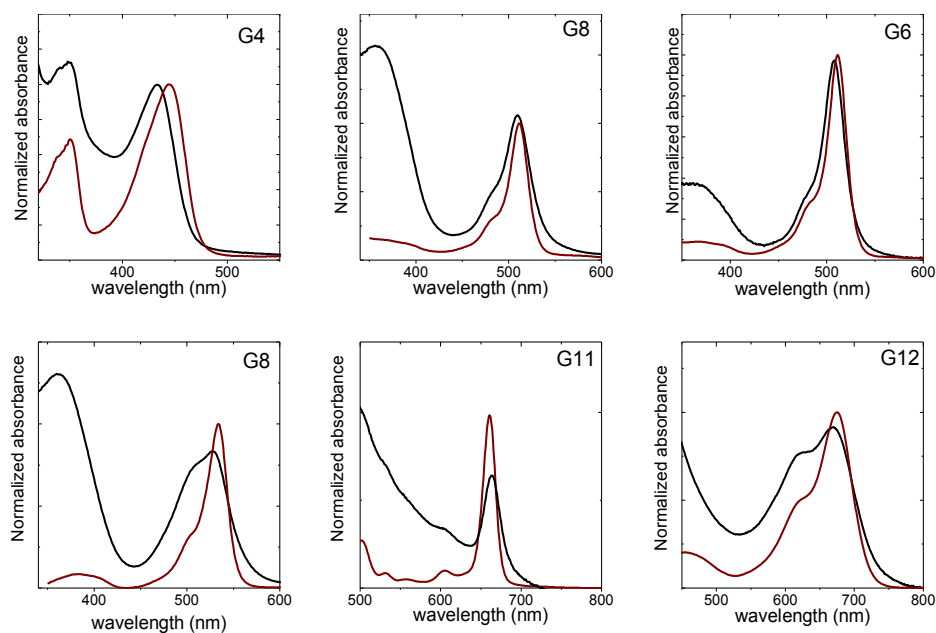


Figure 5.24. Normalized absorption spectra of photosensitizer in solution (brown) and photophotosensitizers tethered in MSN together with PEG and FA (black).

Note here that after the synthesis of some PS-MSN systems, they will be not valid to applicability for PDT for different reasons. For instance, in the case of the photosensitizer SiBDP-4, after anchoring it to hydroxyl groups of the silica, the solution turned from red to white, assigned to a degradation of the dye in polar solvents. As an alternative sample for green illumination, G8 (SiBDP-3) was subsequently synthesized. For the cases of I-BDP-1 (G7) and SiBDP-2 (G10), the amount of PS linked was not enough. Indeed, the amount of SiBDP-2 (G10) covalently linked to the OH groups of the silica was expected to be higher than its analog I-BDP-2 (G12) sample tethered to NH_2 groups of the external silica surface, but the coupling reaction for any reason was not efficient. Finally, sample I-BDP-1 (G7), although the estimated amount of PS linked was not too bad, ($3 \mu\text{mol/g}$, Table 5.13) its suspension hardly show color, Figure 5.23. Thus, due to the low absorbance registered in samples G7 and G10 the singlet oxygen quantification was not possible.

The absorption spectra of several PS-MNS together with the PS in solution are shown in Figure 5.24. Generally, the absorption band is broader and slightly blue-shifted respect to the PS is solution (Figure 5.27 brown), the typical effect described before.

Previous to the test the photodynamic action in HeLa cells, the singlet oxygen generation was studied. Nicely, for samples G6, G9, G11 and G12, the singlet oxygen quantum yield values are approximately the same as in solution, Table 5.12 and Table 5.13. However, for the G4 and G5 the singlet oxygen production decreases in comparison with the PS in solution, Table 5.12 and Table 5.13. The reason can be assigned to the singlet oxygen characterization of these two silylated-BODIPYs (SiBDP-1 and SiDIM) cannot be done in MeOD to avoid self-polymerization and consequently was performed in chloroform. The change of the solvent could be the cause of these differences in the singlet oxygen value. In any case, the singlet oxygen production for G4 and G5 are high enough to induce cellular death under irradiation. Then, all these PS-MSNs have being revealed as promising nanosystems in which PS, PEG and FA have been successfully anchored to the nanoparticles and have demonstrated good stability in MeOD with relatively high singlet oxygen production. Their phototoxicity is now tested by MTT assays in vitro experiments with HeLa cells and compared with their respective PSs in solution (Figure 5.25, 5.26 and 5.27).

The different systems were irradiated under different light source depending on their absorption bands; G4 ($\lambda_{\max} = 435$ nm) under blue irradiation centered at 455 nm at 10 J/cm², G5, G6 and G8 ($\lambda_{\max} = 510$ -530 nm) under green irradiation centered at 518 nm at 10 J/cm² and finally G11 and G12 ($\lambda_{\max} = 635$ -660 nm) were irradiated under deep-red light located at 655 nm at 15 J/cm². Note here that sample G9, with thionine grafted at the external surface, shows an absorption band centered at 600 nm (G9) and there are not suitable light sources (Table 3.4 and Figure 3.11) to irradiate this sample and perform these experiments. The results were compared with those obtained for PSs in solution. Note here that silylated PS cannot be tested in vitro since they will polymerize in the culture media and therefore are compared, if there is, a homologous PS but with carboxylic groups in their molecular structure.

The MTT assay of G4 under blue irradiation (10 J/cm²), Figure 5.25 shows that SiBDP-1 anchored in nanoparticles together with PEG and FA is able to induce a cellular death 70% at 1 μ M. However, in this case, the photoactivity of the PS in solution could not be compared.

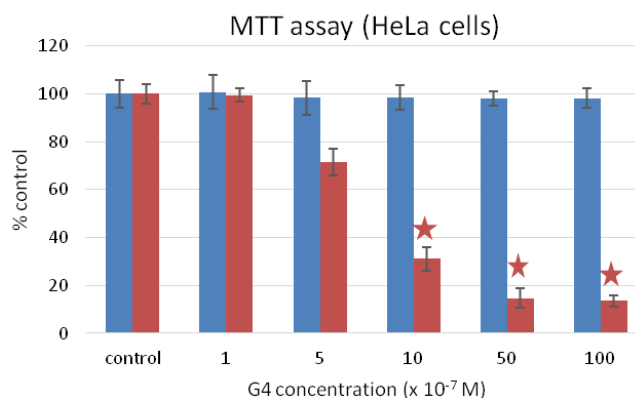


Figure 5.25. MTT assay for the nanosystem G4, in dark condition (blue) and after blue irradiation at 10 J/cm^2 (red). *Significant differences with respect to controls according to the Kruskal Wallis test followed by the Dunn's test or Mann-Whitney's test ($p < 0.05$). Statistical analyses were conducted using the statistical package SPSS v.25 (SPSS Inc., IBM Company, Chicago, USA).

In the case of the nanoparticles with absorption in the green region G5, G6 and G8 the results are recorded in Figure 5.26. The nanomaterial G8 was compared with the I-BDP-1 in solution, Figure 5.26.A-B and G5 and G6 with DIM, Figure 5.26.C, D and E, respectively. Compound I-BDP-1 in solution shows higher phototoxicity than sample G8 at low concentrations. However, for incubated concentrations $\geq 0.5 \mu\text{M}$, both systems demonstrate very efficient phototoxicity action inducing practically 100% of the cellular death. Importantly, the cytotoxicity effect in dark conditions exerts by I-BDP-1 at concentrations $\geq 1 \mu\text{M}$ is eradicated when is tethered in the MSN offering a safer system for clinical applicability. Regarding samples G5 and G6, in which the dimers are tethered to OH- and NH₂- of MSN, respectively, Figure 5.26.D. They are capable of killing 50% of the cell population at $0.1 \mu\text{M}$ concentration, which increases at 80% at $0.5 \mu\text{M}$. Particularly G5 shows a great action under light irradiation practically killing the total cell population at $\geq 1 \mu\text{M}$ concentrations. Indeed their activity to kill cells is similar to systems G8. Then, both systems have enhanced the phototoxicity ability respect to the dimer in solution. Note here, G6 presented dark toxicity at high concentration likely related to the nanoparticle aggregation because the PS at the surface is lowest than the other systems ($4 \mu\text{mol/g}$), Table 5.13, and therefore is required more amount of powder to reach the same PS concentration.

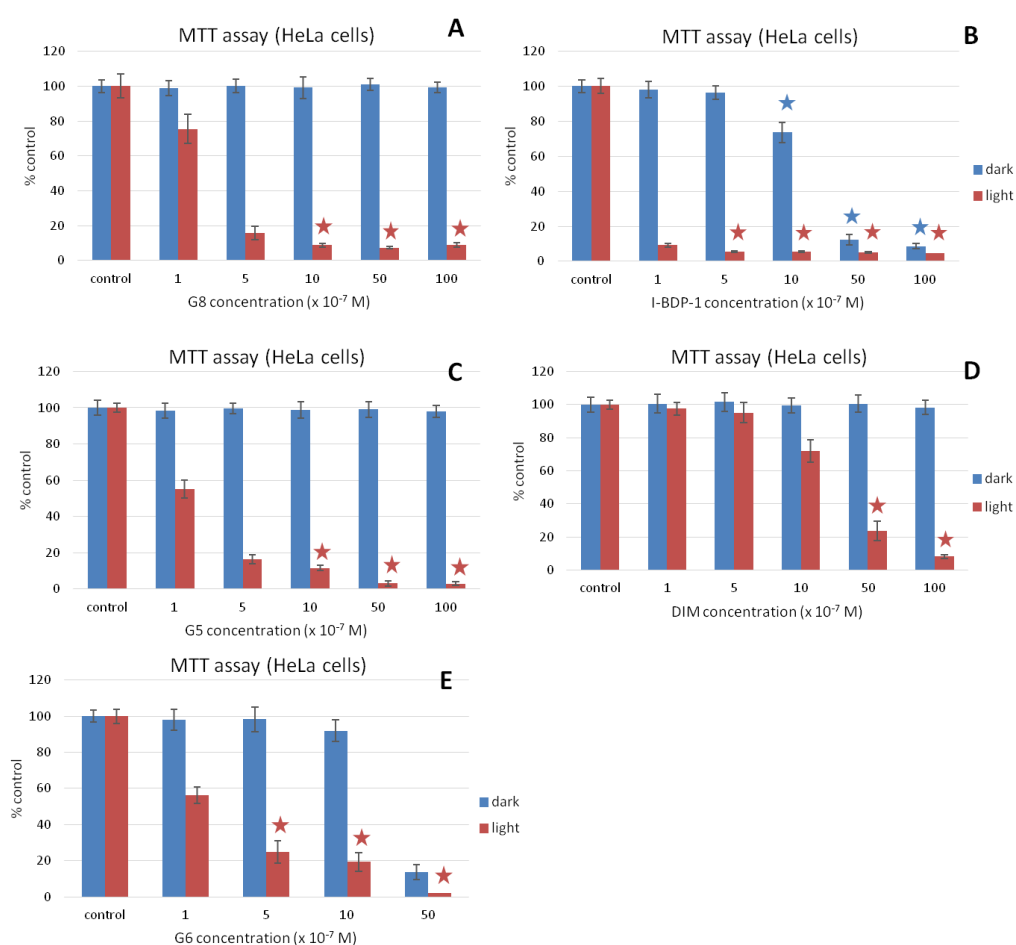


Figure 5.26. MTT assay for the nanosystem G5 (C), G6 (E) and G8 (A) and their homologous PS in solution I-BDP-1 (B) and DIM (D) in dark condition (blue) and after green irradiation at 10 J/cm² (red). *Significant differences with respect to controls according to the Kruskal Wallis test followed by the Dunn's test or Mann-Whitney's test ($p < 0.05$). Statistical analyses were conducted using the statistical package SPSS v.25 (SPSS Inc., IBM Company, Chicago, USA).

Finally, the phototoxicity results of two systems study under deep-red irradiation (15 J/cm²); G11 and G12 are analyzed, Figure 5.27. As in the former cases, the action is compared with the PSs in solution; for G11 with chlorin e6 and for G12 with I-BDP-2, Figure 5.27. One again, the inherent toxicity in dark condition of I-BDP-2 was removed when is anchored to MSN (sample G12), although their phototoxicity has decreased. For instance, I-BDP-2 induced 80 % of the cellular death at 0.1 μ M while

G12 reached 50 % at the same concentration, even though in the highest concentration were less phototoxic inducing around 30 % of the cellular death. In the case of the G11 in which the chlorin e6 was tethered, the nanoparticle also reduced the PS toxicity in dark conditions but did not enhance its phototoxicity effect. Chlorin e6 was able to induce the 70 % of the cellular death at 1 μM , whereas the G11 the 40 %. Nevertheless, G11 was able to destroy 30 % of the cells at 0.1 μM but Chlorin e6 in solution did not show any effect. Then G11 is most efficient at low concentration than the PS in solution and the phototoxicity action could be enhanced increasing the exposition time of the irradiation.⁴⁵

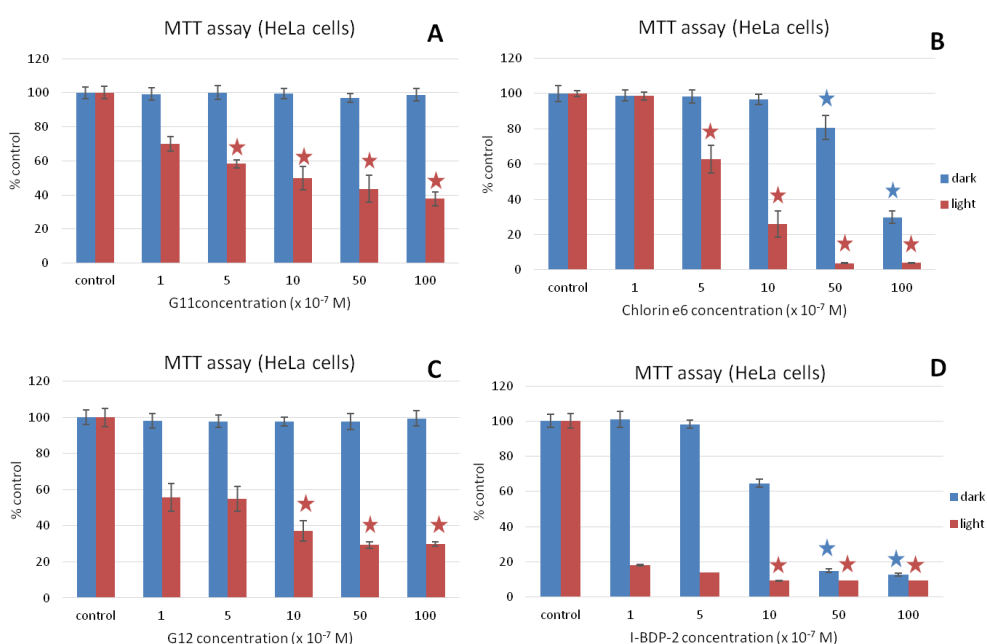


Figure 5.27. MTT assay for the nanosystem G11 (A), and G12 (C) and their homologous PS in solution chlorin e6 (B) and I-BDP-2 (D) in dark condition (blue) and after deep-red irradiation at 15 J/cm² (red). *Significant differences with respect to controls according to the Kruskal Wallis test followed by the Dunn's test or Mann-Whitney's test ($p < 0.05$). Statistical analyses were conducted using the statistical package SPSS v.25 (SPSS Inc., IBM Company, Chicago)

In conclusion, in general, the use of PS-MNS hampered the toxicity of the PS in dark condition, effect sometimes found for PSs in solutions depending on the incubated concentration. Moreover, most of them are able to kill HeLa cells under

relatively low concentration, showing a death population 70 % at 1 μM , with the exception of the samples irradiated under deep-red light with presented less phototoxicity, which is around of 50 % o at this concentration.

5.1.3.3 Conclusions

In this section, the PS-MSN was strategically designed to overcome some of the PS drawbacks; stability in water and selectivity for cancer cells in order to obtain promising nanocarriers for photosensitizers and use them in PDT.

Firstly, a wide study was carried out with a commercial PS, Rose Bengal, to optimize the anchorage of the different molecules (PS, PEG and FA) at the surface of the nanoparticles. The most favorable combination was tethering PEG of 2000 Da at the hydroxyl groups. Besides, in PB-MSN was demonstrated that attaching FA as biotarget for cancer cells enhanced the nanocarriers internalization in HeLa cells

Then, other commercial and new lad-made based-BODIPY PSs MSN were synthesized, photophysically characterized and tested in HeLa cells. Generally, the final hybrid nanosystems displayed enhanced properties with respect to PSs in solutions such as a higher solubility in aqueous media, and negligible cytotoxic effect under dark conditions. Generally, the nanosystems are able to destroy HeLa cells under low concentration achieving a death cell higher than 70 % at 1 μM . Note that, the cellular death induced by these nanosystems would be enhanced increasing the irradiation exposition time avoiding side-effects under dark-conditions. In this regard, G5 and G6, can be considered as the most promising nanosystems demonstrating a much higher phototoxicity effect that PSs in solution, able to induce a cellular death of 80 % at submicromolar concentrations.

5.2. Laponite-clay as nanocarrier for Photodynamic Therapy

Clay minerals were widely used in pharmaceutical and cosmetic products, due to their natural abundance, low cost, favorable physicochemical properties, high adsorption capacities and biocompatibility. For instance, they are being applied for the treatment of acne, infections or indigestion.⁵²⁻⁵⁴ In this work, a commercial nanoclay, Laponite, is used, similarly as the MSN, as a nanocarrier of photosensitizers for potential applications in photodynamic therapy.

Generally, clay minerals are laminar aluminosilicates formed by the condensation of tetrahedral SiO_2 (T) and octahedral Al_2O_3 or MgO (O) sheets. The layers usually present a negative charge, due to the isomorphous substitution of some tetrahedral Si^{4+} and/or octahedral Al^{3+} or Mg^{2+} cations for other cations with lower valence. The net negative charge at the layers is compensated by hydrated interchangeable inorganic cations.⁵⁵ The stacking of clay layers usually forming the so-called tactoid structure (Figure 5.31) with two main adsorption surfaces: a) the external surface and b) the internal surface.

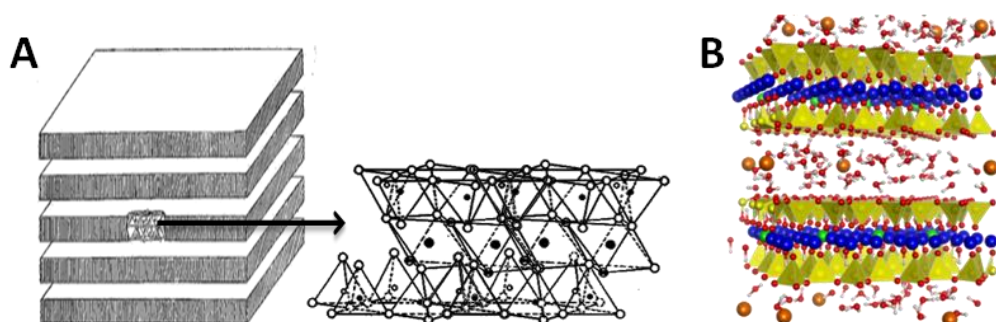


Figure 5.31. Representation of tactoid structure and the composition of TOT layer (A). Laponite-clay structure; Si atoms are represented in yellow, Na in orange, Mg in blue, Li in green, O in red, and H in white (B).

The clay minerals are mainly subdivided (Table 5.13) based on the clay layer structure (TO or TOT) and their charge layer density (x). In this regards, there are neutral clays (such as kaolinite), clays with a moderate charge smectites-types (such as Montmorillonite), and clays with a high net negative charge such as vermiculite and mica-types, Table 5.13.^{56,57}

Table 5.13. Classification of different types of mineral clays, depending on their isomorphic substitution.

Layer type	x = net charge per unit cell	O sheets; Dioctahedral	O sheets; Trioctahedral	Adsorption capacity
TO	Null ($x \approx 0$)	Kaolinite	Serpentine	No
TOT	Null ($x \approx 0$)	Pirofilite	Talc	No
	Moderate ($x \approx 0.2-0.7$)	Smectites (Montmorillonite) (Hectorite, Laponite)		Optimum
	High-moderate ($x \approx 0.7-1$)	Verticulite		yes
	High ($x \approx 1-2$)	Micas		no

In this thesis, it is worked with Laponite (lap), a smectite-type clay. Lap is a trioctahedral synthetic clay mineral with a chemical composition of $[\text{Si}_8]^{\text{T}}[\text{Mg}_{6-x}\text{Li}_x]^{\text{O}}\text{O}_{20}(\text{OH})_4$ and TOT layer structure. The net charge, x , is between 0.6-0.7 valence per cell unit, attributed to the isomorphic substitution of Mg^{2+} by Li^+ in the O layer. Laponite is homoinic clay with sodium as exchangeable cation, characterized by a Cationic Exchange Capacity, CEC, of 73.3 meq/100g. The commercial available Laponite is characterized by flat particles of around 50-100 nm size.^{8,58} The external surface is covered by hydroxyl groups, offering the opportunity to covalently anchor organic molecules by condensation similarly as it has been described for silica nanoparticles (experimental section, chapter 3, section 3.1.2.2 *Shell functionalization*, Scheme 3.7.)

In this section, Laponite is used as nanocarrier for the commercial PS; rose bengal, grafted at the external surface together with PEG-2000 and FA. Firstly, the morphology and particle size of Laponite are analyzed by TEM and DLS (section 5.2.1). Then, the anchorage of RB and PEG and FA, following the formerly described routes, is carried out. The stability in water of these hybrid nanosystems is studied by DLS, as well as its photophysical properties are determined. Finally, the ability of the system to be internalized into the cells and its photoactivity action under irradiation are tested in HeLa cells (section 5.2.3).

5.2.1 Structural characterization

TEM images show single particles of Laponite (Figure 5.32) of plate-like shape with a homogeneous size distribution at around 100 ± 10 nm. Lap nanoparticles in aqueous suspensions show a hydrodynamic size of around 85 nm and zeta potential of -25 mV. The size of these Lap nanoparticles, although bigger than the spherical MSN, could be also suitable for PDT applications.

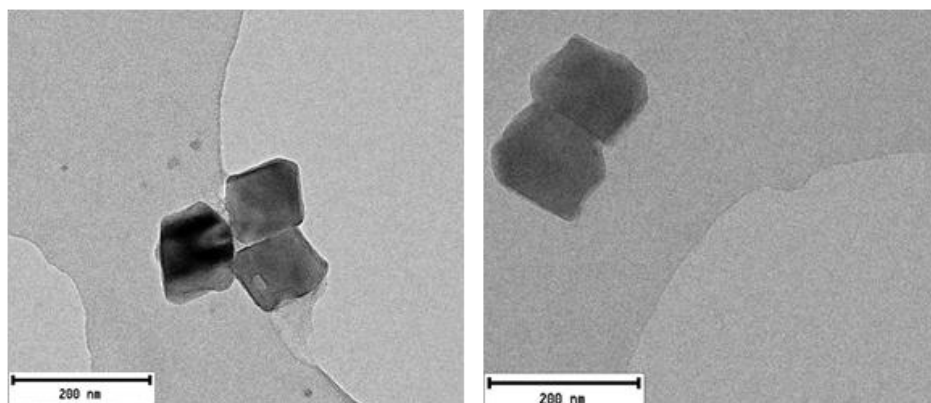


Figure 5.32. TEM images of laponite-clay nanoparticles in water

5.2.2 Rose Bengal and Laponite nanoparticle for photodynamic therapy

Firstly, RB dye is tethered to the external hydroxyl groups of the Lap (Lap-1, Table 5.14). The amount of RB at the nanoclay ($85 \mu\text{mol/g}$, Table 5.14) is higher in comparison with the homologous MSN system G3 ($20 \mu\text{mol/g}$, Table 5.11.). Even though, the RB-nanoclay system is stable in water ($Z_{\text{pot}} = -28$ mV, Table 5.14). The stability is being increased by the presence of PEG molecules at the surface (LAP-2, $Z_{\text{pot}} = -35$ mV, Table 5.14). Indeed, the absorption spectra of Lap-1 and Lap-2 in water confirms this result (Figure 5.33.A). The absorption band of RB of Lap-1 is broader than Lap-2, showing discernible shoulders at both sites of the main absorption band, indicative of the presence of dye aggregates. The nanoparticle aggregation in water is further reduced, as the nanosystem became more complex (LAP-3), and the recorded absorption band of Rose Bengal become even narrower with respect to RB-nanoclay without FA at the external surface.

Table 5.14. Different RB-LAP synthesized and the results obtained the nanoparticle size by DLS in water and their Zeta potential

System	Characteristic	DLS size (nm)	Zpot (mV)	[RB] ($\mu\text{mol/g}$)
LAP	OH-LAP	85	-25	-
LAP-1	RB-OH-LAP	91	-28	85
LAP-2	RB-OH-LAP PEG-OH-LAP	92	-35	85
LAP-3	RB-OH-LAP PEG-OH-LAP FA-OH-LAP	104	-24	47

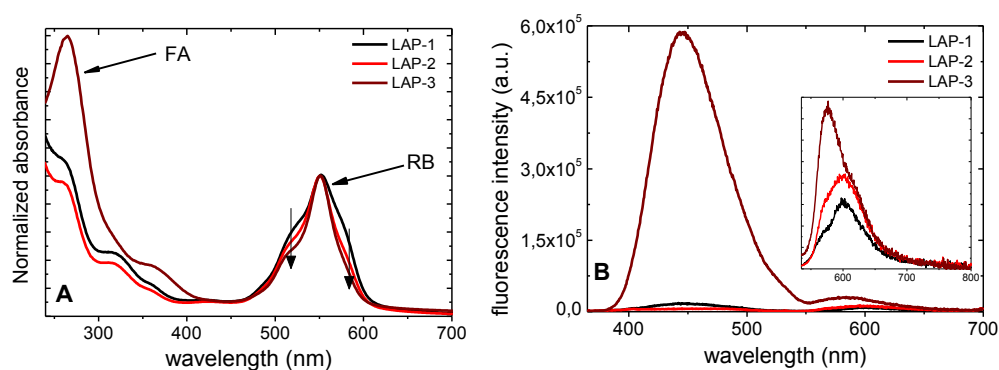


Figure 5.33. Normalized absorption spectra to rose bengal height (A), and emission spectra excited at 355 nm and at 525 nm (inset) (B), for LAP-1 (black), LAP-2 (red) and LAP-3 (brown) in water.

Moreover, the absorption band in the UV region (Figure 5.33.A), only recorded for LAP-3, is indicative of the presence of FA. The anchoring of FA is also confirmed by the fluorescence band registered at 450 nm^{51} for the sample LAP-3 after exciting directly the FA at 355 nm. Note here that the emission of RB is also detected, at 580 nm, under 525 nm excitation (Figure 5.33 B-inset). These samples show a fluorescence quantum yield of 13% and a high singlet oxygen production of 0.84-0.88 % (reference RB in MeOD=0.86).

The good features showed by these three RB-Lap nanosystems in terms of good stability in aqueous media, high singlet oxygen generation and, although modest, fluorescence emission, allow the study of their internalization and phototoxicity action in vitro experiments in HeLa cells. Note that LAP-3 will be compared with the homologous sample G-3-FA (RB, PEG and FA at MSN, section 5.1.3.1).

5.2.3 Rose Bengal Laponite-clay nanoparticle in vitro

In order to analyze the nanoclays internalization and their ability to induce cellular death, LAP-1, LAP-2 and LAP-3 were studied in dark conditions and under green irradiation at a light dose of 10 J/cm^2 .

Firstly, LAP-3 was studied under fluorescence microscopy at $1 \mu\text{M}$ in order to analyze the internalization inside the cells. As it is shown in Figure 5.36, the system is able to be accumulated into the cells, mainly in the lysosomes but not exclusively, being excluded from the nucleus of cells. Note here the amount of the LAP-3 internalized inside the cells seems lower with respect to systems G3-FA, but considerably higher than the amount of internalized RB in solution (Figure 5.25).

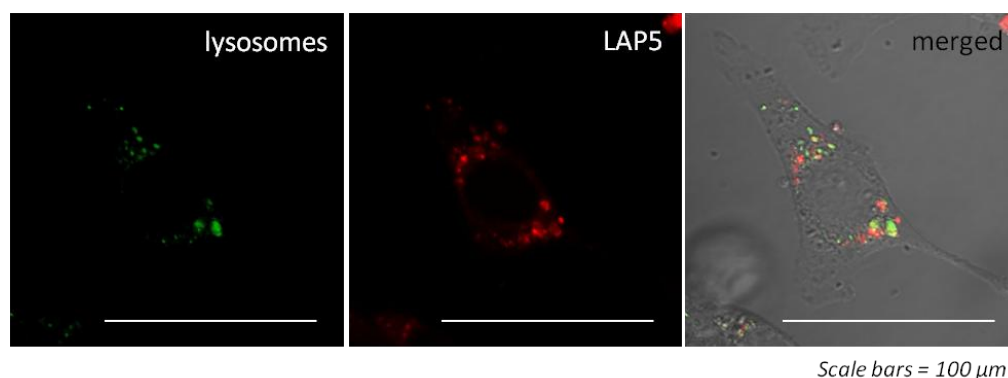


Figure 5.36. Fluorescence microscopy image of LAP-3 nanoparticles internalized in the HeLa cells at $1 \mu\text{M}$. Scale bar equal to $100 \mu\text{m}$.

The results of MTT assays (Figure 5.37) indicate a slight cytotoxicity effect in dark conditions at high RB-LAP concentration ($\geq 5 \mu\text{M}$). Regarding the phototoxicity action, the systems follow the tendency $\text{LAP-3} > \text{LAP-2} \sim \text{LAP-1}$. For instance, a $0.5 \mu\text{M}$ of RB attached at nanoclay, induced cell death of 40 % in sample LAP-1 and LAP-2, whereas 70 % is reached for LAP-3. The higher phototoxic efficiency of LAP-

3 is likely indorsed to the assistance of FA in the nanoparticle internalization. This fact previously stayed for the RB-MSN systems (see section 5.1.3.1).

Importantly, a greater phototoxicity effect is found for LAP-3 in comparison with G3-FA (RB and PEG at the OH-groups of the MSN and FA at external NH_2 - groups, Figure 5.24). Nonetheless, both systems have enhanced the ability to kill HeLa cells respect to RB in solution ability (Figure 5.24), making them interesting nanosystems for PDT applications.

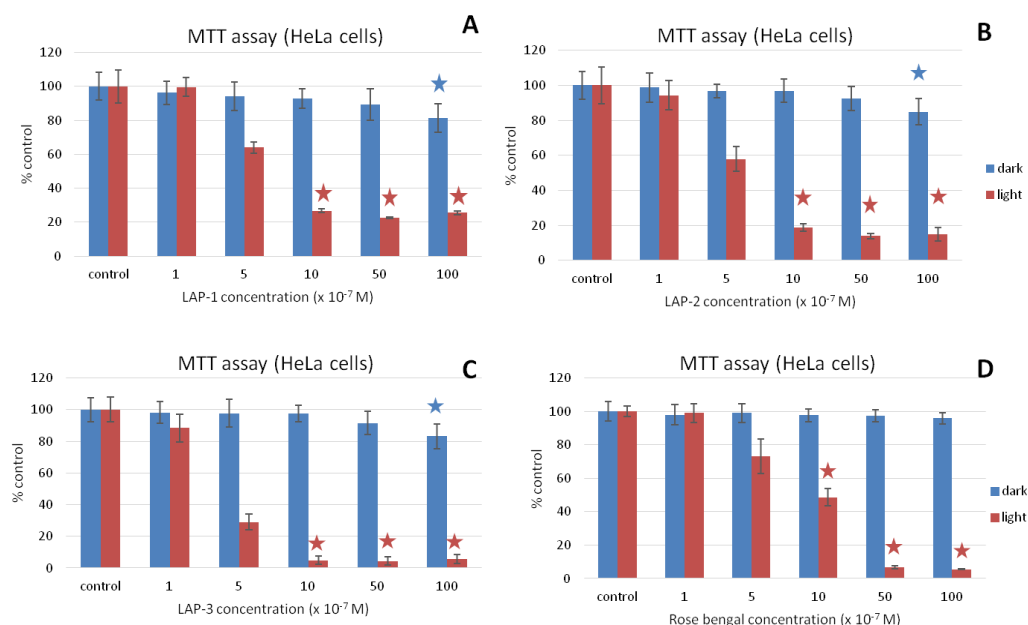


Figure 5.37. MTT assay for LAP-1 (A), LAP-2 (B), LAP-3 (C) and rose bengal in solution (D) in dark condition (blue) and under green irradiation at 10 J/cm^2 (red). *Significant differences with respect to controls according to the Kruskal Wallis test followed by the Dunn's test or Mann-Whitney's test ($p < 0.05$). Statistical analyses were conducted using the statistical package SPSS v.25 (SPSS Inc., IBM Company, Chicago, USA).

5.2.4 Conclusions

In this last section, it was demonstrated that the laponite-clay is an interesting nanocarrier for photosensitizers despite having only hydroxyl functional groups at their external surface. The cytotoxic effect at dark condition induces at high concentration was reduced when the PEG and FA are also anchored at the nanoclay

surface. Moreover, this complete system with PS, PEG and FA tethered (sample LAP-3) offer greater phototoxicity than the respective systems without FA (LAP-1 or LAP-2), indicating the key function of the folic acid in the systems. The FA at the external surface has enhanced its internalization and consequently its phototoxic effects under green irradiation. Finally, LAP-3 shows higher phototoxicity under irradiation if it is compared with its equivalent system G3-FA with mesoporous silica as nanocarrier, although LAP-3 shows slight cytotoxicity in dark condition at high concentration. Thus, depending on the amount of the PS required to induce the cellular death, one nanosystem would be better than the other, *i.e.* for low concentration laponite (avoiding their toxicity in dark) and for high concentration MSN because it is not toxic.

5.3. Bibliography

1. Conde, J., Dias, J. T., Grazú, V., Moros, M., Baptista, P. V. & de la Fuente, J. M. Revisiting 30 years of biofunctionalization and surface chemistry of inorganic nanoparticles for nanomedicine. *Front. Chem.* **2**, (2014).
2. Lucky, S. S., Soo, K. C. & Zhang, Y. Nanoparticles in Photodynamic Therapy. *Chem. Rev.* **115**, 1990–2042 (2015).
3. Mirabello, V., Calatayud, D. G., Arrowsmith, R. L., Ge, H. & Pasqu, S. I. Metallic nanoparticles as synthetic building blocks for cancer diagnostics: from materials design to molecular imaging applications. *J. Mater. Chem. B* **3**, 5657–5672 (2015).
4. Chaturvedi, V. K., Singh, A., Singh, V. K. & Singh, M. P. Cancer Nanotechnology: A New Revolution for Cancer Diagnosis and Therapy. *Curr. Drug Metab.* **20**, 416–429 (2018).
5. Ribeiro, T., Prazeres, T. J. V., Moffitt, M. & Farinha, J. P. S. Enhanced Photoluminescence from Micellar Assemblies of Cadmium Sulfide Quantum Dots and Gold Nanoparticles. *J. Phys. Chem. C* **117**, 3122–3133 (2013).
6. Pérez, N., Ruiz-Rubio, L., Vilas, J. L., Rodríguez, M., Martínez-Martínez, V. & León, L. M. Synthesis and characterization of near-infrared fluorescent and magnetic iron zero-valent nanoparticles. *J. Photochem. Photobiol. A Chem.* **315**, 1–7 (2016).
7. Bobo, D., Robinson, K. J., Islam, J., Thurecht, K. J. & Corrie, S. R. Nanoparticle-Based Medicines: A Review of FDA-Approved Materials and Clinical Trials to Date. *Pharm. Res.* **33**, 2373–2387 (2016).
8. Zhuang, Y., Zhao, L., Zheng, L., Hu, Y., Ding, L., Li, X., Liu, C., Zhao, J., Shi, X. & Guo, R. LAPONITE-Polyethylenimine Based Theranostic Nanopatform for Tumor-Targeting CT Imaging and Chemotherapy. *ACS Biomater. Sci. Eng.* **3**, 431–442 (2017).
9. Alexis, F., Pridgen, E., Molnar, L. K. & Farokhzad, O. C. Factors affecting the clearance and biodistribution of polymeric nanoparticles. *Mol. Pharm.* **5**, 505–515 (2008).
10. Mousa, M., Evans, N. D., Oreffo, R. O. C. & Dawson, J. I. Clay nanoparticles for regenerative medicine and biomaterial design: A review of clay bioactivity. *Biomaterials* **159**, 204–214 (2018).
11. Rudramurthy, G. R. & Swamy, M. K. Potential applications of engineered nanoparticles in medicine and biology: an update. *JBIC J. Biol. Inorg. Chem.* **23**, 1185–1204 (2018).
12. Jeevanandam, J., Barhoum, A., Chan, Y. S., Dufresne, A. & Danquah, M. K. Review on nanoparticles and nanostructured materials: history, sources, toxicity and regulations. *Beilstein J. Nanotechnol.* **9**, 1050–1074 (2018).

13. Malvindi, M. A., Brunetti, V., Vecchio, G., Galeone, A., Cingolani, R. & Pompa, P. P. SiO₂ nanoparticles biocompatibility and their potential for gene delivery and silencing. *Nanoscale* **4**, 486 (2012).
14. Wheeler, P. A., Wang, J., Baker, J. & Mathias, L. J. Synthesis and characterization of covalently functionalized laponite clay. *Chem. Mater.* **17**, 3012–3018 (2005).
15. Manzano, M. & Vallet-Regí, M. Mesoporous Silica Nanoparticles for Drug Delivery. *Adv. Funct. Mater.* **30**, 1902634 (2020).
16. Vallet-Regí, M., Colilla, M., Izquierdo-Barba, I. & Manzano, M. Mesoporous silica nanoparticles for drug delivery: Current insights. *Molecules* **23**, 1–19 (2018).
17. Dawidczyk, C. M., Kim, C., Park, J. H., Russell, L. M., Lee, K. H., Pomper, M. G. & Searson, P. C. State-of-the-art in design rules for drug delivery platforms: Lessons learned from FDA-approved nanomedicines. *J. Control. Release* **187**, 133–144 (2014).
18. Santiago, A. M., Ribeiro, T., Rodrigues, A. S., Ribeiro, B., Frade, R. F. M., Baleizão, C. & Farinha, J. P. S. Multifunctional Hybrid Silica Nanoparticles with a Fluorescent Core and Active Targeting Shell for Fluorescence Imaging Biodiagnostic Applications. *Eur. J. Inorg. Chem.* **2015**, 4579–4587 (2015).
19. Son, J., Yang, S. M., Yi, G., Roh, Y. J., Park, H., Park, J. M., Choi, M. & Koo, H. Folate-modified PLGA nanoparticles for tumor-targeted delivery of pheophorbide a in vivo. *Biochem. Biophys. Res. Commun.* **498**, 523–528 (2018).
20. Dam, G. M. Van, Themelis, G., Crane, L. M. A., Harlaar, N. J., Pleijhuis, R. G., Kelder, W., Sarantopoulos, A., Jong, J. S. De, Arts, H. J. G., Zee, A. G. J. Van Der, Bart, J., Low, P. S. & Ntziachristos, V. Technical Reports Intraoperative tumor-specific fluorescence imaging in ovarian cancer by folate receptor- α targeting : first in-human results. *Nat. Med.* **17**, 1315–1319 (2011).
21. Stöber, W., Fink, A. & Bohn, E. Controlled growth of monodisperse silica spheres in the micron size range. *J. Colloid Interface Sci.* **26**, 62–69 (1968).
22. Wu, S.-H., Mou, C.-Y. & Lin, H.-P. Synthesis of mesoporous silica nanoparticles. *Chem. Soc. Rev.* **42**, 3862 (2013).
23. Lin, Y.-S. & Haynes, C. L. Impacts of Mesoporous Silica Nanoparticle Size, Pore Ordering, and Pore Integrity on Hemolytic Activity. *J Am Chem Soc* **132**, 4834–4842 (2010).
24. Mai, W. X. & Meng, H. Mesoporous silica nanoparticles: A multifunctional nano therapeutic system. *Integr. Biol.* **5**, 19–28 (2013).
25. Manzano, M. & Vallet-Regí, M. Mesoporous silica nanoparticles in nanomedicine applications. *J. Mater. Sci. Mater. Med.* **29**, (2018).

26. Villaverde, G., Baeza, A., Melen, G. J., Alfranca, A., Ramirez, M. & Vallet-Regí, M. A new targeting agent for the selective drug delivery of nanocarriers for treating neuroblastoma. *J. Mater. Chem. B* **3**, 4831–4842 (2015).
27. Crucho, C. I. C., Baleizão, C. & Farinha, J. P. S. Functional Group Coverage and Conversion Quantification in Nanostructured Silica by ¹H NMR. *Anal. Chem.* **89**, 681–687 (2017).
28. Ribeiro, T., Baleizão, C. & Farinha, J. P. S. Synthesis and characterization of perylenediimide labeled core-shell hybrid silica-polymer nanoparticles. *J. Phys. Chem. C* **113**, 18082–18090 (2009).
29. Ribeiro, T., Raja, S., Rodrigues, A. S., Fernandes, F., Farinha, J. P. S. & Baleizão, C. High performance NIR fluorescent silica nanoparticles for bioimaging. *RSC Adv.* **3**, 9171 (2013).
30. Cardelli, A., Ricci, L., Ruggeri, G., Borsacchi, S. & Geppi, M. Optical properties of a polyethylene dispersion with a luminescent silica prepared by surface grafting of a perylene derivative. *Eur. Polym. J.* **47**, 1589–1600 (2011).
31. Kolmakov, K., Belov, V. N., Bierwagen, J., Ringemann, C., Müller, V., Eggeling, C. & Hell, S. W. Red-emitting rhodamine dyes for fluorescence microscopy and nanoscopy. *Chem. - A Eur. J.* **16**, 158–166 (2010).
32. Epelde-Elezcano, N., Prieto-Montero, R., Martínez-Martínez, V., Ortiz, M. J., Prieto-Castañeda, A., Peña-Cabrera, E., Belmonte-Vázquez, J. L., López-Arbeloa, I., Brown, R. & Lacombe, S. Adapting BODIPYs to singlet oxygen production on silica nanoparticles. *Phys. Chem. Chem. Phys.* **19**, 13746–13755 (2017).
33. Martins Estevão, B., Miletto, I., Marchese, L. & Gianotti, E. Optimized Rhodamine B labeled mesoporous silica nanoparticles as fluorescent scaffolds for the immobilization of photosensitizers: a theranostic platform for optical imaging and photodynamic therapy. *Phys. Chem. Chem. Phys.* **18**, 9042–9052 (2016).
34. Zhang, X. F., Zhang, Y. & Liu, L. Fluorescence lifetimes and quantum yields of ten rhodamine derivatives: Structural effect on emission mechanism in different solvents. *J. Lumin.* **145**, 448–453 (2014).
35. Magde, D., Rojas, G. E. & Seybold, P. G. Solvent Dependence of the Fluorescence Lifetimes of Xanthene Dyes. *Photochem. Photobiol.* **70**, 737–744 (1999).
36. López Arbeloa, T., López Arbeloa, F., Hernández Bartolomé, P. & López Arbeloa, I. On the mechanism of radiationless deactivation of rhodamines. *Chem. Phys.* **160**, 123–130 (1992).
37. Vlachy, N., Touraud, D., Heilmann, J. & Kunz, W. Determining the cytotoxicity of cationic surfactant mixtures on HeLa cells. *Colloids Surfaces B Biointerfaces* **70**, 278–280 (2009).

38. Hwang, T. L., Sung, C. T., Aljuffali, I. A., Chang, Y. T. & Fang, J. Y. Cationic surfactants in the form of nanoparticles and micelles elicit different human neutrophil responses: A toxicological study. *Colloids Surfaces B Biointerfaces* **114**, 334–341 (2014).
39. Loe, D. W. & Sharom, F. J. Interaction of multidrug-resistant Chinese hamster ovary cells with the peptide ionophore gramicidin D. *BBA - Biomembr.* **1190**, 72–84 (1994).
40. Connor, E. E., Mwamuka, J., Gole, A., Murphy, C. J. & Wyatt, M. D. Gold nanoparticles are taken up by human cells but do not cause acute cytotoxicity. *Small* **1**, 325–327 (2005).
41. Yildirim, A., Turkaydin, M., Garipcan, B. & Bayindir, M. Cytotoxicity of multifunctional surfactant containing capped mesoporous silica nanoparticles. *RSC Adv.* **6**, 32060–32069 (2016).
42. Martins Estevão, B., Cucinotta, F., Hioka, N., Cossi, M., Argeri, M., Paul, G., Marchese, L. & Gianotti, E. Rose Bengal incorporated in mesostructured silica nanoparticles: structural characterization, theoretical modeling and singlet oxygen delivery. *Phys. Chem. Chem. Phys.* **17**, 26804–26812 (2015).
43. Kabanov, V., Press, D. J., Huynh, R. P. S., Shimizu, G. K. H. & Heyne, B. Assessment of encapsulated dyes' distribution in silica nanoparticles and their ability to release useful singlet oxygen. *Chem. Commun.* **54**, 6320–6323 (2018).
44. Kim, B., Sui, B., Yue, X., Tang, S., Tichy, M. G. & Belfield, K. D. In Vitro Photodynamic Studies of a BODIPY-Based Photosensitizer. *European J. Org. Chem.* **2017**, 25–28 (2017).
45. Bharathiraja, S., Moorthy, M. S., Manivasagan, P., Seo, H., Lee, K. D. & Oh, J. Chlorin e6 conjugated silica nanoparticles for targeted and effective photodynamic therapy. *Photodiagnosis Photodyn. Ther.* **19**, 212–220 (2017).
46. Paris, J. L., Villaverde, G., Cabañas, M. V., Manzano, M. & Vallet-Regí, M. From proof-of-concept material to PEGylated and modularly targeted ultrasound-responsive mesoporous silica nanoparticles. *J. Mater. Chem. B* **6**, 2785–2794 (2018).
47. Freitas, L. B. de O., Bravo, I. J. G., Macedo, W. A. de A. & de Sousa, E. M. B. Mesoporous silica materials functionalized with folic acid: preparation, characterization and release profile study with methotrexate. *J. Sol-Gel Sci. Technol.* **77**, 186–204 (2016).
48. Zwicke, G. L., Ali Mansoori, G. & Jeffery, C. J. Utilizing the folate receptor for active targeting of cancer nanotherapeutics. *Nano Rev.* **3**, 18496 (2012).
49. Gianotti, E., Martins Estevão, B., Cucinotta, F., Hioka, N., Rizzi, M., Renò, F. & Marchese, L. An Efficient Rose Bengal Based Nanoplatfor for Photodynamic Therapy. *Chem. - A Eur. J.* **20**, 10921–10925 (2014).

50. Pérez-Herrero, E. & Fernández-Medarde, A. Advanced targeted therapies in cancer: Drug nanocarriers, the future of chemotherapy. *Eur. J. Pharm. Biopharm.* **93**, 52–79 (2015).
51. Kristian, M., Engeset, A., Carmen, A., Juzeniene, A., Vorobey, A., Johnsson, A. & Moan, J. Ultraviolet photodegradation of folic acid. **80**, 47–55 (2005).
52. Zadaka, D., Rabinovitz, O. N. N., Serban, C., Groisman, L. & Rubin, B. Water Purification from Organic Pollutants by Optimized Micelle - Clay Systems. *Environ. Sci. Technol* **39**, 2343–2348 (2005).
53. Cheng, S.-H., Lee, C.-H., Yang, C.-S., Tseng, F.-G., Mou, C.-Y. & Lo, L.-W. Mesoporous silica nanoparticles functionalized with an oxygen-sensing probe for cell photodynamic therapy: potential cancer theranostics. *J. Mater. Chem.* **19**, 1252 (2009).
54. Tomás, H., Alves, C. S. & Rodrigues, J. Laponite®: A key nanoplatform for biomedical applications? *Nanomedicine Nanotechnology, Biol. Med.* **14**, 2407–2420 (2018).
55. López-Arbeloa, F., López Arbeloa, T. & López Arbeloa, I. Electronic Spectroscopy of Rhodamine Dyes Adsorbed at Clay Surfaces. in *Encyclopedia of Surface and Colloid Science 2nd Edition* (ed. Somasundaran, P.) 2325–2337 (2006).
56. Auerbach, S. M., Carrado, K. a. & Dutta, P. K. *Handbook of Layered Materials. Handbook of Layered Materials* (2004). doi:10.1201/9780203021354.
57. López Arbeloa, F., Martínez Martínez, V., Arbeloa, T. & López Arbeloa, I. Photoresponse and anisotropy of rhodamine dye intercalated in ordered clay layered films. *J. Photochem. Photobiol. C Photochem. Rev.* **8**, 85–108 (2007).
58. Xu, F., Liu, M., Li, X., Xiong, Z., Cao, X., Shi, X. & Guo, R. Loading of indocyanine green within polydopamine-coated laponite nanodisks for targeted cancer photothermal and photodynamic therapy. *Nanomaterials* **8**, 1–16 (2018).

6

GENERAL CONCLUSIONS

General conclusions

Along with this thesis, new biocompatible systems with fluorescence, singlet oxygen production or also dual activity as well as solubility in aqueous media and selectivity to specific organelles or cancer cells to be implemented in medical applications, to detect and treat cancer, are attained. Particularly, fluorescence biomarkers for bioimaging (diagnosis) and improved photosensitizers for photodynamic therapy, PDT, (treatment) are developed. The most relevant aspects of this work are listed below.

In the first part, it is demonstrated how the rich chemistry of BODIPY dyes allows a rational modification of its skeleton to tune their chemo-physical properties aimed to:

- i) Increase the solubility of BODIPYs dyes in aqueous media by the addition of tetra- and octaethylene glycol chains or zwitterionic (sulfobetaine) hydrophilic tags through the boron atom via a one-pot direct post-functionalization process. The resultant new BODIPYs are highly fluorescent and stable under the most common aqueous conditions used in biological settings (pH 6-8). The live-cell studies demonstrate a high cell membrane permeability for the BODIPY-tetraethylene glycol derivatives allowing its use as stains of cells at high concentrations (section 4.1.1. *BODIPYs soluble in water*).
- ii) Induce specificity to stain mitochondria organelle by the incorporation of the biomolecule, L-carnitine, to the BODIPY through the boron atom forming a B-spiro system. In contrast to other mitotrakers, the BDP-carnitine is the first fluorescent probe that is actively channeled into the mitochondrial matrix by specific mitochondrial membrane transport in living cells (4.1.2. *L-carnitine BODIPY*).
- iii) Increase the triplet state population in detriment of the inherent high fluorescence efficiency of BODIPYs to achieve new photosensitizers with high singlet oxygen production for PDT applications or balanced both properties for theragnosis (biomaging + PDT). The BODIPY is transformed into excellent photosensitizers via different approaches to enhance the probability of intersystem crossing (ISC) process: by the addition of heavy atoms, *i.e.* iodine atoms (4.2.1. *Halogenated BODIPYs*), or by attaching electron-donor groups (4.2.2. *Halogen-free BODIPYs*) to activate intramolecular charge transfer states. The main achievements are:

- A Iodinated-BODIPY-derivative, 8-methylthio-2,6-diiodoBODIPY, MeSBDP, is proposed as a universal reference for singlet oxygen quantum yield calculation by direct method under UV-blue and Visible irradiation. It has shown a high singlet oxygen quantum yields in a variety of solvents, under UV-blue and green region of the electromagnetic spectrum, together with the absence of deactivation of singlet oxygen by MeSBDP itself and its noticeable photostability (4.2.1.1. *MeSBDP as standard reference*).
- Several iodinated-BODIPYs with intense absorption bands into the clinic window (> 650 nm) or panchromatic spectra and with a good balance between the fluorescence efficiency and singlet oxygen production were studied. In vitro experiments demonstrated that some of them are internalized into HeLa cells showing good phototoxicity effects under deep-red irradiation or white light illumination (4.2.1.2 *I-BODIPY in the red region*).
- Halogen-free BODIPYs with dual action (fluorescence and singlet oxygen) were designed by the chemical manipulation of the push-pull character of the BODIPY chromophore, by attaching different electron-donating groups, *i.e.* functionalization at-boron with BINOL moieties (4.2.1.3. *Binol-based BODIPYs*) or at-*meso* position with enamines (4.2.1.4. *Enamine-based BODIPYs*). These purely organic dyes reduce the inherent toxicity of halogen-photosensitizers, and generally offer higher triplet lifetimes, increasing their performance in PDT applications.

In the second part, the delivery to tumor cells of the different photoactive compounds (fluorophores or photosensitizers) is enhanced by the use of functionalized silica-based nanoparticles as carriers. The synthesis of hybrid nanosystems is aimed to improve their bioimaging and photodynamic therapy abilities. The main achievements were:

- i) Three different types of spherical silica nanoparticles, nonporous, mesoporous and ormosil, of suitable size of around 50 nm with homogeneous distribution and functionalized external surface with different groups to allow the anchorage of organic molecules of interest are synthesized. In this way, the nanoparticles can be coated by the photoactive molecule (fluorophore or photosensitizer), PEG-2000 to stabilize the nanoparticle suspension in water and to prolong the

circulatory time, and folic acid (FA) as active biotarget for cancer cells (5.1.1 *Structural characterization*).

- ii) Fluorescent nanoparticles are obtained by loading commercial fluorophores, perylene and rhodamine, mainly in the core by different approaches depending on the silica nanoparticle type: chemical condensation in case of nonporous nanoparticles or physical dye occlusion for mesoporous and ormosil silica nanoparticles. The in vitro experiments show a good internalization into HeLa cells, being selectively accumulated in lysosomes (5.1.2 *Fluorescent silica nanoparticles for bioimaging*).
- iii) PS-mesoporous silica nanoparticles are strategically designed to overcome some of the PS limitations (stability in water and selectivity for cancer cells). By the covalent linking of different photosensitizers (commercial as Rose Bengal, Thionine and Chlorine e6 and lab-made based on BODIPY derivatives with graftable groups), besides PEG and FA, at the external surface of MSN, a better performance respect to the PS in solutions, in terms of higher internalization, improved phototoxicity action without any cytotoxicity in dark conditions, is reached in HeLa cells (5.1.3 *Photosensitizer-silica nanoparticles for photodynamic therapy*).
- iv) PS-Laponite nanoclay is demonstrated to be also a good nanosystem for PDT (5.2 *Laponite-clay as nanocarrier PDT*). It shows a higher phototoxicity effect under irradiation respect to PS-MSN but on the contrary, also induces cytotoxicity in dark conditions at high-incubated concentrations. Thus, PS-LAP would bring a more effective photoaction but PS-MSN would offer safer conditions for clinical applicability minimizing side-effects. Indeed, the effectiveness of the treatment can be regulated by playing with the light doses and the irradiation exposition time.

List of publications

Published

1. Gómez-Infante, A., Bañuelos, J., Valois-Escamilla, I., Cruz-Cruz, D., Prieto-Montero, R., López-Arbeloa, I., Arbeloa, T. & Peña-Cabrera, E. Synthesis, Properties, and Functionalization of Nonsymmetric 8-MethylthioBODIPYs. *European Journal of Organic Chemistry*. **2016**; (29) 5009-5023.
2. Epelde-Elezcano, N., Prieto-Montero, R., Martínez-Martínez, V., Ortiz, M. J., Prieto-Castañeda, A., Peña-Cabrera, E., Belmonte-Vázquez, J. L., López-Arbeloa, I., Brown, R. & Lacombe, S. Adapting BODIPYs to singlet oxygen production on silica nanoparticles. *Physical Chemistry Chemical Physics*. **2017**; 19(21):13746-13755.
3. Palao-Utiel, E., Montalvillo-Jiménez, L., Esnal, I., Prieto-Montero, R., Agarrabeitia, A. R., García-Moreno, I., Bañuelos, J., López-Arbeloa, I., de la Moya, S. & Ortiz, M. J. Controlling Vilsmeier-Haack processes in meso-methylBODIPYs: A new way to modulate finely photophysical properties in boron dipyrromethenes. *Dye and Pigments*. **2017**; 141:286-298.
4. Prieto-Montero, R., Sola-Llano, R., Montero, R., Longarte, A., Arbeloa, T., López-Arbeloa, I., Martínez-Martínez, V. & Lacombe, S. Methylthio BODIPY as a standard triplet photosensitizer for singlet oxygen production: a photophysical study. *Physical Chemistry Chemical Physics*. **2019**; 21(36):20403-20414.
5. Blázquez-Moraleja, A., Álvarez-Fernández, D., Prieto Montero, R., García-Moreno, I., Martínez-Martínez, V., Bañuelos, J., Sáenz-de-Santa-María, I., Chiara, M. D. & Chiara, J. L. A general modular approach for the solubility tagging of BODIPY dyes. *Dye and Pigments*. **2019**;170,107545-107556.
6. Jimenez, J., Prieto-Montero, R., Maroto, B.L., Moreno, F., Ortiz, M. J., Oliden-Sánchez, A., López-Arbeloa, I., Martínez-Martínez, V. & Moya, S. Manipulating Charge Transfer States in BODIPYs: A Model Strategy to Rapidly Develop Photodynamic Theragnostic Agents. *Chemistry A European Journal*. **2019**; 26 (3) 601-605.

7. Blázquez-Moraleja, A., Sáenz-de-Santa, M. I., Chiara, M.D., Álvarez-Fernández, D., García-Moreno, I., Prieto-Montero, R., Martínez-Martínez, V., López Arbeloa, I. & Chiara, J. L. Shedding light on the mitochondrial matrix through a functional membrane transporter. *Chemical Science*. **2020**; 11 (4) 1052-1065.

Submitted

8. Prieto-Montero, R., Prieto-Castañeda, A., Sola-Llano, R., Agarrabeitia, A.R., García-Fresnadillo, D., López-Arbeloa, I., Villanueva, A. Martinez-Martinez, V., de la Moya, S. & Ortiz, M.J., Exploring BODIPY Derivatives as Singlet Oxygen Photosensitizers for PDT. Special issue in memory of Prof. Thomas Dougher in Photochemistry and Photobiology

Conference papers

9. Palao, E., Prieto-Montero, R., Prieto-Castañeda, A., Epelde-Elezcano, N., Agarrabeitia, A. R., Moreno, F., Maroto, B. L., Martinez-Martinez, V., de la Moya, S., Prieto-Castañeda, A. & Ortiz, M. J. Exploring BODIPY meso-enamines as singlet-oxygen photosensitizers for PDT (*ECSOC conference Presentation proceeding*) **2017**. doi: 10.3390/ecsoc-21-04785
10. Martinez-Martinez, V., Sola-Llano, R., Prieto-Montero, R., Prieto-Castañeda, A., Tabero, A., López-Arbeloa, I., Villanueva, A., Agarrabeitia, R. A., de la Moya, S., Ortiz, M. J. & Martínez-Martínez, V. Alternative photosensitizers based on BODIPY chromophore (*Proc.SPIE, 17th International Photodynamic Association World Congress, conference Presentation proceeding*). **2019**;11070. doi:10.1117/12.2525343

In preparation

- i. *Iodinated-BODIPY photosensitizers as theragnostic agents for PDT.*
- ii. *Halogen-free Photosensitizers based on enamine-BODIPY for bioimaging and photodynamic therapy*
- iii. *Fluorescence dye loaded silica nanoparticles for bioimaging*
- iv. *Photosensitizer-silica nanoparticles as new systems for photodynamic therapy*
- v. *Laponite-clay as potential nanocarrier of PSs for cancer therapy by PDT*